ANALYSIS OF THE SEISMIC RESPONSE OF HIGHWAY BRIDGES TO MULTIPLE SUPPORT EXCITATIONS

A Thesis
Submitted in Partial Fulfilment
of
the Requirements for the Degree
of Doctor of Philosophy in Civil Engineering
at the
University of Canterbury
Christchurch
New Zealand

by

Jiachen Wang

June 2003

ABSTRACT

It is recognized that the spatial variability of the ground motion has an important effect on the seismic responses of extended structures, but it is not well known how these structural responses will be affected. The aim of this study was to gain insight of the effect of asynchronous inputs on the elastic and inelastic responses of long bridges in order to improve the earthquake resistant design of bridges.

In this research, a simple method of generating the asynchronous input motions, conditioned by the recorded time-histories, is proposed. Two assumptions were adopted in this method. The first assumption was that the spatial correlation function depended only on the predominant frequency of the earthquake motion. The second assumption was that in the time domain, there was no correlation between the acceleration elements in the same record. With the aid of these two assumptions, the modified Kriging method proposed by Hoshiya could be easily used to simulate ground motions in the time domain. Numerical examples showed that the spectra of simulated time-histories and the specified earthquake record closely correlated with each other and the variation of the simulated accelerations with the separation distance between the supports, the propagation velocity and the dispersion factor followed the trends expected.

It was observed that the velocity of propagation of seismic waves had a significant effect on the transverse response of long bridges in travelling wave cases. The transverse responses of the bridges to the travelling waves can be more critical than those to the synchronous input. The transverse response parameters investigated were the maximum pier drifts, the maximum pier shear forces and the maximum section curvature ratios of the piers. The responses of the bridges subjected to asynchronous inputs consist of two parts: the dynamic components induced by the inertial forces and the pseudo-static components due to the differential displacements between the adjacent supports. The response was dominated by the pseudo-static component when the travelling wave velocity was low. The pseudo-static component reduced and the dynamic component increased as the travelling wave velocity increased. The response was dominated by the dynamic component when the travelling wave velocity was high. The local variations of the responses with the travelling wave velocity were due to the variations in the acceleration spectra of the input motions with the travelling wave velocity.

It was found that the geometric incoherence effect also played an important role in the responses of the bridges through the pseudo-static components. In the cases that the combined

geometric incoherence and wave passage effects of the spatial variability of the seismic motion were considered, the pseudo-static component of the seismic response of long bridges was not only caused by the wave passage effect, but was also due to the geometric incoherence effect. The pseudo-static component caused by the geometric incoherence effect dominated the total responses when wave dispersion was greatest. Because the variations of the accelerograms at different pier supports were random, the value of the pseudo-static component due to the geometric incoherence effect was also random. Therefore the total responses were unpredictable when the wave dispersion was great. The influence of the pseudo-static component in the total response decreased as the wave dispersion decreased. When dispersion was least the trends of the variations of the response with the travelling wave velocity were similar to those for the travelling wave cases without wave dispersion.

The longitudinal responses of the bridge models with movement joints subjected to asynchronous inputs were also investigated. It was found that the relative displacement of the bridge deck across the movement joints and the relative displacement between the girder end and the top of the abutment consist of two parts: the dynamic components due to the difference between the vibrations of the two frames separated by the movement joints and the pseudo-static components caused by the phase shifts between the vibrations. The dynamic components changed with the travelling wave velocity due to the changes of the acceleration spectra in the asynchronous motion cases. The pseudo-static components were not only dependent on the phase shifts, but were also related to the shapes of the response displacement time-histories of the bridge deck.

ACKNOWLEDGMENTS

The research work reported in this thesis was carried out in the Department of Civil Engineering, University of Canterbury, New Zealand.

I wish to express my deepest gratitude to Dr. A. J. Carr, Associate Professor N. Cooke and Associate Professor P. J. Moss, Supervisors of this research for their invaluable advice and patience.

The financial support provided by the Doctoral Scholarship of the University of Canterbury are gratefully acknowledged.

Thanks are extended to my wife, A. Liu, for her understanding and encouragement.

TABLE OF CONTENTS

NOTATION

α the incoherence factor; the coefficient of viscous damping

a_1, a_2 constants

$\alpha_1(\omega)$, $\alpha_2(\omega)$ frequency dependent parameters

β the coefficient of viscous damping; the ratio of the amplitude envelope at $t_{\max}$ to that during the stationary phase $(t_1 \le t \le t_2)$

$\Delta\kappa$ the wave-number step

$\Delta\omega$ the frequency step

Δ_s the soil deformation

Δt the time step; the time interval between two support points

$\varepsilon(x_r)$ the error vector

ε_u the reinforcement strain at ultimate stress

ϕ_l the random phase angles with uniform distributions over $(0, \quad 2\pi)$

ϕ_y the equivalent yield curvature

Φ_y the pier yield curvature for a bilinear moment-curvature approximation

$\gamma_{ij}(\xi,\omega)$ the coherency function

γ_n the Lagrange multiplier

κ_{ij} the covariances of random field

λ the wavelength of the incident wave along its propagation path

λ_i the fraction of critical damping

λ_{in}, $\lambda_{ikl}(x_r)$ Kriging weights

μ the mean value of a random variate

υ_s Poisson's ratio

θ the angle between the direction of the approaching waves and the longitudinal axis of the bridge

$\theta_{ij}(\xi,\omega)$ a frequency dependent phase angle

θ_H the angle of incidence measured from plane of ground surface

θ_V the angle of incidence measured from x-z plane of the structure

ρ the mass density of the superstructure

$\rho_{u_k u_l}$, $\rho_{u_k s_{ij}}$ and $\rho_{s_{ki} s_{lj}}$ three cross-correlation coefficients

σ	a standard deviation of the field
σ_i^2	the variances of a random variety
σ_z	the root-mean-square of the response $z(t)$
τ	the time lag between any two supports, gross propagation time delay
ω	the circular frequency(in rad/sec)
ω_d	the predominant frequency of the earthquake
ω_f	the characteristic ground frequency representing the local site condition
ω_g	the frequency of the high-pass filter
ω_i	n equally spaced discrete frequency points at $\Delta\omega$ increments
ω_k	the modal frequency
ξ	the separation distance
ξ^L	the projected horizontal distance in the longitudinal direction of waves
ς_f	the characteristic ground damping ratio representing the local site condition
ς_g	the damping ratio of the high-pass filter
ς_k	the fraction of modal damping
$a(t)$	the ground acceleration process
$a_i(t)$	the ground acceleration processes at stations i
a_k	the effective influence factors
A	the cross-sectional area of the bearing pads
A_0	the area of the shear flow in a tubular section
A_i	a zero-mean, uncorrelated random amplitudes with mean squares $E[A_i^2] = \sigma_i^2$
A_{ve}	the effect shear area
b	a correlation length
b_i	the width of a beam member
b_{ki}	the effective modal participation factors
$\mathbf{C}$	the damping matrix
d	the wave dispersion factor
D	the diameter of the piers, pile diameter
$D_k(\omega_i, \zeta_i)$	the response spectrum for the support degree of freedom k
E	Elastic modulus; the ensemble average

E_b	Young's modulus of the beam
E_n	the stochastic variate of error $(F_n - F_n^e)$
E_s	Young's modulus
$\mathbf{E_s}$, $\mathbf{E_b}$	the rigid body displacement vectors
f	the acceleration frequency
$\mathbf{f}(x)$	a homogeneous n-variate Gaussian random vector field
$f_0(t)$	a zero mean homogeneous Gaussian (one-dimensional and one-variate) random process
$f_c^{'}$	the design concrete cylinder strength
f_i	the realizations of F_i
$f_l^e(x)$	the Kriging estimate of l th component $f_l(x)$ of the multi-variate random field
f_n^e	the best linear unbiased estimate of the unknown realization
f_u	the reinforcement ultimate strength
f_y	the reinforcement nominal yield strength
$F(t)$	the one-dimensional and univariate stationary process
F_i	denoting $F(t_i)$ in the discretised version of a univariate stationary process $F(t)$
F_n^c	the conditional simulation of F_n
F_n^e	the estimated value
$\mathbf{g}(x_i)$	a set of realizations of the vector field $\mathbf{f}(x)$ at locations x_i
G	Shear modulus
G_{elast}	the assumed shear modulus for the bearing elastomer
h	the height of the bearing pads
H	the pier height
$H_k(\omega)$	the frequency response function (transfer function) for mode k
$H_m(\omega)$	the frequency-response function of the soil column at station m
I_b	the moment of inertia of a beam
I_e	the effective moment of inertia
I_y , I_z	Moment of inertia
j_{iz}	the rotational mass moment of inertia of a beam member
J_e	the effective torsional moment of inertia

J_x Torsional moment of inertia

k the modulus of subgrade reaction

k^* the depth-independent subgrade reaction modulus

k_s a soil reaction coefficient

$\mathbf{K}$ the stiffness matrix

$[K]$ Kriging matrix

K_i Discrete soil spring stiffness at depth z_i

l a characteristic structural dimension

l_i the length of a beam member

L the distance between the two bridge supports, the plastic hinge length

m_i the lumped mass of a beam member

M the number of locations

$\mathbf{M}$ the mass matrix

M_y the ideal yield moment for a bilinear moment-curvature approximation

N the number of values in the record

p the peak factor, a contact pressure at the soil-pile interface

p_0 the perimeter of the shear flow in a tubular section

$\mathbf{P}_b$ the vector of reaction forces at the base

p_z the corresponding peak factor

$R[f(x_i), f(x_j)]$ the autocorrelation function of an isotropic, zero-mean univariate random field

$R(\tau)$ the autocorrelation function

$R(\xi, \tau)$ the space-time covariance function

R_{ij} the correlation function between F_i and F_j

R_L dimensionless frequencies

$R^p(\omega_k, \xi_k)$ a modified ground response spectrum for the case of partially correlated support motions

$S(\omega)$ the power spectral density function

$S(\kappa, \omega)$ the frequency-wavenumber spectrum

$S_1(\omega)$ the one-sided spectral density function

$S_{CP}(\omega)$ the normalized Clough-Penzien spectrum

S_0 the scale factor of Clough-Penzien spectrum

$S_{ii}(\omega)$ the auto-power spectral densities of the processes $a_i(t)$

$S_{ij}(\xi,\omega)$ the cross-power spectral density of the processes $a_i(t)$ and $a_j(t)$

$S_{\ddot{u}_k}(\omega)$ the spectral density function of the modal support motion

$S_{y_k}^p(\omega)$ the spectral density function of y_k for the case of partially correlated excitations

t the wall thickness of a tubular section

$t_{\max}$ time-history duration, duration of the process

T_0 the period of free vibration

$u_{k,\max}$ the mean peak ground displacement

$\mathbf{U}_s^s$ a pseudostatic component of the displacement

v the mean apparent seismic wave velocity

v_{app} the surface apparent wave velocity

v_s the shear wave velocity of the medium, the propagation velocity of the wave

$\mathbf{V}$ the gross apparent propagation velocity vector

$|\mathbf{V}_n|$ the determinant of variance matrix $\mathbf{V}_n$

V_s the shear wave velocity of the elastic half-space

$\mathbf{V}_s$ a dynamic component of the displacement

$Var[\varepsilon_i(x)]$ the variance of the error $\varepsilon_i(x)$

x_r any unrecorded location

x_i the recorded location

y_k the modal displacement

$|y_k^p|_{\max}$ the mean value of the maximum modal response for the case of partially correlated support motions

z the depth

$z(t)$ the generic response quantity

CHAPTER 1

INTRODUCTION

1.1 The Significance and Aim of This Study

In earthquake resistant design, it is common to assume that the entire base of a structure is subjected to a uniform ground motion. This can be a realistic assumption for most structures because their foundations extend over a limited area where dimensions are small relative to the seismic vibration wavelengths. However this is not the case for extended structures, such as long bridges and pipelines, large industrial buildings and dams. These structures can be subjected to very different motions along their length due to the spatial variability of the input seismic motion. Observations [Housner 1990] during earthquakes have clearly demonstrated that seismic ground motions can vary significantly over distances of the same order of magnitude as the dimensions of these extended structures.

The effect of the spatial variation of the seismic ground motions on the response of extended structures has been of concern for a number of decades [Bogdanoff et al. 1965]. So far, most of these studies focus on the elastic behaviour of the structure. Kiureghian [1996] summarized that spatial variability of the strong ground motion can significantly influence internal forces induced in structures with multiple supports. The variability in the support motions usually tends to reduce the inertia-generated forces within the structure, as compared to the forces generated in the same structure when the supports move uniformly. However, differential support motions generate additional forces, known as pseudo-static forces, which are absent when the structure is subjected to uniform support motions. The resultants of the two sets of forces can exceed the level of forces generated in the structure with uniform support motions, particularly when the structure is stiff. Bridge structures are usually designed to behave inelastically under moderate or severe earthquakes. Few existing bridge piers have enough strength to permit them to respond elastically to a major earthquake, thus most piers need to respond inelastically in a ductile manner. Unfortunately, very few nonlinear analyses of extended structures subjected to asynchronous inputs have been performed.

The seismic performance of bridges is a matter of special importance, especially those bridges that play an important role in post-earthquake rescue operations. The access to the affected

area by road or rail can be completely cut by failure of these critical bridges. Further, from a financial viewpoint, the true economic cost of the loss of a critical bridge includes additional costs associated with use of alternative transportation systems or routes, as well as the direct repair cost itself. Hence it is desirable to understand the effect of asynchronous inputs on the inelastic responses of the bridges. Spectacular failures of bridges due to unseating of the deck have been observed in every major earthquake and have also highlighted the need for a better understanding of the effect of asynchronous inputs on the inelastic response of the bridges. The aim of this study is to gain insight of the effect of asynchronous inputs on the elastic and inelastic responses of the bridges in order to improve earthquake design of long bridges.

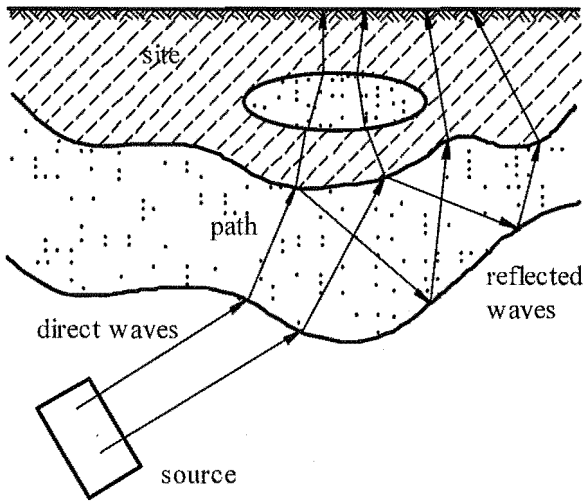

Figure 1.1 Illustration showing seismic wave propagation and scattering (after Harichandran 1999)

The spatial variation of seismic ground motion may be schematically thought of as the result of the combination of three different phenomena (see Figure 1.1):

(1) the **wave passage effect**, which is the difference in the arrival times of seismic waves at different stations.

(2) the **geometric incoherence effect**, resulting from reflections and refractions of waves through the soil during their propagation, as well as the difference in the manner of superposition of waves arriving from an extended source at various stations.

(3) the **local site effect**, due to the difference in local soil conditions at each station and the manner in which they influence the amplitude and frequency content of the motion transmitted from the bedrock.

The empirical studies based on recordings of strong motion arrays (essentially the SMART-1 array in Lotung, Taiwan [Abrahamson 1987]) have shed light on the nature of these effects

and their relative importance. Many empirical and theoretical expressions for the spatial variability of the seismic motion in terms of a coherency function have been developed on the base of an assumed stochastic model [Harichandran and Vanmarcke 1986; Luco and Wong 1986; Hao et al. 1989; Kiureghian 1996].

Presently, dynamic analysis with spatially varying input motions can be performed using the method of random vibrations, the response spectrum method, or the time-history approach. The random vibration method is based on a statistical characterization of the set of motions at the support points [Abdel-Ghaffar 1982; Harichandran and Wang 1988; Zerva 1990]. Typically, a stationary analysis is performed and the set of support motions is specified in terms of a matrix of auto- and cross-power spectral density functions that define the amplitudes and frequency contents of the motions. The cross-power spectral density for any pair of support motions is usually defined in terms of the respective auto-power spectral densities and a coherency function. The advantage of the random vibration method is that it provides a statistical measure of the response, which is not controlled by an arbitrary choice of the input motions. However, from the viewpoint of design, a full random field analysis to address this problem would be impractical.

To provide a practical approach, Berrah and Kausel [1992] suggested a modified response spectrum method on the basis of random vibration theory. Each spectral value of the given design response spectrum is adjusted by a correction factor that depends on the structural properties and on the characteristics of the wave propagation phenomenon. Kiureghian and Neuenhofer [1992] developed a new response spectrum method, which is also based on random vibration theory and properly accounts for the effects of correlation between the support motions as well as between the modes of vibration of the structure. They derived a combination rule known as the multiple support response spectrum (MSRS) method, which yields approximately the mean maximum response.

Time-history analyses utilize particular input accelerations at the various support points in terms of their complete time-histories and provide bridge response quantification for these earthquake inputs in the form of time-histories of the various response quantities. Only the time-history approach can be used for nonlinear structural analyses. The disadvantage of the time-history analyses is that the results produced from the analysis are specific to the set of selected time histories. The so-called Monte Carlo techniques [Shinozuka 1972; Shinozuka and Deodatis 1991] can be used to overcome this problem, in which the random process

simulations are employed to obtain the needed time-histories that reflect the statistical properties of the ground motion families. Provided that appropriate ground motion time-histories are used, a nonlinear analysis of a bridge subjected to asynchronous input motions does not present any more difficulties than does an analysis using a synchronous input motion.

In this study a method for generating the asynchronous input motions for the given specified earthquake records is proposed. Then the time-history approach is employed to carry out the elastic and inelastic responses of long bridges subjected to asynchronous input motions in order to gain insight into the effect of asynchronous inputs on the elastic and inelastic responses of long bridges. The transverse and longitudinal responses of long bridges with different configurations are investigated respectively using different natural earthquake records for both the travelling wave and the wave dispersion cases. RUAUMOKO (3-Dimensional Version) [Carr 2001] was used to produce piece-wise time-history responses of the long bridges.

1.2 The Organisation of This Thesis

The brief history of this subject has been reviewed. The main findings found so far and the methods used in previous studies are summarized and discussed in Chapter 2.

In Chapter 3 a simple and effective method is proposed to generate the asynchronous input motions for a known specified earthquake records based on the modified Kriging method. In the proposed method the asynchronous seismic input motions are assumed as a Multi-variate Gaussian random field and the modified Kriging method is employed to simulate the random field conditionally, with two assumptions being made to simplify the process of the conditional simulation.

Chapter 4 gives the details of the prototype bridges and their structural modelling. In this study, the bridge deck, piers and piles are modelled as three-dimensional frame members and the bearings and the interactions between the pile and soils are modelled as three-dimensional spring members. The methods for determining the properties of the frame and the spring members are also given.

The wave passage effect of the variability of the seismic motion on the elastic and inelastic responses of the long bridges is investigated in Chapter 5. The elastic and inelastic transverse responses of six bridge models with different configurations are produced for the travelling wave cases and synchronous cases. Three natural earthquake records are employed as input motions respectively. The investigated response parameters are the maximum pier drifts, the maximum shear forces in the piers and the maximum section curvature ratios of the piers. The variations of the investigated response parameters with the travelling wave velocity are analysed.

Chapter 6 deals with the combined geometric incoherence and wave passage effects of the seismic motion on the transverse seismic response of long bridges. Three wave dispersion factors, d = 100, 10 and 1, were used in the wave dispersion cases. The bigger the value of d the higher the expected correlation between the points of the random field motion. The variations of the investigated response parameters with the degree of the geometric incoherence effect are discussed. The responses are also compared with those in the simple travelling wave cases.

In Chapter 7 the longitudinal responses of the bridge models are carried out for both the travelling wave and the wave dispersion cases. The investigated response parameters are the maximum relative displacements of the bridge deck across the movement joints and the maximum relative displacements between the girder ends and the top of the abutments. The factors that affect the response parameters investigated in the asynchronous input case are discussed.

Chapter 8 summarises this research and Chapter 9 gives the main conclusions drawn from this study and some recommendations for further study.

CHAPTER 2

LITERATURE REVIEW

2.1 The Damage to Bridges in Recent Earthquakes

In recent earthquakes, bridges have not performed as well as might be expected. Even some modern bridges designed specifically for seismic resistance have collapsed or have been severely damaged. The damage to bridges in recent earthquakes can be broadly grouped into three categories [Priestley and Park 1984]: (1) spans falling from piers under the seismically induced response displacement, due to inadequate seating provisions, and a lack of restraints from pier caps or adjacent spans; (2) failure of piers or piles in flexure or shear, resulting from the seismic inertia forces induced in the bridge superstructure; (3) failure of foundation materials (slumping of abutments, liquefaction of sandy foundations). The observed damage cannot be directly identified with the effect of asynchronous ground motion, as this aspect is not yet fully understood. Amongst the failures, some of unseating of spans are thought to be directly attributed to asynchronous input ground motion, or asynchronous motion at the tops of the piers.

The unseating of bridge spans is a common type of seismic failure in bridges. The bridge girders move off their supports because the relative movement of the spans in the longitudinal direction exceeds the seating widths. Asynchronous ground displacement effects may play an important role in this. However, the structural differences between sections separated by movement joints and the local soil conditions may increase the relative movements across the movement joints. Another case that may result in span unseating is when the spans are skewed. It has been observed that skewed spans develop larger displacements than right spans, as a consequence of a tendency for the skew span to rotate in the direction of decreasing skew, thus tending to drop off the supports at the acute corners. Spans unseating have been observed in most major earthquakes.

Earthquake of March 27, 1964, Gulf of Alaska (magnitude 8.5). The steel trusses of the Copper River and Northwestern Railroad Bridge near Round Island were shifted between a third and two-thirds of a metre [USA National Oceanic & Atmospheric Administration website]. Figure 2.1 shows one of the displaced trusses, which pounded against an adjacent

steel girder span. The girder span was moved, its concrete pedestal was rotated, and the girder span almost fell into the river. Note the shortening indicated by buckling of the guardrail.

Figure 2.1 Damage to Railroad Bridge by Alaska Earthquake of 1964

Earthquake of June 16, 1964, Niigata, (magnitude 7.4). The Showa Bridge pictured in Figure 2.2 had seven spans across the river, each supported by piers, consisting of structural steel girders carrying the reinforced concrete decks. Two of the piers collapsed. The corresponding spans of the bridge collapsed and dropped into the river. The successive spans toward the west bank also dropped while one end of each span remained connected at the top of successive piers. The construction was such that one end of the girders was fixed to a pier and the other end was free to slide longitudinally off the pier after about 30 cm of movement [USA National Oceanic & Atmospheric Administration website].

Figure 2.2 Damage to Showa Bridge by Niigata Earthquake of 1964

The San Fernando earthquake of February 9, 1971, (magnitude 6.6). The interchange between the I-5 (Golden State) and C-14 (Antelope Valley) was under construction at the time of the earthquake. The central portion of the curved, nine-span South Connector Overcrossing collapsed, which was structurally complete at the time of the earthquake (Figure 2.3). The collapsed section consisted of a two-span prestressed post-tensioned box girder supported by a central column and by reinforced concrete box sections at the ends. Although linkage restrainer bolts were provided across the movement joints in this bridge, they had insufficient strength to restrain the relative longitudinal movement [Fung et al. 1971].

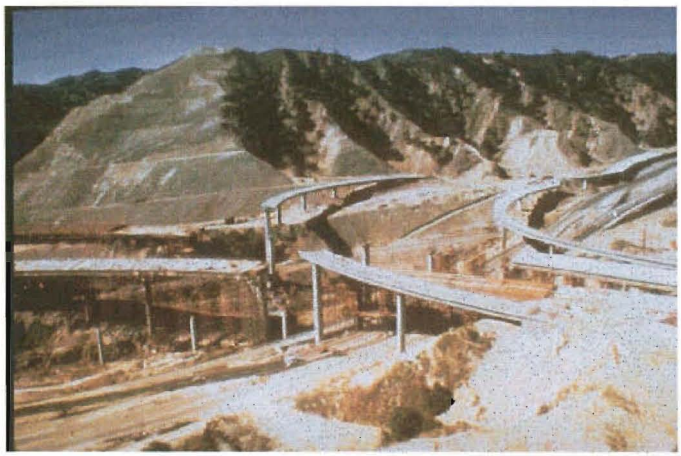

Figure 2.3 The span collapse of I-5 and C-14 interchange
in San Fernando earthquake of 1971

Earthquake of February 4, 1976, Guatemala (magnitude 7.5). Figure 2.4 shows the collapse of three central spans of the Agua Caliente Bridge on the road to the Atlantic Ocean. Both ground shaking and ground failure contributed to this collapse [USA National Oceanic & Atmospheric Administration website].

Figure 2.4 Agua Caliente Bridge was damaged by Guatemala Earthquake of 1976

Earthquake of October 17, 1989, Loma Prieta, (magnitude 7.1). Figure 2.5 shows damage of the San Francisco-Oakland bay bridge [EERI 1990]. At pier E-9 there is an abrupt change in the structural system, dimensions and spans. On the westward side, there is a span of 154m, where the truss has an overall height of 25.6m. On the eastward side, a shorter span of 88m exists, and the truss height is 12m. The collapsed 15m connecting span was simply supported on the two trusses mentioned above. Failure was due to relative motions between the two end trusses in excess of the 12.7cm (5″) provided by the seating length.

Figure 2.5 Damage to San Francisco-Oakland Bay Bridge by 1989 Loma Prieta Earthquake

Costa Rica earthquake of April 22, 1991 (magnitude 7.5). Figure 2.6 shows span failure of a modern bridge in Costa Rica after the earthquake [EERI 1991]. The supports of the bridge were skewed at about 30° to the transverse axis, and the spans were thrown off the internal support in the direction of decreasing skew, due to relative displacement between the abutment and an internal pier at a site with soft soils.

Figure 2.6 Unseating of Rio Bananito Bridge in 1991 Costa Rica Earthquake

The Northridge Earthquake of January 17,1994, (magnitude 6.8). In this earthquake, several segments of the I-5 and C-14 interchange collapsed again as shown in Figure 2.7 [EERI 1995].

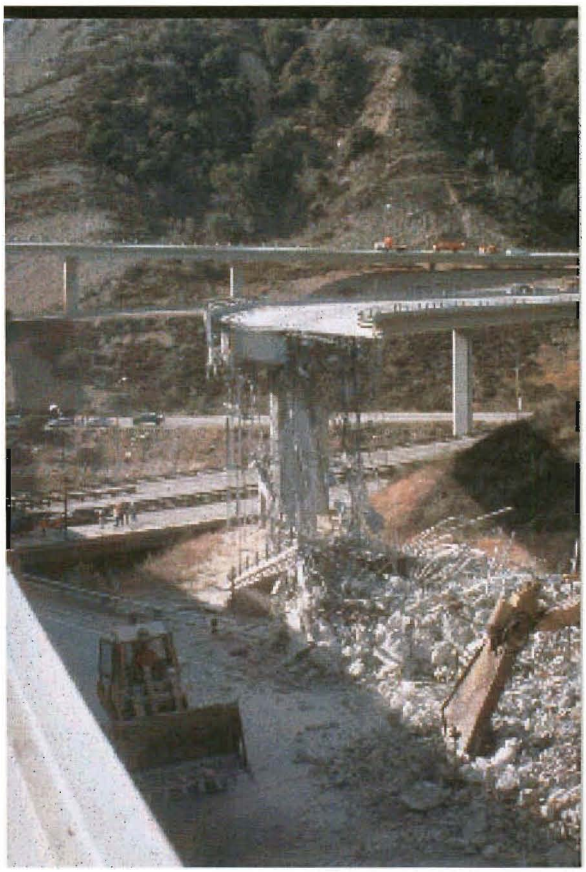

Figure 2.7 Damage to I-5 and C-14 interchange by Northridge Earthquake of 1994

The January 17, 1995 Kobe earthquake (magnitude 7.0). Figure 2.8 shows the failure of the east link span to the 250m Nishinomiya-ko arch bridge of the Wangan expressway [Priestley et al. 1995]. This 50m simply supported span has unseated due to large movements of the arch bridge support. Elevated highways in Japan typically consist of single spans that have roller bearings at one end and are fixed at the other. A number of these single spans fell off their supports at the expansion joints because of the large longitudinal differential displacements induced between piers as shown in Figure 2.9.

The behaviour exhibited by the long elevated structures indicates that longitudinal seismic actions played an important part in their performance. In these cases the damage appeared consistent with displacements being applied which were much greater than the strength or displacement capabilities of the components. It can therefore be concluded that the peak

forces on these long elevated bridges resulted from non-synchronous longitudinal ground displacement effects rather than the synchronous response of the structure to ground shaking. That is, the longitudinal ground displacement effects are caused by out of phase displacements which occur as the seismic wave pass along the structures [Park et al. 1995].

Figure 2.8 Unseating of Nishinomiya-ko bridge in Kobe Earthquake of 1995

Figure 2.9 Collapsed sections of expressways in Kobe Earthquake of 1995

These deck collapses which were observed in these major earthquakes cannot be fully attributed to the asynchronous ground motion but it seems that non-uniform earthquake motions could play an important role in the seismic response of bridge and needs to be investigated further.

2.2 The Asynchronous Input Accelerations

To perform a time-history analysis with spatially varying input motions, the asynchronous input accelerations are usually specified in one of three ways: (1) selection of a ground motion array previously recorded in a setting similar to the design situation at hand; (2) generation of time-histories based on modelling of the seismic source and propagation of waves in an elastic medium; and (3) simulation of time-histories based on the random vibration approach.

The theoretical, seismological approach based on the modelling of the seismic source and the propagation of waves through the soil is generally successful at low frequencies (less than 1 Hz) only. As an alternative, observed seismograms from small earthquakes can be used as empirical Green's functions in place of the theoretical functions [Wald et al. 1988]. The empirical Green's functions allow an approximate inclusion of higher frequencies. The seismological approaches require detailed knowledge of the source mechanism and geological materials along the wave path, which is not always available. In earthquake engineering, the spatial variation is described by the coherency functions defined in terms of the cross-spectral density functions and the local power spectral density functions. Simulation techniques based on the random vibration theory [Shinozuka and Jan 1972; Spanos and Mignolet 1990; Ramadan and Novak 1993] are then used to generate spatially incoherent seismic ground motions matching the prescribed, or target, values of either the power spectral density and coherency function, or the cross-spectral density matrix.

2.2.1 Coherency function and SMART-1 array

In the context of stationary random processes, the coherency function represents the cross-power spectral density of the motions at two stations, normalized by the square root of the corresponding auto-power spectral densities. For ground acceleration records $a_i(t)$ and $a_j(t)$ at stations i and j, respectively, the coherency function $\gamma_{ij}(\xi,\omega)$ is defined by

$$\gamma_{ij}(\xi,\omega)=\begin{cases}\dfrac{S_{ij}(\xi,\omega)}{\sqrt{S_{ii}(\omega)S_{jj}(\omega)}} & for \quad S_{ii}(\omega)S_{jj}(\omega)\neq 0\\ 0 & for \quad S_{ii}(\omega)S_{jj}(\omega)=0\end{cases} \tag{2.1}$$

where ω denotes the circular frequency, ξ denotes the separation distance, $S_{ii}(\omega)$, $S_{jj}(\omega)$ denote the auto-power spectral densities of the processes $a_i(t)$ and $a_j(t)$, and $S_{ij}(\xi,\omega)$ denote the cross-power spectral density of the processes $a_i(t)$ and $a_j(t)$. In general, $\gamma_{ij}(\xi,\omega)$ is complex. Separating $\gamma_{ij}(\xi,\omega)$ into its absolute value and phase angle, equation (2.1) can be written in the form

$$\gamma_{ij}(\xi,\omega) = \left|\gamma_{ij}(\xi,\omega)\right| \exp\left(i\theta_{ij}(\xi,\omega)\right) \tag{2.2}$$

where $i=\sqrt{-1}$, and $\theta_{ij}(\xi,\omega) = \tan^{-1}\dfrac{\mathrm{Im}\,\gamma_{ij}(\xi,\omega)}{\mathrm{Re}\,\gamma_{ij}(\xi,\omega)}$ is a frequency dependent phase angle, where Im and Re refer to the imaginary and real parts of the complex function. The two terms in equation (2.2) characterize distinct effects of spatial variability: the real-valued function $\left|\gamma_{ij}(\xi,\omega)\right|$ characterizes the incoherence effect, whereas the complex term $\exp\left(i\theta_{ij}(\xi,\omega)\right)$ characterizes the wave-passage and site-response effects. It is common to use the absolute value of the coherency to describe the similarity of the waveforms at two stations without regard to the difference in the arrival times of the waves. In contrast, the wave passage effect depends only on the time delays in the arrival of waves.

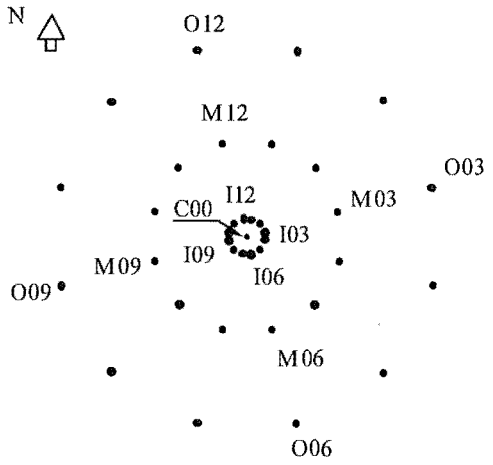

Figure 2.10 The SMART-1 array

The SMART-1 array in Lotung, Taiwan (see Figure 2.10) is the first large density digital array of strong-motion seismographs where soil conditions are more or less uniform through out the array [Abrahamson 1987]. It consists of a centre instrument C00 and other instruments arranged on three concentric circles, with radii of 200m, 1000m and 2000m respectively; along the circumference of each circle are twelve equally spaced strong motion

accelerometers having a common time basis. SMART-1 allows measurement of the spatial correlation of ground motion, evaluation of the variability of the ground motion within a small area, computation of torsion and rocking components of ground motion as well as ground strain, identification of wave types and estimation of their apparent horizontal velocity. These properties of the free-field ground motion have important implications for the seismic response of extended structures. The various spectra are estimated for numerous accelerogram pairs. Extensive analysis of data from SMART-1 indicated that [Harichandran and Vanmarcke 1986, Harichandran 1991]:

1. The auto spectral density functions of accelerograms at locations with the dimensions of engineered structures are similar, i.e., the local site effect can often be neglected.
2. Typically, coherency becomes smaller as the distance between stations *l* and *m* increase.
3. Typically, coherency decreases with increasing frequency *f*.
4. The decay of the absolute value of the coherency spectrum $|\gamma_{lm}(f)|$ is not overly direction sensitive.

The observations suggest the following simplifications:

1. The auto spectral density function (SDF) at any location can be given by a point SDF *S(f)* estimated as the average of all the auto SDFs.
2. The absolute coherency decay between all pairs of stations can be described by a single function $|\gamma(\xi, f)|$, where ξ = separation between *l* and *m*.
3. The phase spectra can be (grossly) simplified as $\phi(\xi, f) = -2\pi\tau$, where $\tau = {\mathbf{V}\cdot\xi}/{|\mathbf{V}|^2}$ = propagation time delay, and $\mathbf{V}$ = apparent propagation velocity vector.

Some empirical coherency functions developed from the array recordings are introduced here.

Harichandran and Vanmarck's model, which is based on the recorded data of Event 20 at the SMART-1 array, is described by the following equation [Harichandran and Vanmarck 1986]

$$\gamma_{ij}(\xi,\omega) = A\exp\left[-\frac{2|\xi|(1-A+aA)}{a\theta(\omega)}\right] + (1-A)\exp\left[-\frac{2|\xi|(1-A+aA)}{\theta(\omega)}\right] \tag{2.3}$$

in which $\theta(\omega) = k\left[1+\left({|\omega|}/{2\pi f_0}\right)^b\right]^{\frac{1}{2}}$, $A = 0.736$, $a = 0.147$, $k = 5210m$, $f_0 = 1.09Hz$,

$b = 2.78$, and $|\cdot|$ indicates the absolute value. This model has been used frequently in seismic response analyses of large structures.

Luco and Wong [1986] developed the following model

$$\gamma_{ij}(\xi,\omega) = \exp\left[-\left(\frac{\alpha\omega\xi}{v_s}\right)^2\right]\exp\left[i\frac{\omega\xi^L}{v_{app}}\right] \tag{2.4}$$

in which α is an incoherence factor, ξ is the horizontal separation distance between two stations, ξ^L denotes the projected horizontal distance in the longitudinal direction of the waves, v_s is the shear wave velocity of the medium, and v_{app} is the surface apparent wave velocity. This model assumes increasing incoherence with increasing frequency or distance between the two stations, and considers the phase angle as a linear function of the frequency. Because of its simplicity, many other investigators have used this model.

Hao et al. [1989] suggested the following relation for the coherency function

$$\gamma_{ij}(\xi^L,\xi^T,\omega) = \exp\left(-\beta_1\xi^L - \beta_2\xi^T\right)\exp\left[-\left(\alpha_1(\omega)\sqrt{\xi^L} + \alpha_2(\omega)\sqrt{\xi^T}\right)\omega^2\right]\exp\left(i2\pi\omega\frac{\xi^L}{v_a}\right) \tag{2.5}$$

where ξ^L and ξ^T are projected separation distances along and normal to the dominant direction of wave propagation, respectively; β_1 and β_2 are constant parameters; $\alpha_1(\omega)$ and $\alpha_2(\omega)$ are frequency dependent parameters. The parameters and functions in the equation are obtained through regression analysis of the data.

More recently, **Kiureghian** [1996] proposed a theoretical model for the coherency function. He assumed the ground acceleration process $a(t)$ as a stationary process. Thus, it can be approximately decomposed into a set of discrete frequency components in the form

$$a(t)^d = \sum_{i=1}^{n} A_i \cos(\omega_i t + \phi_i) \tag{2.6}$$

where A_i, $i = 1, 2, \cdots, n$, are zero-mean, uncorrelated random amplitudes with mean squares $E[A_i^2] = \sigma_i^2$, $\omega_i = \omega_1 + (i-1)\Delta\omega$ are n equally spaced discrete frequency points at $\Delta\omega$ increments, and ϕ_i are random phase angles with uniform distributions over $(0, 2\pi)$ and statistically independent of each other. Then, by using the definition of the coherency function and a set of simplifying assumptions including a plane wave arriving at a single incidence angle at the two stations, a one-dimensional shear wave propagating vertically in

the local soil medium, and the linear characterization of soil behavior, he obtained the expression of this model as the following:

$$\gamma_{ij}(\xi,\omega) = \gamma_{ij}(\xi,\omega)^{incoherence} \cdot \gamma_{ij}(\xi,\omega)^{wave-passage} \cdot \gamma_{ij}(\xi,\omega)^{site-response}$$
$$= \cos[\beta(\xi,\omega)]\exp\left[-\frac{1}{2}\alpha^2(\xi,\omega)\right]\exp\left\{i\left[\theta_{ij}(\xi,\omega)^{wave-passage} + \theta_{ij}(\xi,\omega)^{site-response}\right]\right\} \quad (2.7)$$

where the phase angles,

$$\theta_{ij}(\xi,\omega)^{wave-passage} = -\frac{\omega\xi^L}{v_{app}(\omega)} \quad (2.8)$$

$$\theta_{ij}(\omega)^{site-response} = \theta_i(\omega) - \theta_j(\omega) = \tan^{-1}\frac{\mathrm{Im}[H_i(\omega)H_j(-\omega)]}{\mathrm{Re}[H_i(\omega)H_j(-\omega)]} \quad (2.9)$$

and $H_m(\omega)$ denotes the frequency-response function of the soil column at station m $(m = i,\ j)$. The model is composed of three components characterising the distinct effects that give rise to the spatial variability, namely, the incoherence effect, the wave-passage effect, and the site-response effect. The incoherence component of the coherency function is a real-valued, non-negative, decaying function of frequency and inter-station distance. It is shown to be formed of two sub-components: one representing the effect of random phase angle variations, and one representing the effect of random amplitude variations between the wave components at two stations. The wave passage component of the coherency function is represented in terms of a phase angle expressed as a function of frequency, inter-station distance, and the apparent velocity of the seismic waves. The site response component is also represented in terms of a phase angle function. However, for this effect, the phase angle is dependent on the properties of the local soil profile at each station. This model provides a mathematical framework that may allow better calibration with recorded data, as well as specification of design motions for regions or geologic settings where no array recordings are available.

2.2.2 Power spectral density function

The power spectral density (PSD) function of the seismic ground motion is most commonly described by the well-known modified Kanai-Tajimi spectrum of ground accelerations [Clough and Penzien 1993]:

$$S_a(\omega) = S_{CP}(\omega) \cdot S_0$$

$$= \frac{\left[1 + 4\varsigma_f^2 \left(\omega/\omega_f\right)^2\right] \cdot \left(\omega/\omega_g\right)^4}{\left\{\left[1 - \left(\omega/\omega_f\right)^2\right]^2 + 4\varsigma_f^2 \left(\omega/\omega_f\right)^2\right\}\left\{\left[1 - \left(\omega/\omega_g\right)^2\right]^2 + 4\varsigma_g^2 \left(\omega/\omega_g\right)^2\right\}} \cdot S_0 \qquad (2.10)$$

and that of displacements as $S_u(\omega) = S_a(\omega)/\omega^4$. The power spectral density function is expressed in terms of a constant power spectral density function S_0, representing white noise bedrock excitation, multiplied by the transfer functions $H_1(i\omega)$, $H_1(-i\omega), H_2(i\omega)$, and $H_2(-i\omega)$, in which $H_1(i\omega)$ and $H_2(i\omega)$ are given by the following equations.

$$H_1(i\omega) = \frac{1 + 2i\varsigma_f \left(\omega/\omega_f\right)}{\left[1 - \left(\omega/\omega_f\right)^2\right] + 2i\varsigma_f \left(\omega/\omega_f\right)} \qquad (2.11)$$

$$H_2(i\omega) = \frac{\left(\omega/\omega_g\right)^2}{\left[1 - \left(\omega/\omega_g\right)^2\right] + 2i\varsigma_g \left(\omega/\omega_g\right)} \qquad (2.12)$$

The function $H_1(i\omega)$ is the well-known Kanai-Tajimi filter function. Parameters ω_f and ς_f may be thought of as some characteristic ground frequency and characteristic damping ratio, respectively, representing the local site condition and parameters ω_g and ς_g are the frequency and damping ratio of the high-pass filter, they must be set appropriately for the desired filtering of the very low frequencies. The factor S_0 depends on the peak ground acceleration (PGA) according to the following relation

$$S_0 = \frac{PGA^2}{p^2 \, \mathrm{var}^*} \qquad (2.13)$$

where p = peak factor, given by $p = \sqrt{2\ln\frac{2.8\Omega t_{\max}}{2\pi}}$, in which $t_{\max}$ = duration of the process, and $\Omega = \sqrt{\frac{E[\dot{x}^2]}{\mathrm{var}[x]}}$ where $E[\dot{x}^2] = \int_{-\infty}^{\infty} \omega^2 S(\omega) d\omega$ is the mean square of the derivative of the process; and $\mathrm{var}[x] = \int_{-\infty}^{\infty} S(\omega) d\omega$ is the variance (total power) of the process, and $\mathrm{var}^*[x] = \int_{-\infty}^{\infty} S_{CP}(\omega) d\omega$. The characteristic ground frequency ω_f of the Clough-Penzien spectrum depends on the soil type (F = firm, M = medium, S = soft) [Clough and Penzien

1993] as follows: $\omega_f(F) = 15^{rad}/_{s}$; $\omega_f(M) = 10^{rad}/_{s}$; $\omega_f(S) = 5^{rad}/_{s}$, while the other parameters can be determined as follows: $\varsigma_f = \omega_f/15$; $\omega_g = \omega_f/10$; $\varsigma_g = 0.6$. The values of var* and Ω for the three soil types are $\text{var}^*(F) = 184.111$; $\text{var}^*(M) = 125.529$; $\text{var}^*(S) = 90.164$; $\Omega(F) = 46.276rad$; $\Omega(M) = 21.963rad$; $\Omega(S) = 6.498rad$.

2.2.3 Unconditional simulation of multisupport seismic ground motions

Simulation of single random processes, both stationary and nonstationary, has been common for many years, but simulation of spatially incoherent random fields has received relatively little attention until the installation of the SMART-1 array. The methods used for simulation of spatially incoherent random fields can be categorized primarily into two classes: (1) methods based on the summation of trigonometric functions (wave superposition), also known as spectral representation methods; (2) methods based on the convolution of white noise with a kernel function or integration of a differential equation driven by white noise (digital filtering).

The spectral representation method has been the most popular method, perhaps due to its simplicity. It was Shinozuka [1972; Shinozuka and Jan 1972] who first applied this method for simulation purposes including multi-dimensional, multi-variate and nonstationary cases. Yang [1972, 1973] showed that the Fast Fourier Transform (FFT) technique could be used to dramatically improve the computational efficiency of the algorithm and proposed a formula to simulate random envelope processes. Shinozuka [1974] extended the application of the FFT technique to multidimensional cases. Deodatis and Shinozuka [1989] extended the spectral representation method to simulate stochastic waves.

Simulation of multivariate processes based on digital filtering can be accomplished by first simulating a family of uncorrelated processes and subsequently imposing the appropriate correlation structure by a transformation [Kareem 1978; Iannuzzi and Spinelli 1987]. More recent developments in digital filtering techniques include state space modelling, autoregressive (AR), moving average (MA), and the combination autoregressive and moving averages (ARMA) models [Reed and Scanlan 1984; Samaras et al. 1985; Spanos and Mignolet 1990; Kareem and Li 1992].

2.2.3.1 Simulation of random processes according to the spectral representation method

Consider a zero mean homogeneous Gaussian (one-dimensional and one-variate) random process $f_0(t)$ with autocorrelation function $R(\tau)$ and spectral density $S(\omega)$, in which τ and ω indicate time lag and frequency (in seconds and rad/sec), respectively. $R(\tau)$ and $S(\omega)$ are even functions of their respective arguments and obey the Wiener-Khintchine transformation, e.g.

$$\begin{cases} R(\tau) = \int_{-\infty}^{\infty} S(\omega)\cos\omega\tau d\omega = \int_{-\infty}^{\infty} S(\omega)e^{i\omega\tau}d\omega \\ S(\omega) = \dfrac{1}{2\pi}\int_{-\infty}^{\infty} R(\tau)\cos\omega\tau d\tau = \dfrac{1}{2\pi}\int_{-\infty}^{\infty} R(\tau)e^{-i\omega\tau}d\tau \end{cases} \tag{2.14}$$

The random process $f_0(t)$ could be expressed in the form of the sum of the cosine functions [Rice 1954]:

$$f(t) = \sqrt{2}\sum_{k=1}^{K} A_k \cos(\omega_k t - \phi_k) \tag{2.15}$$

where ϕ_k are random angles distributed uniformly between 0 and 2π, and

$$A_k = [S_1(\omega_k)\Delta\omega]^{1/2}, \qquad \omega_k = \left(k - \frac{1}{2}\right)\Delta\omega \tag{2.16}$$

with $S_1(\omega) = 2S(\omega)$ being the one-sided spectral density function (Figure 2.11). Accordingly,

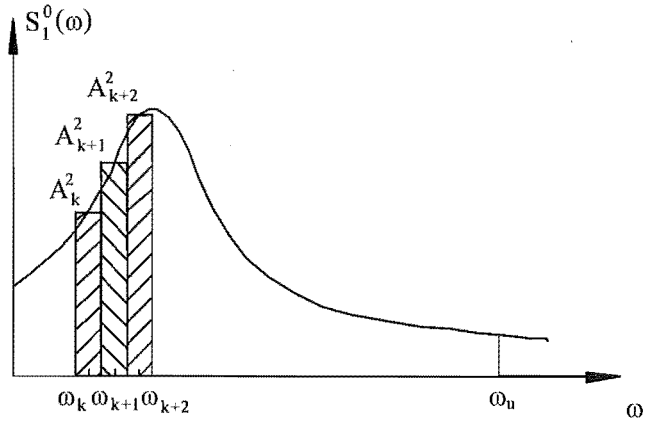

Figure 2.11 One-sided spectral density

Shinozuka [1972; Shinozuka and Jan 1972] suggested that the digital simulation of a sample function $\overline{f}(t)$ of $f(t)$ could be done by using equation (2.15) with ϕ_k being replaced by their realized values φ_k:

$$\overline{f}(t) = \sqrt{2}\sum_{k=1}^{K} A_k \cos(\omega_k t - \varphi_k) \tag{2.17}$$

Equation (2.17) is valid if there is an upper cut-off frequency $\omega_u = K\Delta\omega$ above which the contribution of the power spectral density (PSD) to the simulations is negligible for practical purposes. The following characteristics are inherent in the simulations: (*i*) they are asymptotically Gaussian as $K \to \infty$ due to the central limit theorem; (*ii*) they are periodic with period $T_0 = 4\pi/\Delta\omega$; (*iii*) they are ergodic, at least up to the second moment, over an infinite time domain or over the period of the simulation; and (*iv*) as $K \to \infty$ the ensemble mean, auto-correlation and power spectral density functions of the simulations become identical to those of the process itself, because of the orthogonality of the cosine functions in equation (2.17).

A significant improvement in the efficiency of digital simulation has been suggested by Yang [1972, 1973] writing

$$f(t) = \sqrt{\Delta\omega}\,\mathrm{Re}\,F(t) \tag{2.18}$$

in which $\mathrm{Re}\,F(t)$ represents the real part of $F(t)$ and

$$F(t) = \sum_{k=1}^{N} \sqrt{2S_1(\omega_k)}e^{i\phi_k}e^{i\omega_k t} \tag{2.19}$$

is the finite complex Fourier transform of $\sqrt{2S_1(\omega_k)}e^{i\phi_k}$. The advantage of equation (2.18) is such that function $F(t)$ can readily be computed by applying the Fast Fourier Transform (FFT) algorithm, hence avoiding the time-consuming computation of a large number of cosine functions.

2.2.3.2 Simulation of space-time random fields according to the spectral representation method

Shinozuka [1974; 1987] extended the spectral representation method to multivariate, multidimentional random fields. Consider a homogeneous, stationary space-time random field with zero mean, space-time covariance function $R(\xi,\tau)$, ξ being the separation distance, and τ being the time lag, and frequency-wave number $(F-K)$ spectrum $S(\kappa,\omega)$, in which κ indicates the wave number and ω indicates the frequency. The frequency-wave number spectrum and the covariance function are Wiener-Khintchine transform pairs and possess the same symmetries.

$$\begin{cases} R(\xi,\tau) = \int_{-\infty}^{\infty}\int_{-\infty}^{\infty} S(\kappa,\omega)e^{i(\kappa\xi+\omega\tau)}d\kappa d\omega \\ S(\kappa,\omega) = \dfrac{1}{(2\pi)^2}\int_{-\infty}^{\infty}\int_{-\infty}^{\infty} R(\xi,\tau)e^{-i(\kappa\xi+\omega\tau)}d\xi d\tau \end{cases} \tag{2.20}$$

The space-time random field can be simulated through [Zerva 1992; Shinozuka 1987]:

$$\begin{aligned} f(x,t) = \sqrt{2}\sum_{j=0}^{J-1}\sum_{n=0}^{N-1}\Big\{ & \left[2S(\kappa_j,\omega_n)\Delta\kappa\Delta\omega\right]^{1/2}\cos\left(\kappa_j x+\omega_n t+\varphi_{jn}^{(1)}\right) \\ & +\left[2S(\kappa_j,-\omega_n)\Delta\kappa\Delta\omega\right]^{1/2}\cos\left(\kappa_j x-\omega_n t+\varphi_{jn}^{(2)}\right)\Big\} \end{aligned} \tag{2.21}$$

in which $\varphi_{jn}^{(1)}$ and $\varphi_{jn}^{(2)}$ are two sets of independent random phase angles uniformly distributed between $(0,2\pi]$, $\kappa_j = \left(j+\frac{1}{2}\right)\Delta\kappa$ and $\omega_n = \left(n+\frac{1}{2}\right)\Delta\omega$ are the discrete wave-number and frequency, respectively, and $\Delta\kappa$ and $\Delta\omega$ are the wave-number and frequency steps, respectively. Equation (2.21) is valid, if there exist an upper cut-off wave number $\kappa_u = J\times\Delta\kappa$ and an upper cut-off frequency $\omega_u = N\times\Delta\omega$, above which the contribution of the F-K spectrum to the double summation in equation (2.21) is insignificant for practical purposes. The Fast Fourier Transform (FFT) algorithm also can be introduced in equation (2.21), to improve the computational efficiency of the method.

2.2.4 Shape functions

In engineering, a nonstationary process $x(t)$ can often be represented fairly well using the quasi-stationary form

$$x(t) = z(t)\cdot f(t) \tag{2.22}$$

where $z(t)$ is a fully prescribed function of time and $f(t)$ is a stationary process. If $f(t)$ is a Gaussian process, $x(t)$ will also be Gaussian, in which case the covariance function $E[x(t)x(t+\tau)] = z(t)z(t+\tau)R_f(\tau)$ completely characterizes the process.

One function commonly used for artificial seismic ground motions is

$$\begin{aligned} & z(t) = \left(\frac{t}{t_1}\right)^2; \quad for \quad 0\le t\le t_1 \\ & z(t) = 1; \quad for \quad t_1\le t\le t_2 \\ & z(t) = \exp\left\{\frac{t-t_2}{t_{\max}-t_2}\cdot\ln\beta\right\}; \quad for \quad t_2\le t\le t_{\max} \end{aligned} \tag{2.23}$$

where t_1, t_2= ramp duration and decay starting time, respectively; t_{max}= time-history duration; and β= ratio of the amplitude envelope at t_{max} to that during the stationary phase ($t_1 \le t \le t_2$). Another function that has been used for this purpose is

$$z(t) = a_1 t \exp(-a_2 t) \tag{2.24}$$

where the constants a_1 and a_2 are assigned values after considering such factors as earthquake magnitude and epicentral distance. For the general class of accelerograms recorded during the San Fernando, California earthquake, statistical studies show that constants a_1 and a_2 can be assigned the values 0.45 and 0.167, respectively [Clough and Penzien 1993].

2.2.5 Conditional simulation of seismic ground motions

If motions have been recorded or specified for design purposes at a number of closely spaced points, the conditional simulation techniques of a random field can be used to generate compatible accelerograms at nearby locations where motions are not available. Throughout the history of stochastic process and field simulation the unconditional simulation has been the main theme and widely applied in structural and related engineering over the last three decades or so. However, the development of the method of conditional simulation for the random processes and fields is of relatively recent origin. So far, conditional simulation can be carried out by the use of either the Kriging method or the conditional probability density function (CPDF) method.

Kriging methodology, which provides the best linear unbiased estimate built on data of a stochastic field, has been developed by many researchers mainly in geostatistics [Krige 1966; Matheron 1967; Journel 1974]. Vanmarcke and his co-workers directly applied the kriging method to conditional simulation problems in earthquake engineering [Vanmarcke and Fenton 1991; Vanmarcke et al. 1993]. Hoshiya and his co-worker [Hoshiya 1994; Hoshiya and Marugama 1994; Hoshiya 1995] modified the Kriging method and used the modified version for conditional simulation in relation to earthquake engineering applications. The modification by Hoshiya and his co-worker represents a significant improvement that has made the Kriging method theoretically much cleaner and computationally more efficient [Shinozuka and Zhang 1996].

The conditional probability density function (CPDF) method was developed and applied in earthquake engineering by Kameda and Morikawa [1991, 1992, 1994]. This method takes advantage of the ease with which the conditional probability density function can be analytically derived for Gaussian variables, and presents (mathematically) a more straightforward method. Here the one-dimensional and univariate stationary stochastic process is used to illustrate these two methods in their application to the conditional simulation of stochastic processes.

2.2.5.1 Kriging method

The one-dimensional and univariate stationary process $F(t)$ with known mean and correlation functions may be approximated by its discretised version (F_1, F_2, $\cdots$, F_n) with F_i denoting $F(t_i)$. Thus, the problem now is to simulate the stochastic variate F_n under the condition that $(n-1)$ realizations f_i of $F_i, i=1,\ 2,\ \cdots,\ (n-1)$ are known. Following Journel and Huijbregts [1978], the best linear unbiased estimate of the unknown realization f_n, denoted as f_n^e, is constructed linearly in terms of $(n-1)$ known realizations as follows:

$$f_n^e = \sum_{i=1}^{n-1} \lambda_{in} f_i \tag{2.25}$$

This process of evaluating the best linear unbiased estimate is the original meaning of the Kriging method. Equation (2.25) may also be presented in the estimator form involving the corresponding stochastic variates

$$F_n^e = \sum_{i=1}^{n-1} \lambda_{in} F_i \tag{2.26}$$

In equation (2.25) and (2.26), the Kriging weights λ_{in} are determined based on the unbiased condition

$$\begin{aligned} E(F_n^e - F_n) &= E\left(\sum_{i=1}^{n-1} \lambda_{in} F_i - F_n\right) \\ &= \sum_{i=1}^{n-1} \lambda_{in} \mu - \mu \\ &= 0 \end{aligned} \tag{2.27}$$

and on the minimum estimation variance

$$\begin{aligned} E[(F_n^e - F_n)^2] &= E\left[\left(\sum_{i=1}^{n-1} \lambda_{in} F_i - F_n\right)^2\right] \\ &= \sum_{i=1}^{n-1}\sum_{j=1}^{n-1} \lambda_{in}\lambda_{jn} R_{ij} - 2\sum_{i=1}^{n-1} \lambda_{in} R_{in} + R_{nn} \end{aligned} \tag{2.28}$$

where E= ensemble average, R_{ij}= correlation function between F_i and F_j, and $\mu = \mu_i$= mean value of F_i. The Hamiltonian may then be established by introducing a Lagrangian multiplier γ_n as

$$H = \sum_{i=1}^{n-1}\sum_{j=1}^{n-1}\lambda_{in}\lambda_{jn}R_{ij} - 2\sum_{i=1}^{n-1}\lambda_{in}R_{in} + R_{nn} + \gamma_n\left(\sum_{i=1}^{n-1}\lambda_{in} - 1\right) \tag{2.29}$$

The necessary condition to minimise the estimation variance of (2.28) subjected to the condition (2.27) is

$$\begin{aligned} &\frac{\partial H}{\partial \gamma_n} = 0 \\ &\frac{\partial H}{\partial \lambda_{in}} = 0, \quad i = 1, \quad 2, \quad \cdots, \quad n-1 \end{aligned} \tag{2.30}$$

Substitution of (2.29) into (2.30) yields

$$\sum_{i=1}^{n-1}\lambda_{in} = 1 \tag{2.31}$$

$$\sum_{i=1}^{n-1}\lambda_{in}R_{ij} + \frac{1}{2}\gamma_n = R_{jn}, \quad j = 1, \quad 2, \quad \cdots, \quad n-1 \tag{2.32}$$

Equations (2.31) and (2.32) are solved for λ_{in} and γ_n as follows:

$$\begin{Bmatrix} \lambda_{1n} \\ \lambda_{2n} \\ \vdots \\ \lambda_{(n-1)n} \\ \gamma_n/2 \end{Bmatrix} = \begin{bmatrix} R_{11} & R_{12} & \cdots & R_{1(n-1)} & 1 \\ R_{12} & R_{22} & \cdots & R_{2(n-1)} & 1 \\ \vdots & \vdots & \ddots & \vdots & \vdots \\ R_{1(n-1)} & R_{2(n-1)} & \cdots & R_{(n-1)(n-1)} & 1 \\ 1 & 1 & \cdots & 1 & 0 \end{bmatrix}^{-1} \begin{Bmatrix} R_{1n} \\ R_{2n} \\ \vdots \\ R_{(n-1)n} \\ 1 \end{Bmatrix} = [K]^{-1} \begin{Bmatrix} R_{1n} \\ R_{2n} \\ \vdots \\ R_{n(n-1)} \\ 1 \end{Bmatrix} \tag{2.33}$$

where $[K]$= Kriging matrix. It can be seen from equation (2.33) that matrix $[K]$ depends only on the statistics of the $(n-1)$ known ground motions and not on the statistics of the variate to be estimated. The Kriging method may be used to obtain the best linear unbiased estimate or the Kriged values for the stationary stochastic process with unknown non-zero mean since the Kriging weights determined in equation (2.33) and thus the Kriged value, equation (2.26), can be obtained without knowledge of the non-zero mean of the stochastic process. Substitution of equations (2.31) and (2.32) into (2.28) yields the following minimum estimation variance known as the Kriging variance, for the non-zero mean stochastic process,

$$\begin{aligned} \sigma_k^2 &= \min\left\{E\left[(F_n^e - F_n)^2\right]\right\} \\ &= R_{nn} - \sum_{i=1}^{n-1}\lambda_{in}R_{in} - \frac{1}{2}\gamma_n \end{aligned} \tag{2.34}$$

However, the problem here is not just the matter of estimation, but the matter of simulating the stochastic variate F_n under the condition that $(n-1)$ ground motions are known. The simulation in the context of the Kriging method proceeds with the aid of the following identity:

$$F_n = F_n + F_n^e - F_n^e = F_n^e + (F_n - F_n^e) = F_n^e + E_n \tag{2.35}$$

where F_n^e = estimated value obtained from equation (2.26), and E_n = stochastic variate of error $(F_n - F_n^e)$. The realizations $e_n = f_n - f_n^e$ of $E_n = F_n - F_n^e$ are never known since the true f_n is unknown. However, if another stochastic process F^s can be simulated, which is independent of F and isomorphic to F, then $(F_n^s - F_n^{se})$ is isomorphic and independent of $(F_n - F_n^e)$. On the basis that the kriging estimator has the following orthogonal property

$$E[F_n^e (F_n - F_n^e)] = 0 \tag{2.36}$$

Journel and Huijbregts [1978] suggested that $(F_n - F_n^e)$ in equation (2.35) could be replaced by $(F_n^s - F_n^{se})$. Thus equation (2.35) becomes

$$F_n^c = F_n^e + (F_n^s - F_n^{se}) = F_n^e + E_n^s \tag{2.37}$$

where the conditional simulation of F_n^c is of course isomorphic to F_n. However, equation (2.36) does not guarantee the independence of F_n^e and $(F_n - F_n^e)$ unless $F(t)$ and thus F_n^e and $(F_n - F_n^e)$ are Gaussian. Therefore, the Kriging method can be applied to the conditional simulation only if the stochastic process under consideration is Gaussian.

As an alternative, Hoshiya [1994, 1995] proposed a modified conditional simulation procedure for the error E_n, which is described below. The statistics of error E_n can be found as

$$E(E_n) = E[(F_n - F_n^e)] = 0 \tag{2.38}$$

$$\begin{aligned} E(E_n E_m) &= E[(F_n - F_n^e)(F_m - F_m^e)] \\ &= E(F_n F_m) - E(F_n F_m^e) - E(F_m F_n^e) + E(F_n^e F_m^e) \\ &= R_{nm} - E(F_n \sum_{i=1}^{n-1} \lambda_{im} F_i) - E(F_m \sum_{i=1}^{n-1} \lambda_{in} F_i) + E[(\sum_{i=1}^{n-1} \lambda_{in} F_i)(\sum_{i=1}^{n-1} \lambda_{im} F_i)] \\ &= R_{nm} - \sum_{i=1}^{n-1} \lambda_{im} R_{in} - \sum_{i=1}^{n-1} \lambda_{in} R_{im} + \sum_{i=1}^{n-1} \sum_{i=1}^{n-1} \lambda_{in} \lambda_{im} R_{ij} \end{aligned} \tag{2.39}$$

With the aid of equation (2.32) associated with Kriging weights for F_n^e and F_m^e, equation (2.30) becomes

$$E(E_n E_m) = R_{nm} - \sum_{i=1}^{n-1} \lambda_{in} R_{im} - \frac{1}{2}\gamma_n$$
$$= R_{nm} - \sum_{i=1}^{n-1} \lambda_{im} R_{in} - \frac{1}{2}\gamma_m \tag{2.40}$$

The correlation (covariance) of errors between E_n and E_m in equation (2.40) is not zero in general, indicating that the to-be-simulated stochastic errors are correlated. Thus, Hoshiya asserts that the statistics of the errors $E_m (m = n, \quad n+1, \quad \cdots, \quad N)$ derived in (2.40) can be directly used for the simulation of errors. This assertion forms the basis of the conditional simulation by means of the modified Kriging method.

2.2.5.2 Conditional probability density function method

Similar to the aforementioned description of the problem, a one-dimensional and univariate stationary stochastic process is discretized as $F_i \quad (i = 1, \quad 2, \quad \cdots, \quad n)$, the first $(n-1)$ observations are known a priori, and the stochastic variate F_n needs to be simulated under the condition that the first $(n-1)$ realizations are known. Since each random variate F_i is Gaussian-distributed, the n-dimensional joint probabilistic density function for $F_1, \quad F_2, \quad \cdots, \quad F_n$ are also Gaussian and can be shown to be

$$p_{F_1 \cdots F_n}(f_1, \quad \cdots, \quad f_n) = \frac{1}{\sqrt{(2\pi)^n |\mathbf{V}_n|}} \exp\left(-\frac{1}{2}\mathbf{f}^T \mathbf{V}_n^{-1} \mathbf{f}\right) \tag{2.41}$$

where

$$\mathbf{f}^T = [(f_1 - \mu_1) \quad (f_2 - \mu_2) \quad \cdots \quad (f_n - \mu_n)] \tag{2.42}$$

and $|\mathbf{V}_n|$ = determinant of variance matrix $\mathbf{V}_n$ defined by

$$\mathbf{V}_n = \begin{bmatrix} \sigma_1^2 & \cdots & \kappa_{1(n-1)} & \kappa_{1n} \\ \vdots & \ddots & \vdots & \vdots \\ \kappa_{1(n-1)} & \cdots & \sigma_{n-1}^2 & \kappa_{(n-1)n} \\ \kappa_{1n} & \cdots & \kappa_{(n-1)n} & \sigma_n^2 \end{bmatrix} \tag{2.43}$$

in which the variances $\sigma_i^2 (= \sigma_j^2)$ and covariances κ_{ij} are known a priori. The $(n-1)$ dimensional joint density function for $F_1, \quad F_2, \quad \cdots, \quad F_{n-1}$ may be derived from (2.41) as a marginal density function

$$p_{F_1 \cdots F_{n-1}}(f_1, \quad \cdots, \quad f_{n-1}) = \int_{-\infty}^{\infty} p_{F_1 \cdots F_n}(f_1, \quad \cdots, \quad f_n) df_n$$
$$= \frac{1}{\sqrt{(2\pi)^n |\mathbf{V}_n|}} \sqrt{\frac{2\pi}{a_{nn}}} \exp\left\{\frac{a_{nn}}{2}\left[\sum_{i=1}^{n-1} \frac{a_{in}}{a_{nn}}(f_i - \mu_i)\right]^2 - \frac{1}{2}\sum_{i=1}^{n-1}\sum_{j=1}^{n-1}(f_i - \mu_i)(f_j - \mu_j)a_{ij}\right\} \tag{2.44}$$

where a_{ij} = elements of matrix $\mathbf{V}_n^{-1}$. Then, the conditional probability density function for F_n conditional to observations f_1, f_2, $\cdots$, f_{n-1} of F_1, F_2, $\cdots$, F_{n-1} is obtained as

$$p_{F_n|F_1F_2\cdots F_{n-1}}(f_n|f_1,f_2,\cdots,f_{n-1}) = \frac{p_{F_1F_2\cdots F_n}(f_1,f_2,\cdots,f_n)}{p_{F_1F_2\cdots F_{n-1}}(f_1,f_2,\cdots,f_{n-1})} = \frac{1}{\sqrt{(2\pi)}\sigma_n^c}\exp\left[-\frac{1}{2}\frac{(f_n-\mu_n^c)^2}{(\sigma_n^c)^2}\right] \tag{2.45}$$

where

$$\mu_n^c = \mu_n - \frac{1}{a_{nn}}\sum_{i=1}^{n-1} a_{in}(f_i-\mu_i) \tag{2.46}$$

$$(\sigma_n^c)^2 = \frac{1}{a_{nn}} \tag{2.47}$$

If the covariances between $F_i (i=1,\ 2,\ \cdots,\ n-1)$ and F_n are zero, i.e., $\kappa_{in}=0$, the equations (2.46) and (2.47) degenerate into $\mu_n^c = \mu_n$ and $\sigma_n^c = \sigma_n$, which are consistent with the corresponding degenerated case of the unconditional probabilistic density function. It can be seen from (2.45) to (2.47) that the conditional stochastic variate F_n^c, i.e., stochastic variate F_n conditional to the known observations f_1, f_2, $\cdots$, f_{n-1} of stochastic variates F_1, F_2, $\cdots$, F_{n-1}, is still a Gaussian distribution. However, the mean and variance are modified to accommodate the known observations and the resulting change in statistics.

2.3 *The Effect of Asynchronous Motions on the Response of Extended Structures*

The effect of the spatial variation of the seismic ground motions on the response of extended structures was recognized a number of decades ago [Bogdanoff et al.1965]. However, the spatial variability has only been attributed to the wave passage effect because of insufficient knowledge of the mechanisms underlying the spatial variability of the motion. The influences of travelling waves on the responses of bridges were investigated by Bogdanoff et al.[1965], Vanmarcke [1977], Werner et al. [1979], Somaini [1987] and Bayrak [1996]. A breakthrough occurred with the installation of the strong motion arrays and the analyses of the recorded data, especially the data from SMART-1 array, which suggested that the seismic waves not only propagate on the ground surface, but they also change in shape at various locations; this latter effect may also significantly affect the response of extended structures. Since then, the

spatial variability of the seismic ground motions and its effects on extended structures has attracted significant research interest.

2.3.1 The steady-state response to harmonic waves

Werner et al. [1979] computed the three-dimensional steady-state response of a single-span bridge resting on the surface of an elastic half-space and subjected to incident plan SH-waves that were assumed to be harmonic waves. The bridge used in the study and shown in Figure 2.12(a) is 36.5m long, 21.5m wide, and 6.1m high. The bridge was modelled using the system of undamped beam elements shown in Figure 2.12(b). The free-field excitation from the incident SH-waves have a surface amplitude of 2.0, an arbitrary excitation frequency (up to 25 Hz maximum), and a zero phase angle at the upstream foundation, which is the origin of the coordinate system for these analyses. The orientation of these excitations and the direction of wave propagation are represented by the two angles of incidence, θ_H, angle of incidence measured from x-y plane of ground surface and, θ_V, angle of incidence measured from x-z plane of the structure, as shown in Figure 2.12(a). Five different excitation cases were run.

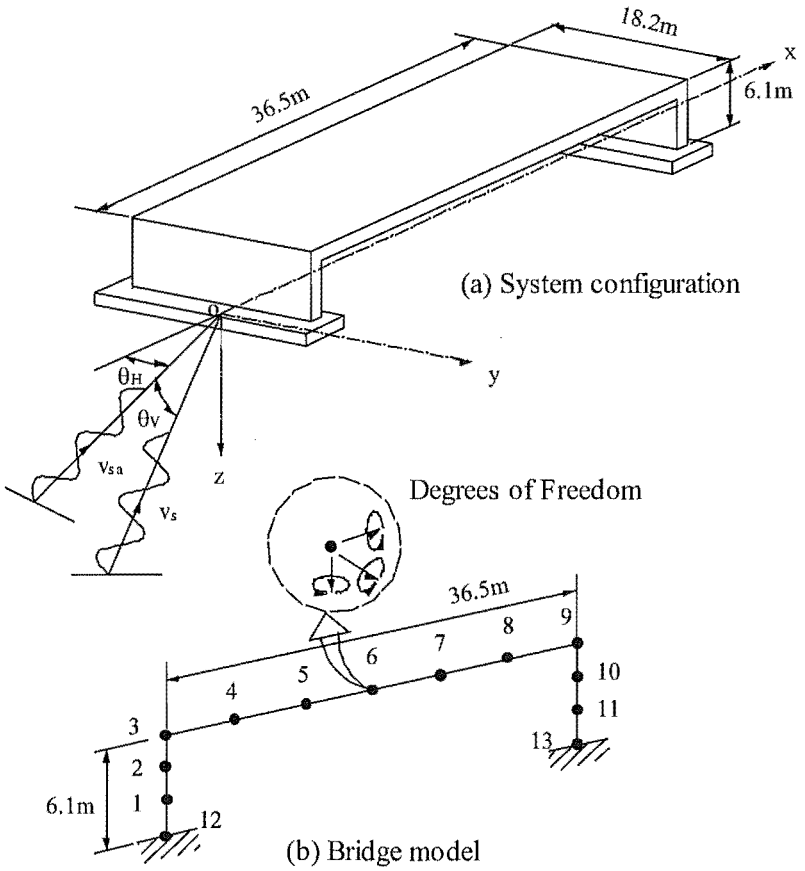

Figure 2.12 Bridge Configuration and Model Used in Analysis

The results of the analyses lead to two main conclusions. First, phase differences in the input ground motions applied to bridge foundations can have significant effects on the bridge response. Second, the nature of the structural response to these travelling waves is strongly dependent on the direction of incidence as well as on the excitation frequency of the seismic waves.

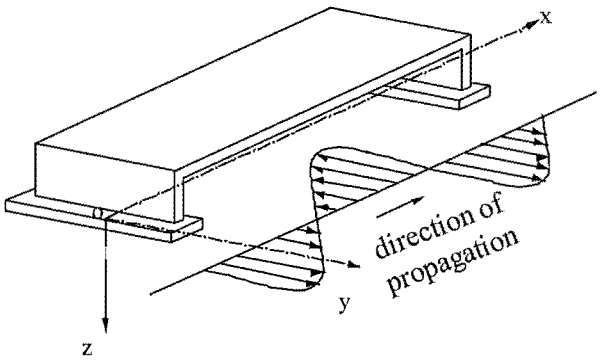

Figure 2.13 Excitation from incident wave

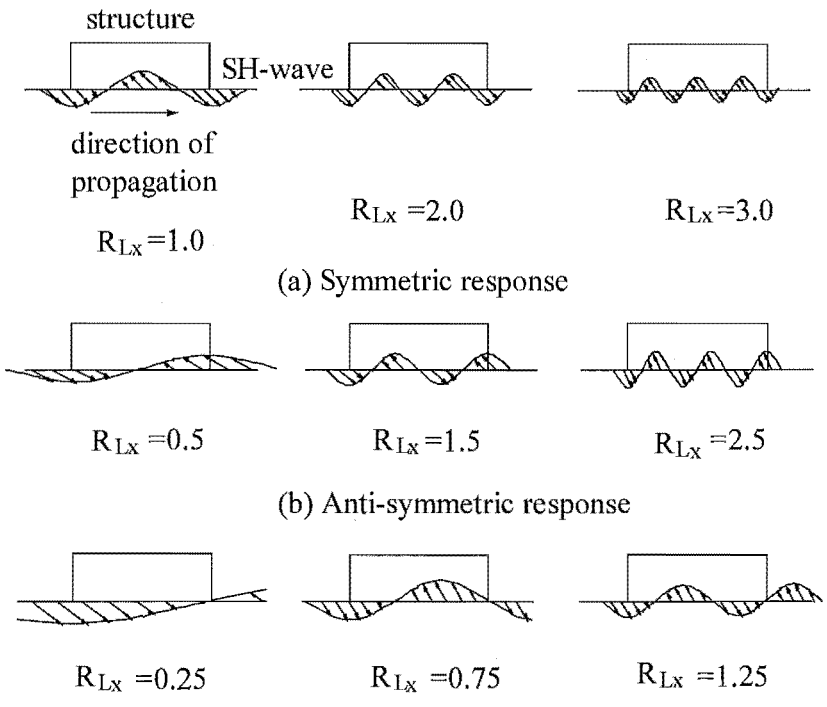

Figure 2.14 Case 4: Relationship between Wavelength of Incident SH-Waves and Bridge Response Characteristics

The analysis results of case 4 (Figure 2.13), as an example, are shown in Figure 2.14. This case considers horizontally incident SH-waves that propagate in a plane parallel to the bridge span and apply excitations to the bridge that are directed along the y-axis. Bridge responses that are symmetric about its midspan occur when the wavelength of the incident wave is such that the excitations applied to each foundation are identical in amplitude and phase. Responses of the bridge that are anti-symmetric about its midspan occur when the wavelength of the incident wave is such that the excitations applied to each foundation are of equal amplitude and opposite phase. A third type of response (whipping) occurs when the wavelengths of the incident waves are such that the excitations applied to each foundation are 90° out of phase. $R_L = l/\lambda = l\omega/2\pi V_s$, in Figure 2.14, is the dimensionless frequencies, in which λ = the wavelength of the incident wave along its propagation path; V_s = the shear wave velocity of elastic half-space; ω = the circular frequency of the excitation; and l = a characteristic structural dimension.

2.3.2 Random vibration analysis method

2.3.2.1 Response of multi-degree-of-freedom system

The coupled equations of motion of a linear, lumped mass, multi-degree-of-freedom, multiple supported structural system subjected to uni-dimensional translational seismic excitations can be written in matrix form as follows:

$$\begin{bmatrix} \mathbf{M}_s & \mathbf{0} \\ \mathbf{0} & \mathbf{M}_b \end{bmatrix} \begin{bmatrix} \ddot{\mathbf{U}}_s \\ \ddot{\mathbf{U}}_b \end{bmatrix} + \begin{bmatrix} \mathbf{C}_s & \mathbf{C}_{sb} \\ \mathbf{C}_{bs} & \mathbf{C}_b \end{bmatrix} \begin{bmatrix} \dot{\mathbf{U}}_s \\ \dot{\mathbf{U}}_b \end{bmatrix} + \begin{bmatrix} \mathbf{K}_s & \mathbf{K}_{sb} \\ \mathbf{K}_{bs} & \mathbf{K}_b \end{bmatrix} \begin{bmatrix} \mathbf{U}_s \\ \mathbf{U}_b \end{bmatrix} = \begin{bmatrix} \mathbf{0} \\ \mathbf{P}_b \end{bmatrix} \tag{2.48}$$

in which the subscripts s and b refer to the structure and the base, respectively; $\mathbf{M}$, $\mathbf{C}$ and $\mathbf{K}$ refer to the mass, damping and stiffness matrices respectively; and $\mathbf{P}_b$ is the vector of reaction forces at the base (support points). In order to solve equation (2.48), it is convenient to separate the displacements in the structure into two parts: a pseudostatic component $\mathbf{U}_s^s$, and a dynamic component $\mathbf{V}_s$:

$$\begin{bmatrix} \mathbf{U}_s \\ \mathbf{U}_b \end{bmatrix} = \begin{bmatrix} \mathbf{U}_s^s \\ \mathbf{U}_b \end{bmatrix} + \begin{bmatrix} \mathbf{V}_s \\ \mathbf{0} \end{bmatrix} \tag{2.49}$$

The pseudostatic component satisfies the equation

$$\begin{bmatrix} \mathbf{K}_s & \mathbf{K}_{sb} \\ \mathbf{K}_{bs} & \mathbf{K}_b \end{bmatrix} \begin{bmatrix} \mathbf{U}_s^s \\ \mathbf{U}_b \end{bmatrix} = \begin{bmatrix} \mathbf{0} \\ \mathbf{P}_b^s \end{bmatrix} \tag{2.50}$$

from which one can solve for $\mathbf{U}_s^s$:

$$\mathbf{U}_s^s = -\mathbf{K}_s^{-1}\mathbf{K}_{sb}\mathbf{U}_b \tag{2.51}$$

Substituting equations (2.49) and (2.51) into equation (2.48), one obtains

$$\mathbf{M}_s\ddot{\mathbf{V}}_s + \mathbf{C}_s\dot{\mathbf{V}}_s + \mathbf{K}_s\mathbf{V}_s = \mathbf{M}_s\mathbf{K}_s^{-1}\mathbf{K}_{sb}\ddot{\mathbf{U}}_b + (\mathbf{C}_s\mathbf{K}_s^{-1}\mathbf{K}_{sb} - \mathbf{C}_{sb})\dot{\mathbf{U}}_b \tag{2.52}$$

Now, both the stiffness and damping matrices satisfy the rigid body conditions

$$\begin{bmatrix}\mathbf{K}_s & \mathbf{K}_{sb}\\ \mathbf{K}_{bs} & \mathbf{K}_b\end{bmatrix}\begin{bmatrix}\mathbf{E}_s\\ \mathbf{E}_b\end{bmatrix} = \begin{bmatrix}\mathbf{0}\\ \mathbf{0}\end{bmatrix}, \qquad \begin{bmatrix}\mathbf{C}_s & \mathbf{C}_{sb}\\ \mathbf{C}_{bs} & \mathbf{C}_b\end{bmatrix}\begin{bmatrix}\mathbf{E}_s\\ \mathbf{E}_b\end{bmatrix} = \begin{bmatrix}\mathbf{0}\\ \mathbf{0}\end{bmatrix} \tag{2.53}$$

where $\mathbf{E}_s$ and $\mathbf{E}_b$ are the rigid body displacement vectors associated with the active direction of support motion. If the damping term in the forcing function is neglected, then the above equation becomes

$$\mathbf{M}_s\ddot{\mathbf{V}}_s + \mathbf{C}_s\dot{\mathbf{V}}_s + \mathbf{K}_s\mathbf{V}_s = \mathbf{M}_s\mathbf{K}_s^{-1}\mathbf{K}_{sb}\ddot{\mathbf{U}}_b \tag{2.54}$$

This equation can be solved by modal superposition, that is assuming $\mathbf{V}_s = \mathbf{\Phi Y}$, multiplying by $\mathbf{\Phi}^T$ and considering the orthogonality conditions as well as the assumptions of proportional modes for the structure:

$$(\mathbf{\Phi}^T\mathbf{M}_s\mathbf{\Phi})\ddot{\mathbf{Y}} + (\mathbf{\Phi}^T\mathbf{C}_s\mathbf{\Phi})\dot{\mathbf{Y}} + (\mathbf{\Phi}^T\mathbf{K}_s\mathbf{\Phi})\mathbf{Y} = \mathbf{\Phi}^T\mathbf{M}_s\mathbf{K}_s^{-1}\mathbf{K}_{sb}\ddot{\mathbf{U}}_b \tag{2.55}$$

or in terms of the k th modal component

$$\ddot{y}_k + 2\varsigma_k\omega_k\dot{y}_k + \omega_k^2 y_k = -\gamma_k\ddot{u}_k \tag{2.56}$$

in which y_k is the modal displacement; ς_k is the fraction of modal damping; ω_k is the modal frequency; and

$$\ddot{u}_k = \mathbf{A}_k\ddot{\mathbf{U}}_b = \sum_{i=1}^{n} A_{ki}\ddot{u}_{bi} = \text{modal support motion} \tag{2.57a}$$

$$\mathbf{A}_k = \frac{\boldsymbol{\varphi}_k^T\mathbf{M}_s\mathbf{K}_s^{-1}\mathbf{K}_{sb}}{\boldsymbol{\varphi}_k^T\mathbf{M}_s\mathbf{E}_s} = [A_{ki}] \tag{2.57b}$$

$$\gamma_k = \frac{\boldsymbol{\varphi}_k^T\mathbf{M}_s\mathbf{E}_s}{\boldsymbol{\varphi}_k^T\mathbf{M}_s\boldsymbol{\varphi}_k} = k \text{ th participation factor} \tag{2.57c}$$

$\mathbf{A}_k$ is a row vector with n components A_{ki}, with n being the total number of degrees of freedom at the support points. In general, however, $\ddot{u}_k$ is known only in a stochastic sense, which implies that equation (2.55) cannot be solved directly by means of a response spectrum for $\ddot{u}_k$. However, it is possible to characterize y_k by means of its spectral density function

$$S_{yk}^p(\omega) = \gamma_k^2\left|H_k(\omega)\right|^2 S_{\ddot{u}_k}(\omega) \tag{2.58}$$

where $S_{yk}^p(\omega)$ is the spectral density function of y_k for the case of partially correlated excitations; $H_k(\omega)$ is the frequency response function (transfer function) for mode k; and

$S_{\ddot{u}_k}(\omega)$ is the spectral density function of the modal support motion. From equation (2.57a), it follows that this function is given by

$$\begin{aligned} S_{\ddot{u}_k}(\omega) &= \sum_{i=1}^{n}\sum_{j=1}^{n} A_{ki}A_{kj}S_{\ddot{u}_i\ddot{u}_j}(\omega) \\ &= \left[\sum_{i=1}^{n} A_{ki}^2 + 2\sum_{i=1}^{n-1}\sum_{j=i+1}^{n} A_{ki}A_{kj}\rho_{ij}(\omega,d_{ij})\right] S_{\ddot{u}_g}(\omega) \\ &= \mathbf{A_k Q A_k^T} S_{\ddot{u}_g}(\omega) \end{aligned} \tag{2.59}$$

where $\mathbf{Q} = [\rho_{ij}]$ =coherency matrix. Combining equation (2.58) and (2.57), one obtains

$$S_{yk}^{p}(\omega) = \gamma_k^2 \left|H_k(\omega)\right|^2 \mathbf{A_k Q A_k^T} S_{\ddot{u}_g}(\omega) \tag{2.60}$$

The mean square value of the total response, u_{sk}, can be obtained by determining the autocorrelation function of u_{sk} and then taking the Fourier transform of the resulting equation which leads the power spectral density function of the total response u_{sk}. The integration of the power spectral density over the frequency domain provides the mean square value of the total response u_{sk}.

2.3.2.2 The results of random vibration analysis

Abdel-Ghaffar and Rubin [1982] studied the vertical response of the Vincent Thomas Suspension Bridge in Los Angeles subjected to multiple-support excitations by means of random vibration theory. The multiple-support earthquake excitations were selected from the records of the 1971 San Fernando earthquake in the Los Angeles area. It was observed that the participation of higher modes in the total response was essential in order to reliably assess the seismic behaviour of such structures and that the response values associated with correlated multiple-support excitations are significantly different from those obtained through the uncorrelated case.

Using the random vibration analysis method Zerva [1990] investigated the response of continuous two- and three- span beams of various lengths subjected to spatially varying seismic ground motions. The spatial correlations of ground motions were assumed to decay exponentially with separation distance and frequency. Various degrees of exponential decay were used in the analysis; thus, a wide range of possible correlations between the motions at the supports of the structures were examined. Square roots of mean-square values of total displacements, bending moments and shear forces were outputs of the analyses. The analyses suggested that input motions with low correlation produce the highest pseudo static response.

As correlation increases, the pseudo static response decreases, and the dynamic response increases. Full correlation produces the highest dynamic response that consists solely of symmetric modes for the symmetric beams examined, the pseudo static response in this case is equal to zero. Fully correlated motions may produce higher or lower response than the one induced by partially correlated motions, depending on the dynamic characteristics of the structures, the position along the beams where the response is evaluated, the different response quantities that are evaluated, the relative location of the natural frequencies of the beams with respect to the dominant frequencies of ground motions, as well as on the degree of partial correlation between the support motions.

Heredia-Zavoni and Vanmarcke [1994] proposed an efficient random vibration methodology for the seismic response analysis of linear multi-support structures. It reduces the response analysis of such structures to that of a series of independent one-degree of freedom modal oscillators in a way that fully accounts for multi-support inputs and the space-time correlation structure of the ground motion.

Venkataramana et al. [1996] analyzed the dynamic response of a multi-span elevated continuous bridge and including the footing-soil, subjected to a spatially varying ground motion using the random vibration approach. The PSDF of the ground accelerations including the spatial variability of ground motions is of the form as

$$\left[S_{\ddot{u}_g\ddot{u}_g}(\omega)\right] = \left[S_{x_m x_n}(\omega)\right]\cdot\left[S_1(\omega)\right]\cdot\left[S_2(\omega)\right]S_0 \tag{2.61}$$

where

$$\left[S_{x_m x_n}(\omega)\right] = \exp\left[-\left(\omega\varsigma_{ef} + i\omega\right)\frac{|x_m - x_n|}{C_s}\right], \quad S_0 = \frac{\sigma^2_{\ddot{u}_g}}{\pi(1+4\varsigma_g^2)\omega_g/(2\varsigma_g)}$$

$$\left[S_1(\omega)\right] = \frac{(\omega/\omega_f)^4}{\left(1-(\omega/\omega_f)^2\right)^2 + 4h_f^2(\omega/\omega_f)^2}, \quad \left[S_2(\omega)\right] = \frac{1+4\varsigma_g^2(\omega/\omega_g)^2}{\left(1-(\omega/\omega_g)^2\right)^2 + 4\varsigma_g^2(\omega/\omega_g)^2}$$

x_m, x_n are coordinates of the reference points, C_s is the phase velocity of the seismic motion, ω_g, ς_g are the filter parameters (characteristic ground frequency and characteristic ground damping ratio respectively) of the well-known Kanai-Tajimi type, $\sigma_{\ddot{u}_g}$ is the *rms* (root mean square) value of ground acceleration, S_0 is the intensity of white noise at a support, ω_f, ς_f are the filter parameters (frequency parameter and damping parameter respectively) of a second filter, introduced to overcome the limitations of the Kanai-Tajimi type filter occurring

in the region of low-frequencies. The results of the random vibration analysis are expressed using *rms* displacements and *rms* sectional forces at typical nodal points of the model. It is shown that, (*i*) several vibration modes, starting from the first, contribute significantly to the dynamic response in terms of displacements and section force of the structure, (*ii*) the response values generally increase with increasing phase velocity and approach a steady value when the phase velocity reaches around 3000m/s, (*iii*) the effects of non-uniform vibration of supports, due to a phase difference of the input seismic wave, are especially important for sectional forces (namely, axial forces, shear forces, bending moments and torsional moments) of structural nodes.

2.3.3 Response spectrum method

Berrah and Kausel [1992] developed a modified response spectrum model for the design of extended structures subjected to single and multi-component ground motion. The technique is an extension to the mode superposition method combined with the response spectrum method. From an engineering viewpoint, the mean value of the maximum modal response is a interesting quantity. When the motions are fully correlated, this value can be obtained from the ground response spectrum $R(\omega,\xi)$

$$|y_k|_{\max} = |\gamma_k| R(\omega_k,\xi_k) \tag{2.62}$$

For the case of partially correlated support motions, the mean value of the maximum modal response, $|y_k^p|_{\max}$, and a modified ground response spectrum, $R^p(\omega_k,\xi_k)$, should also have the similar relationship

$$|y_k^p|_{\max} = |\gamma_k| R^p(\omega_k,\xi_k) \tag{2.63}$$

Based on random vibration theory, Berrah and Kausel found that $R(\omega_k,\xi_k)$ and $R^p(\omega_k,\xi_k)$ are related by an expression of the form

$$R^p(\omega_k,\xi_k) = \left(\mathbf{A_k Q_k A_k^T}\right)^{1/2} R(\omega_k,\xi_k) \tag{2.64}$$

in which $\mathbf{Q_k} = \left[\rho_{ijk}\right]$, $\rho_{ijk} = \dfrac{\int_0^\infty \rho_{ij}|H_k|^2 G_{ii_g}(\omega)d\omega}{\int_0^\infty |H_k|^2 G_{ii_g}(\omega)d\omega}$

In order to simplify the computation of ρ_{ijk}, the design earthquake with response spectrum $R(\omega,\xi)$ will be assumed to be broad-branded; hence its spectral density function G_{u_g} can be approximated by a white noise process, that is G_{u_g} = constant. The coherency function for the ground motion proposed by Loh and Yeh [1988] is adopted, namely

$$\rho_{ij} = e^{-a\omega\tau}\cos\omega\tau \tag{2.65}$$

with $a = 1/16\pi$ and $\tau =$ travel time between support point i and j. The transfer function has the form of

$$|H_k|^2 = \begin{cases} 1/\omega_k^4 & for\omega \le \omega_k \\ \dfrac{1}{\omega_k^3}\left(\dfrac{\pi}{4\xi_k} - 1\right)\delta(\omega - \omega_k) \end{cases} \tag{2.66}$$

with $\delta(\omega - \omega_k)$ being Dirac's delta function. With these assumption ρ_{ijk} becomes

$$\rho_{ijk} = \frac{4\xi_k}{\pi}\left\{e^{-a\omega_k\tau}\left[\frac{\sin\omega_k\tau - a\cos\omega_k\tau}{\omega_k\tau} + \left(\frac{\pi}{4\xi_k} - 1\right)\cos\omega_k\tau\right] + \frac{a}{\omega_k\tau}\right\} \tag{2.67}$$

For frame-type buildings subjected to horizontal earthquake components, it was found that

$$\left(\mathbf{A_k Q_k A_k^T}\right)^{1/2} = \frac{1}{N}\left(\sum_{i=1}^{n}\sum_{j=1}^{n}\rho_{ijk}\right)^{1/2} \tag{2.68}$$

The theoretical model was validated through digital simulation of the seismic ground motion, whereby model predictions were found to be in good agreement with the exact result. This method did not consider the pseudo-static component of the response and cannot account for variation of local-soil conditions.

In general, the expected value of the peak of a stationary process can be related to its root-mean-square value through a 'peak factor'. Accordingly, Kiureghian and Neuenhofer [1992] derived a combination rule known as the multiple-support response spectrum (MSRS) method, which yields approximately the mean maximum response. That is

$$\begin{aligned} E\left[\max|z(t)|\right] &= p_z\sigma_z \\ &= \left[\sum_{k=1}^{m}\sum_{l=1}^{m} a_k a_l \rho_{u_k u_l} u_{k,\max} u_{l,\max}\right. \\ &\quad + 2\sum_{k=1}^{m}\sum_{l=1}^{m}\sum_{j=1}^{n} a_k b_{lj} \rho_{u_k s_{lj}} u_{k,\max} D_l(\omega_j, \zeta_j) \\ &\quad \left. + \sum_{k=1}^{m}\sum_{l=1}^{m}\sum_{i=1}^{n}\sum_{j=1}^{n} b_{kl} b_{lj} \rho_{s_{ki} s_{lj}} D_k(\omega_i, \zeta_i) D_l(\omega_j, \zeta_j)\right]^{1/2} \end{aligned} \tag{2.69}$$

where $z(t)$ is the generic response quantity; p_z is the corresponding peak factor; σ_z is the root-mean-square of the response $z(t)$; a_k and b_{ki} denote the effective influence factors and effective modal participation factors, respectively; $u_{k,\max} = E\left[\max|u_k|\right]$ denotes the mean peak ground displacement; $D_k(\omega_i, \zeta_i) = E\left[\max|s_{ki}(t)|\right]$ denotes the response spectrum for the support degree of freedom k, representing the expected value of the peak of the absolute

response of an oscillator of frequency ω_i and damping ζ_i to the base acceleration $\ddot{u}_k(t)$; $\rho_{u_k u_l}$, $\rho_{u_k s_{lj}}$ and $\rho_{s_{ki} s_{lj}}$ are three cross-correlation coefficients, which depend on both the coherency function and the power spectral density functions of each pair of support motions. The correspondence between the response spectrum and the power spectral density function of the ground acceleration process could be used to circumvent the dependence of the cross-correlation coefficients on the power spectral density functions of each pair of support motions.

In their paper, Kiureghian and Neuenhofer [1992] gave an example application to examine the relative significances of the pseudo-static and dynamic components of the response, as well as the effects of wave passage and incoherence by this response spectrum method. A two-span continuous beam was considered, which had uniform mass and stiffness properties and simple supports. As shown in Figure 2.15, the beam was discretized into 20 elements along each L =

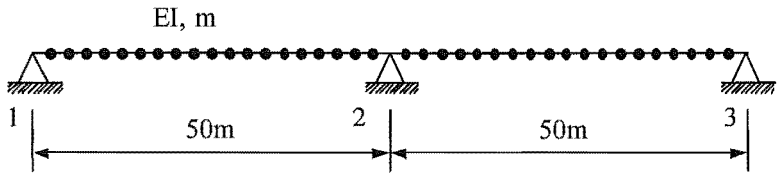

Figure 2.15 Example structure

50 m span and the mass of each element is lumped half at each end of the element. The system was represented by 38 translational and 41 rotational degrees of freedom, and 3 translational support degrees of freedom. Only the first four modes were considered in the analyses. Five different cases were assumed for the coherency function, $\gamma_{kl}(i\omega)$, describing the variation between the support motions:

Case 1: Full coherent (uniform) motions at all three supports.

Case 2: Only the wave passage effect included.

Case 3: Only the incoherence effect included.

Case 4: Both the wave passage and incoherence effects included.

Case 5: Mutually statistically independent support motions.

The results showed that the influence of spatial variability of the ground motion on the response of a multiply supported structure could be significant. It was found that in most cases the spatial variability tended to reduce the response (in relation to the case with uniform support motions), often by a significant amount (e.g. close to 30 per cent). However, this rule cannot be generalized since, under certain conditions (i.e. stiff structures and rapid loss of

coherency), the response may actually amplify due to an increase in the pseudo-static component of the response.

2.3.4 Time-history analysis method

Monti et al. [1996] studied the nonlinear response of bridges under asynchronous motions by using the time-history method. The bridge analyzed was a six-span continuous deck with five piers of the same height H (= 7.5m, 10m and 15m respectively) and 2.5m diameter as shown in Figure 2.16. The span length was 50m. The deck was transversely hinged to the piers and the abutments. The piers were considered as fixed at the ground level. The asynchronous motions were simulated according to the spectral representation method with the coherence function model adopted by Luco and Wong [1986]. Each pier was modelled with two elements in series: a Takeda-type plastic hinge zone at the lower support, having a fixed length equal to one-tenth of the pier height and the remaining elastic part of the pier, whose flexibility was doubled to account for cracking. It was found that incoherent motions led to a decrease of the design forces, and hence to lower amounts of reinforcement, with respect to the synchronous case. This result showed no exceptions for the cases considered. Comparing the role played by each of the two components of the coherence function, it was found that the net dynamic excitation tended to zero when the motions (accelerations) input to the supports are independent (i.e. incoherence effect is dominant). In this case, the response became of purely static nature and it was due to the differential displacements of the ground at the supports and directly related to the assumed shape of the power density spectrum of the ground motions. When only the wave passage effect was considered, the effect on the response consisted essentially in a reduction of the dynamic part due to the incomplete synchronism of the excitation. The results were strictly dependent on the extremely regular bridge configuration examined and on the model describing the spatial variability of the motions. Additional investigations are needed to study the response of irregular bridges with piers of different heights under asynchronous seismic motions modeled with different coherence functions.

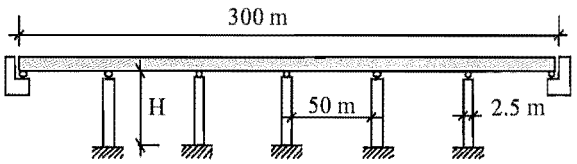

Figure 2.16 Schematic view of bridge

CHAPTER 3

PROPOSED METHOD FOR CONDITIONAL SIMULATION OF STOCHASTIC GROUND MOTIONS

3.1 Introduction

The Monte Carlo Simulation Method is widely used in engineering to solve complicated problems that cannot be treated effectively by purely analytical tools. In earthquake engineering, stochastic approaches are often used to simulate seismic ground motions. Recently, the conditional simulation of random processes and fields has been studied in connection with its application to urban earthquake monitoring. The conditional nature of the simulation stems from the fact that the realizations of the random processes or fields at only some locations have been recorded. One needs to simulate the random field when recorded information is not given. So far, the conditional simulation can be carried out by using either the Kriging method or the conditional probability density function method. Although the theoretical framework of conditional random fields has been established, its use by the earthquake engineering community is viewed as impractical due to its complexity [Jankowski and Wilde 2000].

In this chapter, a new, simple method for the conditional simulation of random processes is proposed and which is intended to be used for engineering purposes to study the effect of spatial variation of seismic input motion on the response of extended structures. In this method, the ground motion is treated as a stochastic field. One spatial correlation function that only depends on the predominant frequency of the earthquake is used to represent the correlation for the band of frequencies of interest [Jankowski and Wilde 2000]. In the time domain, no correlation between the acceleration elements in the same record is assumed. With the aid of these assumptions, the modified Kriging method [Hoshiya 1994; Hoshiya and Marugama 1994; Hoshiya 1995] can be easily used to conditionally simulate ground motions in the time domain.

3.2 Basic Formulation [Ren et al. 1995]

Assume that $\mathbf{f}(x) = [f_1(x), f_2(x), \cdots, f_n(x)]^T$ is a homogeneous n-variate Gaussian random vector field with zero-mean and cross-covariances $R\left[f_k(x_i), f_l(x_j)\right] = E\left[f_k(x_i) f_l(x_j)\right]$; $(k,l = 1,\ 2,\ \cdots,\ n)$; $\mathbf{g}(x_i)$ $(i = 1,\ 2,\ \cdots,\ N)$ is a set of realizations of the vector field $\mathbf{f}(x)$ at locations x_i. Following Hoshiya's technique [Hoshiya 1994; Hoshiya and Marugama 1994], the actual field $\mathbf{f}(x)$ could be represented by its simulated counterpart $\mathbf{f}^S(x)$, i.e. $\mathbf{f}(x) = \mathbf{f}^S(x)$. In component form, they are

$$\begin{aligned} f_l^S(x) &= f_l(x) \\ &= f_l^e(x) + [f_l(x) - f_l^e(x)] \\ &= f_l^e(x) + \varepsilon_l(x) \end{aligned} \tag{3.1}$$

where $f_l^e(x)$ is the Kriging estimate of the lth component $f_l(x)$ of the multi-variate random field $\mathbf{f}(x)$, and has the following form

$$f_l^e(x) = \sum_{i=1}^{N}\sum_{k=1}^{n} \lambda_{ikl}(x) f_k(x) \qquad (l = 1,\ 2,\ \cdots,\ n) \tag{3.2}$$

where λ_{ikl} are Kriging weights. $\varepsilon_l(x)$ in equation (3.1) is the error between the exact field $f_l(x)$ and its Kriging estimate $f_l^e(x)$

$$\varepsilon_l(x) = f_l(x) - f_l^e(x) \tag{3.3}$$

In order for equation (3.2) to be the best linear unbiased estimator, it is required that the variance of the error $\varepsilon_l(x)$ attains a minimum

$$Var[\varepsilon_l(x)] = \text{minimum} \tag{3.4}$$

At any unrecorded location x_r the variance of the error is of the form

$$\begin{aligned} Var[\varepsilon_l(x)] &= E\left\{ \left[f_l(x_r) - f_l^e(x_r)\right]^2 \right\} \\ &= Var[f_l(x_r)] - 2\sum_{i=1}^{N}\sum_{k=1}^{n} \lambda_{ikl}(x_r) R\left[f_k(x_i), f_l(x_r)\right] \\ &\quad + \sum_{i=1}^{N}\sum_{j=1}^{N}\sum_{k=1}^{n}\sum_{m=1}^{n} \lambda_{ikl}(x_r)\lambda_{jml}(x_r) R\left[f_k(x_i), f_m(x_j)\right] \end{aligned} \tag{3.5}$$

Minimizing equation (3.5) with respect to Kriging weights $\lambda_{ikl}(x_r)$, the following set of equations are obtained:

$$\sum_{j=1}^{N}\sum_{m=1}^{n} \lambda_{jml}(x_r) R\left[f_k(x_i), f_m(x_j)\right] = R[f_l(x_r), f_k(x_i)], \qquad (i = 1,2,\cdots,N; k = 1,2,\cdots,n) \tag{3.6}$$

Equation (3.6) consists of $n \times N$ equations, from which $n \times N$ unknown Kriging weights $\lambda_{ikl}(x_r)$ for the component $f_l(x)$ at location x_r can be determined. Substituting equation (3.6) into equation (3.5), it reduces to

$$Var[\varepsilon_l(x_r)] = Var[f_l(x_r)] - \sum_{i=1}^{N}\sum_{k=1}^{n} \lambda_{ikl}(x_r) R[f_k(x_i), f_l(x_r)] \tag{3.7}$$

The error $\varepsilon_l(x_r)$ possesses the following properties.

(i) The mathematical expectation of the error vanishes.

$$\begin{aligned} E[\varepsilon_l(x_r)] &= E\left[f_l(x_r) - \sum_{i=1}^{N}\sum_{k=1}^{n} \lambda_{ikl}(x_r) f_k(x_i) \right] \\ &= E[f_l(x_r)] - \sum_{i=1}^{N}\sum_{k=1}^{n} \lambda_{ikl} E[f_k(x_i)] \\ &= 0 \end{aligned} \tag{3.8}$$

(ii) The error and the random vector of the random field at recorded locations are uncorrelated.

$$\begin{aligned} E[\varepsilon_l(x_r) f_k(x_i)] &= E\left\{ \left[f_l(x_r) - \sum_{j=1}^{N}\sum_{m=1}^{n} \lambda_{jml}(x_r) f_m(x_j) \right] f_k(x_i) \right\} \\ &= R[f_l(x_r), f_k(x_i)] - \sum_{j=1}^{N}\sum_{m=1}^{n} \lambda_{jml}(x_r) R[f_m(x_j), f_k(x_i)] \\ &= 0 \end{aligned} \tag{3.9}$$

(iii) If x_r coincides with one of recorded locations x_i, simply letting $\lambda_{ikk} = 1$ and $\lambda_{jmk} = 0 \quad (j \neq i, \quad or \quad m \neq k)$ will satisfy equation (3.6). Thus

$$\varepsilon_k(x_i) = f_k(x_i) - \sum_{j=1}^{N}\sum_{m=1}^{n} \lambda_{jmk} f_m(x_j) = f_k(x_i) - f_k(x_i) = 0 \tag{3.10}$$

(iv) The error and the Kriging estimate are uncorrelated.

$$\begin{aligned} E[\varepsilon_l(x_r) f_k^e(x_r)] &= E\left\{ \left[f_l(x_r) - \sum_{i=1}^{N}\sum_{s=1}^{n} \lambda_{isl}(x_r) f_s(x_i) \right] \sum_{j=1}^{N}\sum_{m=1}^{n} \lambda_{jmk}(x_r) f_j(x_m) \right\} \\ &= \sum_{j=1}^{N}\sum_{m=1}^{n} \lambda_{jmk}(x_r) R[f_l(x_r), f_k(x_j)] - \sum_{i=1}^{N}\sum_{s=1}^{n} \lambda_{isl}(x_r) R[f_m(x_j), f_s(x_i)] \\ &= 0 \end{aligned} \tag{3.11}$$

(v) The different components of the error vector are correlated and the correlation function is given by

$$\begin{aligned} E[\varepsilon_l(x_r)\varepsilon_k(x_r)] &= E\left\{ \varepsilon_l(x_r) \left[f_k(x_r) - f_k^e(x_r) \right] \right\} \\ &= E[\varepsilon_l(x_r) f_k(x_r)] \\ &= R[f_k(x_r), f_l(x_r)] - \sum_{j=1}^{N}\sum_{m=1}^{n} \lambda_{jml}(x_r) R[f_k(x_r), f_m(x_j)] \end{aligned} \tag{3.12}$$

Equations (3.8) to (3.12) imply that the error vector $\boldsymbol{\varepsilon}(x_r) = [\varepsilon_1(x_r), \varepsilon_2(x_r), \cdots, \varepsilon_n(x_r)]^T$ of $\mathbf{f}(x)$ at an unrecorded location x_r is independent on the random vector $f(x_i)$ and the error vector $\varepsilon(x_i)$ at the recorded location x_i $(i = 1, 2, \cdots, N)$. In addition, it is uncorrelated with the Kriging estimate $f_l^e(x_r)$ $(l = 1, 2, \cdots, n)$ at the unrecorded location x_r. However, different error components are correlated with each other. The above important properties of $\varepsilon(x_r)$ in equations (3.8) to (3.12) guarantee that the error vector $\varepsilon(x_r)$ can be simulated separately from the Kriging estimate. Hence, to simulate the Gaussian random vector field $f(x)$ at a desired location x_r where the field is not recorded, under the condition of knowing realization $\mathbf{g}(x_i)$ $(i = 1, 2, \cdots, N)$ at the recorded locations one can calculate the Kriging estimate of each component $g_l^e(x_r)$ $(l = 1, 2, \cdots, n)$ and simulate the error vector $\varepsilon(x_r)$ separately, and then formulate their sum

$$f_l^s(x_r) = \sum_{i=1}^{N}\sum_{k=1}^{n} \lambda_{ikl}(x_r) g_k(x_i) + \varepsilon_l(x_r) \tag{3.13}$$

The error vector $\boldsymbol{\varepsilon}(x_r)$ is an n-component vector random variable with zero-mean and covariance matrix as given in equation (3.12).

In the particular case that components of $f(x)$ are mutually uncorrelated, namely $R\left[f_k(x_i), f_m(x_j)\right] = 0 \quad for \quad k \neq m$, equation (3.6) reduces to

$$\sum_{j=1}^{N} \lambda_{jkl}(x_r) R\left[f_k(x_i), f_k(x_j)\right] = R\left[f_l(x_r), f_k(x_i)\right], \quad (i = 1,2,\cdots,N; k = 1,2,\cdots,n) \tag{3.14}$$

If $k \neq l$, the right hand side of equation (3.14) is zero and equation (3.14) reduces to

$$\sum_{j=1}^{N} \lambda_{jkl}(x_r) R\left[f_k(x_i), f_k(x_j)\right] = 0 \quad (i = 1, 2, \cdots, N) \tag{3.15}$$

Due to the non-singularity of the auto-covariance matrix $R\left[f_k(x_i), f_k(x_j)\right]$ of the kth component $f_k(x)$, only the trivial solution of equation (3.15) exists

$$\lambda_{jkl} = 0 \quad (j = 1, 2, \cdots, N; \quad k = 1, 2, \cdots, n; \quad k \neq l) \tag{3.16}$$

For $k = l$, equation (3.14) becomes, by letting $\lambda_{jl}(x_r) = \lambda_{jll}(x_r)$ for simplicity

$$\sum_{j=1}^{N} \lambda_{jl}(x_r) R\left[f_l(x_i), f_l(x_j)\right] = R\left[f_l(x_r), f_l(x_i)\right] \quad (i = 1, 2, \cdots, N) \tag{3.17}$$

Equation (3.17) has a unique set of solution $\lambda_{jl}(x_r)$ unless the covariance matrix $R[f_l(x_i), f_l(x_j)]$ of the lth component $f_l(x)$ is singular. Equations (3.2) and (3.7) then become, respectively

$$f_l^e(x_r) = \sum_{i=1}^{N} \lambda_{il}(x_r) f_l(x_i) \tag{3.18}$$

$$Var[\varepsilon_l(x_r)] = Var[f_l(x_r)] - \sum_{i=1}^{N} \lambda_{il}(x_r) R[f_l(x_i), f_l(x_j)] \tag{3.19}$$

The errors $\varepsilon_l(x_r)$ and $\varepsilon_k(x_r)$ for different components $f_l(x_r)$ and $f_k(x_r)$ $(l \neq k)$ are also uncorrelated, since from equations (3.12) and (3.15)

$$\begin{aligned} E[\varepsilon_l(x_r)\varepsilon_k(x_r)] &= R[f_k(x_r), f_l(x_r)] - \sum_{j=1}^{N}\sum_{m=1}^{n} \lambda_{jml}(x_r) R[f_k(x_r), f_m(x_j)] \\ &= -\sum_{j=1}^{N} \lambda_{jkl}(x_r) R[f_k(x_r), f_k(x_j)] \\ &= 0 \end{aligned} \tag{3.20}$$

This implies that for the case of uncorrelated component random field each component $f_l(x)$ of $\mathbf{f}(x)$ can be simulated separately, as in the case of a univariate random field.

3.3 Autocorrelation Function of a Random Field

The autocorrelation function of an isotropic, zero-mean univariate random field is

$$R[f(x_i), f(x_j)] = E[f(x_i) f(x_j)] = E[f(x_i) f(x_j + \xi_{ij})] = R_{ij}(\xi_{ij}) \tag{3.21}$$

where ξ_{ij} is the distance between the two points i, j. The spatial variability of the seismic motion is generally obtained from the time domain analyses of the recorded data, and is usually described by a function that exponentially decays with separation distance and frequency [Hoshiya and Ishii 1983; Luco and Wong 1986; Vanmarcke and Fenton 1991; Zerva and Shinozuka 1991; Kiureghian and Neuenhofer 1992 and Jankowski and Wilde 2000]. Hence the autocorrelation function $R_{ij}(\xi_{ij})$ adopted here is the negative exponential form

$$R_{ij}(\xi_{ij}) = \sigma^2 \exp\left(-\frac{|\xi_{ij}|}{b}\right) \tag{3.22}$$

where σ is a standard deviation of the field and b indicates a correlation length, $b > 0$. Assuming the ergodicity of the ground motion, the value of σ can be calculated from the formula for standard deviation of a history record with zero mean at a given point:

$$\sigma = \left[\frac{1}{N-1} \sum_{i=1}^{N} f_i^2 \right]^{1/2} \tag{3.23}$$

where N is the number of values in the record. Since the band of frequencies which dominates the response of engineering structures like elevated highway bridges or multi-supported pipelines is narrow, only one spatial correlation function can be assumed to represent the correlation for the band of frequencies of interest [Jankowski and Wilde 2000]. Moreover, the functional dependence of the coherency function on distance and frequency has not been fully established. Therefore, the coefficient b may be described in terms of the predominant frequency of the earthquake, ω_d, and the mean apparent seismic wave velocity, v, [Jankowski and Wilde 2000; Vanmarcke and Fenton 1991]

$$b = \frac{2\pi v d}{\omega_d} \tag{3.24}$$

where $d\,(d > 0)$ is a scale parameter which depends on local geological and topographical conditions and is called the wave dispersion factor in this study. The degree of correlation can be controlled by varying the wave dispersion factor d for a fixed separation distance. The bigger the value of d the higher the expected correlation between points of the random field. The predominant frequency of the earthquake, ω_d, can be determined from the acceleration response spectrum of the earthquake record. Substituting equations (3.23) and (3.24) into equation (3.22) yields

$$R_{ij}(\xi_{ij}) = \sigma^2 \exp\left(-\frac{\omega_d |\xi_{ij}|}{2\pi v d} \right) \tag{3.25}$$

By setting

$$c_{ij} = \exp\left(-\frac{\omega_d |\xi_{ij}|}{2\pi v d} \right) \tag{3.26}$$

the covariance matrix of the field described by the autocorrelation function from equation (3.25) takes the form

$$\mathbf{R} = \begin{bmatrix} \sigma^2 & c_{12}\sigma^2 & c_{13}\sigma^2 & \cdots & c_{1n}\sigma^2 \\ c_{21}\sigma^2 & \sigma^2 & c_{23}\sigma^2 & \cdots & c_{2n}\sigma^2 \\ c_{31}\sigma^2 & c_{32}\sigma^2 & \sigma^2 & \cdots & c_{3n}\sigma^2 \\ \vdots & \vdots & \vdots & \ddots & \vdots \\ c_{n1}\sigma^2 & c_{n2}\sigma^2 & c_{n3}\sigma^2 & \cdots & \sigma^2 \end{bmatrix} \tag{3.27}$$

where n is the number of discretized field points.

3.4 Simulation of Ground Motion

The two effects that give rise to the spatial variability of seismic ground motions, the 'geometric incoherence effect' and the 'wave passage effect', are considered separately in the proposed method to generate seismic ground motions with dispersion from an original motion. First, only the 'incoherence effect' is concerned, and the ground motion is assumed to be a space-time random field $\mathbf{f}(t,x)$, which may be approximated by its discretized version $\{f_{t_1}(x), f_{t_2}(x), \cdots, f_{t_n}(x)\}$ with $f_{t_i}(x)$ denoting $f(t_i,x)$. Assume that $\{f_{t_1}(x), f_{t_2}(x), \cdots, f_{t_n}(x)\}$ is a homogeneous n-variate Gaussian random vector field with zero-mean cross-covariances $R[f_{t_k}(x_i), f_{t_l}(x_j)] = E[f_{t_k}(x_i) f_{t_l}(x_j)]$ $(k, \ l=1, \ 2, \ \cdots, \ n)$. Thus the problem now becomes one of how to simulate a homogeneous n-variate Gaussian vector field. For reasons of simplicity, one assumes that in the time domain the elements in the same record are mutually uncorrelated, i.e. $R[f_{t_k}(x_i), f_{t_l}(x_j)] = 0 \ \ for \ \ k \neq l$. In the case of a random field with uncorrelated components, each component $f_{t_l}(x)$ can be simulated separately, as in the case of univariate random field, by the modified Kriging method. Then introducing a time lag between the different points includes the wave passage effect on the simulated motions. The time lag τ between any two supports is given by $\tau = \xi_{ij}/v_a$, where v_a is the apparent wave propagation velocity and ξ_{ij} is the projected separation parallel to the dominant wave propagation direction between the two supports.

A description of an algorithm for the simulation of ground motions at M locations conditioned by the recorded time histories from n points is presented below:

(1) At the first time step $t_1 = \Delta t$:

The simulations of the accelerations $f^c_{t_1 m}$ $(m = n+1, \ n+2, \ \cdots, \ M)$ at M supports conditioned by the known accelerations $f_{t_1 l}$ $(l = 1, \ 2, \ \cdots, \ n)$ at the n supports can be obtained by means of the following steps:

(i) Find the estimate of the Kriged values $f^e_{t_1 m}$ $(m = n+1, \ n+2, \ \cdots, \ M)$ on the basis of the known values $f_{t_1 l}$ $(l = 1, \ 2, \ \cdots, \ n)$ by using equation (2.25):

$$f^e_{t_1 m} = \sum_{l=1}^{n} \lambda_{lm} f_{t_1 l}$$

where l is a number of supports at which the ground motion are known, and λ_{lm} are Kriging weights, which can be obtained from equations (2.31) and (2.32).

(ii) Simulate the error $e^s_{t_i m}$ $(m = n+1,\ n+2,\ \cdots,\ M)$ which is a multivariate normal distribution with zero mean. The variance matrix for the stochastic variates E_m is:

$$\mathbf{V} = \begin{bmatrix} E\left[E^2_{(n+1)(n+1)}\right] & E\left[E_{n+1}E_{n+2}\right] & \cdots & E\left[E_{n+1}E_M\right] \\ E\left[E_{n+2}E_{n+1}\right] & E\left[E^2_{(n+2)(n+2)}\right] & \cdots & E\left[E_{n+2}E_M\right] \\ \vdots & \vdots & \ddots & \vdots \\ E\left[E_M E_{n+1}\right] & E\left[E_M E_{n+2}\right] & \cdots & E\left[E^2_{MM}\right] \end{bmatrix}$$

where from equation (2.40)

$$E\left[E_n E_m\right] = R_{nm} - \sum_{l=1}^{n} \lambda_{ln} R_{lm} - \frac{1}{2}\gamma_n$$

Unconditionally simulate the errors $e^s_{t_i m}$ using the Cholesky decomposition method on the basis of the above variance matrix [Dagpunar 1988].

(iii) The conditionally simulated values are obtained as

$$f^c_{t_i m} = f^e_{t_i m} + e^s_{t_i m} \quad (m = n+1,\ n+2,\ \cdots,\ M)$$

(2) Repeat the steps (i), (ii), (iii) for time steps $t_2 = 2\Delta t$, $t_3 = 3\Delta t$, $\cdots$, $t_N = N\Delta t$ respectively.

(3) Put $f_{t_i m}$ $(i = 1,\ 2,\ \cdots,\ N)$ together to form the total conditionally simulated accelerogram for support m, $(m = n+1,\ n+2,\ \cdots,\ M)$.

(4) Then the acceleration values are shifted by time-delay parameters ΔT_{nm} at support m, $(m = n+1,\ n+2,\ \cdots,\ M)$.

3.5 Examples of Simulation of Ground Motion Field for the Prototype Bridge in Chapter 4

In this section, the new method is applied to generate the input ground motions for several bridge support points when the time-history is specified for one support point. The bridge under consideration is a nine-span continuous deck bridge with a total length of 344m. The spans between the piers are 40m long while the end spans between the abutments and the nearest pier are 32m long as shown in Figure 3.1

Assuming that the earthquake ground motion at abutment 1 is specified, time-histories for other locations, where the piers 2 to 9 and abutment 10 are located, are to be generated. The seismic wave is assumed to travel along the bridge longitudinal direction with the constant apparent velocity of either $v = 200\,m/s$, or $1000\,m/s$. Three values of the wave dispersion factor $d = 1,\ 10,\ 100$ (see Eq. 3.24) are used to describe the different levels of the

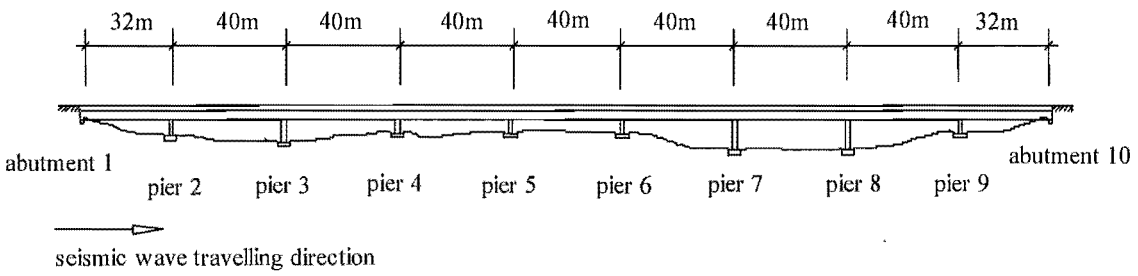

Figure 3.1 Bridge Elevation

coherence [Vanmarcke and Fenton 1991]. When $d = 1$, a very small correlation between the ground motions at different piers is expected and when $d = 100$, a high correlation between the ground motions can be ensured. The North-South components of the El Centro (May 18, 1940) and Kobe (January 17, 1995) earthquakes are used as the specified time-histories for abutment 1. The predominant frequency is 11rad/sec for the El Centro 1940 earthquake record, and 9rad/sec for the Kobe 1995 earthquake record, which were determined from the acceleration response spectra of the earthquake records. The processes of the conditional simulation of the ground motions are shown in Figure 3.2.

Figures 3.3(a) and 3.3(b) show the generated acceleration time-histories for piers 2 to 9 and abutment 10 obtained with the specified acceleration of the North-South components of 1940 El Centro Earthquake record at abutment 1, the propagation velocity $v = 200 m/s$ and the dispersion factor $d = 10$. As expected the generated acceleration time-histories are quite similar to the input acceleration time-history at abutment 1. Figure 3.4 shows the spectral accelerations of the generated time-histories, in which the propagation velocity v = 200m/s and the dispersion factor d = 100, 10 and 1. The spectra of the generated acceleration time-histories are also very close to the input acceleration spectrum and the difference between the generated spectrum and the input one increased with the decrease in the wave dispersion factor *d*. Figures 3.5(a) and 3.5(b) show the differences between the generated acceleration time-histories and the acceleration of the NS components of El Centro Earthquake record for piers 2 to 9 in the case with $v = 200 m/s$ and d = 10. It can be seen that the differences increase with the increase in the distance from the point where the specified record is applied. The relationships between these differences and the separation distance are shown in Figure 3.6. It also can be observed that the larger the value of d the smaller the differences, and the higher travelling wave velocity the smaller the differences. The variations of the differences with the wave dispersion factor or the travelling wave velocity are shown in Figures 3.7 and

3.8. In these figures, the variations of the acceleration differences with separation distance, travelling velocity and dispersion factor d show the expected exponential decay that arises from the trend adopted for the autocorrelation function described in Eq. 3.25.

The generated acceleration time-histories for piers 2 to 9 and abutment 10 obtained with the specified acceleration of the North-South components of 1995 Kobe Earthquake record, the propagation velocity $v = 200 m/s$ and the dispersion factor $d = 10$, are shown in Figures 3.9(a) and 3.9(b). The differences of the accelerations between the generated time-histories and the input earthquake record are shown in Figures 3.10(a) and 3.10(b). The spectra of the generated time-histories and the input earthquake acceleration response spectrum are shown in Figure 3.11 and they follow the same trend as 1940 El Centro earthquake record.

3.6 Summary

A method for conditional simulation of stochastic ground motions for use in seismic analysis was proposed in this chapter, by using the modified Kriging method for multi-variate Gaussian fields. The proposed method was based on the two assumptions that the components of discretized space-time random field $\{f_{t_1}(x), f_{t_2}(x), \cdots, f_{t_m}(x)\}$ were mutually uncorrelated, and only the correlation of the predominant frequency of the earthquake was considered for the frequency dependent spatial correlation function of the ground motion field.

The numerical example presented showed that the method was effective and could be easily implemented in engineering analyses. The variation of the accelerations with the separation distance between the supports and the wave propagation velocity followed the autocorrelation function adopted, which is based on the main characteristics of the spatial variability of the seismic motion indicated by the extensive analyses of the records from arrays of strong-motion seismographs. At the same time the spectra of the simulated time-histories at each support and the specified earthquake record were very close to each other. This is important because that the earthquake actions at a site of interest are related to the specified response spectra in various design codes. The method thus appears to be a useful tool for the design of spatially extended facilities accounting for partially correlated seismic excitations.

In this study, the results have not been compared with those obtained from other approaches and have also not been directly compared with the incoherence observed in recorded ground

motions. This would be a useful next step for future research, and give users added confidence. Also the 'd' factor needs correlation and validation with real field local geological and topographical conditions to allow engineers to produce asynchronous motions suited to the characteristics of a particular site.

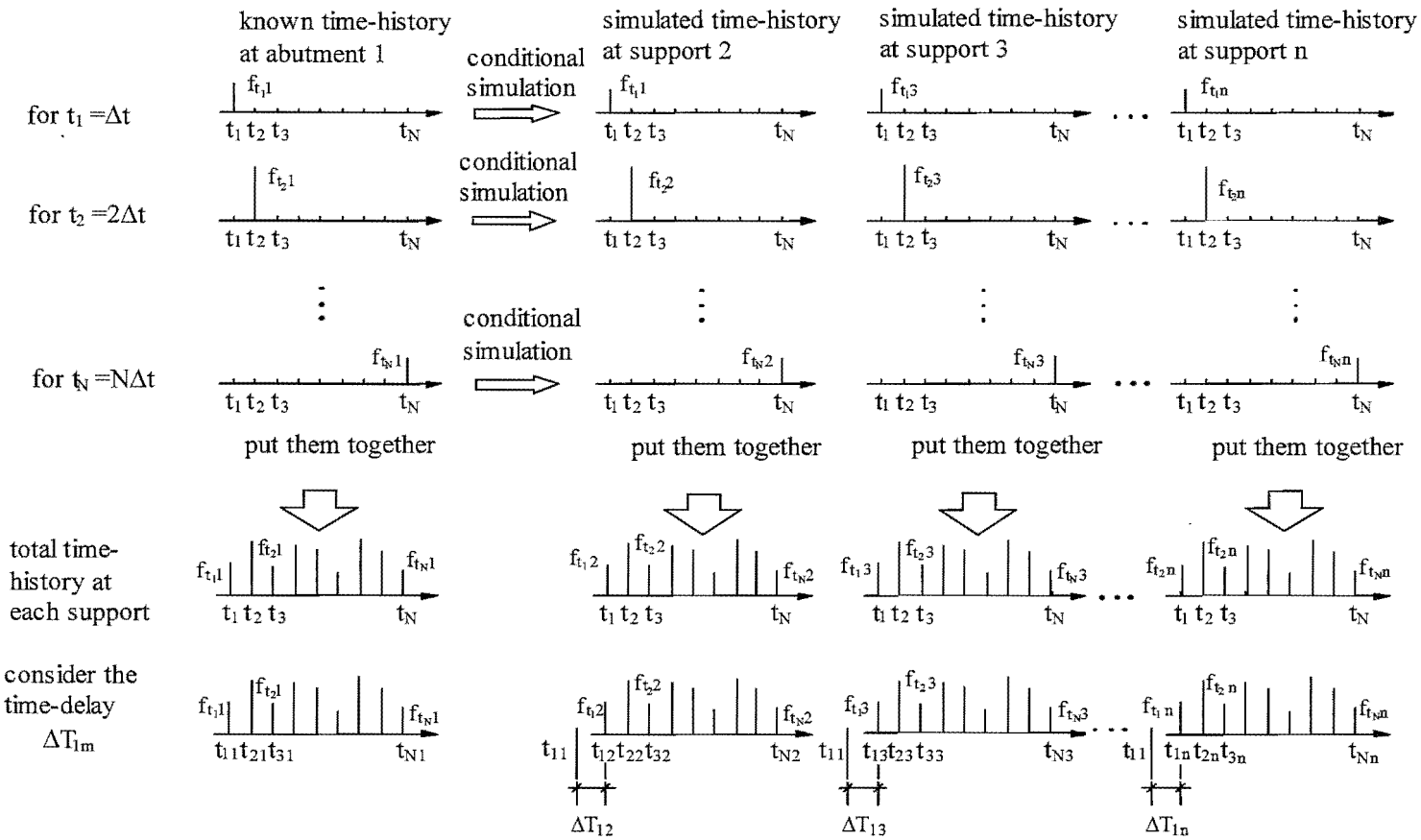

Figure 3.2 Generation of Seismic Waves with Dispersion from Original

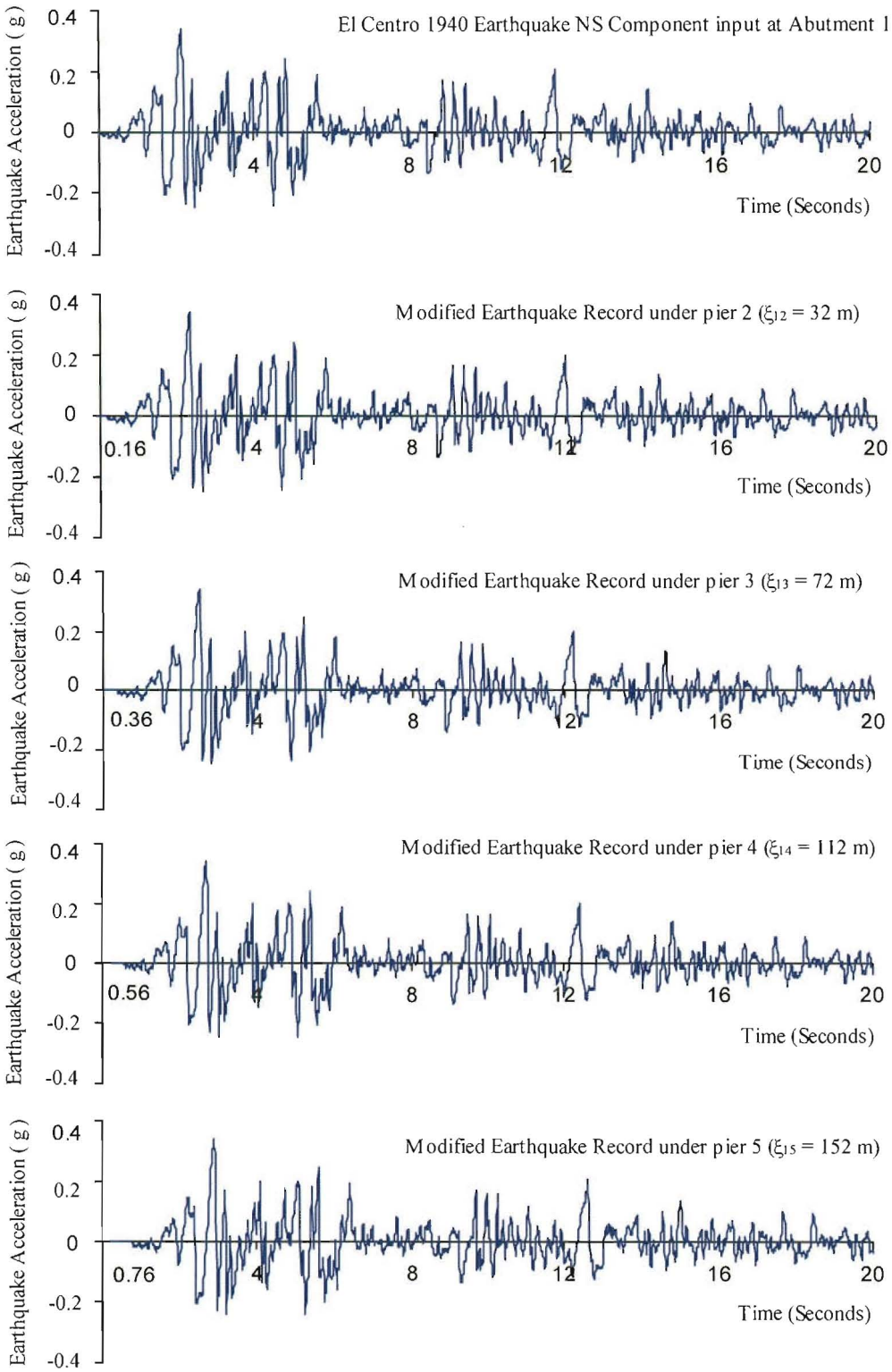

Figure 3.3(a) Generated acceleration time-histories from EL40NSC with v = 200m/s and d = 10

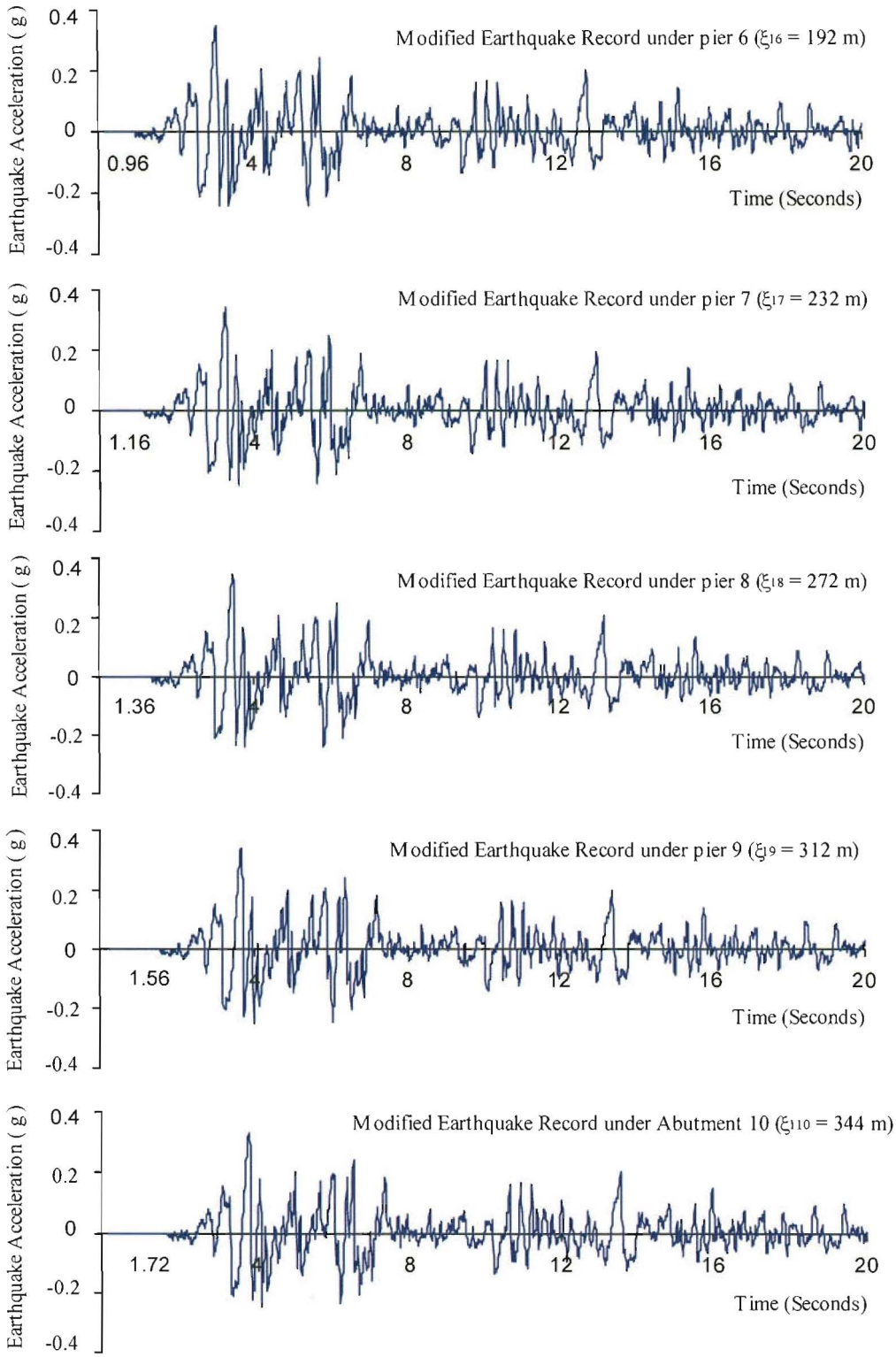

Figure 3.3(b) Generated acceleration time-histories from EL40NSC with v = 200m/s and d = 10

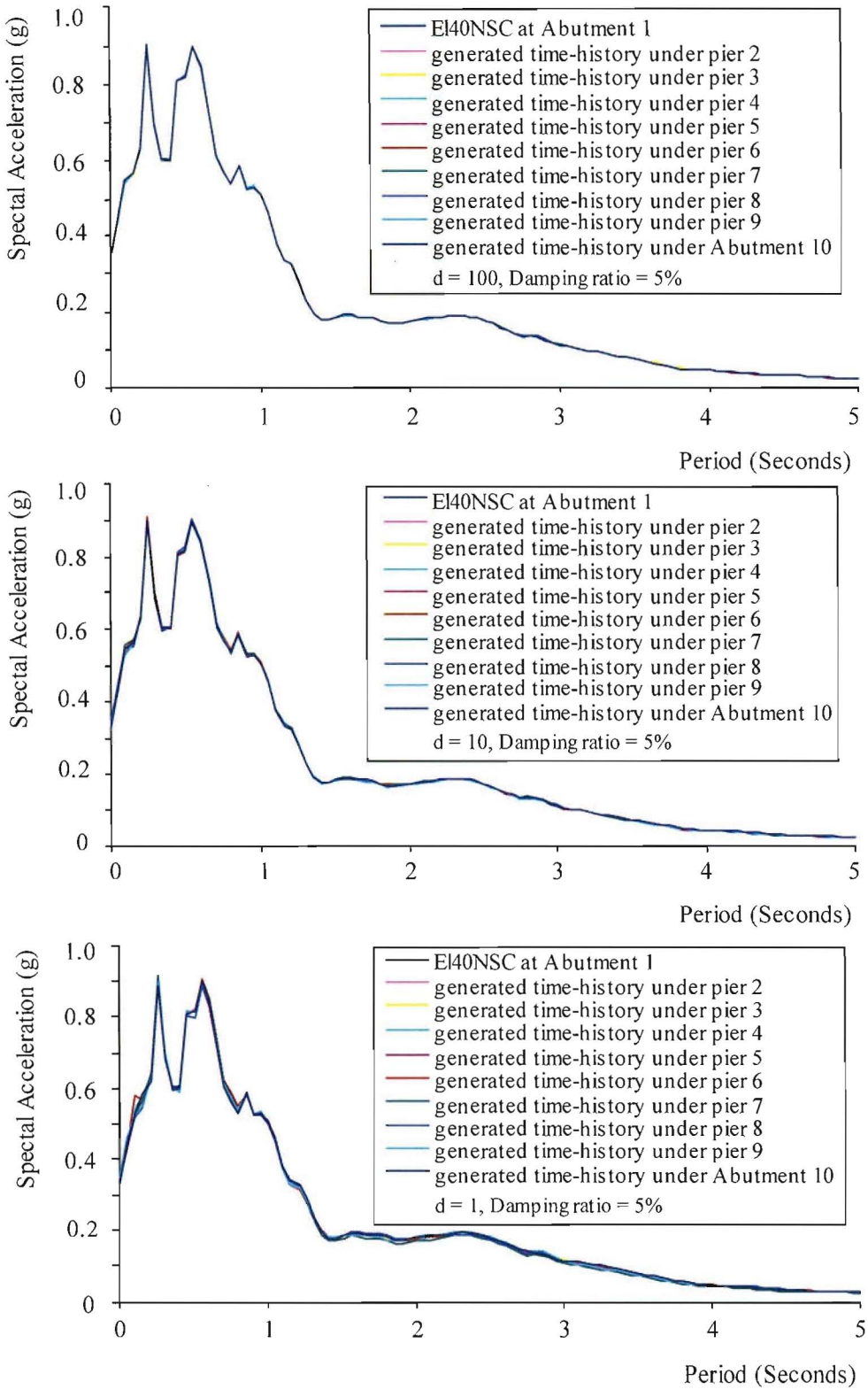

Figure 3.4 The spectral accelerations of the specified earthquake record (EL40NSC) and the generated time-histories with $d = 100$, 10, 1 and $v = 200$m/s

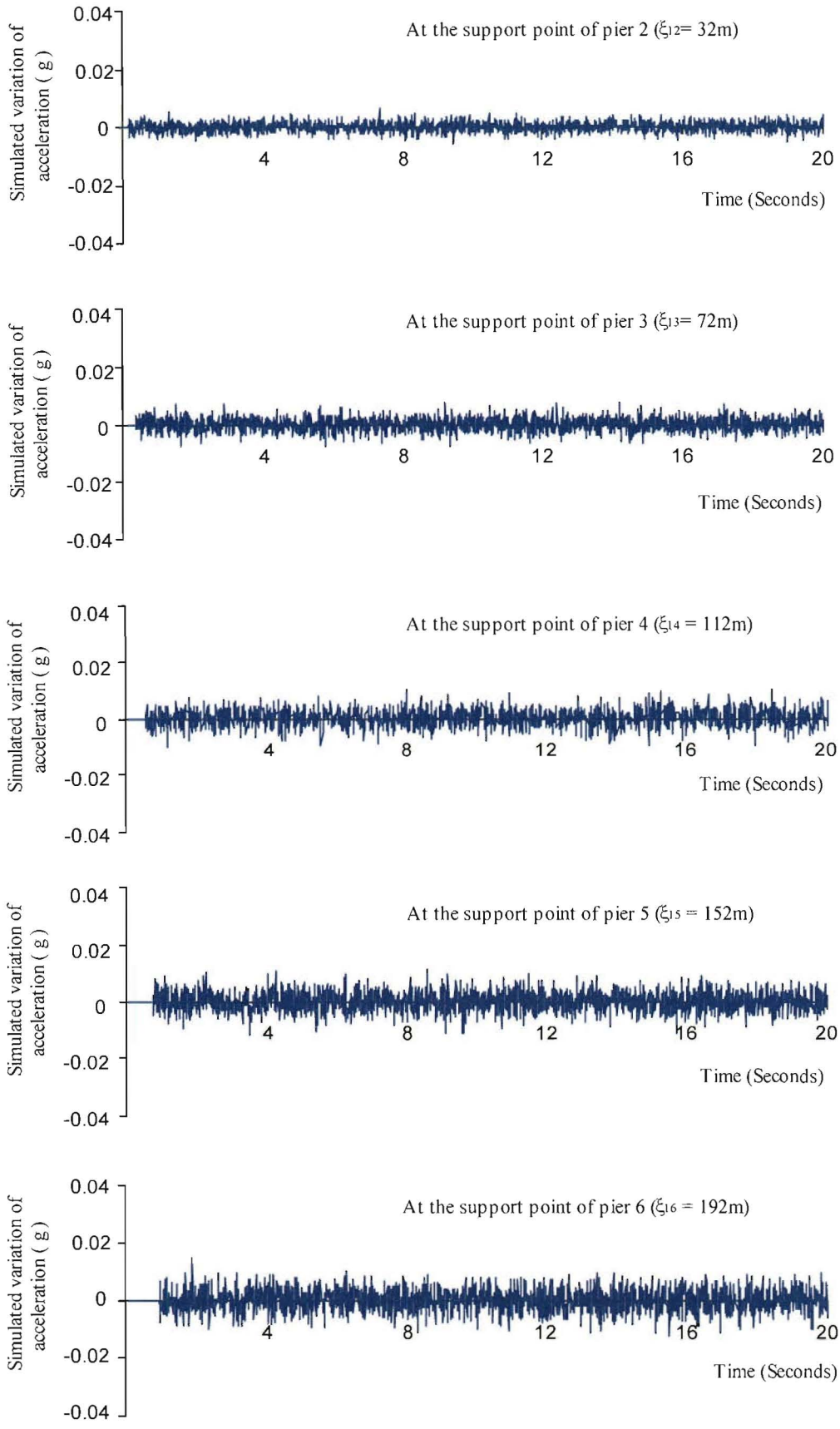

Figure 3.5(a) The differences of acceleration between the specified earthquake record (EL40NSC) and the generated time-histories with v = 200m/s and d = 10

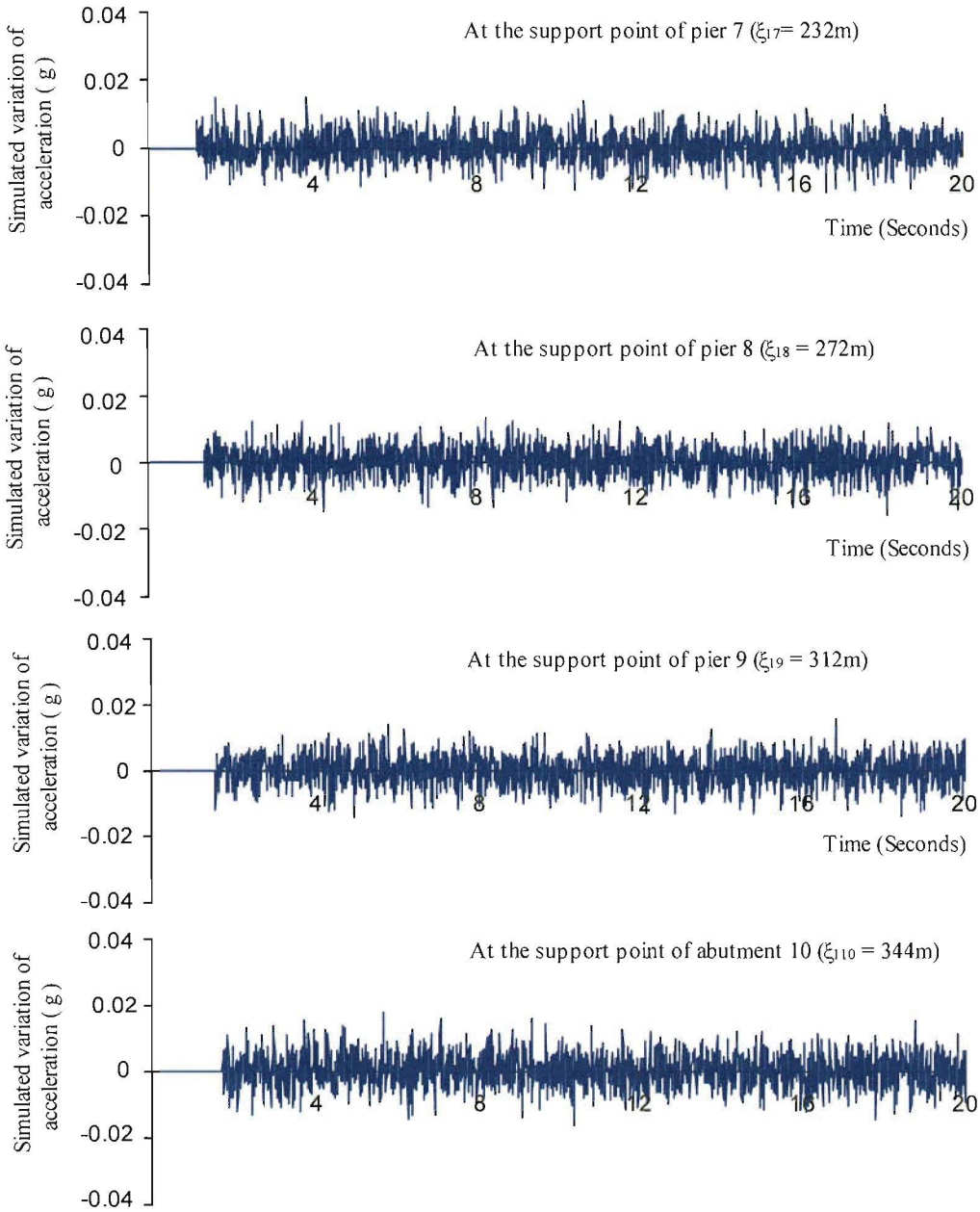

Figure 3.5(b) The differences of acceleration between the specified earthquake record (EL40NSC) and the generated time-histories with v = 200m/s and d = 10

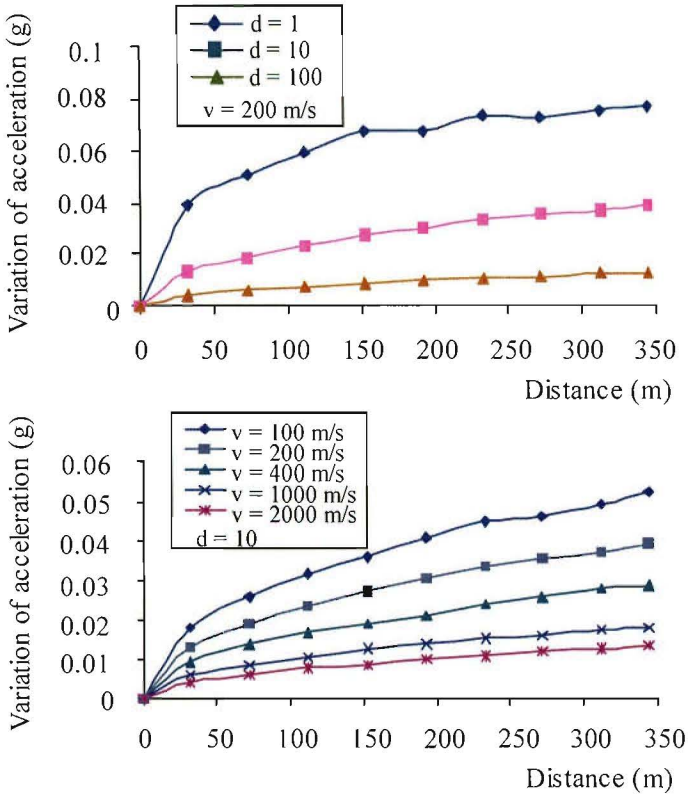

Figure 3.6 The differences of acceleration vs. separation distance for EL40NSC

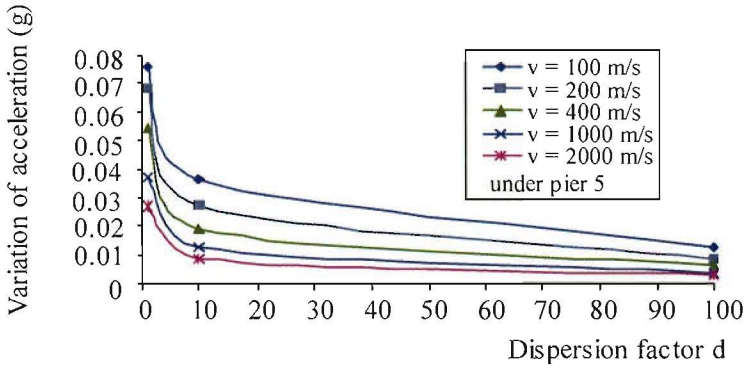

Figure 3.7 The differences of acceleration vs. dispersion factor for EL40NSC

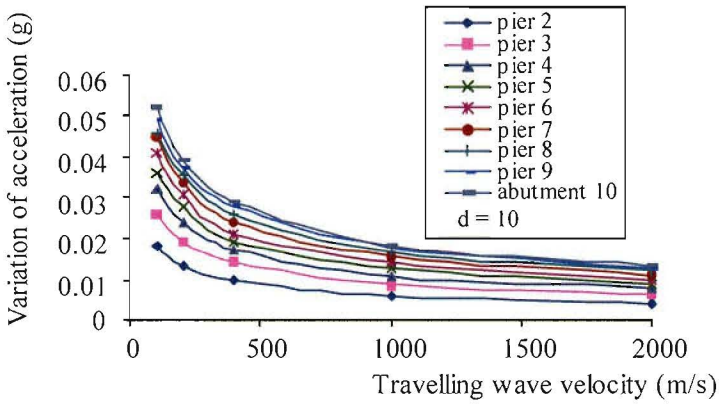

Figure 3.8 The differences of acceleration vs. travelling wave velocity for EL40NSC

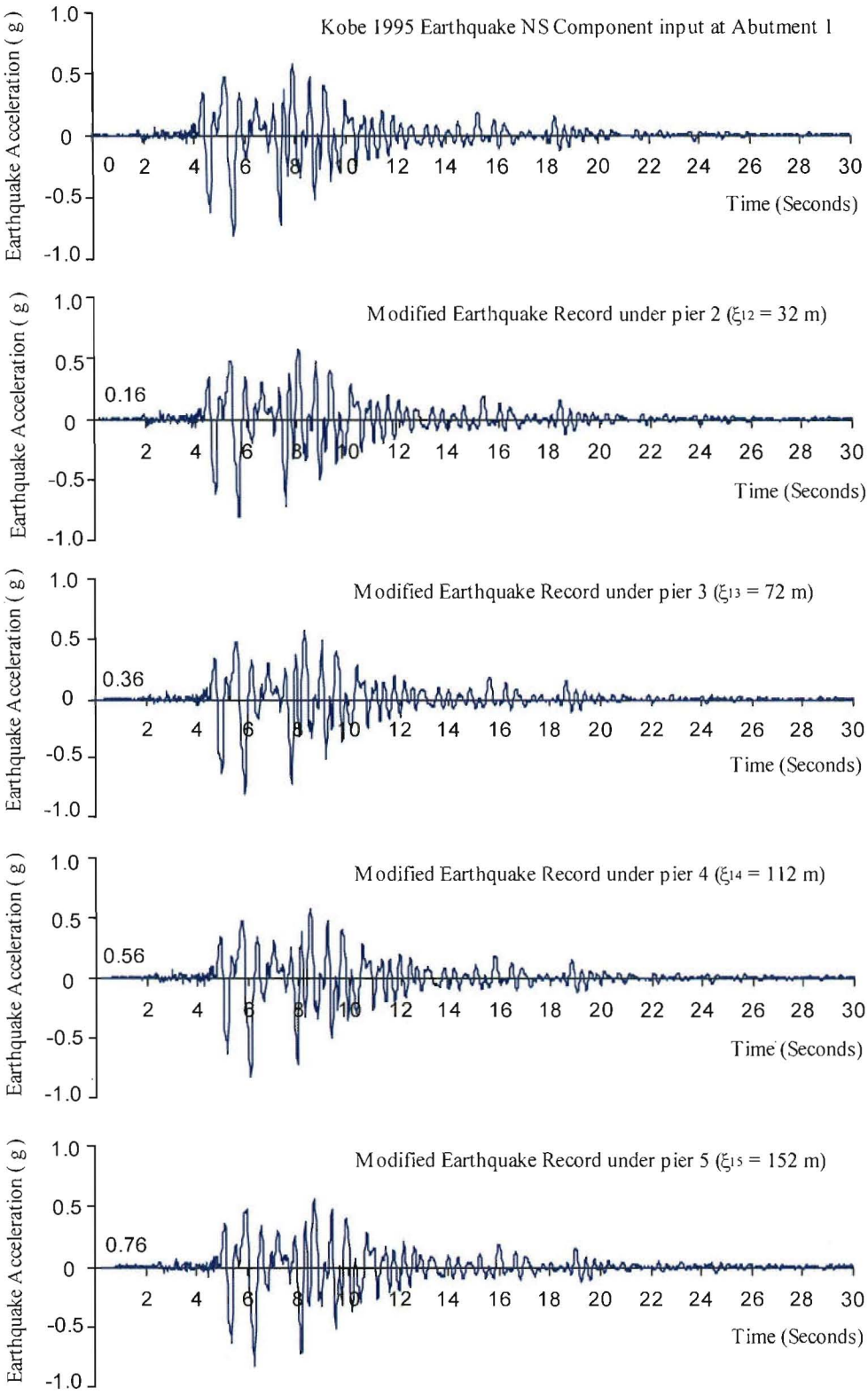

Figure 3.9(a) Generated acceleration time-histories from KOBE95NSC with v = 200m/s and d = 10

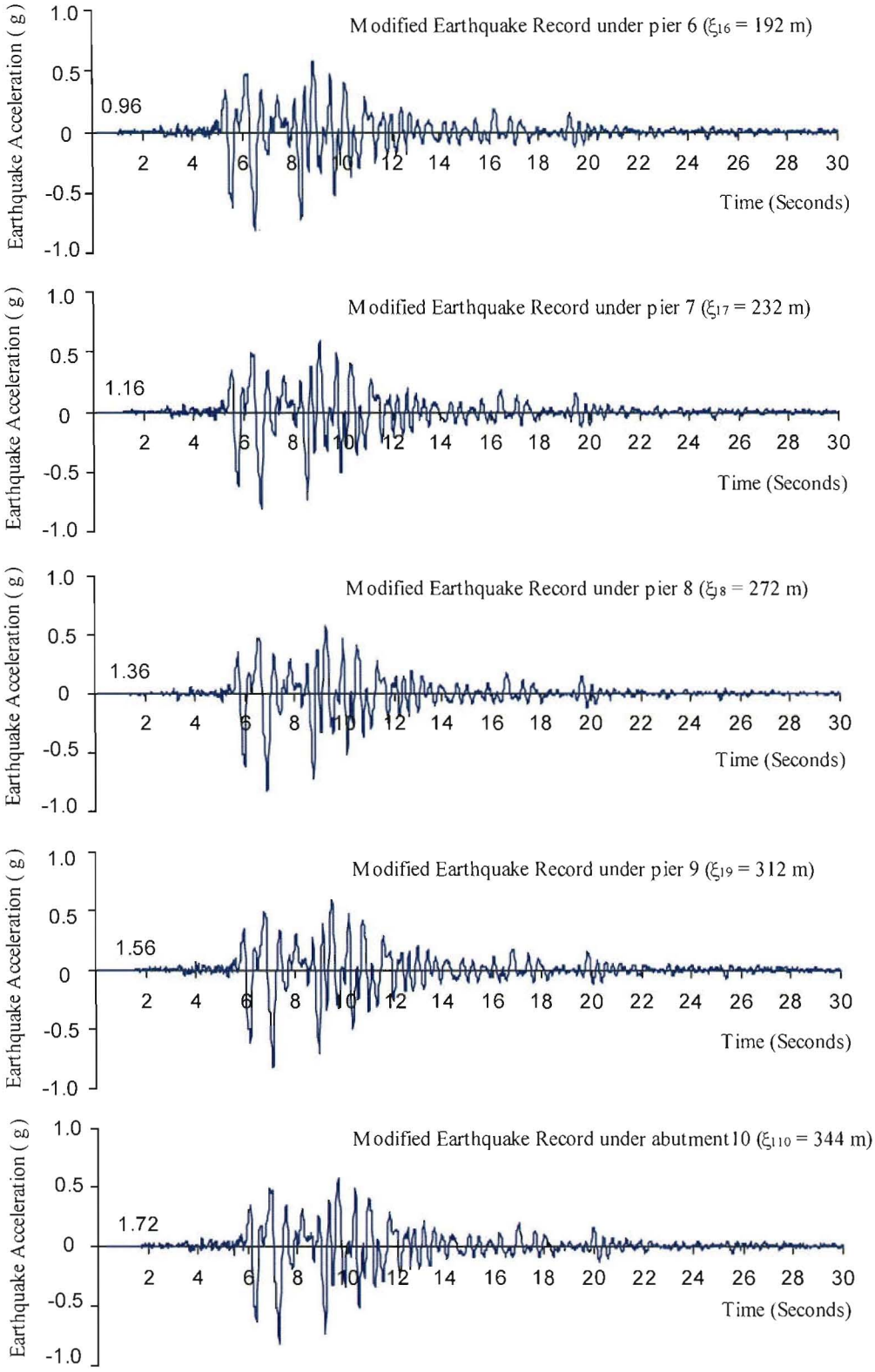

Figure 3.9(b) Generated acceleration time-histories from KOBE95NSC with v = 200m/s and d = 10

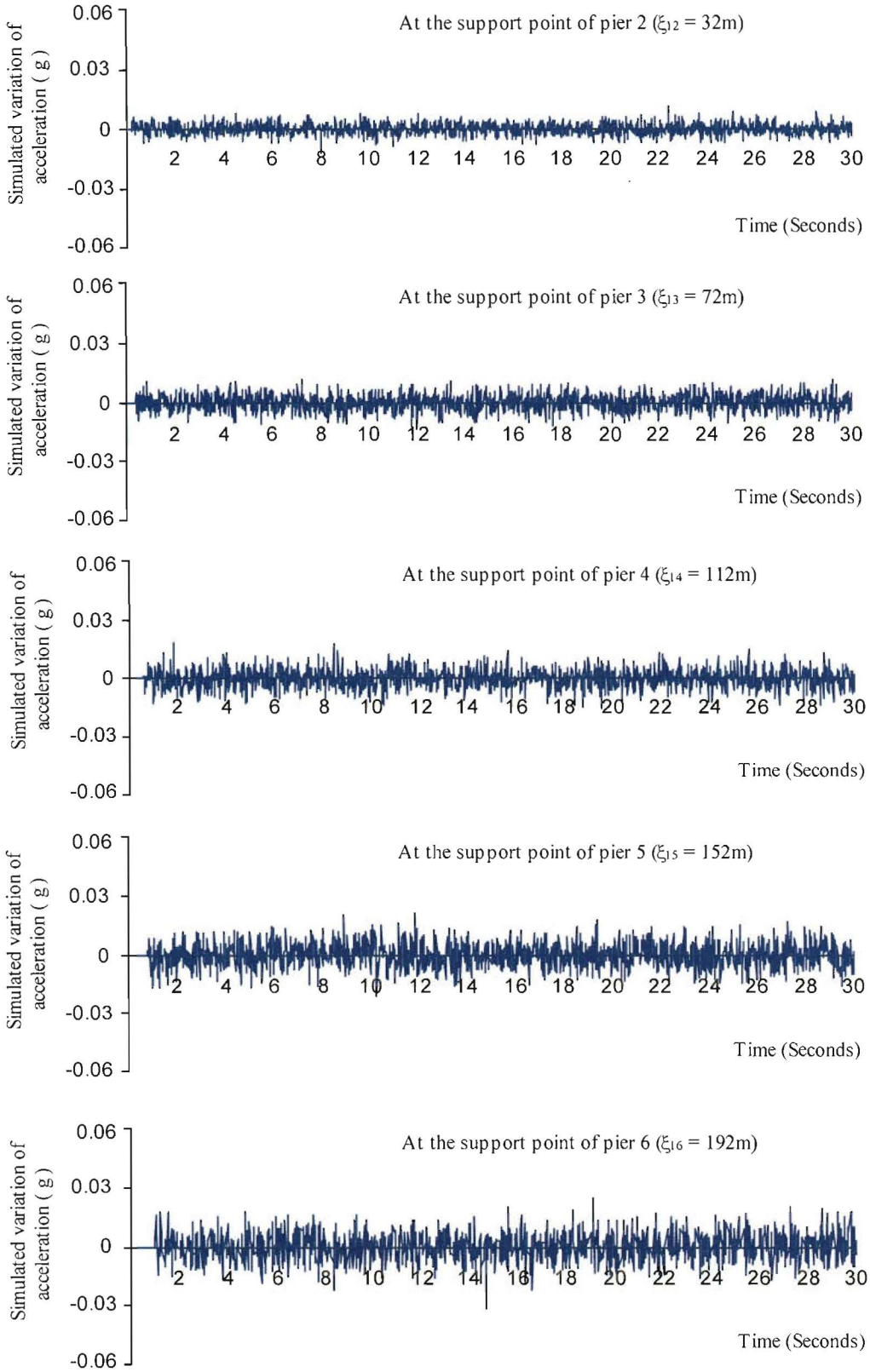

Figure 3.10(a) The differences of acceleration between the specified earthquake record (KOBE95NSC) and the generated time-histories with v = 200m/s and d = 10

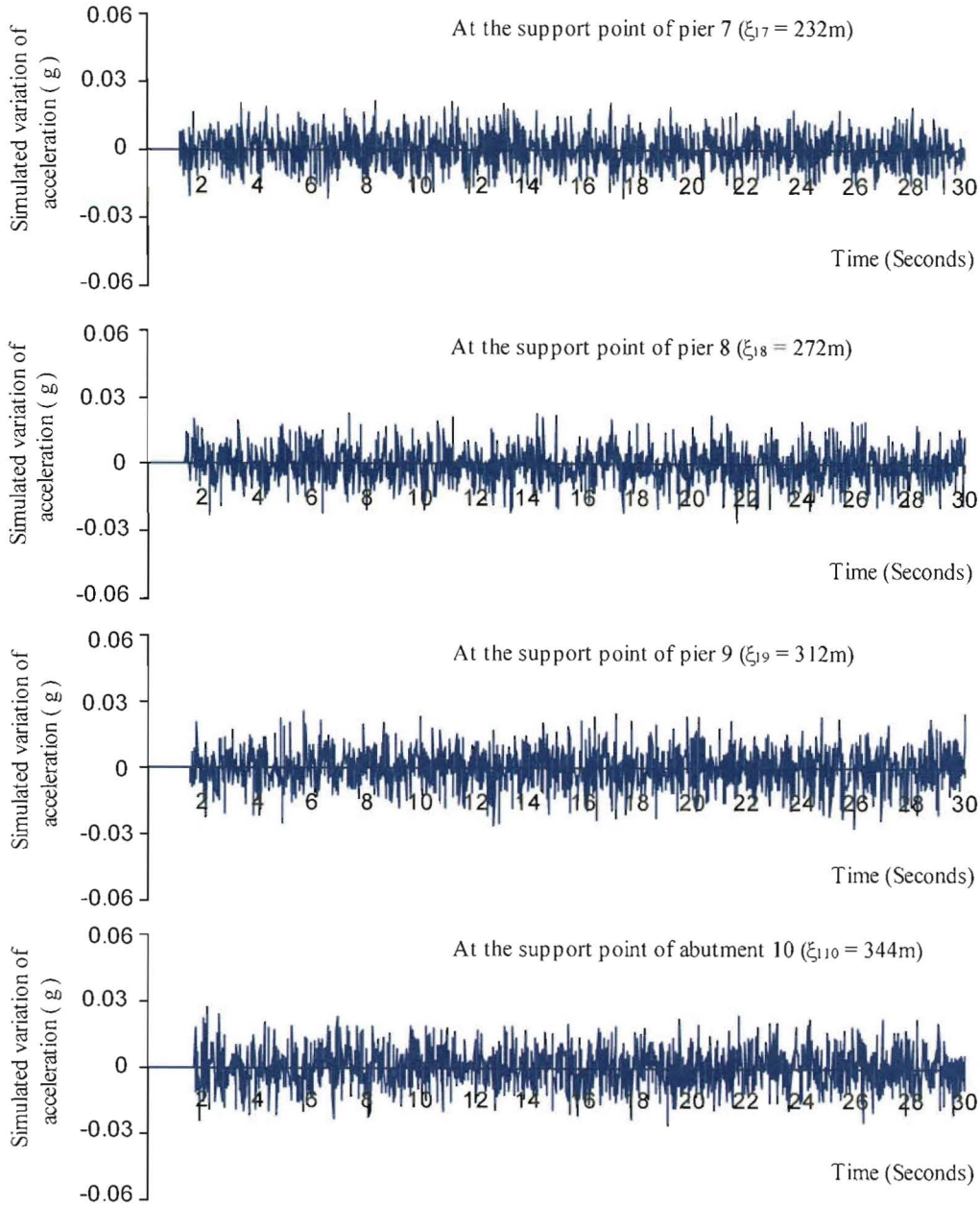

Figure 3.10(b) The differences of acceleration between the specified earthquake record (KOBE95NSC) and the generated time-histories with v = 200m/s and d = 10

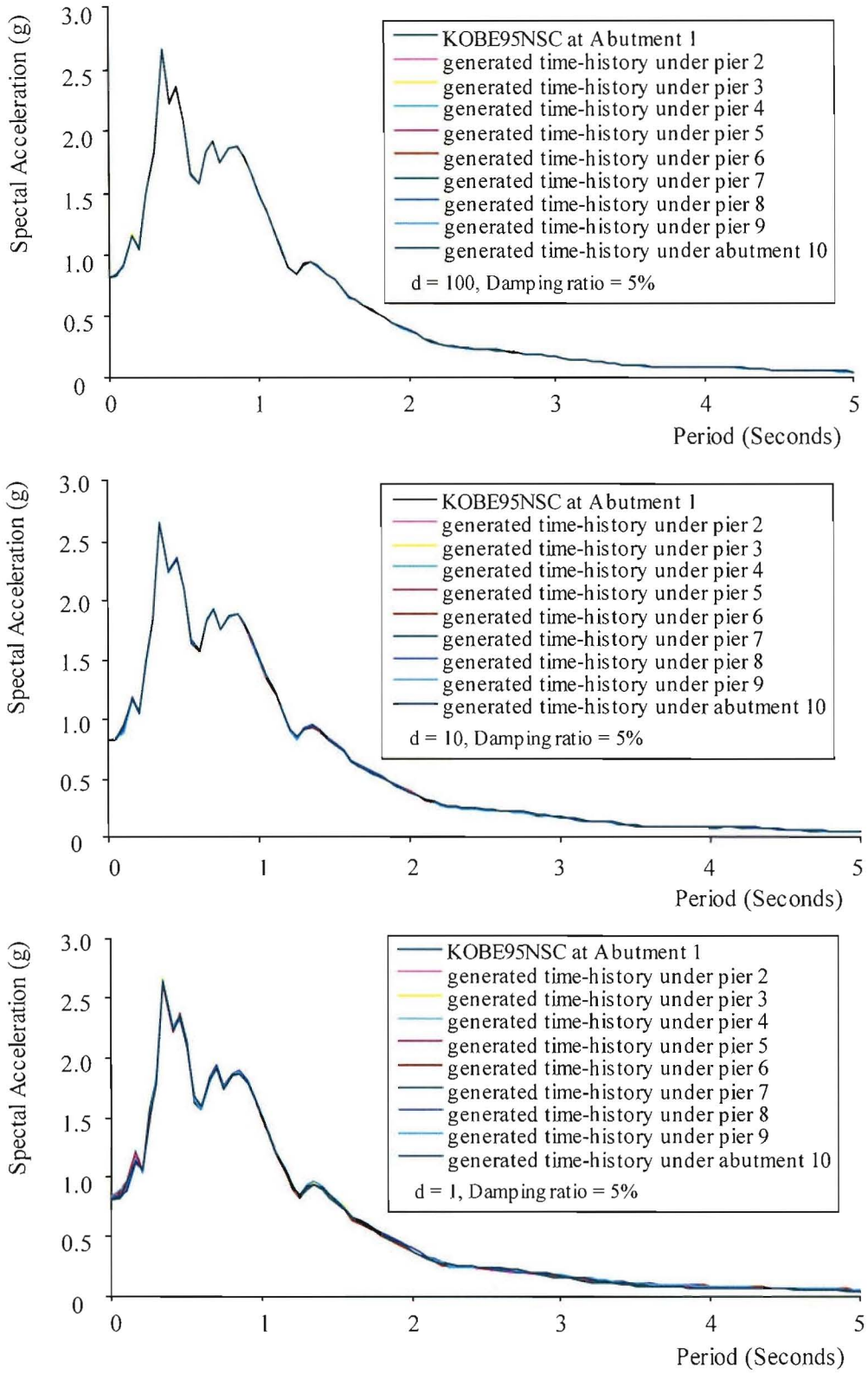

Figure 3.11 The spectral accelerations of the specified earthquake record (KOBE95NSC) and the generated time-histories with $d = 100$, 10, 1 and $v = 200$ m/s

CHAPTER 4

PROTOTYPE BRIDGE AND STRUCTURE MODELLING

4.1 Description of the Prototype Bridge

The prototype bridge used in this study was given as an example of modern multispan bridge in detail in the second international workshop on "seismic design and retrofitting of reinforced concrete bridges" [Park 1994]. It is straight in plan in this study instead of originally slightly curved. This nine-span bridge with a total length of 344m is continuous between abutments. The spans between the piers are 40m long while the two end spans between the abutments and the adjacent piers are 32m long. The deck is a twin-cell box prestressed concrete girder and is supported on single circular piers of varying heights via sliding bearings which permit longitudinal movement of the superstructure relative to the cap beam. The superstructure is restrained from movement transverse to the bridge axis by the shear keys at each pier top. The bridge plan and elevation are shown in Figure 4.1.

Abutment 1 is constructed monolithically with the deck-end diaphragm, and abutment 10 supports the deck-end through sliding bearings with freedom of movement longitudinally, transversely and rotationally (as shown in Figure 4.2). The structures at abutments 1 and 10 are supported by six 1m-diameter reinforced concrete cast in drilled hole (CIDH) cylinders arranged in-line transversely, spaced at 2.5m centres. A knock-off abutment top detail is provided at abutment 10 to allow freedom of movement without impact after initial failure of the knock-off detail.

The circular piers are reinforced concrete of 1.5m-diameter. They are supported by a 4.5 m by 4.5 m by 1.5 m deep footing and four 1m-diameter reinforced concrete cast in drilled hole (CIDH) piles arranged in a square, spaced at 2.5m centres. A 2.5 m deep cap beam is monolithically connected to the top of each pier that have free heights between cap beam and pile cap of 6m, 8m, 5m, 5m, 5m, 11m, 11m and 5m for piers 2 to 9, respectively. The longitudinal reinforcement of the pier consists of 48D32 bars (D = deformed, 32mm diameter) in pairs running the entire height of the pier. The transverse reinforcement consists of D12 bars at 75mm centres for the bottom 20% of the pier free height and 140mm centres for

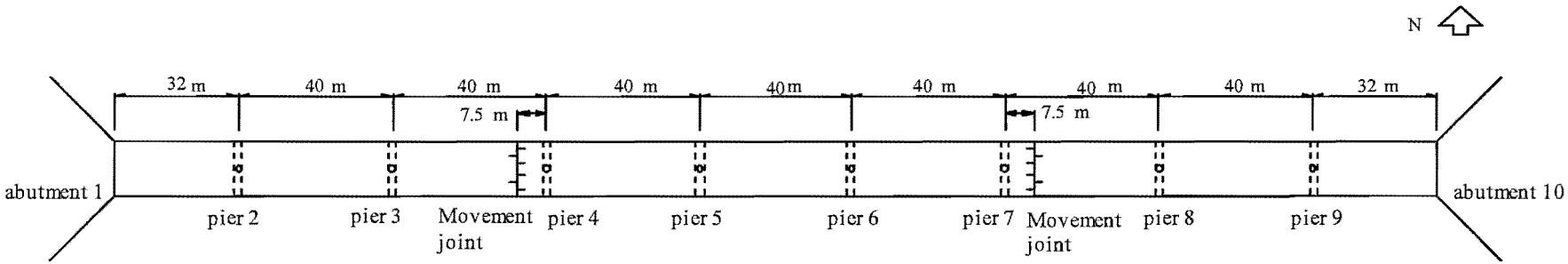

(a) Bridge Plan

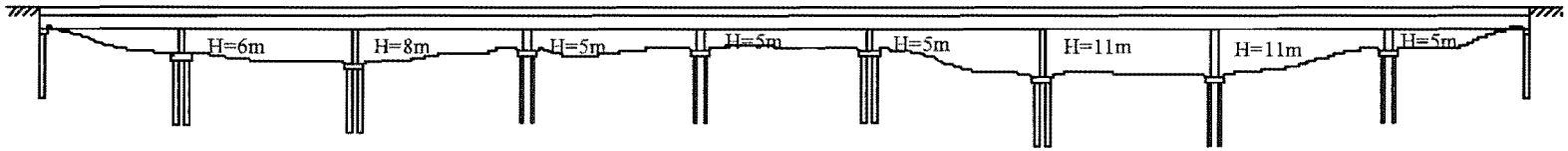

(b) Bridge Elevation

Figure 4.1 Modern Multispan Bridge

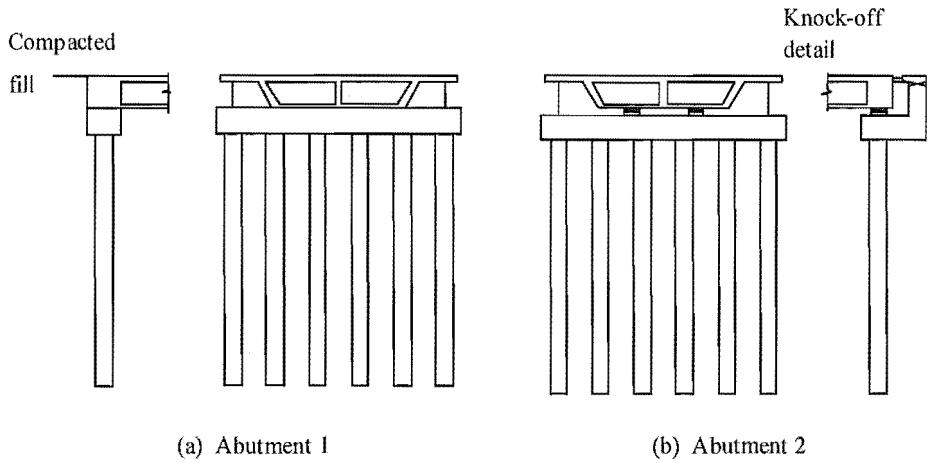

Figure 4.2 Bridge Abutment

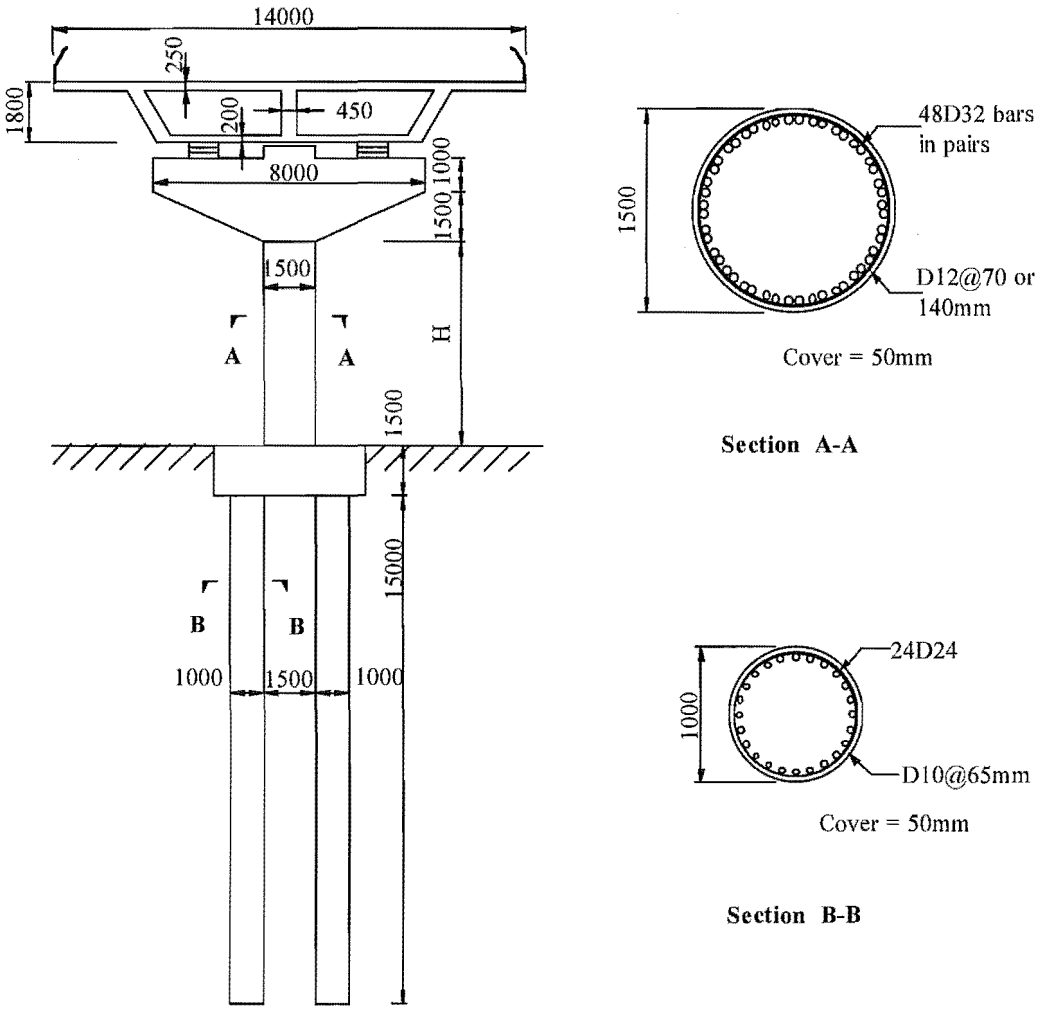

Figure 4.3 Bridge Typical Cross Section

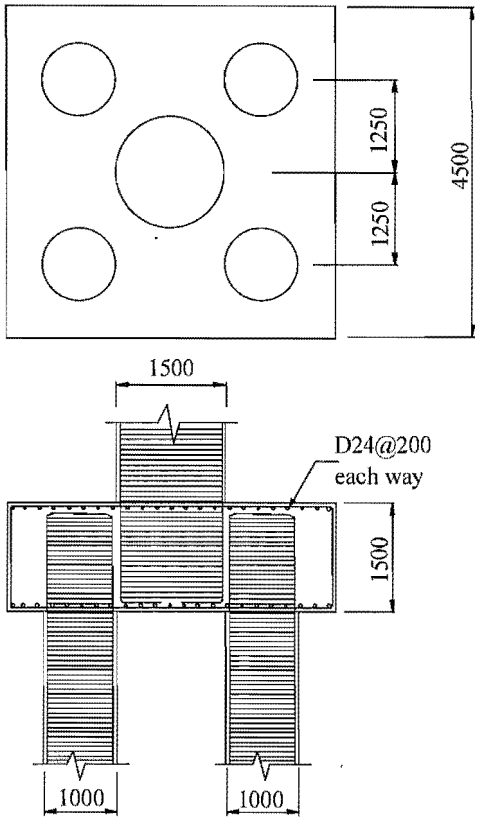

Figure 4.4 Bridge Footing Details

remainder of the pier height. A typical cross section of the bridge is shown in Figure 4.3.

The piles are reinforced with 24D24 longitudinal bars, and D10 spirals with 65mm pitch for the full height. They have a minimum depth of 15m below the base of the pile cap. The reinforcement for the pile cap is $D24@200mm$ centres each way at top and bottom. Bars are hooked at the ends. Transverse reinforcement is provided by nominal ties with vertical D16 bars at 400mm centres each way (see Figure 4.4).

The design concrete cylinder strength is $f_c^{'}=35$ MPa for all substructure elements, and $f_c^{'}=45$ MPa for the prestressed superstructure. Reinforcement nominal yield strength is $f_y=430$ MPa; ultimate strength is $f_u=645$ MPa; strain at ultimate stress is $\varepsilon_u=0.12$. The site has a uniform soil condition, consisting of cohesionless soils with density and stiffness increasing linearly with depth.

The plan view (Figure 4.1 (a)) of the bridge shows movement joints in spans 3-4 and 7-8 as an optional extra included in some of the analyses. These may be assumed to be at 7.5m from the nearest bent centreline (i.e. piers 4 and 7). The joints have an initial opening of 25mm and have two restrainer ties across them. A restrainer unit consists of a circular array of seven cables with swaged fittings. The individual cable has a nominal 20mm diameter and the yield force is 122 KN. The restrainer is 1.83m long with 12mm initial slackness [Fenves and Ellery 1998].

4.2 Structure Modelling

The program RUAUMOKO [Carr 2001] has a wide variety of modelling options available to represent the structure and its supports. In this section, the structural component model used for the prototype bridge is described. Three-dimensional frame members (Figure 4.5) represent the behaviour of the superstructure, as well as the components of the bridge bents. The interaction between the piles and the surrounding soil, the sliding bearings and the movement joints are modelled by three-dimensional spring elements (Figure 4.6). The mass

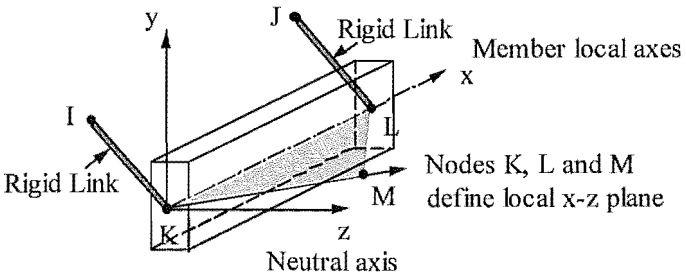

Figure 4.5 Three-Dimensional Frame Member

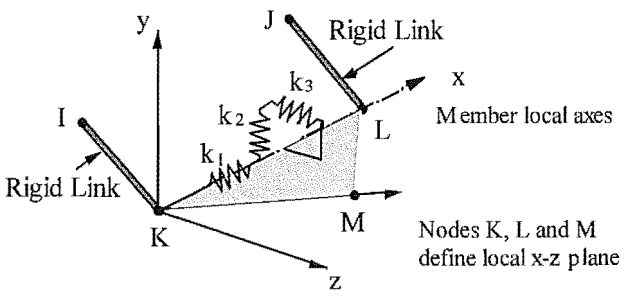

Figure 4.6 Three-Dimensional Spring member

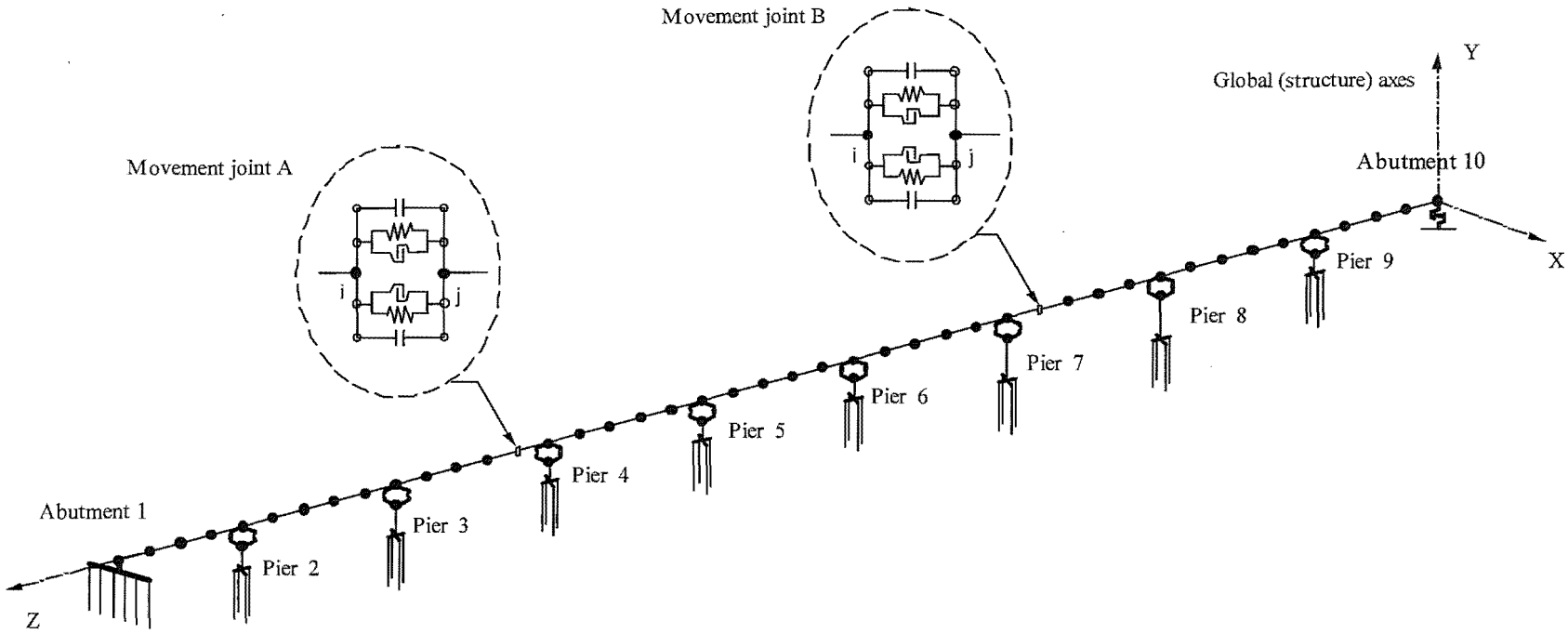

Figure 4.7 Three-Dimensional Model of the Bridge

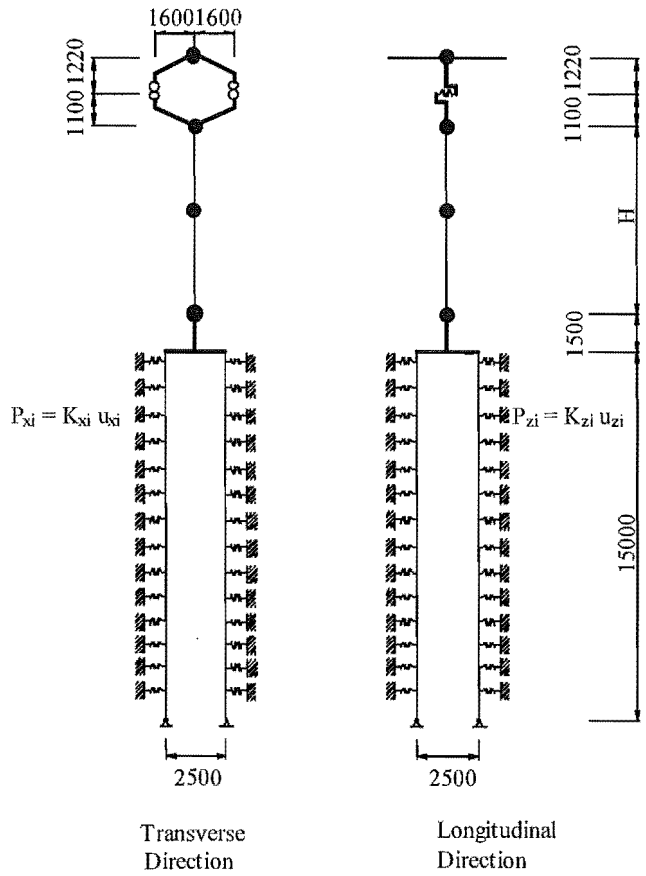

Figure 4.8 The Detail of Pier and Pile Model

representation is via lumped mass matrices. The commonly assumed Rayleigh damping model is used to model the damping exhibited by the structure. The whole bridge structural model is shown in Figures 4.7 and 4.8 and the details of various models are described in the following sections.

4.2.1 Damping

With the Rayleigh or Proportional damping model [Carr 2001], the structure-damping matrix $\mathbf{C}$ is given as

$$\mathbf{C} = \alpha\mathbf{M} + \beta\mathbf{K} \tag{4.1}$$

where $\mathbf{M}$ and $\mathbf{K}$ are the mass and stiffness matrices for the structure. The coefficients α and β are computed to give the required levels of viscous damping at two different frequencies. Assuming that the properties of orthogonality of the mode shapes of free-vibration with respect to the mass and stiffness matrices also apply to the damping matrix it is possible to

specify the desired damping levels at two frequencies. If the required fraction of critical damping is λ_i and λ_j at modes i and j with natural circular frequencies ω_i and ω_j respectively then

$$\alpha = \frac{2\omega_i\omega_j(\omega_i\lambda_j - \omega_j\lambda_i)}{\omega_i^2 - \omega_j^2} \tag{4.2}$$

and

$$\beta = \frac{2(\omega_i\lambda_i - \omega_j\lambda_j)}{\omega_i^2 - \omega_j^2} \tag{4.3}$$

The result of this assumption is that at any other mode with a natural circular frequency ω_n, the fraction of critical damping is given by

$$\lambda_n = \frac{1}{2}\left(\frac{\alpha}{\omega_n} + \beta\omega_n\right) \tag{4.4}$$

This relationship between the damping and the natural frequency of free vibration is shown in Figure 4.9 where it is seen that as the natural frequency increases above ω_j the amount of damping increases almost linearly with frequency. In this study, the fraction of critical damping $\lambda_1 = \lambda_2 = 5\%$ in modes 1 and 2 was adopted.

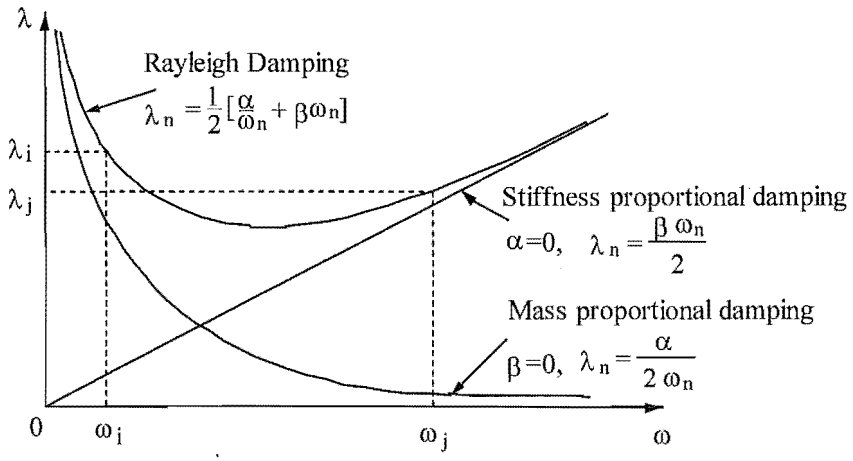

Figure 4.9 Rayleigh Damping model

4.2.2 Superstructure

In bridges, it is generally not practical to provide for plastic hinge formation in the superstructure and the pier hinges at the base of the piers are typically chosen as the site for inelastic deformation [Priestley et al. 1996]. Therefore the superstructure (with the cross

section shown in Figure 4.10) is modelled by linear elastic beam members placed at the geometric centroid of the cross section, having the characteristics given in Table 4.1.

Elastic modulus E (GPa)	31.5	Translational mass (kg)	1496
Shear modulus G (GPa)	13.1	Rotational mass moment of inertia for rotation about the vertical axis $(kg \cdot m^2)$	8540
Moment of inertia $I_y (m^4)$	86.25	Section area (m^2)	6.93
Moment of inertia $I_z (m^4)$	3.16	Member length (m)	8
Torsional moment of inertia $J_x (m^4)$	6.97	Number of members	43

Table 4.1 The member properties for the superstructure

The flexural stiffnesses of the members are calculated based on their uncracked state (i.e. I_y, I_z for gross cross section) for this prestressed box girder. For thin-walled hollow sections the torsional moment of inertia J_x can be found as [e.g. Collins et al. 1991]

$$J_x = \frac{4A_0^2 t}{p_0} \tag{4.5}$$

with A_0 and p_0 represent the area and perimeter of the shear flow in a tubular section of wall thickness t as shown in Figure 4.10. For a bridge with different and varying thickness t_i, an averaged t_{av} can provide a close approximation. In most bridge superstructures the torsion levels in the earthquake case will be significantly below the cracking torque limit state and no torsional stiffness reduction needs to be considered [Priestley 1996]. The gross area of the cross section is also used to model the axial stiffness and the transverse shear stiffness.

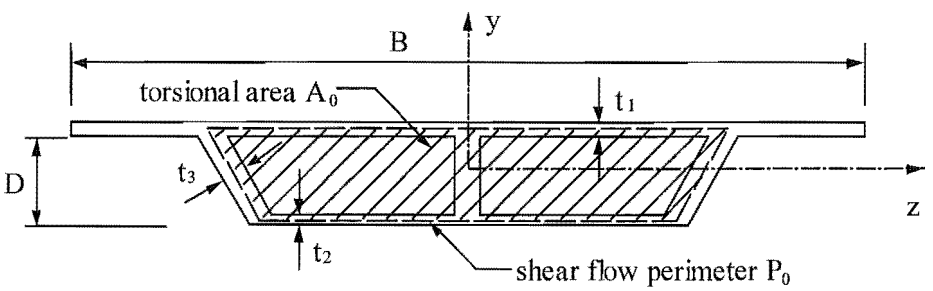

Figure 4.10 Superstructure Cross-Section

The mass of the deck, which contributes to the bridge seismic response in the form of inertia forces, is lumped at the ends of each beam member. The translational mass of node i is

$$m_i = \rho l_i \tag{4.6}$$

and the rotational mass moment of inertia is

$$j_{iz} = m_i \frac{l_i^2 + b_i^2}{12} \tag{4.7}$$

where ρ is the mass density of the superstructure, and l_i, b_i is the length and width of the beam member, respectively.

4.2.3 Piers

Since bridge piers are expected to respond to seismic excitation in an inelastic manner according to the current seismic design philosophy, correct analytical modelling of the piers is of primary importance. Here the piers were modelled as concrete beam-column members using the Giberson one-component model [Carr 2001], which idealises a reinforced concrete beam or column member as a perfectly elastic line element with non-linear rotational springs at the two ends that model the possible plastic hinges as shown in Figure 4.11. For this

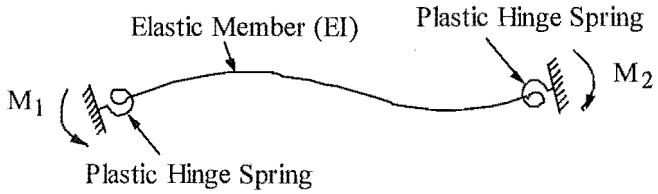

Figure 4.11 Giberson One Component Model

prototype bridge, the plastic hinges can only form at the base of the piers. The bi-linear hysteresis rule (Figure 4.12) was employed for the hinge spring, representing the inelastic behaviour of the member. The stiffness of the hinge is controlled by the tangent stiffness of the current point on the hysteresis rule. A plastic hinge length $L = D$ (D = the diameter of the piers) was assumed. The effective member properties, which reflect the extent of concrete cracking and reinforcement yielding, were used as shown in Table 4.2. The effective stiffness EI_e was determined from section moment-curvature analyses as [Priestley et al. 1996]

$$EI_e = \frac{M_y}{\Phi_y} \tag{4.8}$$

	Gross	Effective
Moment of inertia $I_e(m^4)$	0.248	0.124
Torsional moment of inertia $J_e(m^4)$	0.45	0.15
Shear area $A_{ve}(m^2)$	1.77	0.88

Table 4.2 The member properties for the piers

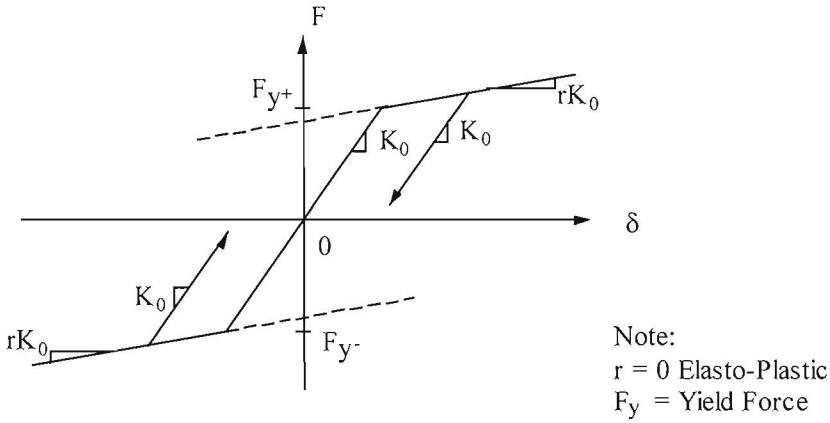

Figure 4.12 Elasto-Plastic and Bi-linear Hysteresis Rules

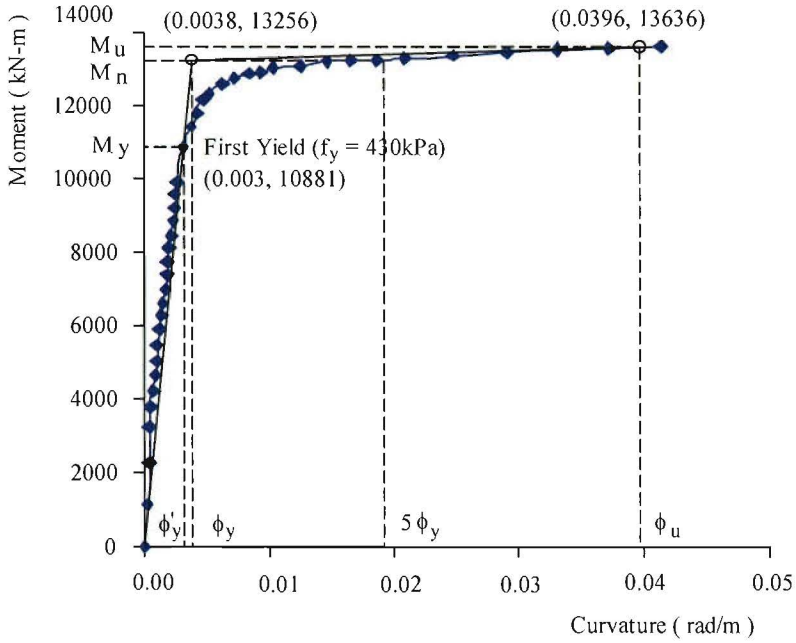

Figure 4.13 Moment-Curvature Relationship for Pier Section

where M_y and Φ_y represent the ideal yield moment and curvature for a bilinear moment-curvature approximation. The result of the section moment–curvature analysis for piers with static axial load of 800 KN is shown in Figure 4.13 [Dodd 1992]. The equivalent yield curvature ϕ_y is found by extrapolating the line joining the origin and conditions at first yield, to the nominal moment capacity M_n. The diagram of the axial force ~ yield moment interaction for the pier section is shown in Figure 4.14.

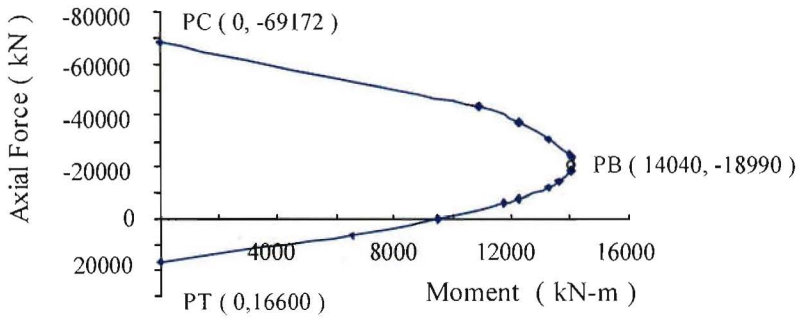

Figure 4.14 Axial Force- Yield Moment Interaction for Pier Section

Due to the lack of specific research data, Priestley [1996] assumed that the effective stiffness reduction in shear can be considered proportional to the effective stiffness reduction in flexure:

$$GA_{ve} = GA_v \cdot \frac{EI_e}{EI_g} \quad or \quad A_{ve} = A_v \cdot \frac{I_e}{I_g} \tag{4.9}$$

For this research, a value of $I_e/I_g = 0.5$ was adopted, hence the torsional moment of inertia was multiplied by a factor of 0.3 to give the effective torsional moment of inertia after Singh and Fenves [1994].

4.2.4 Sliding bearings

The sliding bearings between the superstructure and the cap beam at the piers were modelled as three-dimensional springs that followed an elastic - perfectly plastic hysteresis rule in the longitudinal direction, and an elastic hysteresis rule in the vertical and transverse directions [Fenves and Ellery 1998]. The spring stiffness was based on an idealised shearing deformation given by $G_{elast}A/h$, where $G_{elast} = 1.0MPa$ was the assumed shear modulus for the elastomer, $h = 50mm$ was the height of the bearing pads, and $A = 0.34m^2$ was the cross-

sectional area of the bearing pads. The stiffness was $6800\,KN/m$ and the yield force was $480\,KN$. The maximum horizontal reaction was determined from the dynamic friction coefficient (= 0.12) applied to a constant vertical reaction from gravity loads.

4.2.5 Foundation

Since the ratio of pile spacing to pile cap depth is less than 2:1, the behaviour of the pile cap is similar to that of a deep beam, hence the pile cap could be modelled as a rigid link. The piles were modelled using elastic concrete beam members. They were arranged with shorter elements in the upper region to increase accuracy. The effective moment of inertia came from an analysis of the section moment-curvature as shown in Figure 4.15. The effective properties employed were as following:

	Gross	Effective
Moment of inertia $I_e(m^4)$	0.05	0.025
Torsional moment of inertia $J_e(m^4)$	0.087	0.029
Shear area $A_{ve}(m^2)$	0.78	0.39

Table 4.3 The member properties for piles

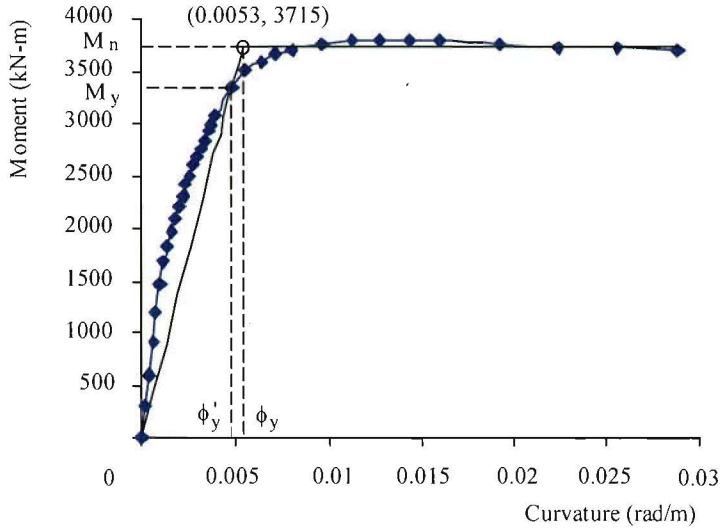

Figure 4.15 Moment-Curvature Relationship for Pile Section

The vertical restraint to the motion of the piles depends on the characteristics of the pile design and installation. For CIDH piles, which are usually assumed to derive their load capacity from end bearing and the toe ends of the piles could therefore be considered as fixed in the vertical direction in the structural model. The interaction between the piles and the surrounding soil in the lateral direction was modelled by Winkler springs arranged along the pile length; these could be either linear or non-linear. This model can provide a reasonable approximation to the pile boundary conditions but does not represent dynamic soil-structure interaction (SSI) since no soil inertia effects, soil wave radiation effects, or viscous effects of soils movement around the pile shaft and modifications of these characteristics by the pile stiffness or the density of pile groups are considered.

For linear springs, the individual soil spring stiffness can be determined based on the following consideration [Priestley et al. 1996]. Assume that a contact pressure p at the soil-pile interface can be expressed as a function of the soil deformation Δ_s:

$$p = k_s \Delta_s \tag{4.10}$$

where k_s $\left(force/length^3\right)$ represents a soil reaction coefficient. Then a Winkler soil reaction modulus or spring constant k along the length of the pile with diameter D can be determined as

$$k = D \cdot k_s \tag{4.11}$$

and is often referred to as the modulus of subgrade reaction. For cohesionless soils and normally consolidated clays, a linear increase of k with depth z measured from the ground surface is a reasonable assumption, and the modulus of subgade reaction k can be expressed as a function of depth z as

$$k(z) = k^* z \tag{4.12}$$

where k^* $\left(force/length^3\right)$ represents the depth-independent subgrade reaction modulus. A discrete soil spring stiffness K_i at depth z_i, can now be determined for a given tributary length B_i of pile shaft as:

$$K_i = k^* z_i B_i \tag{4.13}$$

Values for k or k^* can be obtained from the geotechnical literature in relationship to Young's modulus E_s, which in turn can be found (although with significant variability) from standard penetration tests, shear wave velocity measurements, or direct bearing tests.

Vesic [1961] sought to find the value of the spring stiffness which gave the best agreement between the solutions for an infinite beam on an elastic half space, and those for an infinite beam on a Winkler subgrade. The modulus of subgrade reaction, k, calculated by Vesic, was expressed in terms of Young's modulus, E_s, and Poisson's ratio, v_s, of the elastic half space:

$$k = \frac{0.65E_s}{1-v_s^2}\left(\frac{E_s b^4}{E_b I_b}\right)^{1/12} \tag{4.14}$$

where b = width of the beam; E_b = Young's modulus of the beam; I_b = moment inertia of the beam. For most practical situations, $\left(\frac{E_s b^4}{E_b I_b}\right)^{1/12}$ is approximately equal to 1. Therefore Vesic's equation becomes

$$k = \frac{0.65E_s}{1-v_s^2} \tag{4.15}$$

For the pile foundation case, Bowles [Bowles 1982] has suggested that the modulus of subgrade reaction given by Vesic should be doubled, because the soil is in contact with both faces of the pile.

$$k = 2\times\frac{0.65E_s}{1-v_s^2} = \frac{1.3E_s}{1-v_s^2} \tag{4.16}$$

By examining the results of full-scale pile tests with different diameters, Carter [Carter 1984] indicated that the pile width factor has a significant effect, and the Vesic's equation is best adjusted by a linear correction of the width

$$k = \frac{1.3E_s}{1-v_s^2}\cdot\frac{b}{B_{ref}} \tag{4.17}$$

where B_{ref} = 1m.

Poulos [1971] gave the values of E_s for cohesionless soils assumed as an elastic, homogeneous, isotropic semi-infinite medium, as shown in Table 4.4, on the basis of back-computations from the results of full scale pile tests.

Soil Density	Range of Values of E_s (KPa)	Average E_s (KPa)
Loose	900 - 2070	1720
Medium	2070 - 4140	3450
Dense	4140 - 9650	6900

Table 4.4 The values of E_s for cohesionless soils

For cohesionless soils, the Young's modulus is usually assumed to vary linearly with depth, that is

$$E_s = m\,z \quad (kPa) \tag{4.18}$$

where m = constant (kPa/m); z = depth (m). In this study the values of average E_s given in Table 4.4 were adopted for m.

Table 4.5 lists the typical values of Poisson's ratio for different materials, given by Bowles [Bowles 1982]. A Poisson's ratio of 0.3 is used for sand, therefore, the lateral modulus of subgrade reaction for sand can be taken as:

$$k = \begin{cases} 2500z(kPa) & for \quad Loose \quad Sand \\ 5000z(kPa) & for \quad Medium \quad Sand \\ 10000z(kPa) & for \quad Dense \quad Sand \end{cases} \tag{4.19}$$

Type of Soil	Poisson's Ratio
Clay, Saturated	0.4 – 0.5
Clay, Unsaturated	0.1 – 0.3
Sandy Clay	0.2 – 0.3
Silt	0.3 – 0.35
Sand (Dense)	0.2 – 0.4
Coarse (e = 0.4 – 0.7)	0.15
Fine-grained (e = 0.4 – 0.7)	0.25
Rock	0.1 – 0.4
Loess	0.1 – 0.3
Ice	0.36
Concrete	0.15

Table 4.5 the typical values of Poisson's ratio

However, in all the results that are presented in this thesis the compliant foundation described in this chapter were not used and that all piers were assumed to be fully fixed i.e. the foundation was assumed to be rigid. The original intent had been to consider the effects of foundation compliance but for difficulties in allowing the dispersion and the amount of extra parameters that would need to be considered in developing the conclusions these foundation models were not pursued any further. It is left for future research to extend the work to allow for such foundation models to be included.

4.2.6 Abutments

At Abutment 1, the abutment cap beam is monolithically connected to the deck, so Abutment 1 is modelled as a vertical rigid link between the pile elements and the deck element. Abutment 10 has sliding bearings similar to those installed at the pier cap beams, but it does not restrain transverse movement of the superstructure. The springs used to model the sliding bearings at Abutment 10 have the same properties in both the longitudinal and transverse directions as those at the piers.

4.2.7 Movement joints

Long bridges are divided into sections by movement joints to compensate for deformations from initial shortening due to prestressing, time-dependent effects such as creep and shrinkage, and environmental effects such as temperature deformations. A prototype of a movement joint is shown in Figure 4.16. Seismically, these movement joints have the tendency to allow the separate sections to develop their own characteristic dynamic response and modify this individual dynamic response through complex interaction between frames through the movement joints. Movement joints typically allow deformations in the form of translation in the bridge longitudinal direction and flexural rotation about the movement joint axis but restrict translations perpendicular to the bridge axis by means of shear keys. Vertical shear transfer is provided through bearing seats and vertical restrainers. However, movement joints cannot be viewed only as longitudinal bridge separations in a seismic event since transverse seismic deformation input can open and close movement joints to various degrees depending on the geometry of the bridge structure [Priestley et al.1996].

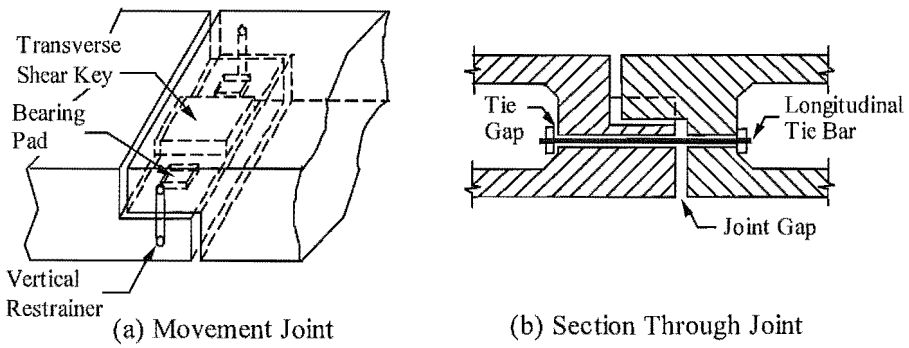

Figure 4.16 Bridge Movement Joint

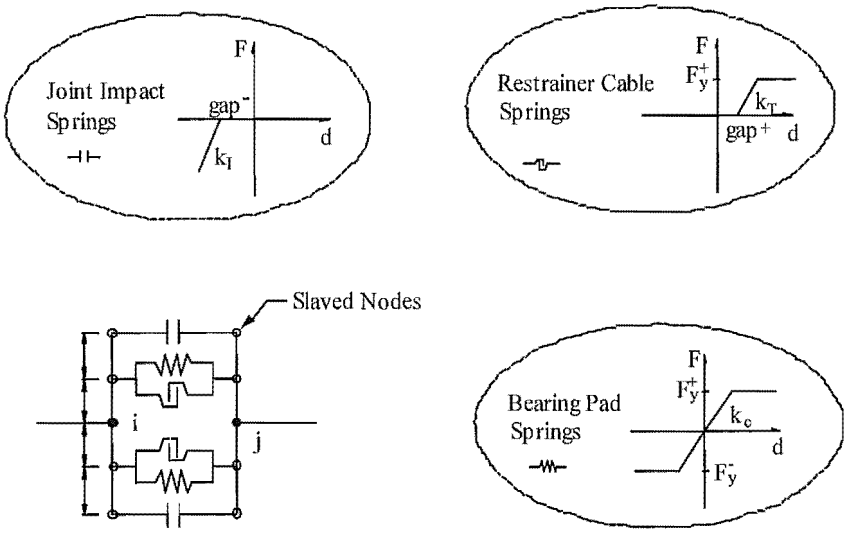

Figure 4.17 Schematic of Joint Model

The nonuniform opening and closing of movement joints makes it essential that movement joints be modelled with their exact geometry. For non-linear dynamic time-history analyses, joint element models with non-linear stiffness characteristics, gapping and Coulomb friction damping have been developed [Tseng and Penzien 1973, Yang et al. 1994, Fenves and Ellery 1998]. The joint element model used in this study is shown in Figure 4.17. The joints were modelled with sets of slaved nodes that were rigidly constrained in a horizontal array of five nodes across the width of the superstructure. The nodes were located where the bearing pads were located and where the pounding could happen. Each set of five nodes represented one side of the joint and was connected to another set of five nodes via zero-length nonlinear spring elements. The joint restrainers were modelled as elastic-perfectly plastic tension-only springs with an initial slackness of 12mm. The stiffness of the restrainers was given by EA/L, where E was the modulus of elasticity for the cables (assumed to be 200 GPa), A was the total cross sectional area of the cables, and L was the length of the restrainer cables. The joint closing was modelled with compressing-only gap elements at the outer edges of the superstructure and with an initial gap of 25mm. The stiffness of the gap spring was 10^{10} KN/m. The bearing pads were modelled as elastic-perfectly plastic springs as mentioned in 4.2.4.

CHAPTER 5

THE WAVE PASSAGE EFFECT ON THE SEISMIC RESPONSE OF LONG BRIDGES

5.1 Introduction

This chapter describes the "wave passage" effect of asynchronous input motions on the response of a long bridge. It was assumed that the variation of the ground motion at the different bridge supports was solely due to the difference in the arrival time of the seismic waves and the seismic motions did not change in shape at the various supports on the ground surface. The time interval between two support points (Δt) is a function of the propagation velocity of the wave (v_s), the distance between the two bridge supports (L), and the angle (θ) between the direction of the approaching waves and the longitudinal axis of the bridge as shown in Figure 5.1. It may be expressed as:

$$\Delta t = L\cos\theta / v_s \tag{5.1}$$

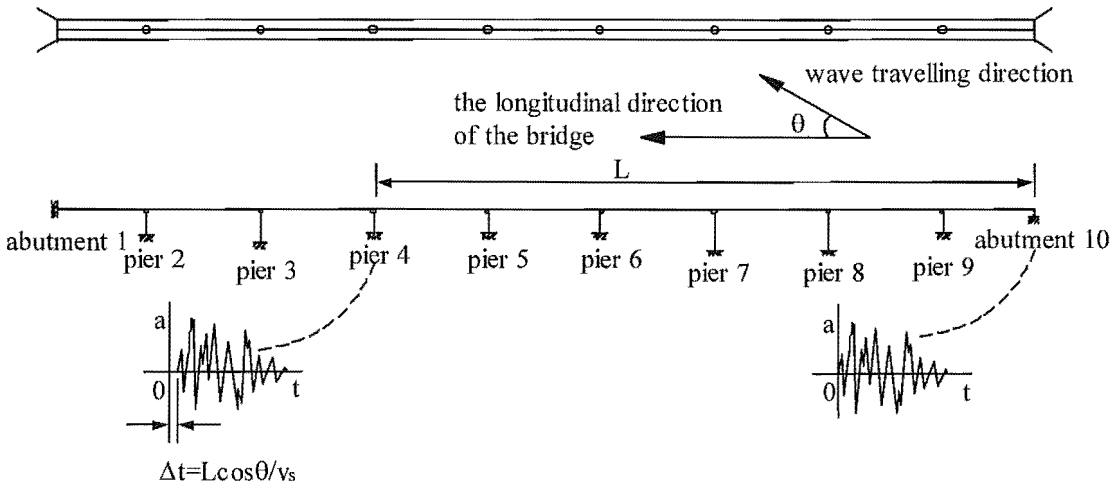

Figure 5.1 Asynchronous Input Motions Due to Wave Passage Effect

For the research reported in this Chapter it was assumed that the seismic motions acted in the transverse direction of the bridge, and travelled along the bridge longitudinal direction from abutment 10 to abutment 1, hence the angle between the direction of the approaching waves and the longitudinal axis of the bridge was zero i.e. $\theta = 0$. Three natural earthquake records

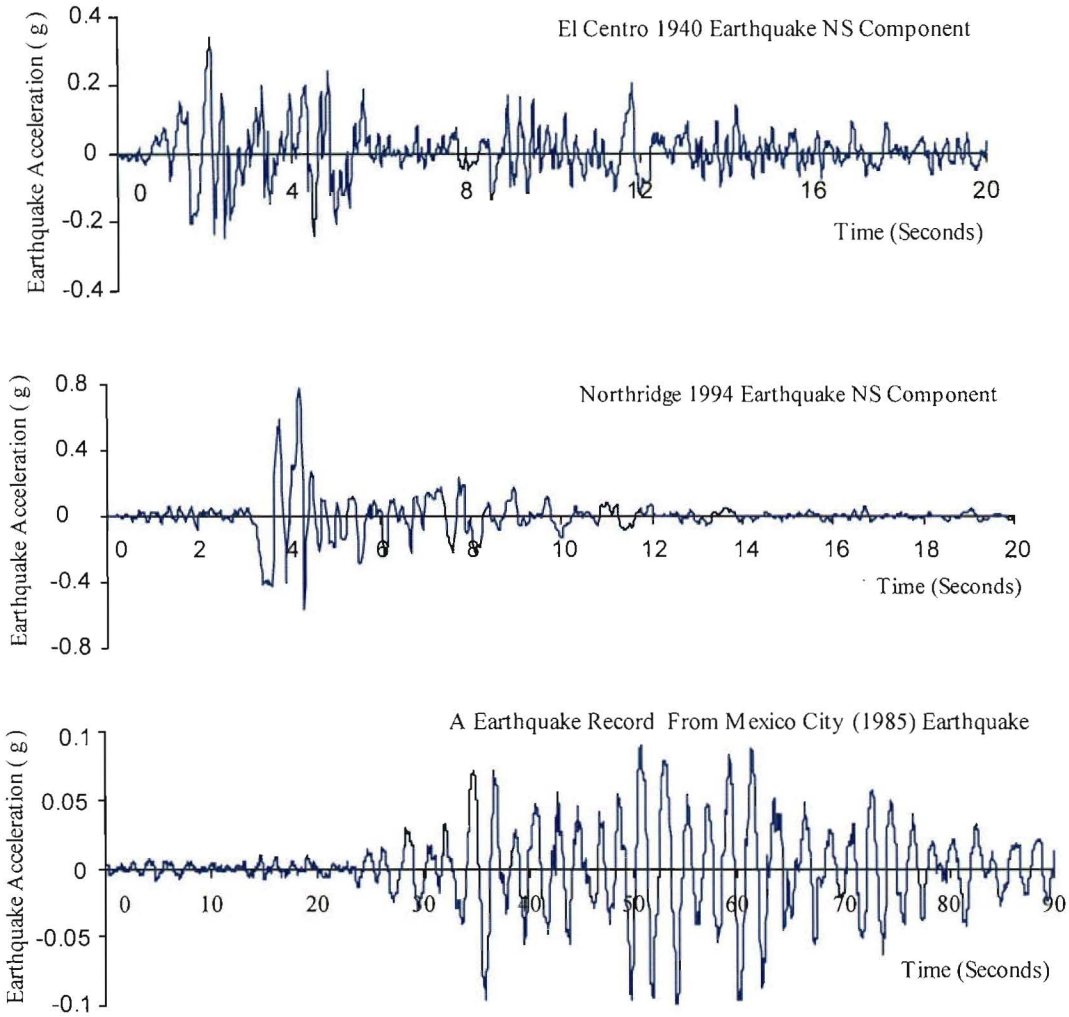

Figure5.2 The three Earthquake records used in the analyses

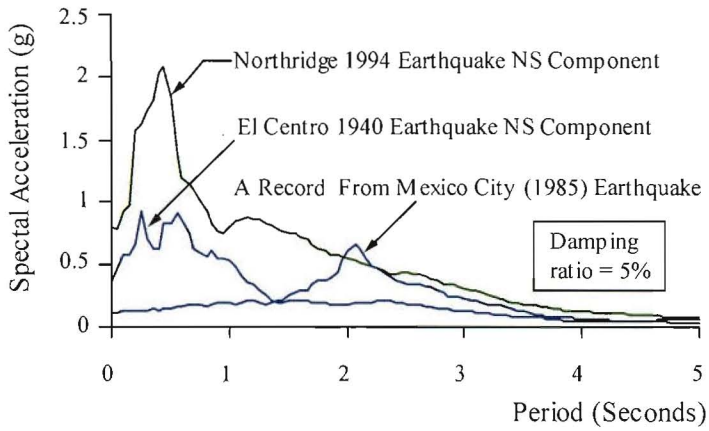

Figure 5.3 The Acceleration Spectra of the Earthquake Records

were used in the analyses. These were the North-South components of the El Centro (May 18, 1940) earthquake (El40NSC) and the Northridge (January 17,1994) earthquake (SYLM949), and one from the Mexico City (1985) earthquake (MEXSCT1L) (see Figures 5.2). The acceleration spectra of these three earthquake records are shown in Figure 5.3. In most seismic time-history analyses the ground acceleration records are normally treated as the input. This is inappropriate in travelling wave studies for inelastic structures. In the program Ruaumoko, for such cases, a total displacement formulation is used and the ground acceleration are integrated by the program to produce the ground velocities and ground displacements which are then used as input to the supporting degrees of freedom in the structure. For the synchronous cases, the natural earthquake record was applied to all of the pier supports. For the asynchronous cases, the natural earthquake record was specified at abutment 10 and there were time delays ($\Delta t = L/v_s$) for the ground motions at other pier supports.

The wave propagation velocities for the analyses were selected to cover a wide range of soil types from soft soil (v_s = 100, 125, 150, 200m/s) to stiff soil (v_s = 300, 400, 500m/s) and rock (v_s =1000, 1500, 2000m/s). Five bridge models with different configurations and boundary conditions were analysed by using the RUAUMOKO (3D Version) computer program [Carr 2001] to show how the wave propagation velocity and the configurations of the bridge influence the structural response.

5.2 The Response of Model 1

Model 1 is the model of the prototype bridge described in Chapter 4. All the piers were assumed to be fixed at the ground level. The superstructure was fixed at the Abutment 1while at the Abutment 10 the superstructure was supported on the abutment sub-structure through sliding bearings with freedom of movement longitudinally, transversely and rotationally about a vertical axis. Model 1 is shown in Figure 5.4.

5.2.1 Eigenvalue Analysis

An eigenvalue analysis was carried out for Model 1. The main characteristics of the first nine modes are given in Table 5.1 and the first nine mode shapes are shown in Figure 5.5. The Rayleigh damping model which was used in this study is simple and very often used but is also recognised as having potential to lead to high amounts of damping in the high modes. For

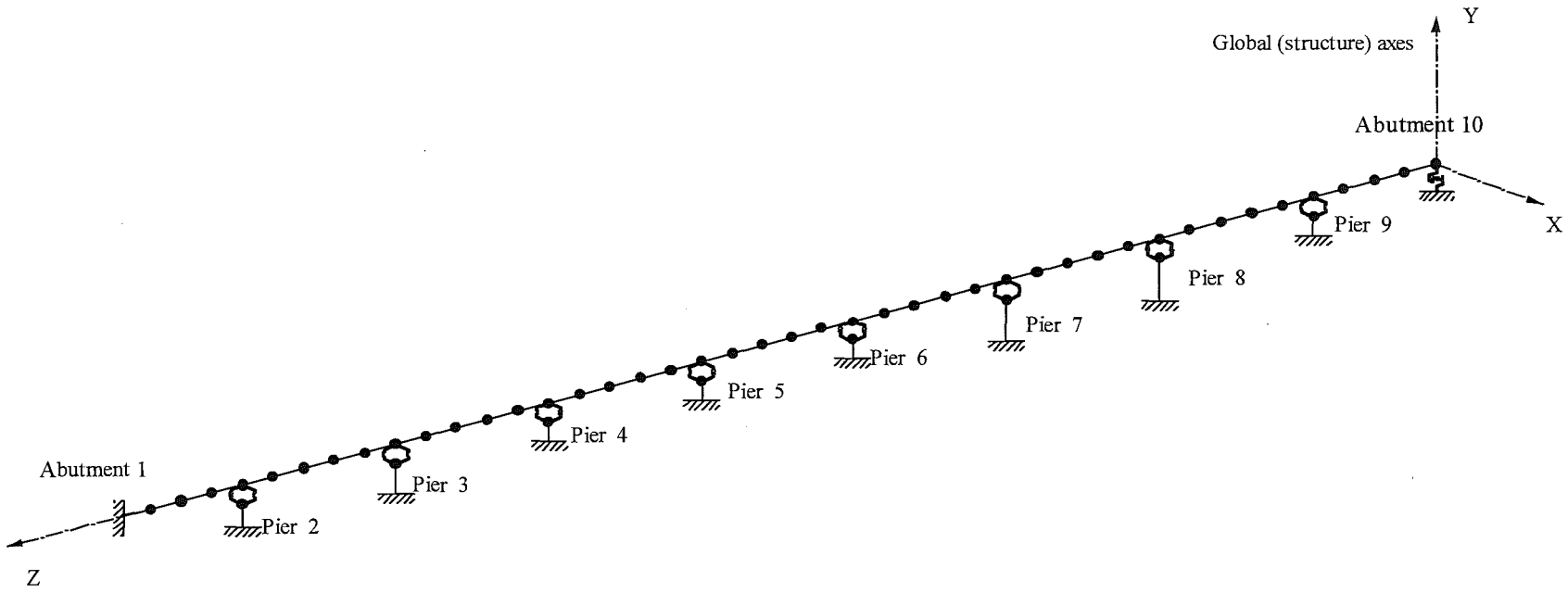

Figure 5.4 Bridge Model 1

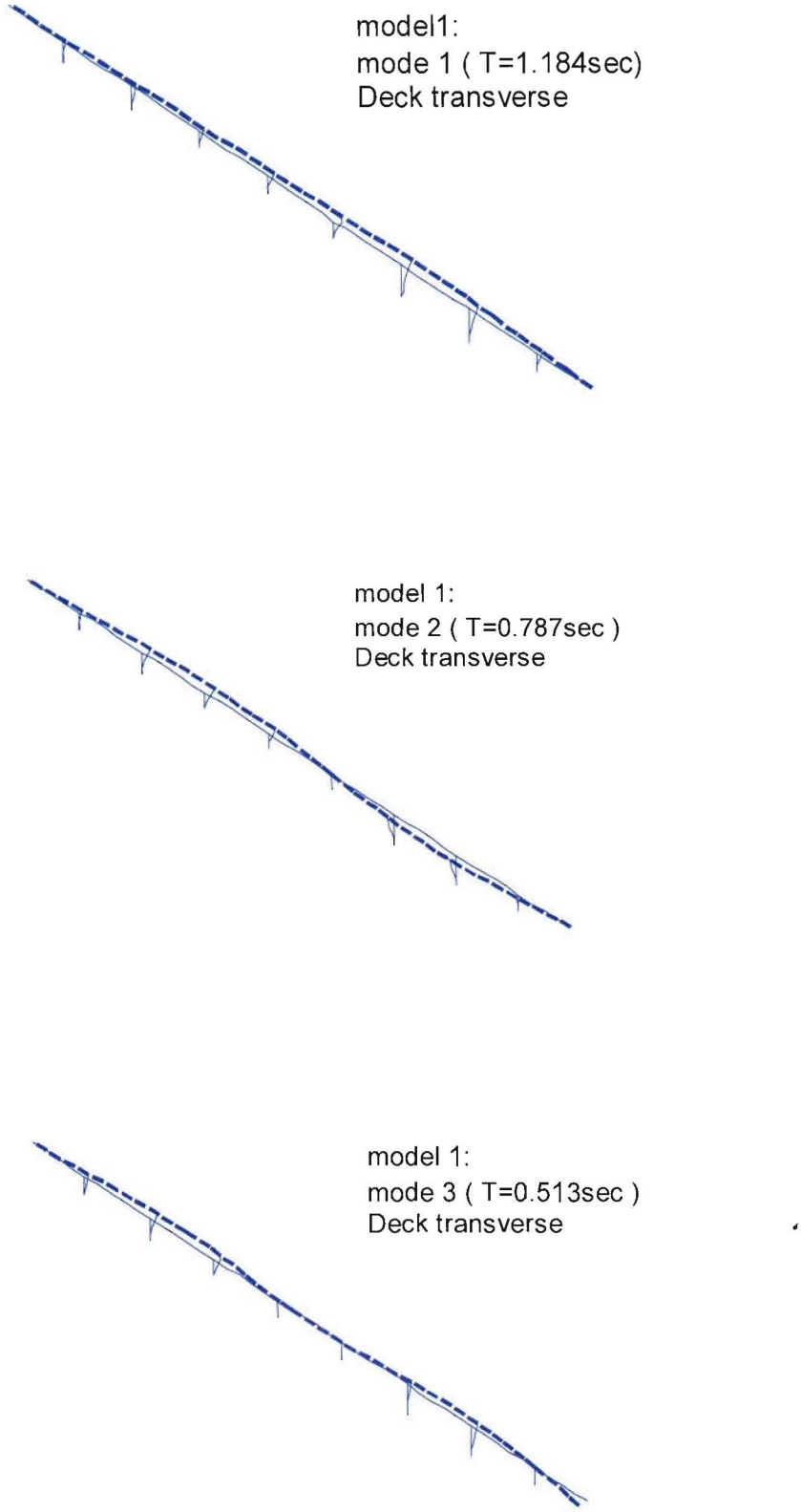

Figure 5.5 (a) The First to Third Mode Shapes of Bridge Model 1

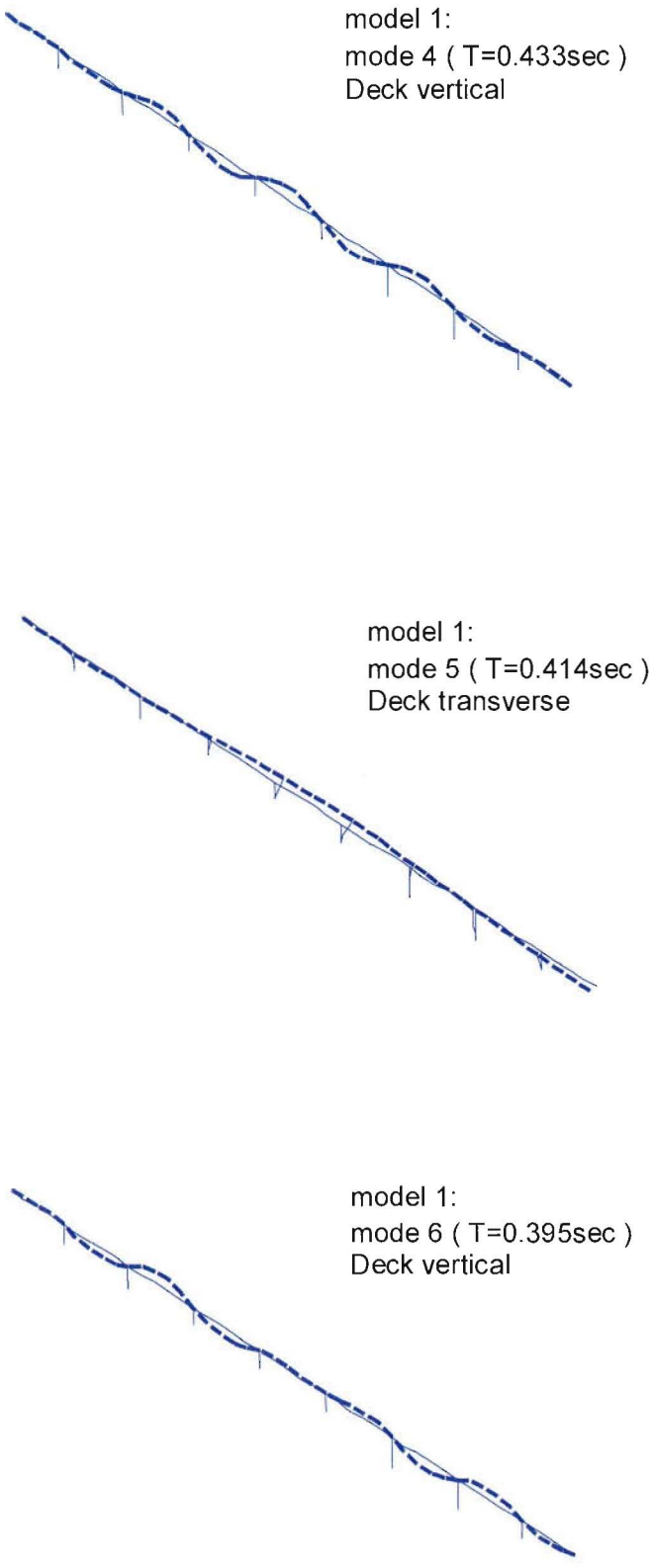

Figure 5.5 (b) The Fourth to Sixth Mode Shapes of Bridge Model 1

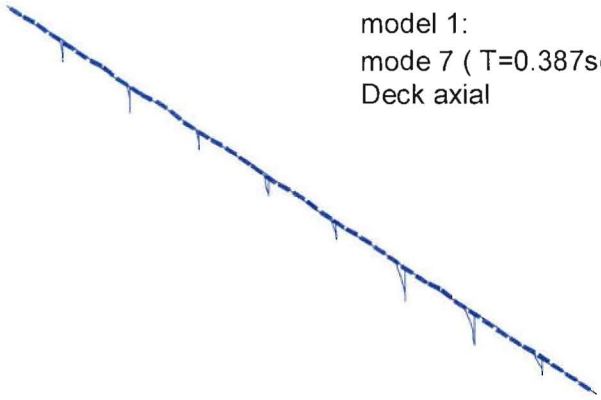

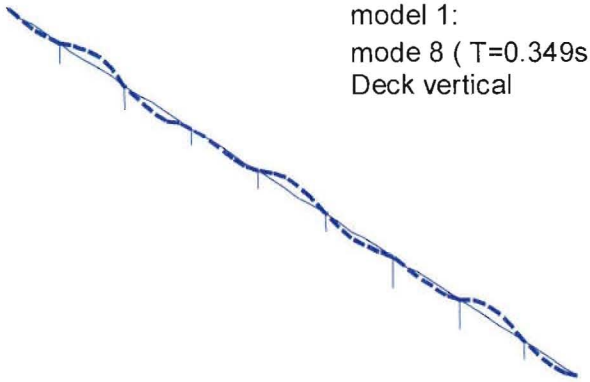

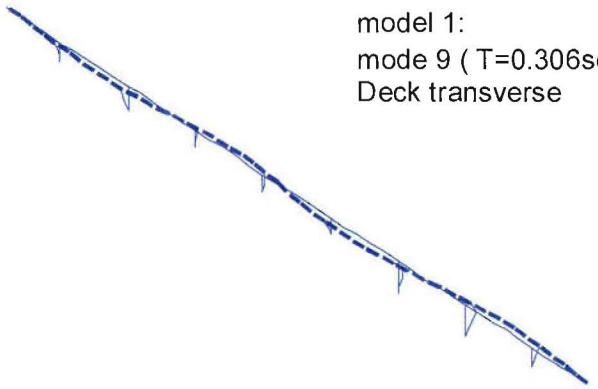

Figure 5.5 (c) The Seventh to Ninth Mode Shapes of Bridge Model 1

Mode	Period (seconds)	Frequency (Hz)	Damping (%)	Characteristics
1	1.184	0.844	5.0	Deck transverse flexure, piers flexure
2	0.787	1.270	5.0	Deck transverse flexure, piers flexure
3	0.513	1.949	5.9	Deck transverse flexure, piers flexure
4	0.433	2.309	6.6	Deck vertical flexure, piers flexure/axial
5	0.414	2.415	6.8	Deck transverse flexure, piers flexure
6	0.395	2.532	7.0	Deck vertical flexure, piers flexure/axial
7	0.387	2.584	7.1	Deck axial, piers flexure/axial
8	0.349	2.865	7.7	Deck vertical flexure, piers flexure/axial
9	0.306	3.268	8.5	Deck transverse flexure, piers flexure

Table 5.1 Natural periods of free vibration and mode shape characteristics of Model 1

Model 1 the levels of damping in the modes that are contributing to the response of the bridges is not large (as shown in Table 5.1) and the very high modes are not likely to significantly excited.

5.2.2 Elastic response

The elastic response parameters investigated were the maximum pier drift (deflection of pier top relative to their base) and the maximum pier shear force. The maximum pier drift provides a measure of the flexural response of the pier and the maximum pier shear force is an indication of the pier shear demand. In the analyses the earthquake records used were scaled in order to ensure that all the piers remain elastic.

The response of Model 1 to the North-South components of the El Centro 1940 earthquake record with a scale factor of 0.5 for the synchronous and asynchronous cases are shown in Table 5.2 and Figure 5.6. The variations of the maximum pier drifts with the travelling wave velocity can be observed as follows. The drifts of all the piers (except pier 5) decreased as the travelling wave velocity was increased from 100m/s to between 200 and 250m/s where the response was a minimum. Only the drift of pier 5 increased before the wave velocity reached 150m/s, then it decreased as the wave travelling velocity was increased from 150m/s to 200m/s. For wave travelling velocities beyond 250m/s, the pier drifts increased as the travelling wave velocity was increased to between 500 and 1000m/s where most pier drifts reached their maximum values. At

high travelling wave velocities, the drifts of piers 2, 3, 4 and 5 decreased with the increase of the travelling wave velocity and the drifts of piers 6, 7, 8 and 9 did not alter significantly.

For the other earthquake records, the variations of the maximum pier drift with the travelling wave velocity showed a very similar pattern to that for the North-South component of the El Centro 1940 earthquake record. Figure 5.7 shows the responses of Model 1 to the North-South component of the Northridge 1994 earthquake with a scale factor of 0.15, and Figure 5.8 shows the responses of Model 1 to the earthquake record from the Mexico City (1985) earthquake with a scale factor of 0.5.

For all the earthquake records, the pier drifts generally decreased as the wave travelling velocity was increased from 100m/s to between 200 and 250m/s where they had a minimum responses, and then the pier drifts increased with the increase of the travelling wave velocity, although there were some local variations. Pier 2 is an exception because its maximum pier drift decreased as the travelling wave velocity was increased over the whole range of travelling wave velocities for all three earthquake records.

The possible explanation for the changing pattern of the maximum pier drifts with the wave propagation velocity is as follows. It is known that the response of an elastic structure subjected to asynchronous inputs at different pier bases can be obtained from the superposition of two contributions: a dynamic component induced by the inertia forces and a so-called pseudo-static component, due to the differential displacements between the adjacent supports [Clough and Penzien 1993]. For the synchronous case, the differential displacements between the adjacent supports are zero and the response can be attributed to the dynamic component only.

As the travelling wave velocity increases, the pseudo-static component decreases because the differential displacements between the adjacent supports reduces sharply with the increase in the travelling wave velocity. Figures 5.9 to 5.11 show the variations of the maximum differential displacements between the adjacent pier bases with the travelling wave velocity for different earthquake records. It can be observed that when the travelling wave velocity is 300m/s, the maximum differential displacements between the adjacent supports dropped to 40% to 45% of the value for the travelling wave velocity of 100 m/s, and when the velocity is 500 m/s, they dropped to 20% to 25%. The percentage depends on the earthquake record that was used in the analysis.

wave travelling velocity (m/s)	*pier2*		*pier3*		*pier4*		*pier5*		*pier6*		*pier7*		*pier8*		*pier9*	
	drift (mm)	$\frac{drift(v)}{drift(v=\infty)}$	*drift* (mm)	$\frac{drift(v)}{drift(v=\infty)}$	*drift* (mm)	$\frac{drift(v)}{drift(v=\infty)}$	*drift* (mm)	$\frac{drift(v)}{drift(v=\infty)}$	*drift* (mm)	$\frac{drift(v)}{drift(v=\infty)}$	*drift* (mm)	$\frac{drift(v)}{drift(v=\infty)}$	*drift* (mm)	$\frac{drift(v)}{drift(v=\infty)}$	*drift* (mm)	$\frac{drift(v)}{drift(v=\infty)}$
100	31.3	4.89	33.9	1.78	32.1	1.22	15.7	0.48	27.6	0.65	57.8	1	51.1	0.99	15.7	0.66
125	26.3	4.11	38.5	2.03	21.3	0.81	19	0.58	28.6	0.67	40.7	0.71	29.8	0.58	14.5	0.61
150	24.6	3.84	32.9	1.73	24.4	0.92	25.6	0.79	23.7	0.56	40.3	0.7	32	0.62	15.8	0.67
200	15.9	2.48	14.6	0.77	11	0.42	14.4	0.44	17.4	0.41	18	0.31	16.2	0.31	14.2	0.6
250	12.7	1.98	13.8	0.73	11.4	0.43	12.9	0.4	15.4	0.36	16.1	0.28	15	0.29	10.5	0.44
300	11.6	1.81	10.8	0.57	16.6	0.63	16.1	0.5	19.8	0.47	22	0.38	20.4	0.4	10.8	0.46
400	11.6	1.81	26	1.37	26.1	0.99	27.5	0.85	26.1	0.61	32.5	0.56	27.7	0.54	14.6	0.62
500	15.7	2.45	35.1	1.85	32.4	1.23	35	1.08	33	0.78	39.8	0.69	35.1	0.68	17.9	0.76
1000	9.2	1.44	29.4	1.55	38.6	1.46	41.7	1.28	42.3	1	46.9	0.81	44.6	0.87	19.8	0.84
1500	8.3	1.3	27.5	1.45	36.4	1.38	40.2	1.24	43.4	1.02	50.6	0.88	45.9	0.89	21	0.89
2000	8.1	1.27	26.1	1.37	34.6	1.31	38.9	1.2	43.4	1.02	52.4	0.91	46.5	0.9	21.6	0.91
synchronous ($v=\infty$)	6.4	1	19	1	26.4	1	32.5	1	42.5	1	57.6	1	51.5	1	23.7	1

Table 5.2 Maximum pier drifts in Model 1 for NS component of EL Centro 1940 earthquake record with an input scale factor of 0.5

Note: drift (v) refers to the drift for the travelling wave cases.
drift ($v = \infty$) refers to the drift for the synchronous case.

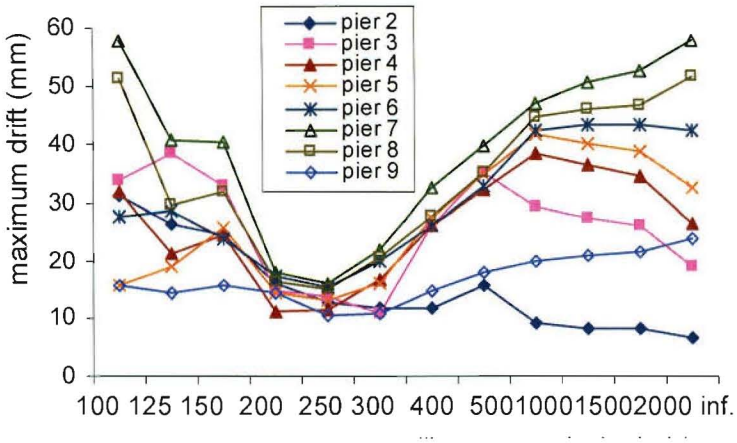

Figure 5.6 Maximum pier drifts versus travelling wave velocity (EL40NSC with an input scale factor of 0.5)

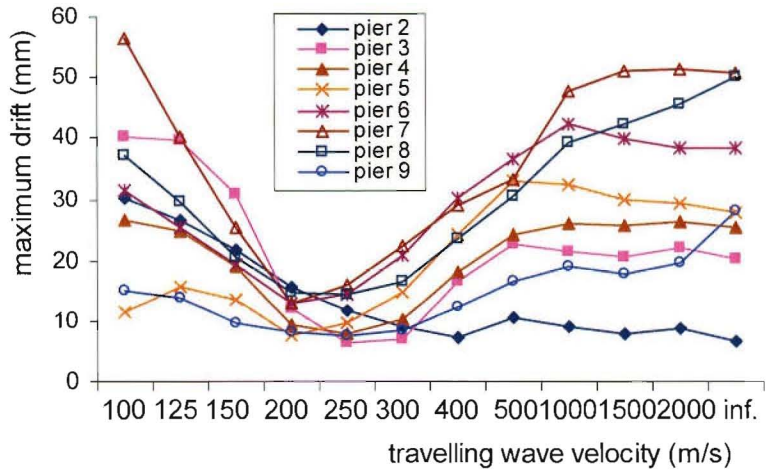

Figure 5.7 Maximum pier drifts versus travelling wave velocity (SYLM949 with an input scale factor of 0.15)

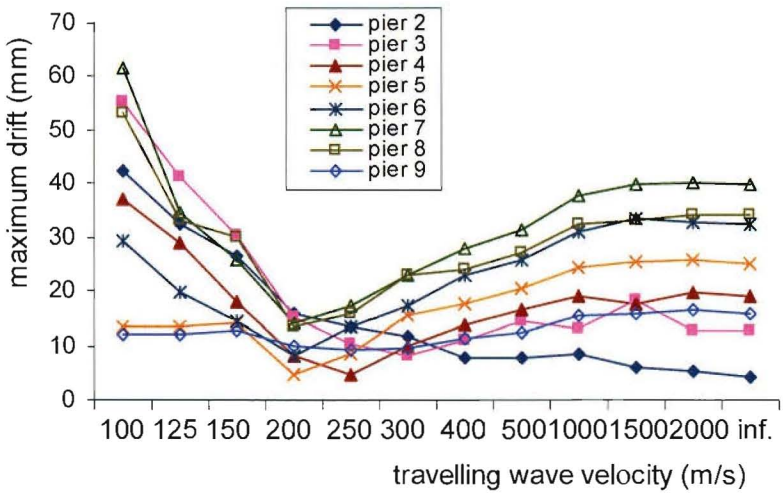

Figure 5.8 Maximum pier drifts versus travelling wave velocity (MEXSCT1L) with an input scale factor of 0.5

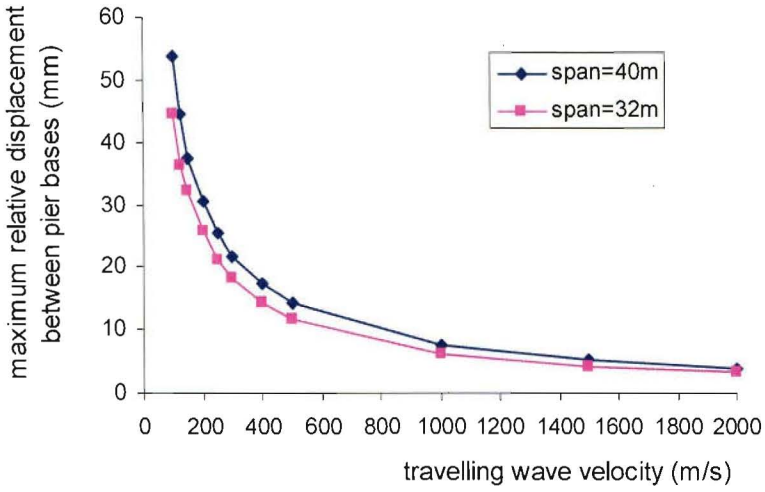

Figure 5.9 Maximum differential displacements between pier bases (EL40NSC) with an input scale factor of 0.5

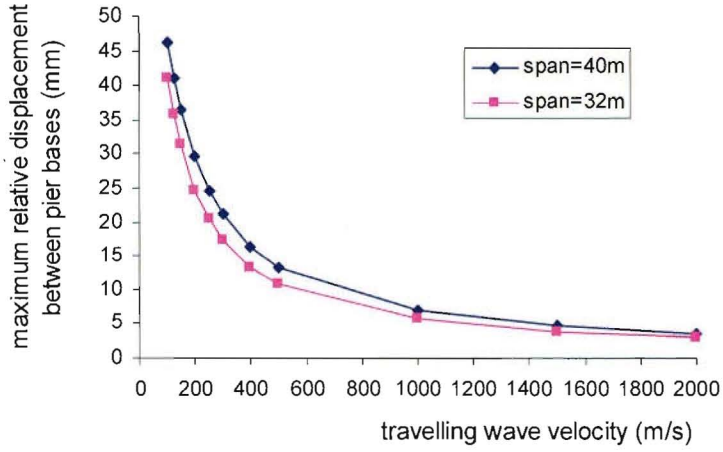

Figure 5.10 Maximum differential displacements between pier bases (SYLM949) with an input scale factor of 0.15

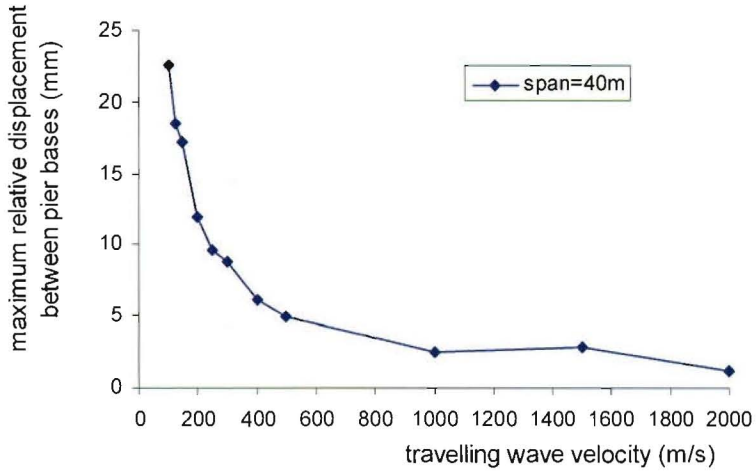

Figure 5.11 Maximum differential displacements between pier bases (MEXSCT1L) with an input scale factor of 0.5

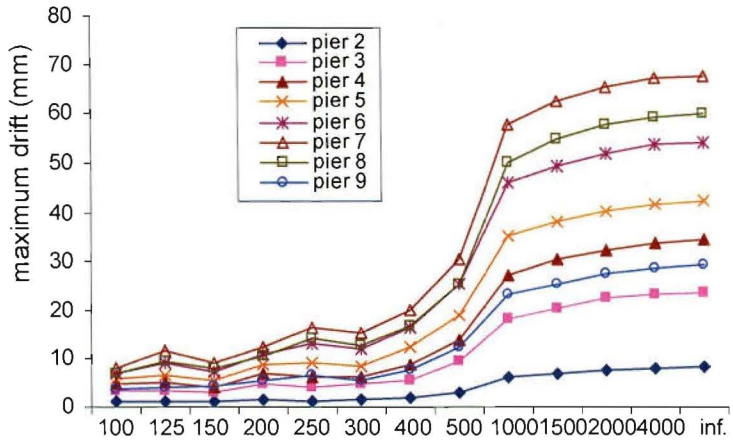

Figure 5.12 Maximum pier drifts (averaged earthquake record applied synchronously, EL40NSC with an input scale factor of 0.5)

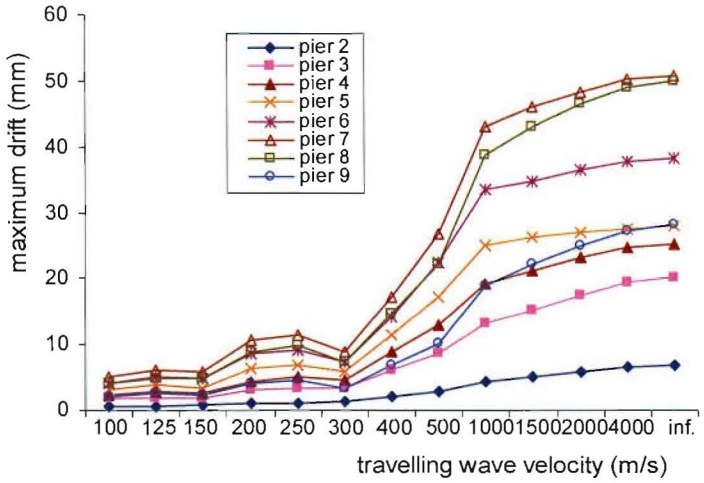

Figure 5.13 Maximum pier drifts (averaged earthquake record applied synchronously, SYLM949 with an input scale factor of 0.15)

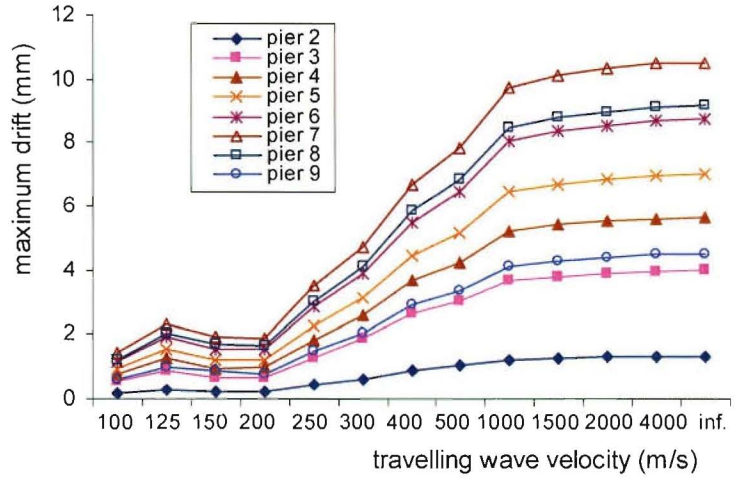

Figure 5.14 Maximum pier drifts (averaged earthquake record applied synchronously, MEXSCT1L with an input scale factor of 0.5)

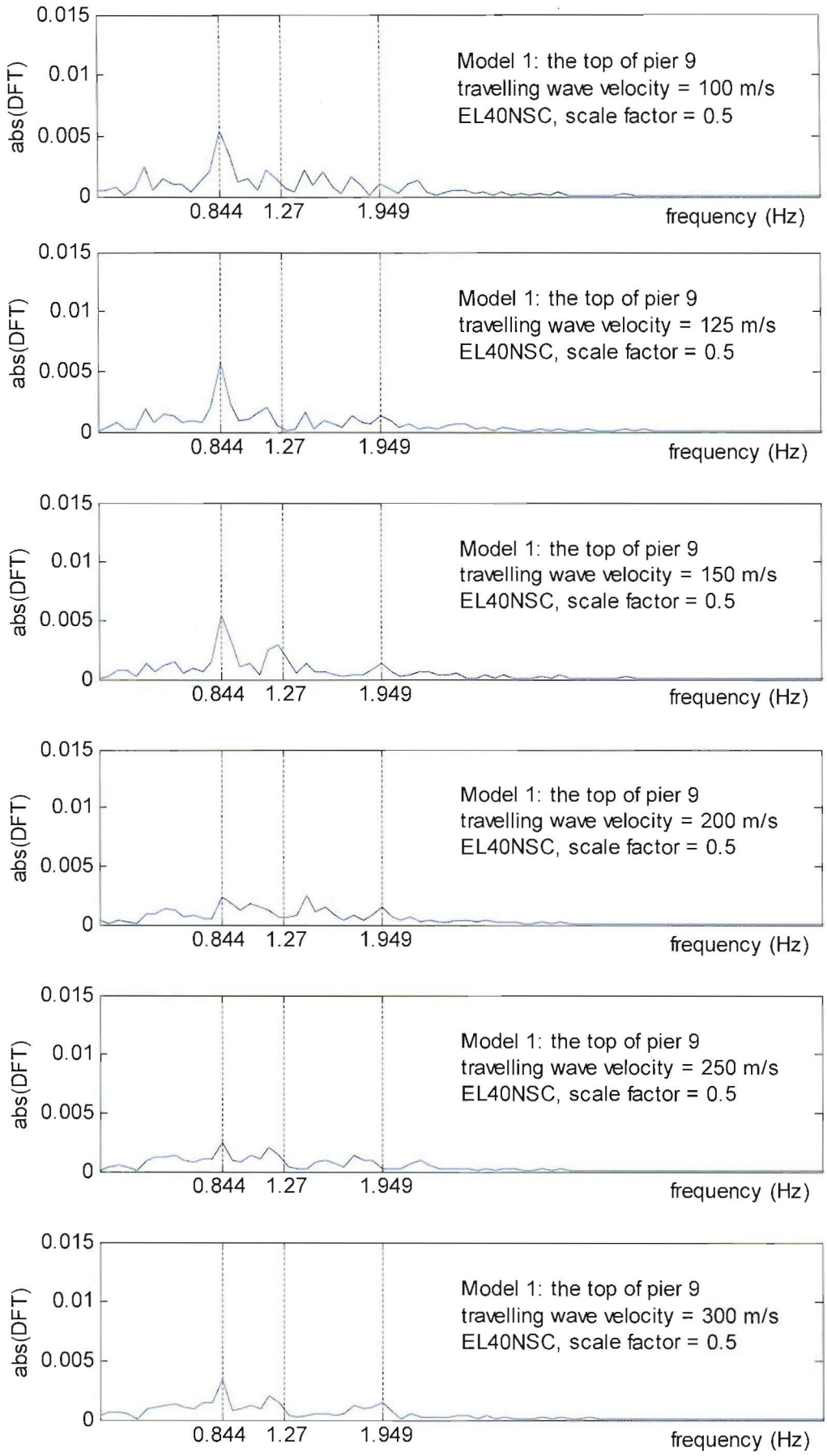

Figure 5.15 (a) Fourier spectrum of the displacement at the top of pier 9

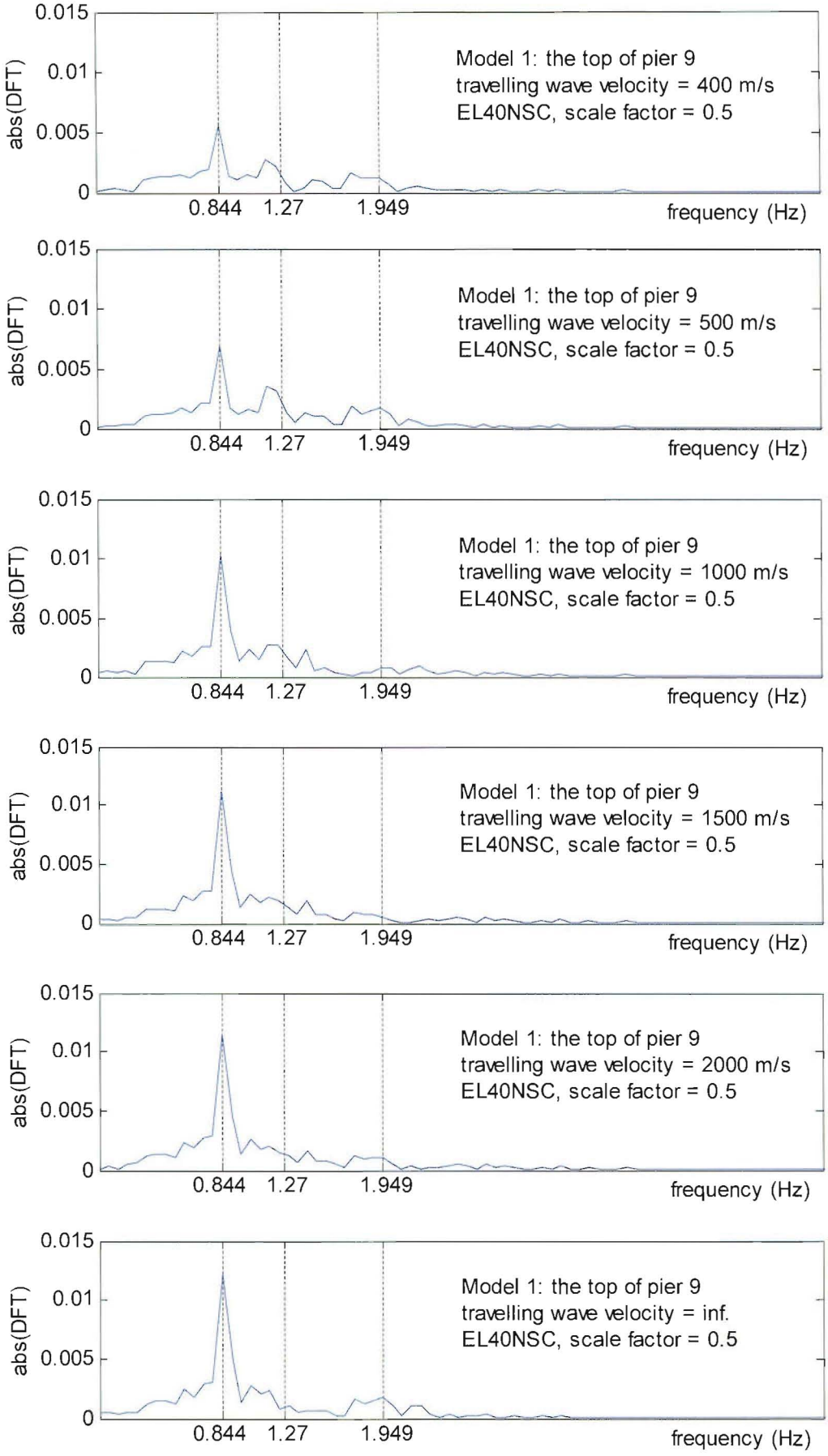

Figure 5.15 (b) Fourier spectrum of the displacement at the top of pier 9

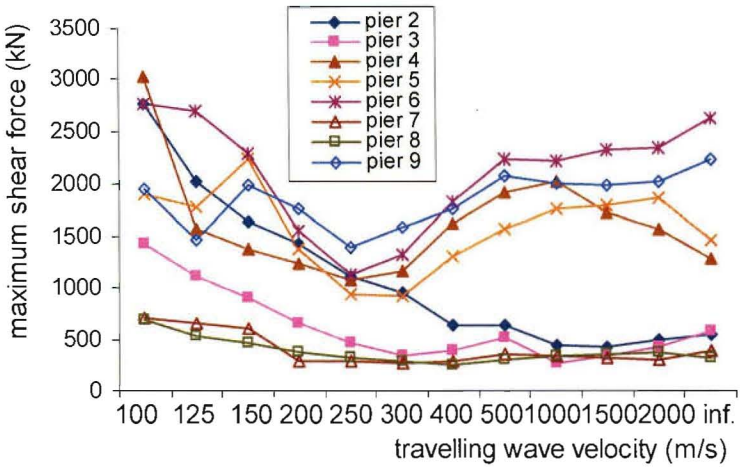

Figure 5.16 Maximum pier shear forces (EL40NSC with an input scale factor of 0.5)

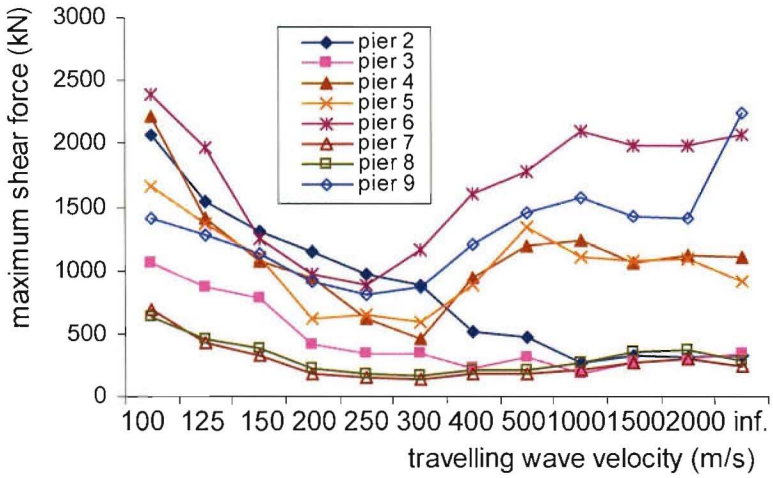

Figure 5.17 Maximum pier shear forces (SYLM949 with an input scale factor of 0.15)

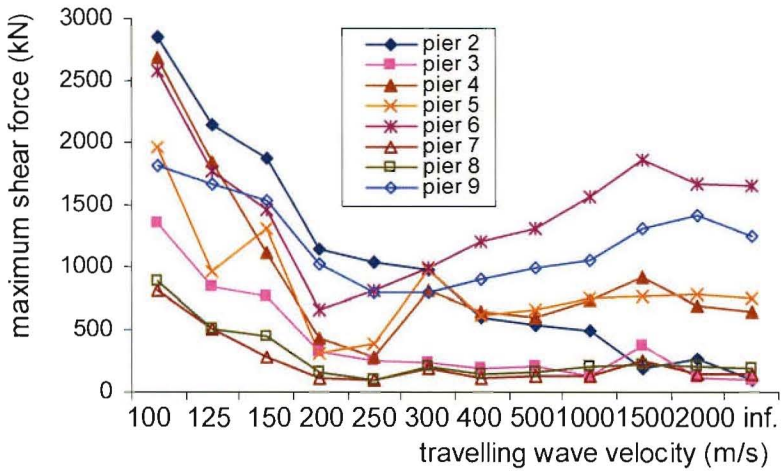

Figure 5.18 Maximum pier shear forces (MEXSCT1L with an input scale factor of 0.5)

In order to investigate the variation of the dynamic component of the response with the travelling wave velocity, several synchronous cases were investigated. The time-histories used in these synchronous cases were the average of the ten travelling wave time-histories that had been applied to the ten bridge supports in each of the previous asynchronous cases. The responses of these synchronous cases were considered to represent approximately the dynamic components of the responses of asynchronous cases corresponding to the various travelling velocities. The results of these synchronous cases analyses are shown in Figures 5.12 to 5.14 for different earthquake records. It can be seen that when the time-histories used in these synchronous cases derived from the asynchronous cases with travelling wave velocities higher than 1000m/s, the maximum pier drifts were almost the same as those under the natural earthquake records. When the time-histories used in these synchronous cases derived from the asynchronous cases with travelling wave velocities lower than 1000m/s, the maximum pier drifts decreased as the travelling wave velocity decreased. When the travelling wave velocity decreased to 300m/s, the maximum pier drifts dropped to 20% of the values that occurred in the synchronous case subjected to the El Centro earthquake record, to 16% of the values that was observed in the case subjected to the Northridge earthquake record, and to 45% of the values that occurred in the case subjected to the Mexico City earthquake record.

A clear trend was observed when comparing the maximum pier drifts in the travelling wave cases (Figures 5.6 to 5.8), the maximum differential displacements between the adjacent pier bases (Figure 5.9 to 5.11) and the maximum pier drifts in those synchronous cases in which the combined earthquake records were used (Figures 5.12 to 5.14). When the travelling wave velocity of the seismic motion was lower than 200 ~ 250 m/s, the responses of the bridge structure to asynchronous motion were dominated by the pseudo-static components and the dynamic components were much smaller than the pseudo-static components. When the travelling wave velocity was higher than 200 ~ 250 m/s, the pseudo-static components reduced considerably and the dynamic components increased very rapidly, and the responses of the structure to asynchronous motion were more dependent on its dynamic components.

The behaviour of pier 2 was more dominated by the pseudo-static effect rather than the dynamic effect because pier 2 was the closest pier to the fixed end of the deck where the structural stiffness was very large and the dynamic component was small. This probably explains why the maximum relative drifts of pier 2 decreased as the travelling wave velocity was increased as seen in Figures 5.6 to 5.8.

The total response of the bridge structure to asynchronous motion could also be affected by the fact that the frequency spectrum of the average excitation to which the whole bridge was subjected was different from that of the synchronous case. The frequency spectrum of the excitation changes with the travelling wave velocity, although the time histories of the seismic motion did not change in shape at the various supports on the ground surface. This can be seen from the Fourier spectra of the pier drift of pier 9 in Figure 5.15, for example, which shows that the relative significance of the frequency of the first mode of the bridge vibration changed with the travelling wave velocity. For the synchronous case ($v = \infty$) the response was dominated by the first mode, but for the asynchronous cases the higher modes were excited also by the travelling seismic motions as indicated by other researchers [Tzanetos et al. 1998]. Any local variation of pier drift could be attributed to the change in the frequency spectrum of the asynchronous motion consistent with the travelling wave velocity.

The combination of these three aspects: the pseudo-static effect, the dynamic effect, and the change of the frequency spectrum of excitation with the travelling wave velocity could make the response of the bridge to travelling wave excitation greater than those under the synchronous input excitation.

The maximum pier shear forces varied with the travelling wave velocity in approximately the same way as the pier drifts, for all of the earthquake records that were used (Figures 5.16 to 5.18). For piers 7 and 8, the maximum pier shear forces do not change much with the wave propagation velocity of the seismic motion unlike the case for the other piers. This is because piers 7 and 8 were longer than other piers and consequently the stiffnesses were smaller than those of the other piers and therefore they attracted smaller shear forces.

5.2.3 Inelastic response

Under moderate or severe earthquakes, bridge structures are usually designed to behave inelastically, hence the wave-passage effect on the inelastic responses of the Model 1 is considered. The parameters investigated for the inelastic response were the maximum pier drift, the maximum pier shear force, and the maximum section curvature ratio of the pier. The maximum section curvature ratio is the curvature reached in the analysis divided by the yield curvature of the pier and indicates the curvature ductility demand of the pier.

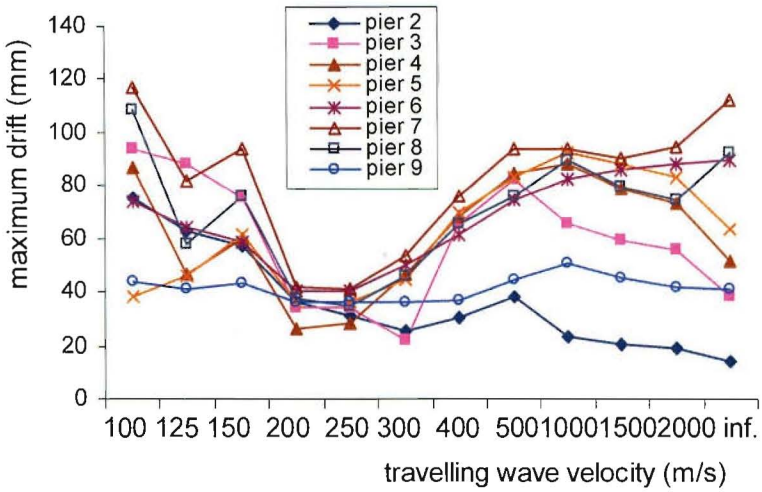

Figure 5.19 Maximum pier drifts under EL40NSC with a scale factor of 1.0

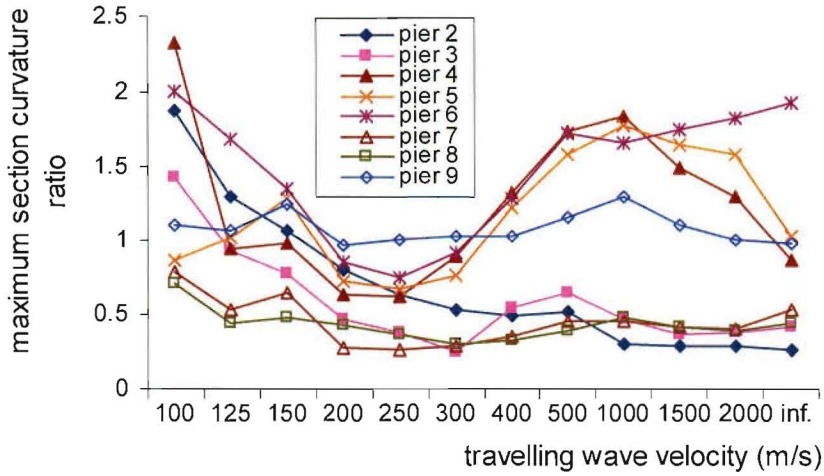

Figure 5.20 Maximum section curvature ratios under EL40NSC with a scale factor of 1.0

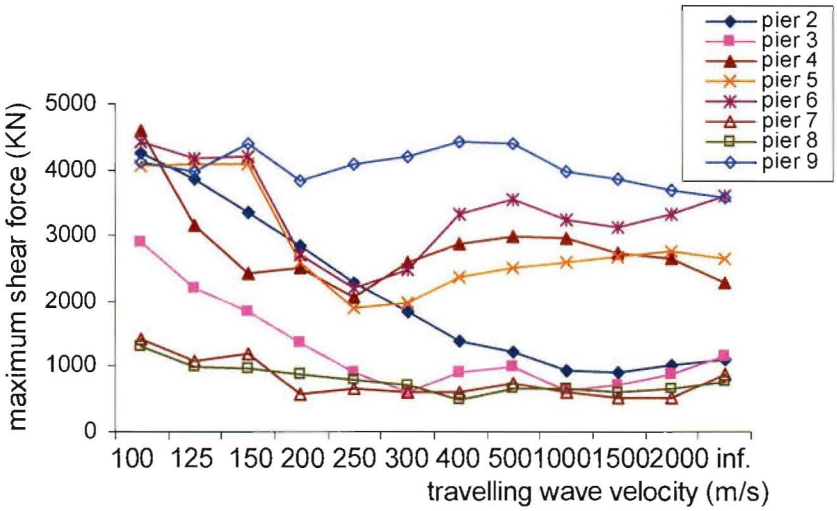

Figure 5.21 Maximum shear force in piers under EL40NSC with a scale factor of 1.0

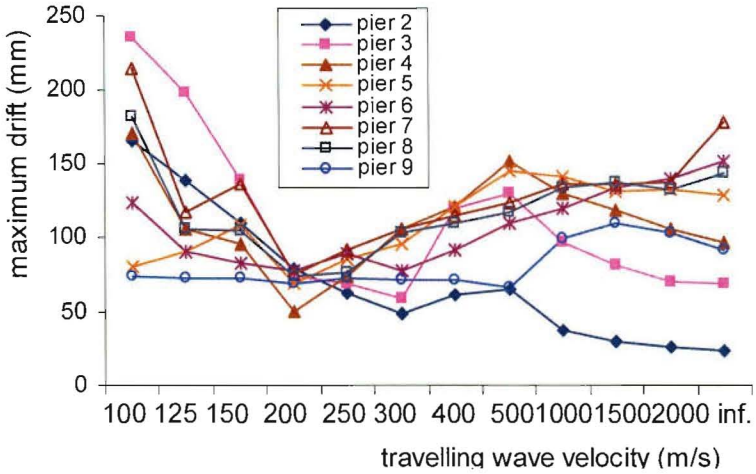

Figure 5.22 Maximum pier drifts under EL40NSC with a scale factor of 2.0

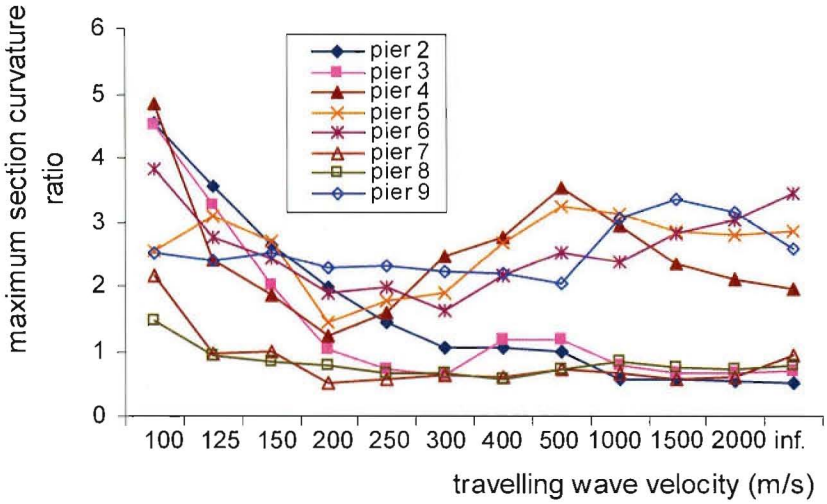

Figure 5.23 Maximum curvature ratios under EL40NSC with a scale factor of 2.0

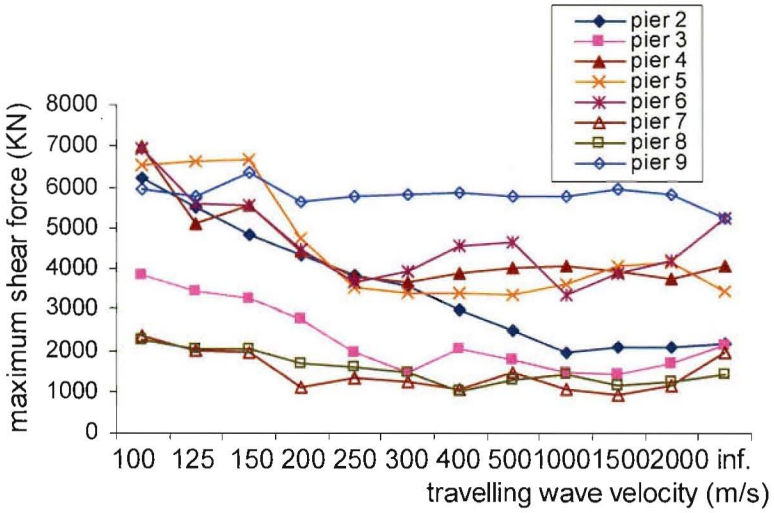

Figure 5.24 Maximum shear force in piers under EL40NSC with a scale factor of 2.0

Different input scale factors were used in order to investigate the responses of the bridge subjected to earthquakes with different intensities. Figures 5.19 to 5.24 show the inelastic responses of Model 1 to the North-South component of El Centro 1940 earthquake record with scale factors of 1.0 and 2.0. For both these cases, it was observed that the variations in the maximum pier drifts with the travelling wave velocity had similar trends to those for the elastic cases. As the travelling wave velocity was increased from 100m/s to infinity, the maximum pier drifts first decreased to a minimum between 200 and 250m/s after which the pier drifts increased again although there were some local variations. Several cases were also seen where the travelling wave cases were more critical than the synchronous case.

The variations of the maximum section curvature ratios of the piers and the maximum pier shear forces with the travelling wave velocity also followed the trends shown for the pier drifts. The variations of the maximum section curvature ratios with the travelling wave velocity were a little different when a different earthquake input scale factor was used because the periods of the bridge vibration were affected by the inelastic behavior of the pier. The maximum section curvature ratios of the piers 2, 3, 7 and 8 did not change much with the travelling wave velocity because pier 2 is the closest pier to the fixed end of the girder and piers 3, 7 and 8 were longer than the others, therefore their dynamic components were smaller than those of the shorter piers. The variations of the maximum pier shear forces with the travelling wave velocity followed a similar pattern to the section curvature ratios.

5.3 The Responses of Other Bridge Models

In order to enable less structure-specific conclusions to be drawn, four additional bridge models with different configurations were analysed and described. Table 5.3 lists the characteristics of the configurations of all five bridge models used in this study.

The elastic responses of Models 2 to 5 to the NS component of the El Centro 1940 earthquake record are shown in Appendix Figures A.1 to A.4. The inelastic responses of Models 2 to 5 to the NS component of the El Centro 1940 earthquake record with an input scale factor of 1.0 are shown in Figures 5.25 to 5.28. Very similar trends to those observed in Model 1 could be seen for the variation of maximum pier drift, section curvature ratio, and maximum shear forces with the propagation velocity of seismic motions in responses of Models 2 to 5, even though the bridge configurations had considerable differences in pier heights and support conditions at abutments.

	The free heights of piers	Boundary conditions
Model 1	6m, 8m, 5m, 5m, 5m, 11m, 11m, 5m for piers 2 to 9	At abutment 1 the superstructure was completely fixed while at abutment 10 the superstructure was supported on the abutment structure through sliding bearings (vertical support only)
Model 2	6m, 8m, 5m, 5m, 5m, 11m, 11m, 5m for piers 2 to 9	At abutment 1 and abutment 10 the superstructure was supported on the abutment structure through sliding bearings (vertical support only)
Model 3	11m for all piers	Same as model 2
Model 4	11m for all piers	Same as model 1
Model 5	5m for all piers	Same as model 2

Table 5.3 The description of bridge models

Model 2 was identical with Model 1 except that abutment 1 was also supported on sliding bearings as was abutment 10. Comparing Figure 5.19 with Figure 5.25, it can be seen that in Model 2 with the modified support at Abutment 1, the maximum drift of pier 2 increased considerably when the travelling wave velocity was higher than 250m/s, but the maximum drifts of other piers were not significantly affected. The increase of the maximum drift of pier 2 was due to the increase of its dynamic component, because of the decrease in transverse stiffness of Abutment 1. Hence the variation of the maximum drift of pier 2 with the travelling wave velocity now had the same trends as for other piers.

Mode	Period (seconds)	Frequency (Hz)	Damping (%)	Characteristics
1	2.09	0.479	5.0	Deck transverse flexure, piers flexure
2	1.343	0.745	5.0	Deck axial, piers flexure/axial
3	1.21	0.826	5.1	Deck transverse flexure, piers flexure
4	0.772	1.296	6.4	Deck transverse flexure, piers flexure
5	0.557	1.795	8.1	Deck transverse flexure, piers flexure
6	0.435	2.299	10.0	Deck vertical flexure, piers flexure/axial

Table 5.4 Natural periods of free vibration and mode shape characteristics of Model 3

Model 3 represented a symmetric bridge structure. Its regularity and relative simplicity made the interpretation of the results easier. The characteristics of the first six modes of Model 3 are given in

Table 5.4. From the responses of Model 3 (in Figures 5.26 and 5.29), it can be seen that for the synchronous case, the distribution of the maximum pier drifts along the bridge was symmetric and similar to the shape of the first mode of vibration of the bridge, but in the asynchronous travelling wave cases the shape of maximum pier drifts were asymmetric and tended to become flatter as the travelling wave velocity decreased. It is an important feature of the response of Model 3 that despite the structural symmetry, the response is unsymmetrical in the travelling wave cases. The response is dependent on the direction of wave travel i.e. which end of the bridge the earthquake comes from. In a design situation you would have to consider wave travel from both directions, and the plots of maximum pier response would become symmetric. For example, in Figure 5.26 the pier 9 response would math the pier 2 response. This 'direction of travel' dependence will also affect the responses of the other irregular bridge models. The unsymmetry of the response of Model 3 also suggests that the first mode of vibration of the bridge dominated the response in the synchronous case, and higher modes were excited by travelling waves in the asynchronous cases as indicated by other researchers (Monti et al. 1996, Tzanetos et al. 1998). For the asynchronous cases, the maximum drifts of piers 2, 3, 4 and 5 were always larger than the maximum drifts of piers 9, 8, 7 and 6 as the travelling wave velocity decreased from 2000 to 250 m/s. This fact indicates that the third mode (second mode for transverse flexure) of vibration of Model 3 played an important role in the responses to asynchronous input motions. The Fourier spectra of the drift of pier 2 (Figures 5.30) also shows that the relative significance of the frequency of the first mode of vibration changed with the travelling wave velocity. The change of the relative significance of the first and third modes in the response meant that the drift of pier 2 reached the maximum value when the travelling wave velocity was 300 m/s as shown in Figure 5.26. From these facts it could be concluded that the local variations of pier drift were attributed to the change in the frequency spectrum of the asynchronous motions with the change in travelling wave velocity.

The third mode of the bridge vibration also played an important role in the variations of the section curvature ratios with the travelling wave velocity. The maximum section curvature ratios of pier 6, 7, 8 and 9 decreased with the decrease in travelling wave velocity until the travelling wave velocity was equal to 150m/s. The maximum section curvature ratios of piers 5, 4, 3 and 2 were different in that, they increased first and then decreased as the travelling wave velocity increased. Hence the variations of the maximum section curvature with the travelling wave velocity were dependent on the mode shapes that were excited by the asynchronous input motions as well.

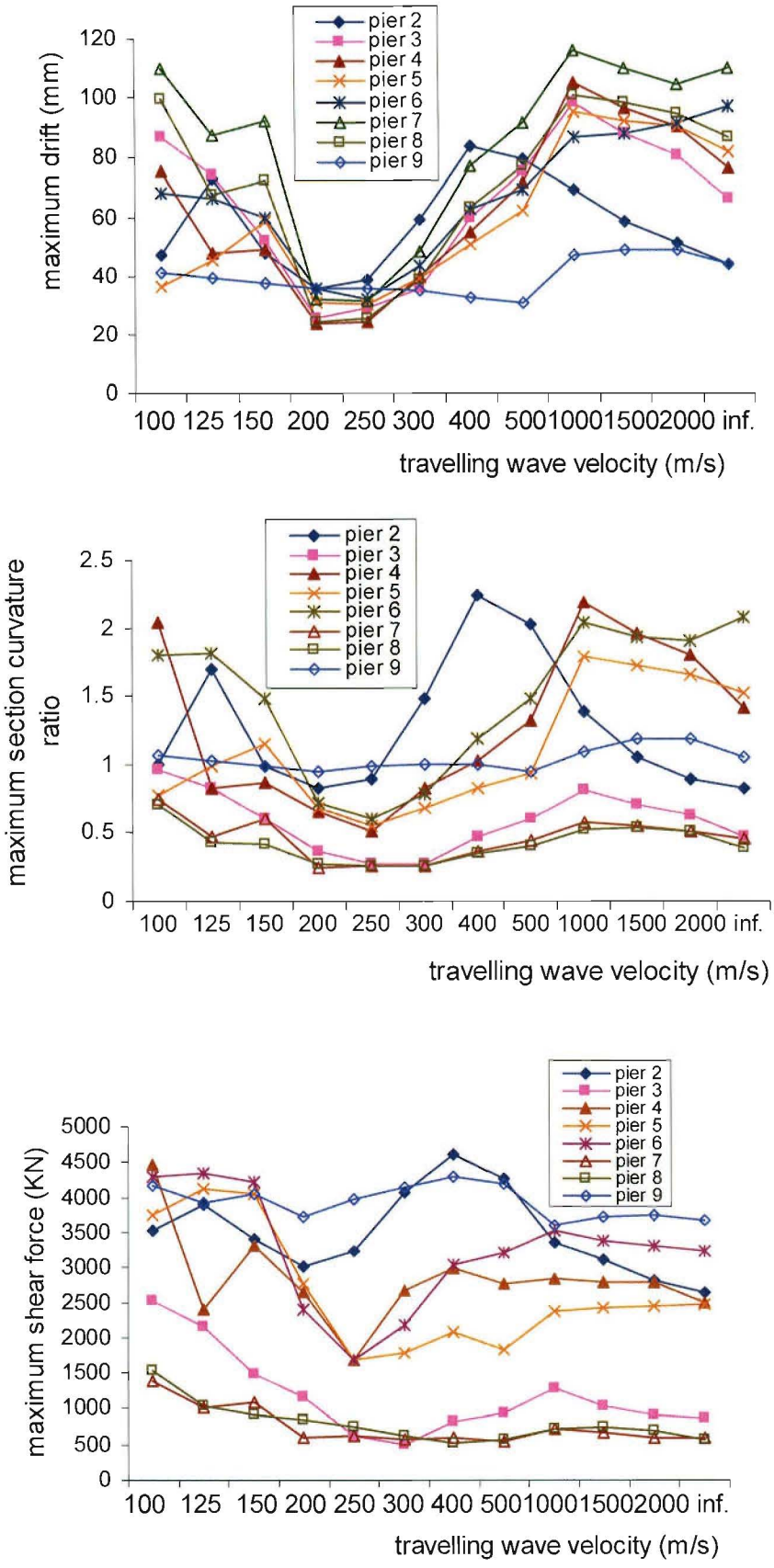

Figure 5.25 The responses of Model 2 to EL40NSC with an input scale factor of 1.0

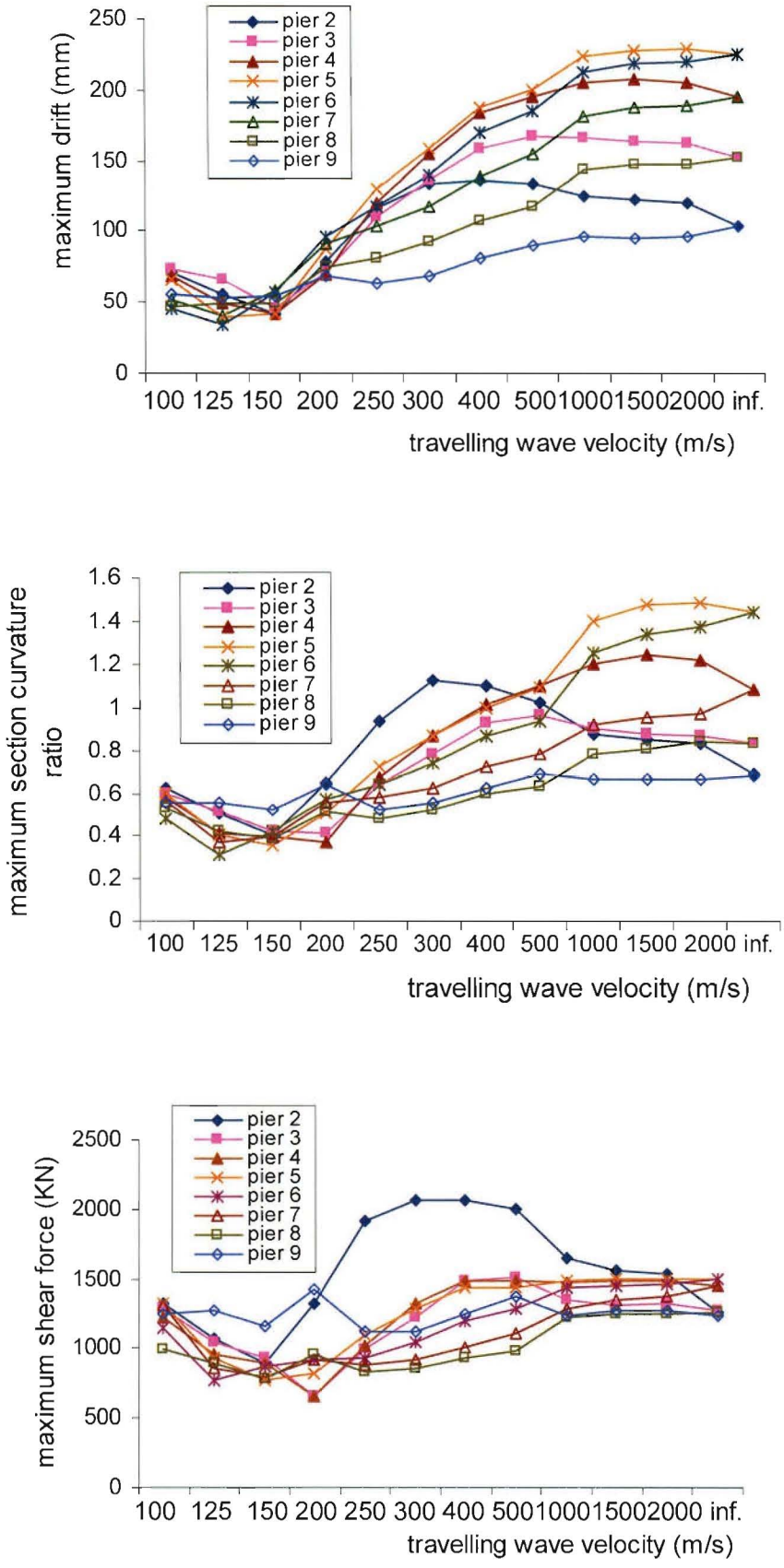

Figure 5.26 The responses of Model 3 to EL40NSC with an input scale factor of 1.0

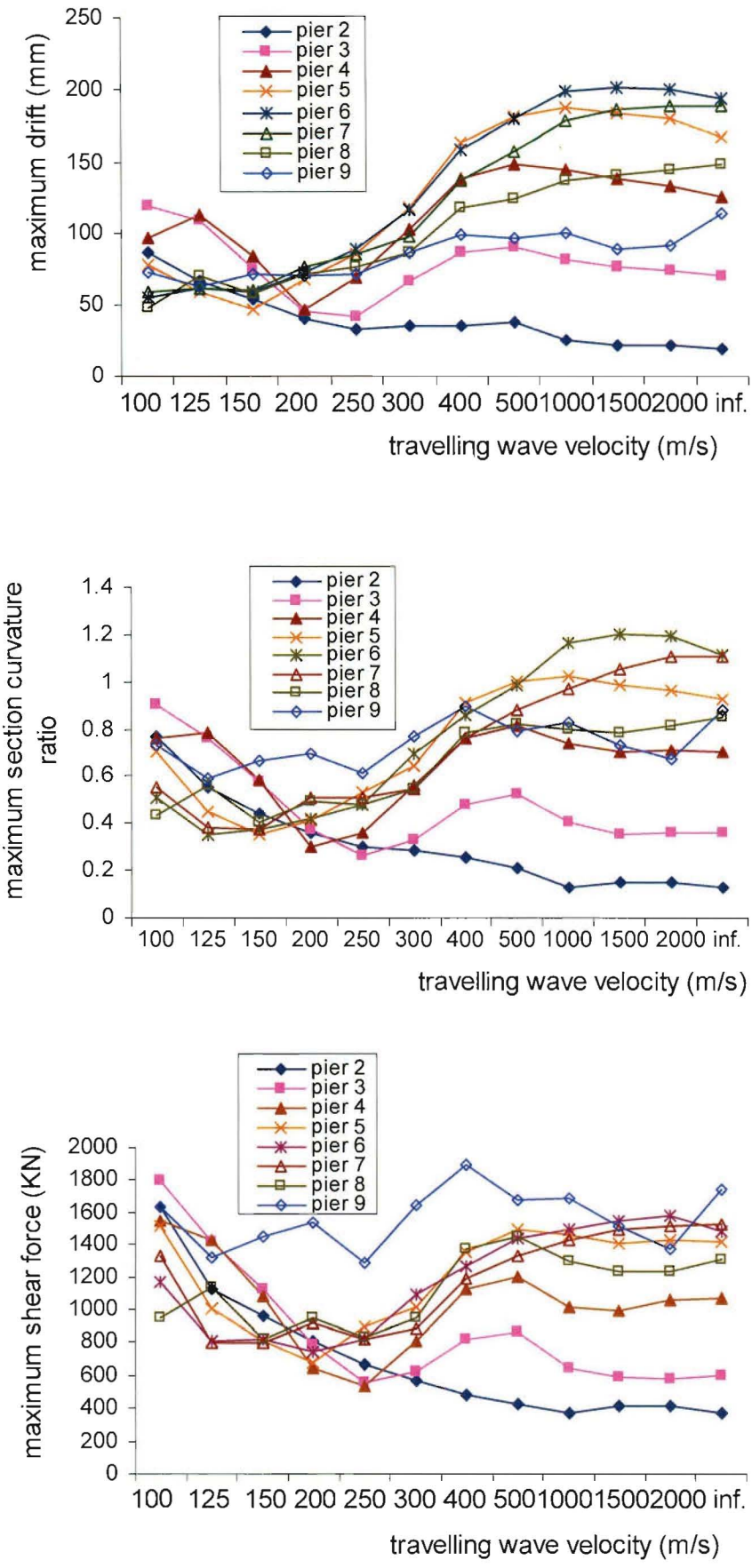

Figure 5.27 The responses of Model 4 to EL40NSC with an input scale factor of 1.0

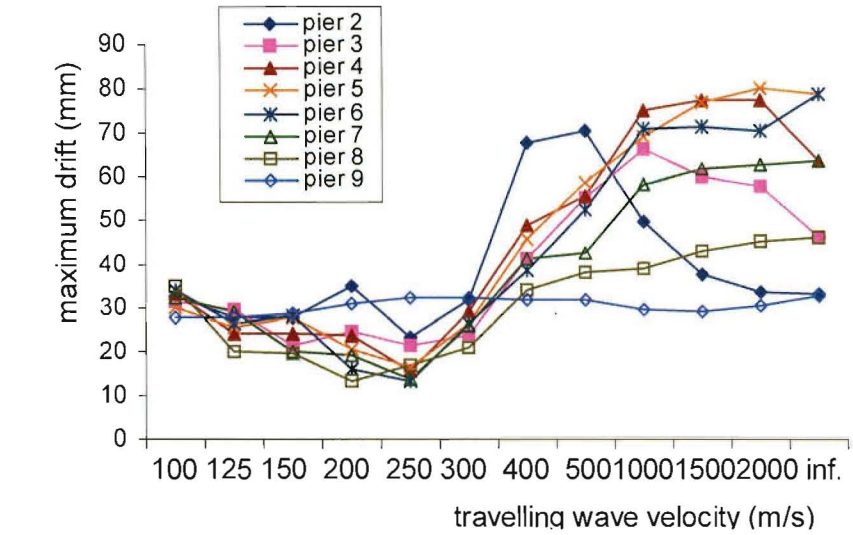

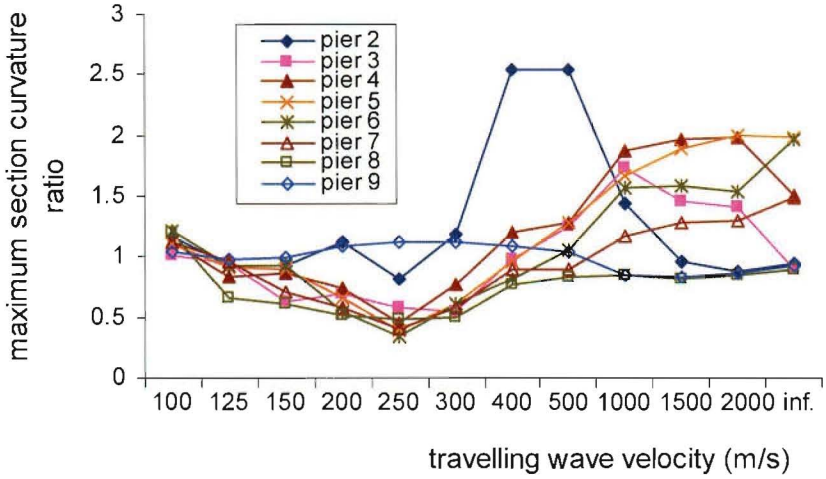

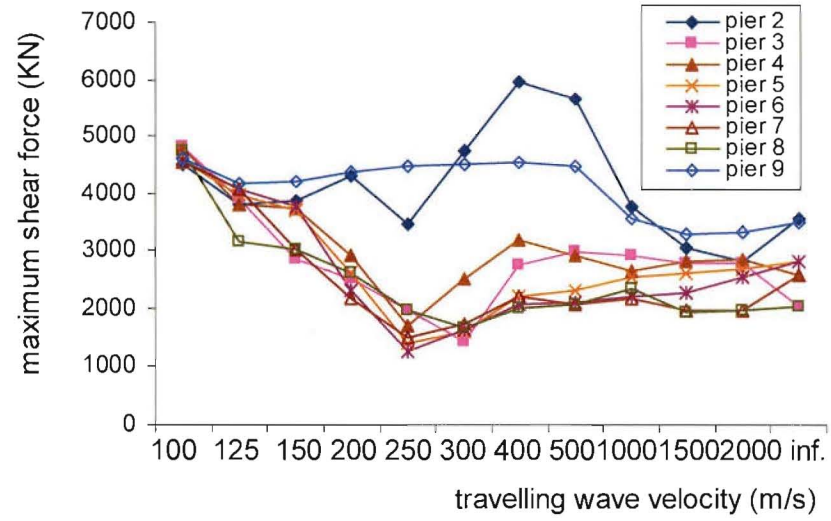

Figure 5.28 The responses of Model 5 to EL40NSC with an input scale factor of 1.0

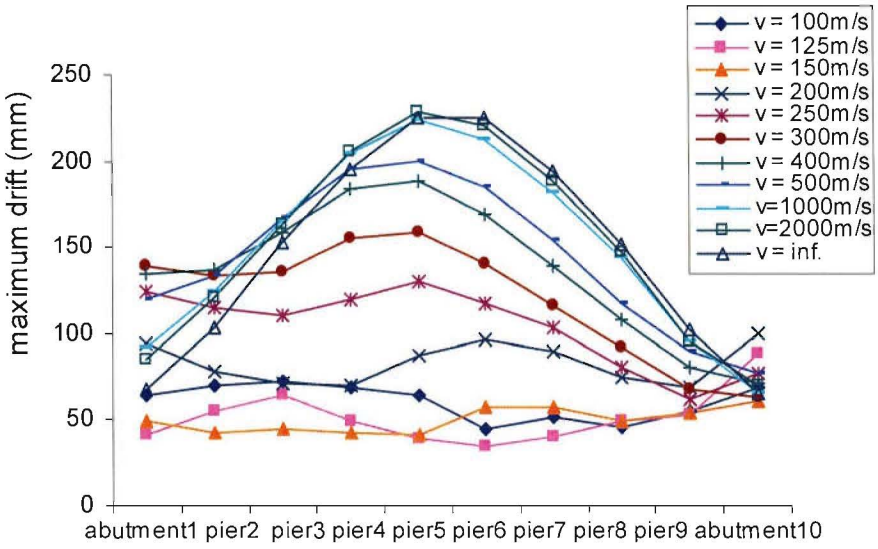

Figure 5.29 Maximum pier drifts of Model 3 to EL40NSC with an input scale factor of 1.0

Model 4 was the same as Model 3, except that Abutment 1 was fixed while Abutment 10 was supported on sliding bearings. Model 5 had the same boundary conditions at the abutments as Model 3, but the free height was 5m for every pier. The responses of Model 4 and Model 5 also showed that the variations of maximum pier drifts, section curvature ratio and maximum shear forces with the propagation velocity had similar trends to those observed in the Models 1 and 3.

It is significant that the magnitude of the travelling wave velocity associated with minimum pier drifts, varied according to the structural stiffness. It was 200 to 250m/s in Models 1 and 2, 150m/s in Model 3, 150 to 200m/s in Model 4, and 250m/s in Model 5. It seems that the stiffer the bridge, the greater is the effect of the pseudo-static component on the responses, therefore the travelling wave velocity associated with minimum pier drifts is greater.

5.4 Summary

In this chapter the travelling wave effect of the spatially variable motions on the seismic response of a long bridges was investigated. The elastic and inelastic responses of five bridge models with different configurations were investigated for both asynchronous and synchronous excitation. Three natural earthquake records were employed as input motions for Model 1, and one earthquake record

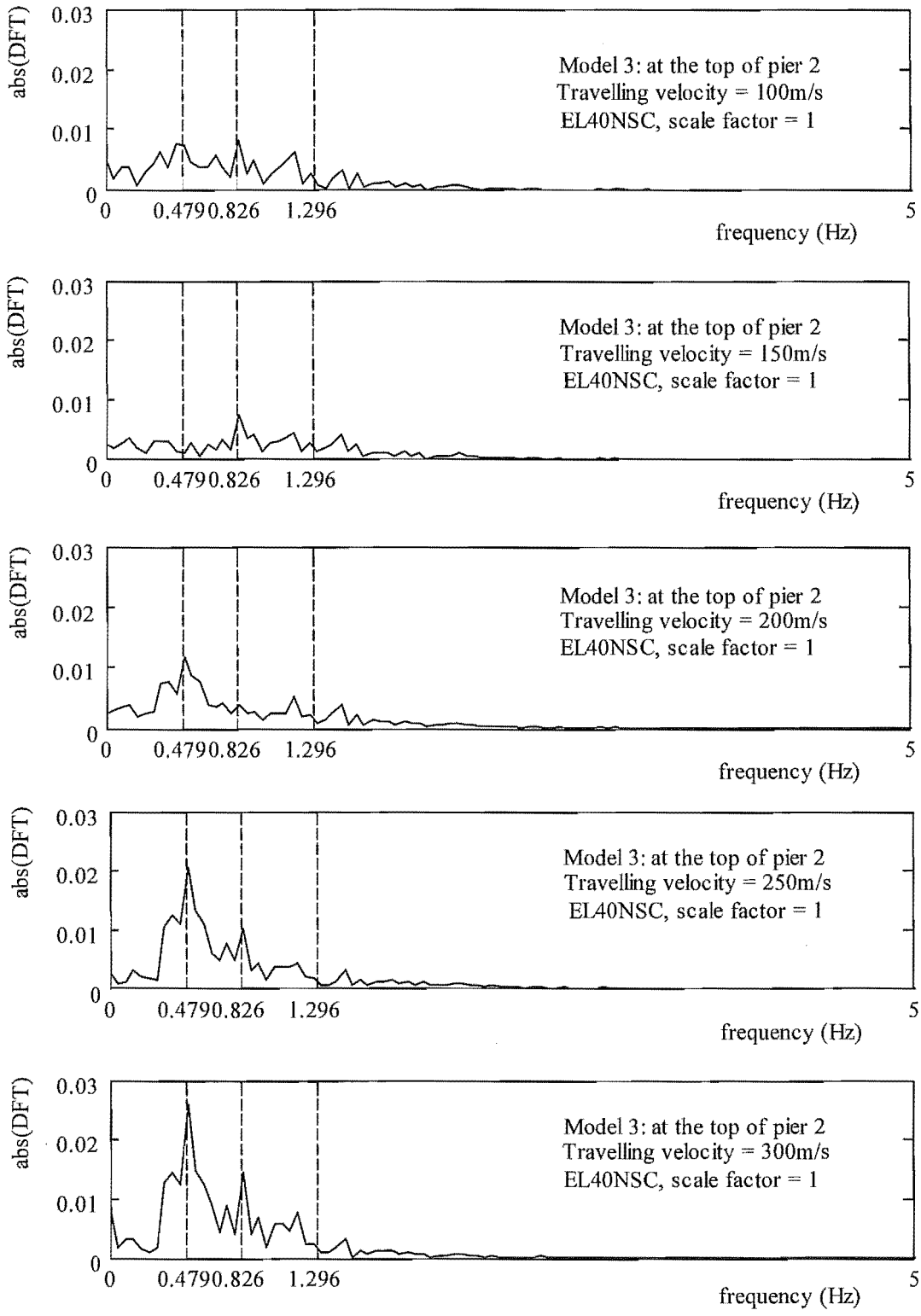

Figure 5.30(a) The Fourier spectrum of the drifts of pier 2 in the responses of Model 3 subjected to EL40NSC

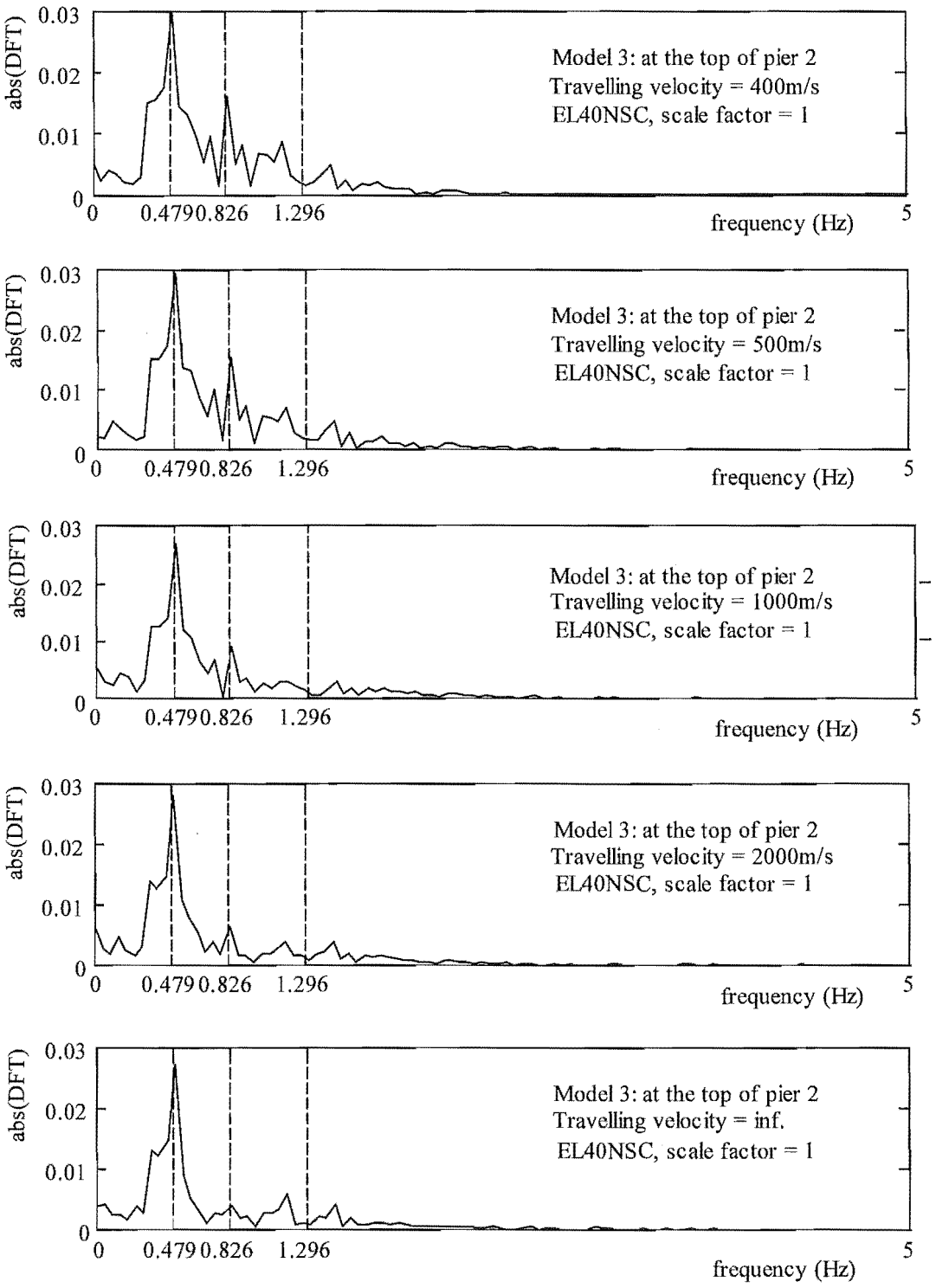

Figure 5.30(b) The Fourier spectrum of the drifts of pier 2 in the responses of Model 3 subjected to EL40NSC

was used for Models 2 to 5. The seismic wave propagation velocity used in the analyses covered a wide range from 100 m/s to 2000 m/s.

Despite the bridge models having different configurations, the variations of maximum pier drifts with the travelling wave velocity followed very similar patterns for all three natural earthquake records for both the elastic and inelastic analyses. Generally, when the travelling wave velocity was between 150 m/s to 250 m/s the maximum pier drift had a minimum value. When the travelling wave velocity was less than 150 m/s, the maximum pier drifts increased as the travelling wave velocity was decreased. When the travelling wave velocity was more than 250 m/s, the maximum pier drifts increased as the travelling wave velocity increased. Several cases were observed in which a response to asynchronous input motion was more critical than that for synchronous input motion.

When the travelling wave velocity was greater than between 150 m/s to 250 m/s, the seismic responses were dominated by the dynamic components that increased considerably with the increase in travelling wave velocity and were close to the responses of the synchronous cases when the travelling velocity was greater than 1000 m/s. When the travelling wave velocity was less than between 150 m/s to 250 m/s, the seismic responses were dominated by the pseudo-static components that increased as the travelling wave velocity decreased. The pseudo-static component arises because of the differential displacements between adjacent pier supports, which increased considerably with the decrease of the travelling wave velocity. The local variations of the maximum pier drifts with the travelling wave velocity were attributed to the change of the spectra of the average input motions with the travelling wave velocity.

The variations of the maximum section curvature ratio and maximum shear forces with the travelling wave velocity in the asynchronous cases followed the same trends as did the maximum pier drift, and were also dependent on the mode shapes that were excited by the asynchronous input motions.

From the responses of Models 3 and 5 (regular symmetric structures), the 'direction of travel' dependence of the responses to travelling waves can be noticed. The response is dependent on the direction of wave travel i.e. which end of the bridge the earthquake comes from. In a design situation the engineer would have to consider wave travel from both directions.

Comparing the results of Models 1 to 5, it was obvious that the bridges with irregularity of pier heights or shorter (stiffer) pier enhanced the pseudostatic component of the response. In the responses to 1940 El Centro earthquake (EL40NSC), the maximum pier drift of pier 2 in the travelling wave case reached to 5.4, 2.2 and 1.3 times that reached in the synchronous motion case for Models 1 (varying pier heights), 5 (regular, 'shorter' pier) and 3 (regular 'taller' piers) respectively.

From the designer point of view, it is important that for Models 3 and 5 (regular symmetric structures) the maximum pier drifts and section curvature ratios of most piers (including those with the greatest demands in the synchronous case) is very little changed for wave velocities down to 1000m/s and then decreases significantly with decreasing wave velocity. Only the maximum shear forces in piers in the travelling wave cases could be greater than those in the synchronous case because as the pier height decrease the pseudostatic component of the response increases. In the responses to EL40NSC, the maximum shear forces in most piers (except pier 2) of Model 3 ('taller' piers) in the travelling wave case were smaller than those in the synchronous case but the maximum shear forces in all piers of Model 5 ('shorter' piers) in the lower travelling wave velocity case were greater than those in the synchronous cases by a factor of 1.2 to 2.

Comparing the responses of Models 3 and 5 to EL40NSC with input scale factor of 1.0, and the responses of Models 1 and 4 to EL40NSC with input scale factor of 1.0, it can be seen that the influences of the wave passage effect on the responses of long bridges heavily depends on the stiffness of long bridges. The stiffer the bridge, the greater the influence of the wave passage effect on the responses of long bridges. The synchronous motion case still generally dominates the design demands when the long bridges are flexible enough (such as Model 3). Hence if foundation compliance was included in the bridge models, the wave passage effect should have less influence on the responses of long bridges.

Comparing the responses of same models (for Models 1 ~ 5) to EL40NSC with different input scale factors, it can be seen that the same conclusions are generally valid for inelastic response as for elastic response.

CHAPTER 6

THE EFFECTS OF THE COMBINED GEOMETRIC INCOHERENCE AND WAVE PASSAGE ON THE SEISMIC RESPONSE OF LONG BRIDGES

6.1 Introduction

The previous chapter dealt with the wave-passage effect on the seismic response of bridges. However, as mentioned in Chapter 1, three phenomena are responsible for the spatial variations of seismic ground motions: (1) the wave passage effect, (2) the geometric incoherence effect, and (3) the local site effect. In this chapter, the combined geometric incoherence and wave passage effects on the seismic response of bridges are investigated.

It was assumed that the seismic input motions acted in the transverse direction of the bridge and propagated from Abutment 10 to Abutment 1 in the bridge longitudinal direction as before. For the asynchronous input motions, a natural earthquake record was specified at Abutment 10 and the conditionally simulated time-histories were used at other pier supports and Abutment 1. The simulated time-histories were generated using the wave dispersion method (proposed in Chapter 3) with the condition of knowing the earthquake record at Abutment 10. Three natural earthquake records, the El Centro 1940 and the Northridge 1994 NS components, and one from the Mexico City (1985) earthquake, were employed at Abutment 10 as the specified earthquake motion.

In generating the input motions, different values of the dispersion factor d (= 1, 10, 50 and 100) were used to simulate different levels of the geometric incoherence effect, and the travelling wave velocities used covered the range from 100m/s to 2000m/s as in the previous chapter. As mentioned in Chapter 3, the dispersion factor d represents the degree of correlation between the points of the random field, and depends on the site geological and topographical conditions. The larger the value of d, the higher the degree of correlation expected. A set of input motions and their spectra are shown in Figure 6.1; these were generated using a dispersion factor of d = 10, propagation velocity $v = 200\,m/s$, and the El Centro earthquake NS component record specified at Abutment 10. Three different bridge models, Models 1, 3, and 5 (see Table 5.3), were used to investigate the geometric incoherence effect in conjunction with the wave passage effect on the seismic responses. The

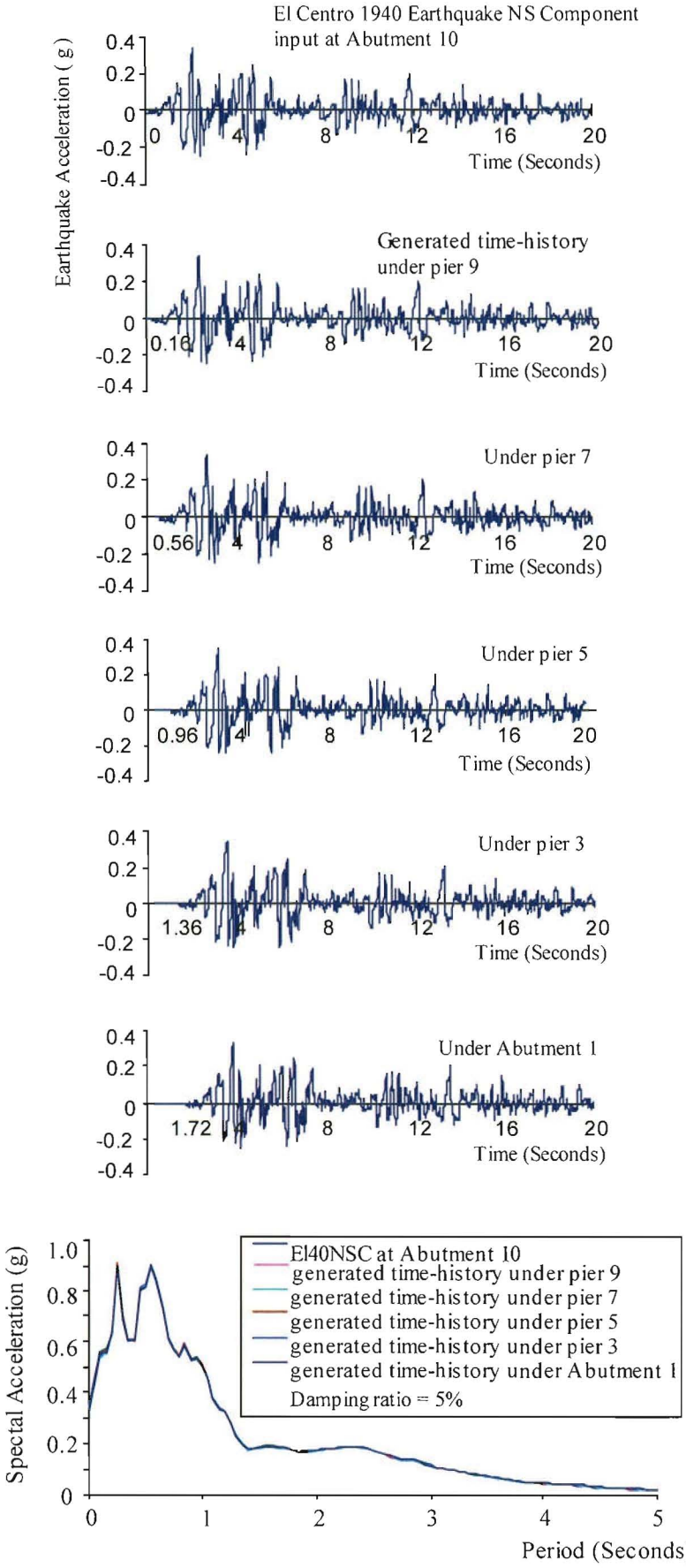

Figure 6.1 A set of input motions with EL40NSC at Abutment 10, v = 200m/s and d = 10, and their spectra

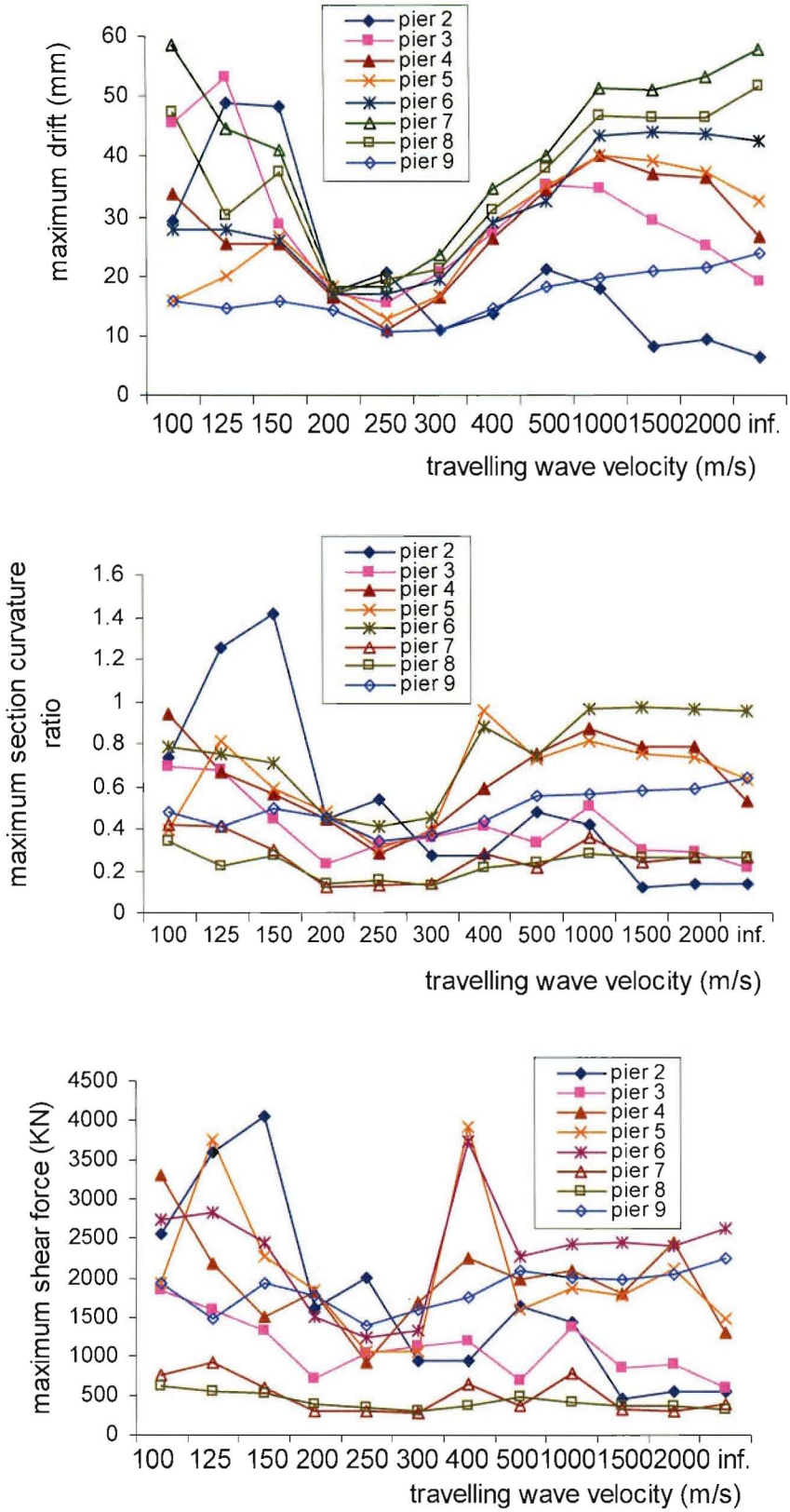

Figure 6.2 The responses of Model 1to EL40NSC with an input scale factor of 0.5 at Abutment 10 and the generated time-histories at the other supports with a dispersion factor d = 100

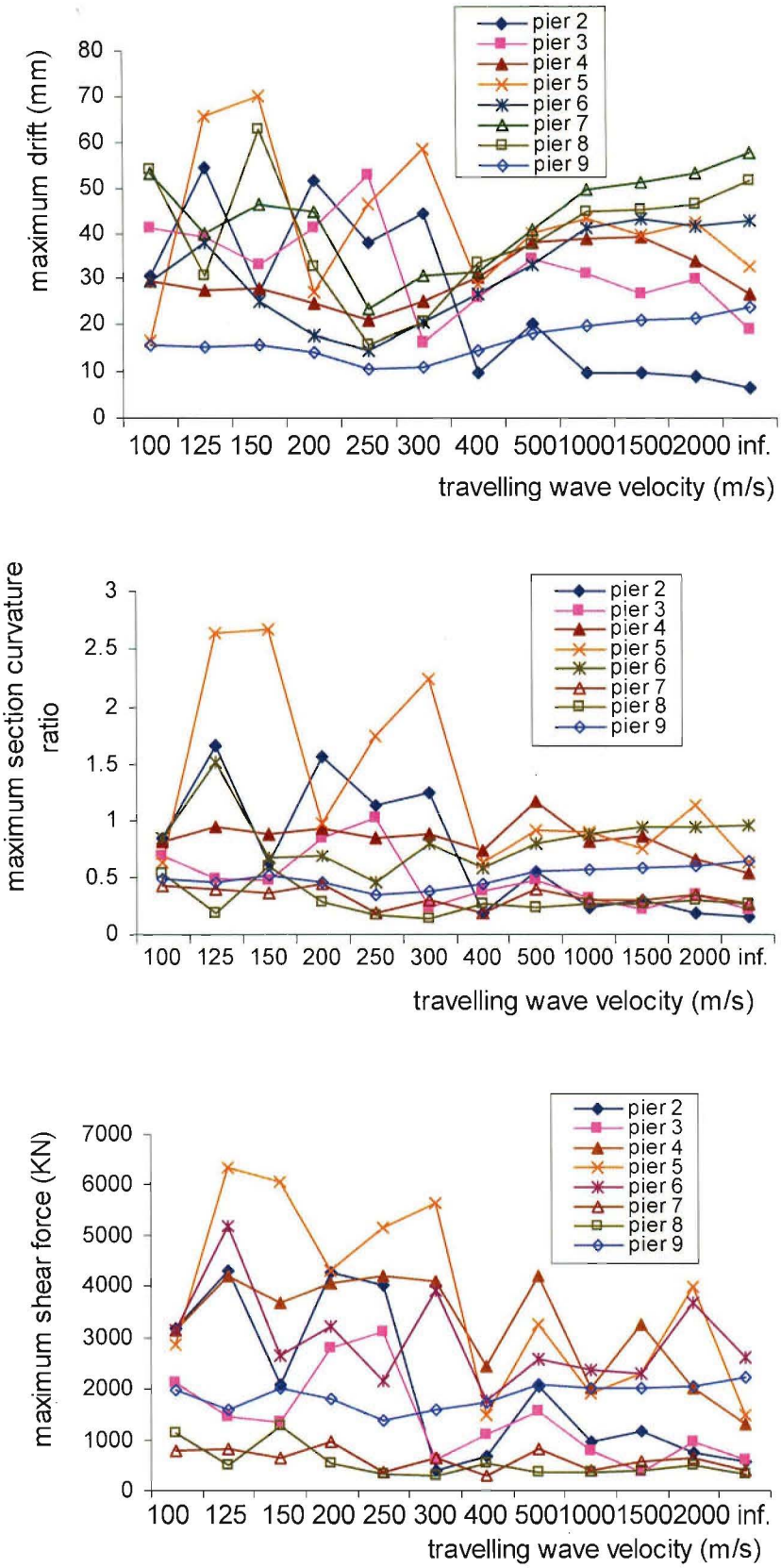

Figure 6.3 The responses of Model 1to EL40NSC with an input scale factor of 0.5 at Abutment 10 and the generated time-histories at the other supports with a dispersion factor d = 50

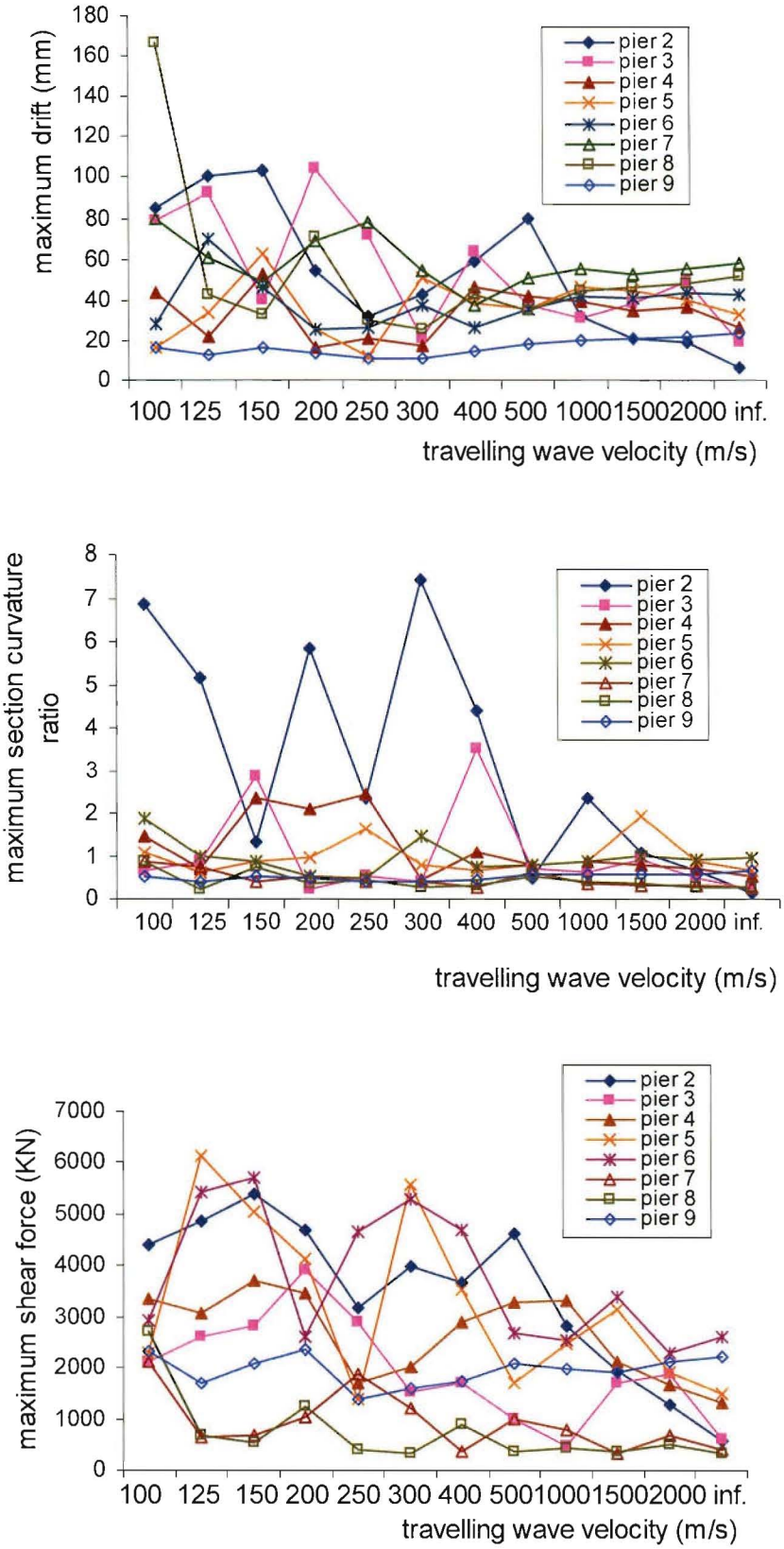

Figure 6.4 The responses of Model 1to EL40NSC with an input scale factor of 0.5 at Abutment 10 and the generated time-histories at the other supports with a dispersion factor d = 10

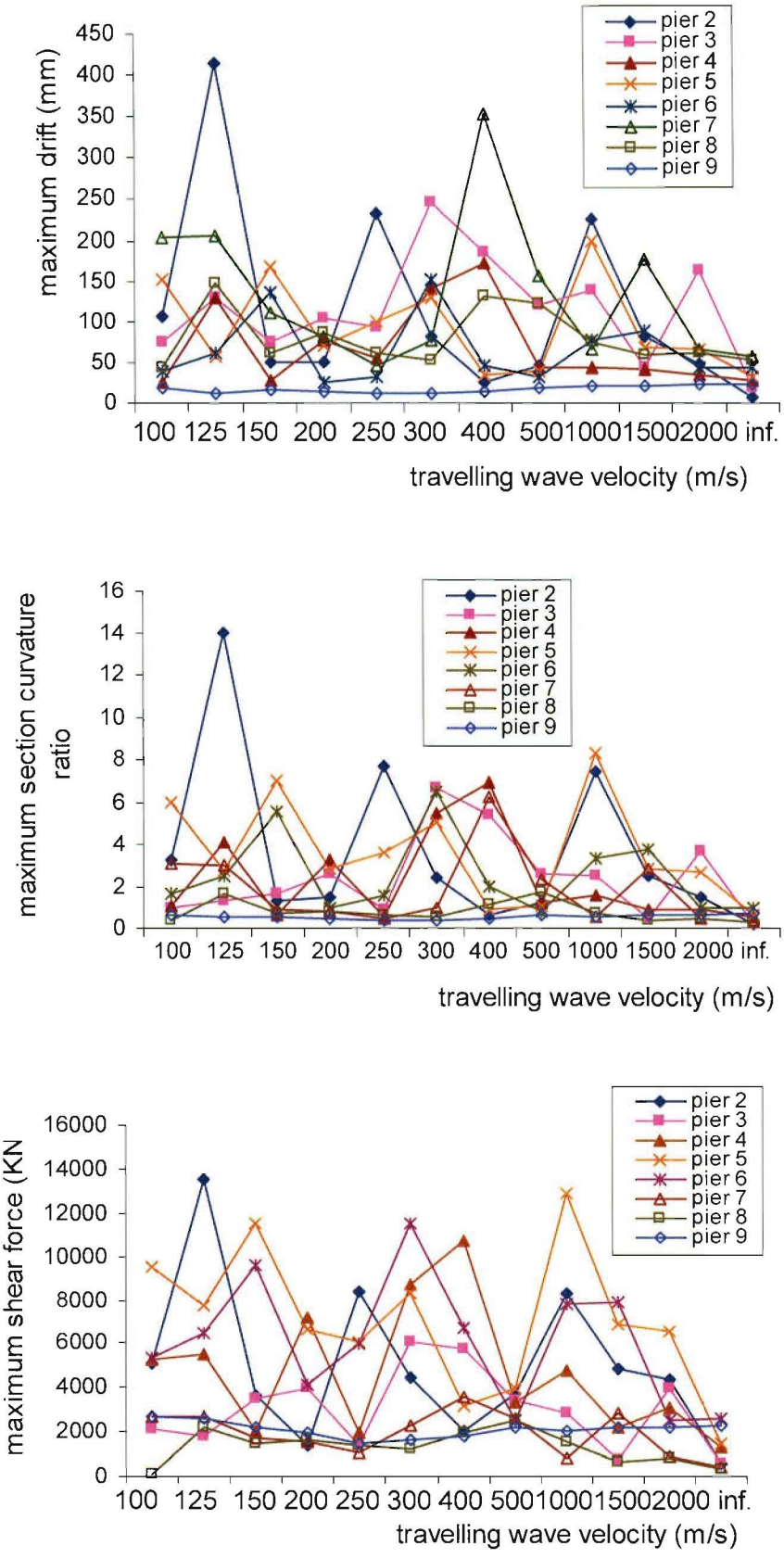

Figure 6.5 The responses of Model 1to EL40NSC with an input scale factor of 0.5 at Abutment 10 and the generated time-histories at the other supports with a dispersion factor d = 1

investigated response parameters, as in Chapter 5, were the maximum pier drifts, the maximum pier shear forces and the maximum section curvature ratios of the piers. The cases, in which the combined geometric incoherence and wave passage effects were considered, are referred to as wave dispersion cases in the sections that follow.

6.2 The Responses of Model 1

The responses of Model 1 subjected to the NS component of the El Centro 1940 earthquake record with an input scale factor of 0.5 at Abutment 10 and the generated time-histories at other piers and Abutment 1 are shown in Figures 6.2 to 6.5. For the cases with the least dispersion (d = 100), the variations of the maximum pier drifts with the travelling wave velocity followed similar trends to those in the travelling wave effect only cases (compare Figure 6.2 with Figure 5.6), though there were some minor local variations from the earlier travelling wave cases. However, the corresponding values of the maximum pier drift in these wave dispersion cases and the travelling wave cases were slightly different and these differences increased for piers 2 and 3 (compare Table 6.1 with Table 5.2).

For the cases with the greatest dispersion (d = 1), the variations of the maximum pier drifts with the travelling wave velocity (Figure 6.5) did not follow any observable trend and were very different from the travelling wave cases (see Table 6.4).

The results for the cases with a dispersion factor of 50 and 10 showed a mixed behaviour. When the travelling wave velocity was greater than 400 (for d = 50) or 1000m/s (for d = 10) the response varied with the travelling wave velocity in the same way as the travelling wave cases, but when the travelling wave velocity was less than these, there was not any noticeable trend (see Figures 6.3 and 6.4). The differences in response between the wave dispersion cases and the travelling wave cases increased with the decrease of the dispersion factor d (see Tables 6.2 and 6.3).

The variations in maximum section curvature ratios and maximum pier shear forces with travelling wave velocity were similar to the drift response. However, even for the cases with least dispersion (d = 100) the local variations of maximum pier shear forces with travelling wave velocity were quite different from those without wave dispersion.

When the Model 1 was subjected to either the NS component of Northridge 1994 earthquake record with input scale factor of 0.15, or the record from Mexico City 1985 earthquake with

wave travelling velocity (m/s)	*pier2*		*pier3*		*pier4*		*pier5*		*pier6*		*pier7*		*pier8*		*pier9*	
	drift (*mm*)	$\frac{drift(d)}{drift(v)}$	*drift* (*mm*)	$\frac{drift(d)}{drift(v)}$	*drift* (*mm*)	$\frac{drift(d)}{drift(v)}$	*drift* (*mm*)	$\frac{drift(d)}{drift(v)}$	*drift* (*mm*)	$\frac{drift(d)}{drift(v)}$	*drift* (*mm*)	$\frac{drift(d)}{drift(v)}$	*drift* (*mm*)	$\frac{drift(d)}{drift(v)}$	*drift* (*mm*)	$\frac{drift(d)}{drift(v)}$
100	29.2	0.93	45.5	1.34	33.7	1.05	15.6	0.99	27.6	1	58.6	1.01	47.2	0.92	15.8	1.01
125	48.8	1.86	53.2	1.38	25.4	1.19	19.9	1.05	27.6	0.97	44.6	1.1	30.1	1.01	14.5	1
150	48.3	1.96	28.6	0.87	25.4	1.04	26.5	1.04	26	1.1	40.9	1.01	37.5	1.17	15.6	0.99
200	17.3	1.09	16.9	1.16	16.2	1.47	18.0	1.25	17.0	0.98	18.2	1.01	17	1.05	14.2	1
250	20.4	1.61	15.3	1.11	10.8	0.95	12.7	0.98	16.8	1.09	18.1	1.12	19.3	1.29	10.6	1.01
300	10.9	0.94	20.4	1.89	16.2	0.98	16.6	1.03	19.2	0.97	23.4	1.06	21.2	1.04	10.8	1
400	13.5	1.16	27.1	1.04	26.2	1	29	1.05	28.9	1.11	34.7	1.07	31.1	1.12	14.4	0.99
500	21.1	1.34	35.4	1.01	34.3	1.06	34.9	1	32.7	0.99	40.2	1.01	37.9	1.08	18	1.01
1000	17.9	1.95	34.7	1.18	40.2	1.04	40.1	0.96	43.3	1.02	51.2	1.09	46.7	1.05	19.7	0.99
1500	8.1	0.98	29.3	1.07	37	1.02	39.1	0.97	43.9	1.01	50.9	1.01	46.4	1.01	20.9	1
2000	9.5	1.17	24.9	0.95	36.4	1.05	37.4	0.96	43.6	1	53.2	1.02	46.4	1	21.5	1
synchronously	6.4	1	19	1	26.5	1	32.5	1	42.5	1	57.6	1	51.5	1	23.7	1

Table 6.1 Maximum relative pier drifts in Model 1 reached with a dispersion factor of 100

Note: drift (d) refers to the cases in which the geometric incoherence and wave passage effects were considered.
drift (v) refers to the cases in which the wave passage effect was considered only.

wave travelling velocity (m/s)	*pier*2		*pier*3		*pier*4		*pier*5		*pier*6		*pier*7		*pier*8		*pier*9	
	drift (mm)	$\frac{drift(d)}{drift(v)}$	*drift* (mm)	$\frac{drift(d)}{drift(v)}$	*drift* (mm)	$\frac{drift(d)}{drift(v)}$	*drift* (mm)	$\frac{drift(d)}{drift(v)}$	*drift* (mm)	$\frac{drift(d)}{drift(v)}$	*drift* (mm)	$\frac{drift(d)}{drift(v)}$	*drift* (mm)	$\frac{drift(d)}{drift(v)}$	*drift* (mm)	$\frac{drift(d)}{drift(v)}$
100	30.7	0.98	41	1.21	29.4	0.92	16.6	1.06	29.5	1.07	53.2	0.92	53.9	1.05	15.5	0.99
125	54.4	2.07	39.1	1.02	27.4	1.29	65.5	3.45	37.7	1.32	40	0.98	30.7	1.03	15.2	1.05
150	27.1	1.1	33.1	1.01	27.6	1.13	69.9	2.73	24.9	1.05	46.1	1.14	62.9	1.97	15.6	0.99
200	51.3	3.23	41	2.81	24.7	2.25	27	1.88	17.7	1.02	44.5	2.47	32.7	2.02	14.2	1
250	37.9	2.98	52.7	3.82	20.9	1.83	46.1	3.57	14.4	0.94	23.4	1.45	15.5	1.03	10.5	1
300	44.1	3.8	16.1	1.49	24.9	1.5	58.3	3.62	20.6	1.04	30.5	1.39	20.7	1.01	10.8	1
400	9.7	0.84	25.6	0.98	30	1.15	28.6	1.04	26.4	1.01	31.2	0.96	33.2	1.2	14.5	0.99
500	20.2	1.29	34.3	0.98	37.8	1.17	39.8	1.14	32.8	0.99	40.5	1.02	37.5	1.07	18	1.01
1000	9.7	1.05	30.8	1.05	38.7	1	43.2	1.04	41	0.97	49.4	1.05	44.6	1	19.8	1
1500	9.8	1.18	26.4	0.96	38.8	1.07	39.3	0.98	43	0.99	51.1	1.01	45.1	0.98	21.1	1
2000	8.7	1.07	29.6	1.13	33.9	0.98	42.4	1.09	41.5	0.96	53	1.01	46.3	1	21.4	0.99
synchronously	6.4	1	19	1	26.4	1	32.5	1	42.5	1	57.6	1	51.5	1	23.7	1

Table 6.2 Maximum relative pier drifts in Model 1 reached with a dispersion factor of 50

Note: drift (d) refers to the cases in which the geometric incoherence and wave passage effects were considered.
drift (v) refers to the cases in which the wave passage effect was considered only.

wave travelling velocity (m/s)	*pier2*		*pier3*		*pier4*		*pier5*		*pier6*		*pier7*		*pier8*		*pier9*	
	drift (mm)	$\frac{drift(d)}{drift(v)}$	*drift* (mm)	$\frac{drift(d)}{drift(v)}$	*drift* (mm)	$\frac{drift(d)}{drift(v)}$	*drift* (mm)	$\frac{drift(d)}{drift(v)}$	*drift* (mm)	$\frac{drift(d)}{drift(v)}$	*drift* (mm)	$\frac{drift(d)}{drift(v)}$	*drift* (mm)	$\frac{drift(d)}{drift(v)}$	*drift* (mm)	$\frac{drift(d)}{drift(v)}$
100	84.6	2.7	79	2.33	43.2	1.35	16.2	1.03	27.8	1.01	79.3	1.37	166.1	3.25	16.2	1.03
125	100.6	3.83	92.1	2.39	21.7	1.02	33.6	1.77	69.5	2.43	60.5	1.49	42.6	1.43	13.1	0.9
150	103.3	4.2	39.7	1.21	52.9	2.17	62.1	2.43	46.2	1.95	49.2	1.22	33	1.03	16.1	1.02
200	54.5	3.43	104.2	7.14	16.3	1.48	24.9	1.73	25.2	1.45	69.1	3.84	70.4	4.35	14	0.99
250	31.5	2.48	71.8	5.2	20.5	1.8	12.1	0.94	26.4	1.71	77.6	4.82	29.5	1.97	10.5	1
300	42.5	3.66	20.5	1.9	17.3	1.04	50.7	3.15	37	1.87	54.6	2.48	25.2	1.24	10.8	1
400	59.2	5.1	63.1	2.43	46	1.76	37.6	1.37	26.6	1.02	37	1.14	42.6	1.54	14.6	1
500	79.9	5.09	36.7	1.05	41.8	1.29	35.4	1.01	34.9	1.06	51	1.28	34.6	0.99	17.8	0.99
1000	31.7	3.45	30.6	1.04	38.9	1.01	46.3	1.11	41.4	0.98	54.8	1.17	44.1	0.99	19.7	0.99
1500	20.5	2.47	37.6	1.37	34.1	0.94	44	1.09	40.8	0.94	52.4	1.04	46.2	1.01	20.4	0.97
2000	19.4	2.4	49	1.88	36.2	1.05	40.2	1.03	43.1	0.99	55.1	1.05	47.6	1.02	21.9	1.01
synchronously	6.4	1	19	1	26.4	1	32.5	1	42.5	1	57.6	1	51.5	1	23.7	1

Table 6.3 Maximum relative pier drifts in Model 1 reached with a dispersion factor of 10

Note: drift (d) refers to the cases in which the geometric incoherence and wave passage effects were considered.
drift (v) refers to the cases in which the wave passage effect was considered only.

wave travelling velocity (m/s)	*pier*2		*pier*3		*pier*4		*pier*5		*pier*6		*pier*7		*pier*8		*pier*9	
	drift (*mm*)	$\frac{drift(d)}{drift(v)}$	*drift* (*mm*)	$\frac{drift(d)}{drift(v)}$	*drift* (*mm*)	$\frac{drift(d)}{drift(v)}$	*drift* (*mm*)	$\frac{drift(d)}{drift(v)}$	*drift* (*mm*)	$\frac{drift(d)}{drift(v)}$	*drift* (*mm*)	$\frac{drift(d)}{drift(v)}$	*drift* (*mm*)	$\frac{drift(d)}{drift(v)}$	*drift* (*mm*)	$\frac{drift(d)}{drift(v)}$
100	106.1	3.39	75.6	2.23	24.9	0.78	151.9	9.68	39	1.41	202.8	3.51	43.9	0.86	17.2	1.1
125	414.2	15.75	128.8	3.35	129.8	6.09	55.9	2.94	60.5	2.12	206.1	5.06	147.9	4.96	11.1	0.77
150	49.4	2.01	73.9	2.25	26.1	1.07	166.3	6.5	135.1	5.7	110.7	2.75	60.8	1.9	15	0.95
200	50	3.14	104.9	7.18	78	7.09	70.4	4.89	25	1.44	82.2	4.57	85.6	5.28	14.3	1.01
250	232.1	18.28	92	6.67	53.9	4.73	100.2	7.77	30.6	1.99	45.8	2.84	60.9	4.06	10.6	1.01
300	82.5	7.11	246.3	22.81	140.2	8.45	129.1	8.02	151.4	7.65	77.4	3.52	52.7	2.58	10.9	1.01
400	25.9	2.23	186.5	7.17	171.1	6.56	34.2	1.24	45.7	1.75	353.3	10.87	130.5	4.71	13.7	0.94
500	44.5	2.83	119.4	3.4	43.7	1.35	38.7	1.11	32	0.97	155.8	3.91	122.7	3.5	18.7	1.04
1000	225.3	24.49	138.9	4.72	42.5	1.1	199.8	4.79	77.7	1.84	64.8	1.38	75.4	1.69	19.8	1
1500	82.5	9.94	42	1.53	40.9	1.12	67.5	1.68	88.9	2.05	176.1	3.48	58	1.26	19.9	0.95
2000	48.3	5.96	161.9	6.2	33.7	0.97	66.2	1.7	43	0.99	64.6	1.23	60.2	1.29	22.1	1.02
synchronously	6.4	1	19	1	26.4	1	32.5	1	42.5	1	57.6	1	51.5	1	23.7	1

Table 6.4 Maximum relative pier drifts in Model 1 reached with a dispersion factor of 1

Note: drift (d) refers to the cases in which the geometric incoherence and wave passage effects were considered.
drift (v) refers to the cases in which the wave passage effect was considered only.

input scale factor of 0.5 at Abutment 10, and the conditionally generated time-histories at other piers and Abutment 1, similar observations were made for the variations of the maximum pier drifts, the maximum section curvature ratios of the piers and the maximum pier shear forces with traveling wave velocity as shown in Appendix Figures A.5 to A.9.

The dynamic components of the responses showed insignificant differences between the dispersion cases and the travelling wave cases because their acceleration spectra at different supports were almost identical (for example see Figure 6.1), following the rule adopted in the generation of the seismic motions. Any differences in the total responses between the dispersion cases and the travelling wave cases can be attributed to the differences in the pseudo-static components. The pseudo-static component consists of two parts, resulting from the geometric incoherence effect and wave passage effect, when these are considered together in the spatial variations of the input motions. Although the changes in the accelerograms between the adjacent supports were very small, the differential displacements between the adjacent supports caused by these changes are not necessarily small, resulting in additional stresses in the structure. Figure 6.6 shows the maximum differential displacements between the adjacent supports for d =10, when subjected to the NS component of the El Centro 1940 earthquake record with an input scale factor of 0.5. Comparing Figure 6.6 with Figure 5.9, it can be seen that the differential displacements between the adjacent supports caused by the geometric incoherence effect were quite large in these cases. Note also that from Figure 5.9, the wave passage effect is nearly a lower bound to the results in Figure 6.6. It follows thatThe pseudo-static component due to the geometric incoherence effect could be more important than that caused by the wave passage effect as the dispersion factor decreases. Furthermore, the differential displacements between the adjacent supports caused by the geometric incoherence effect are random and are therefore unpredictable so the pseudo-static component caused by the geometric incoherence effect is also likely to be unpredictable.

In the case with the least dispersion (d = 100), there were higher correlations between the two accelerograms at the adjacent pier supports so the differential displacements between the adjacent supports caused by the variations in the accelerograms were small. Hence the pseudo-static components caused by the geometric incoherence effect had little effect on the total responses, and the variations of the maximum pier drifts with the travelling wave velocity had similar trends to those for the no wave dispersion cases. However, the corresponding values of the maximum pier drifts for the dispersion cases and the travelling wave cases were different because of the pseudo-static components caused by the geometric

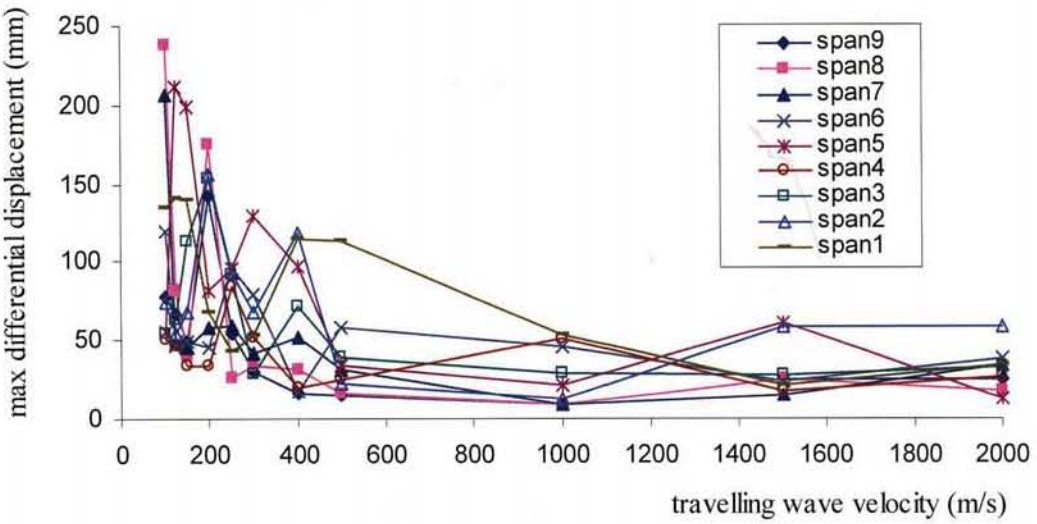

Figure 6.6 Maximum differential displacements between adjacent pier supports in Model 1 when EL40NSC input was at Abutment 10 and the generated time-histories input at the other supports for a dispersion factor d = 10

incoherence effect in the dispersion cases.

In the case of the greatest dispersion (d = 1), the differential displacements between the adjacent supports caused by the variations of accelerograms were large. The pseudo-static component caused by the geometric incoherence effect was large and dominated the total responses over the whole range of the travelling wave velocities. In these cases, the variations of the maximum pier drifts with the travelling wave velocity and the distribution of the maximum pier drift along the bridge are unpredictable because the differential displacements between the adjacent supports caused by the variations of accelerograms are unpredictable and no noticeable trend is apparent.

For those cases with dispersion factors of 50 and 10, the pseudo-static component caused by the geometric incoherence effect increased considerably as the travelling wave velocity decreased. When the travelling wave velocity was greater than 400 (for d = 50) or 1000m/s (for d = 10), the variations of accelerograms between two pier supports were not so large, therefore the pseudo-static component caused by the geometric incoherence effect did not have a significant effect on the total response, and the variations of the responses with the travelling wave velocity followed the similar trends to the cases with a dispersion factor of 100. When the travelling velocity was less than 400 (for d = 50) or 1000m/s (for d = 10), the variations of accelerograms between two pier supports became large so that the pseudo-static

component caused by the geometric incoherence effect dominated the total response, therefore the variations of the responses with the travelling wave velocity were more random, like those in the cases with dispersion factor of 1.

Comparing the responses of the wave dispersion cases (in Tables 6.1 to 6.4) with the corresponding responses for the travelling wave cases of Model 1 (in Table 5.2), it is noticeable that when the geometric incoherence effect and wave passage effect are considered together the responses are generally larger than those reached when only the wave passage effect is taken into account. The maximum pier drifts increase with the increase in the wave dispersion. This indicates that the pseudo-static component caused by the geometric incoherence effect has a very significant influence on the total response in the wave dispersion cases and this influence increases considerably with the decrease of the dispersion factor. Furthermore, in the travelling wave cases, all the piers remain elastic when the input scale factor of 0.5 is used for the input seismic motion of the El Centro 1940 earthquake NS component record, but some piers behave inelastically in the wave dispersion cases even for the cases with d = 100 and the maximum section curvature of the piers and The maximum pier shear forces also increases considerably with the decrease of the dispersion factor.

Figure 6.7 shows the Fourier spectra of the pier drift of the pier 7 in the wave dispersion cases with a dispersion factor of 10. It can be observed that the relative significance of the frequency of the first mode of vibration of the bridge changes with the travelling wave velocity as in travelling wave cases. As indicated by the absolute value of the amplitude of the discrete Fourier transform with zero frequency, the pseudo-static component would be an important part of the total response over the whole range of the travelling wave velocity used in this study.

6.3 The Responses of Other Bridge Models

The bridge Models 3 and 5 employed in Chapter 5 also were used here to analyze their responses to asynchronous input motions where the geometric incoherence and wave-passage effects are considered together. The responses of Model 3 subjected to the El Centro 1940 NS earthquake component with an input scale factor of 1 at Abutment 10 and the generated time-histories at other piers and Abutment 1, are shown in Figures 6.8 to 6.10. The responses of Model 5 subjected to the same seismic motion at Abutment 10 and the generated time-histories at other piers and abutment 1 are shown in Appendix Figures A.10 to A.12.

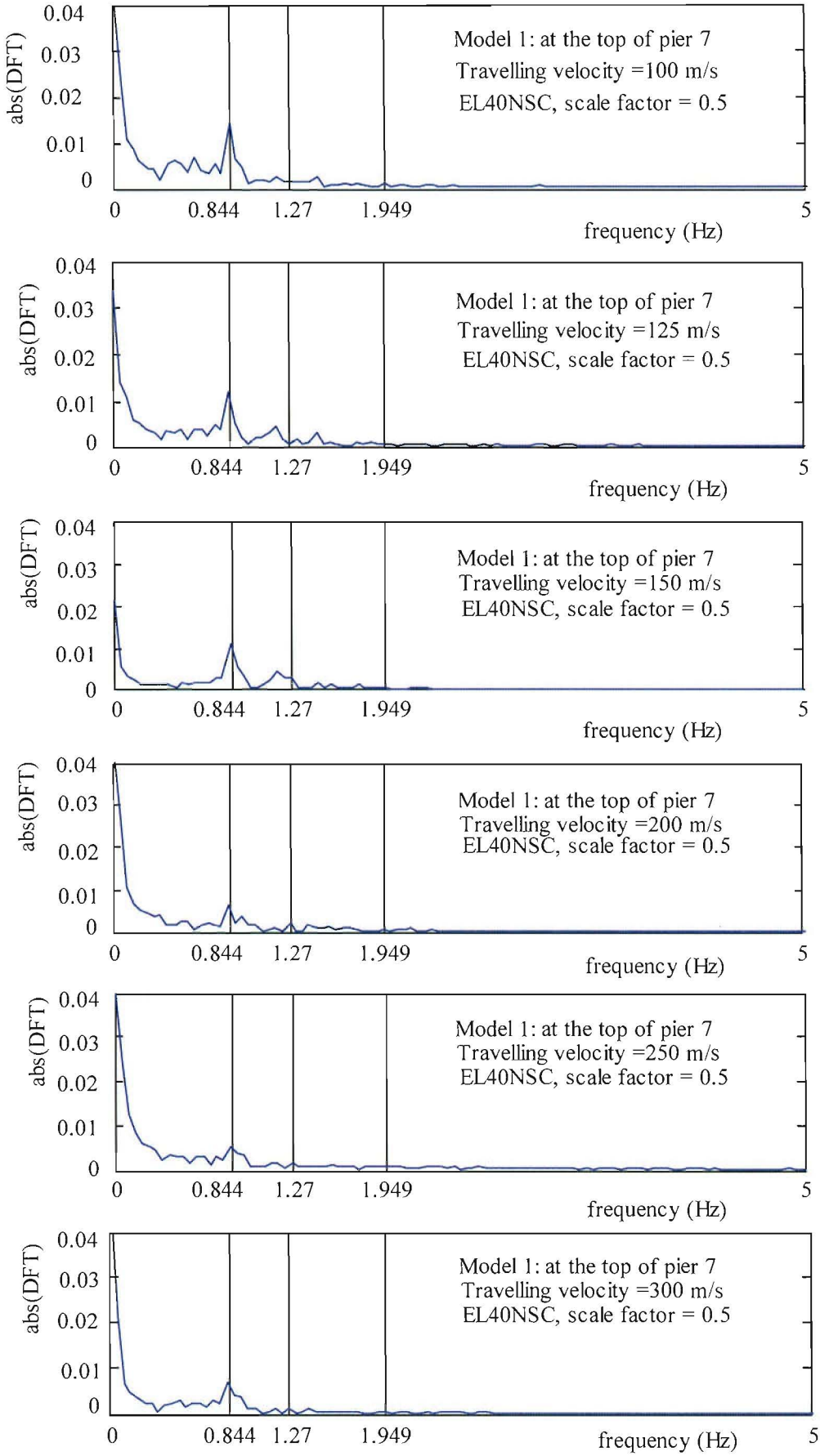

Figure 6.7 (a) The Fourier spectra of the displacement of the top of Pier 7 in model 1

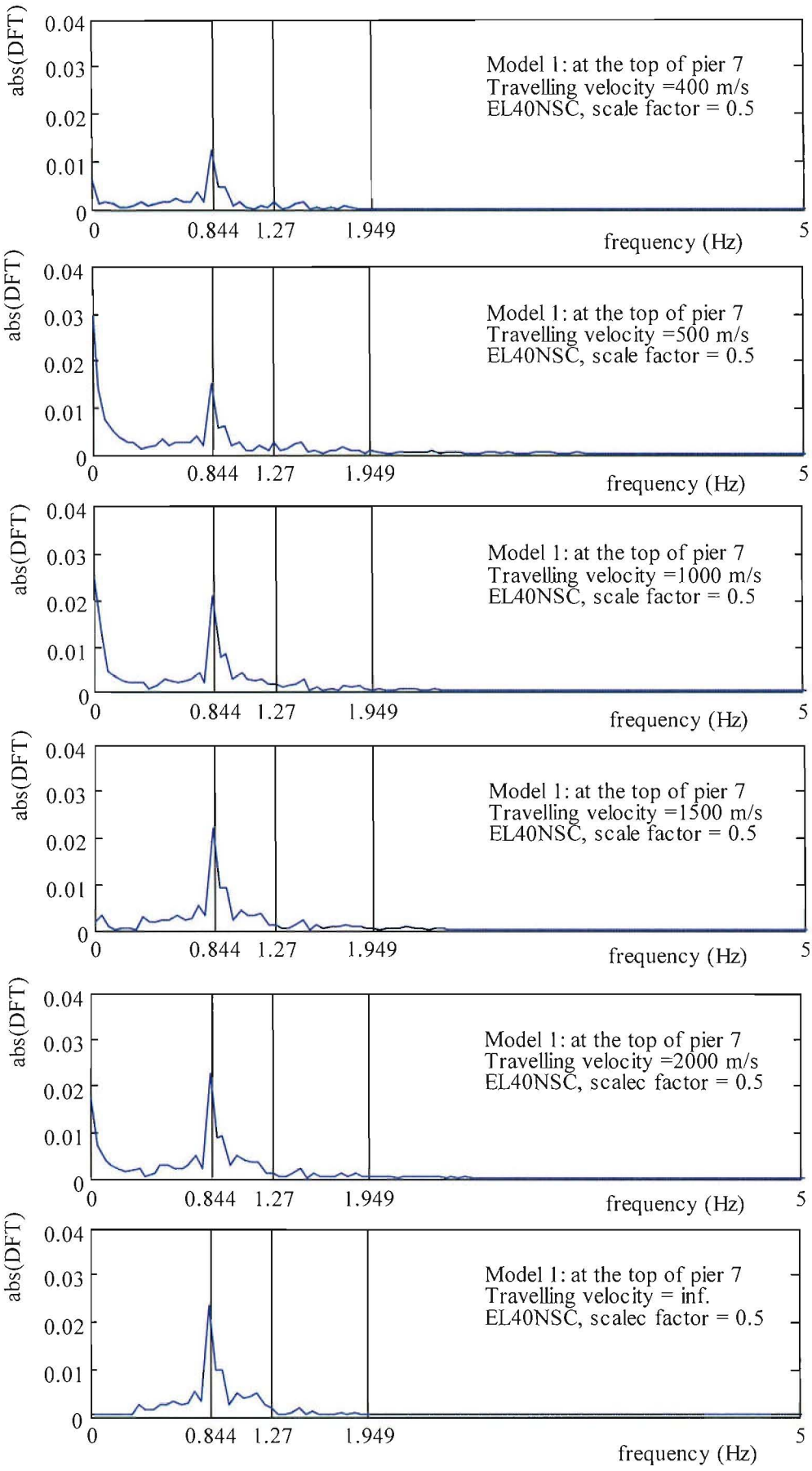

Figure 6.7 (b) The Fourier spectra of the displacement of the top of Pier 7 in model 1

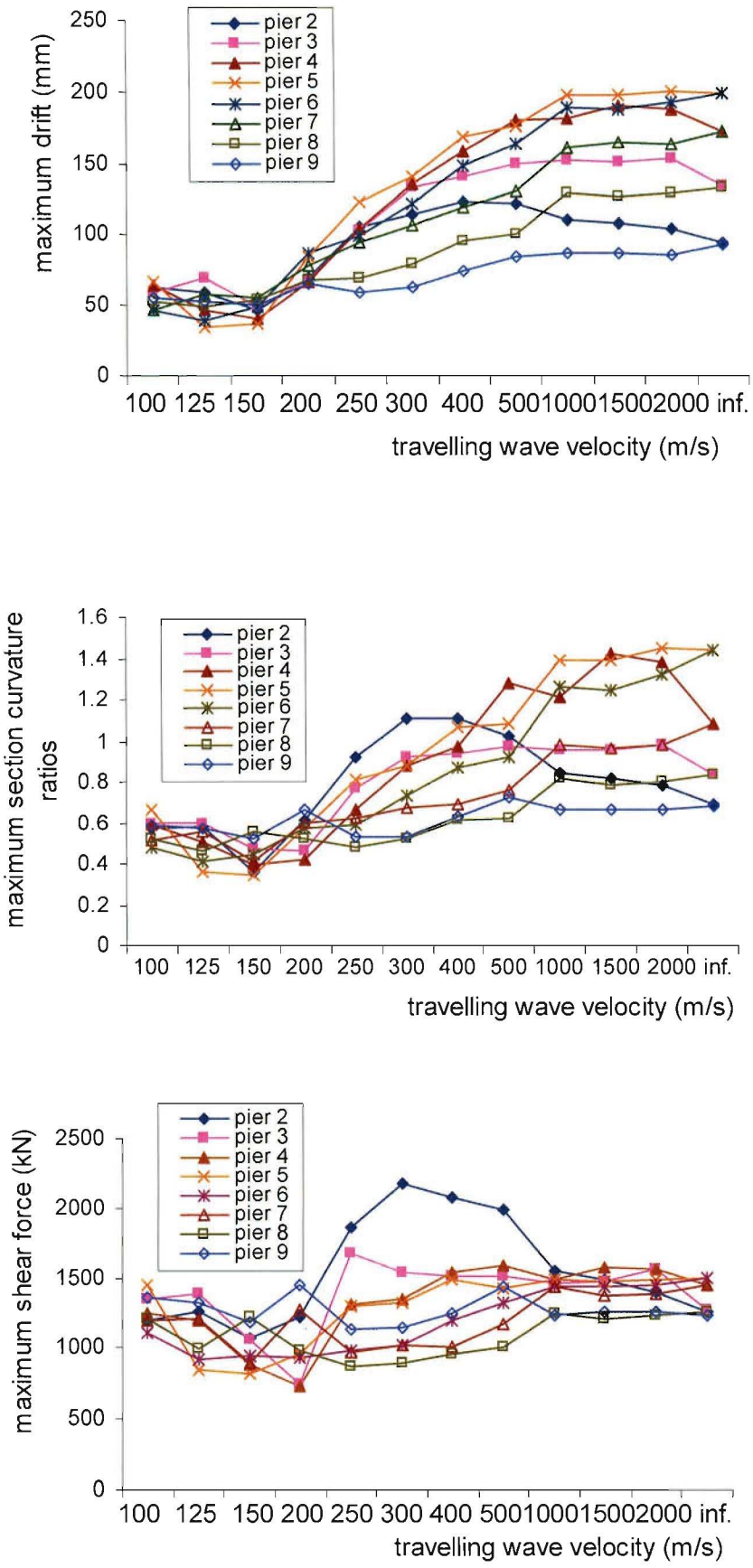

Figure 6.8 The responses of Model 3 to EL40NSC with an input scale factor of 1.0 and a dispersion factor d = 100

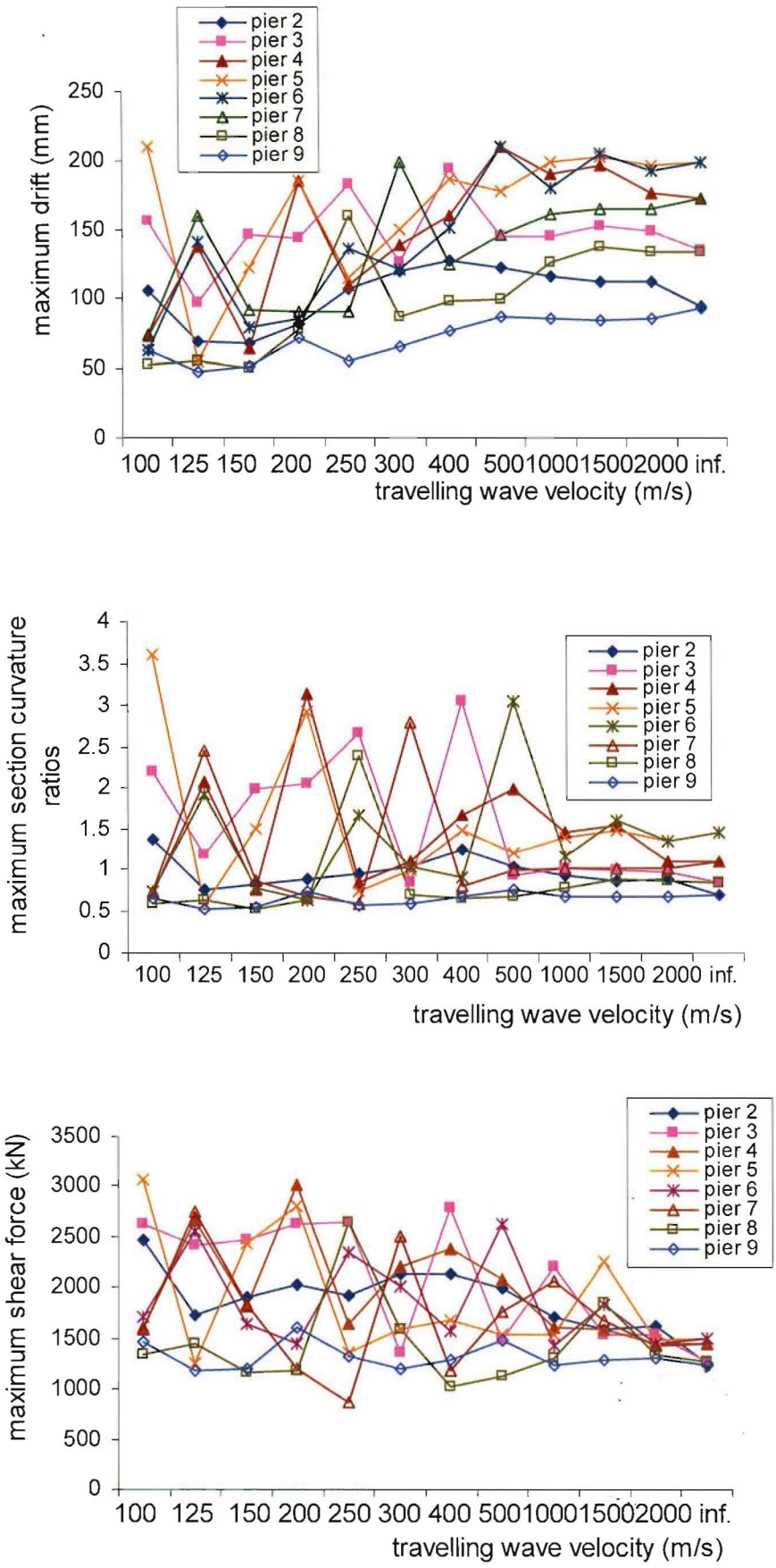

Figure 6.9 The responses of Model 3 to EL40NSC with an input scale factor of 1.0 and a dispersion factor d = 10

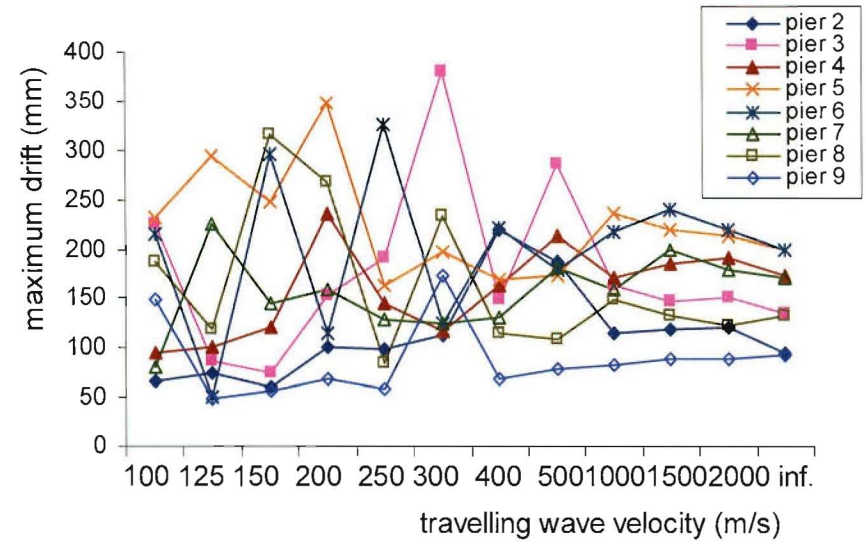

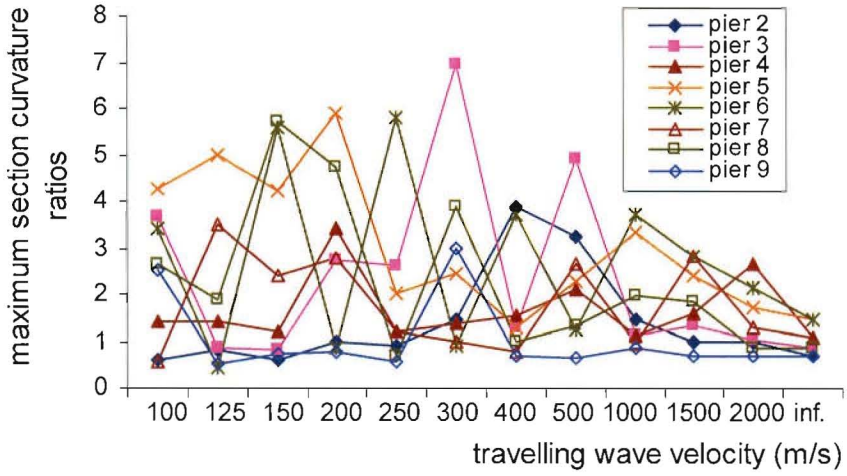

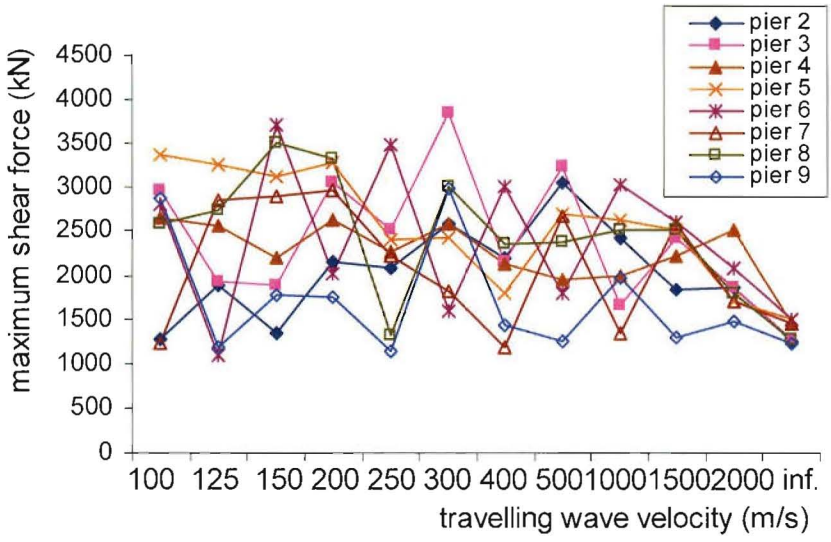

Figure 6.10 The responses of Model 3 to EL40NSC with an input scale factor of 1.0 and a dispersion factor d = 1

Despite the fact that the bridge Models 3 and 5 had very different configurations from Model 1, the variations of the maximum pier drifts, the maximum section curvature ratios of the piers and the maximum pier shear forces with the travelling wave velocity had very similar trends to that observed in the wave dispersion cases for Model 1. For the cases with least dispersion (d = 100), the variations of the responses with the travelling wave velocity were very similar to those cases where only the travelling wave effect was considered. For the cases with the greatest dispersion (d = 1), the variations of the responses with the travelling wave velocity did not follow any noticeable trend. For the cases with a dispersion factor of 10, the results showed a mixed behaviour. When the travelling wave velocity was greater than 1000m/s the variations of the maximum pier drifts with the travelling wave velocity followed similar trends to those in the cases with d = 100, but when the travelling wave velocity was less than 1000m/s the variations of the maximum pier drifts with the travelling wave velocity did not follow any observable trends.

Figures 6.11 to 6.13 show the distribution of the maximum pier drifts along the bridge for Model 3 using different dispersion factors. From the responses of this simple and symmetric model it was easy to see the pattern of the distribution of the maximum pier drift along the bridge. For the cases with the least dispersion (d = 100), the distributions of the pier drifts were very similar to those in the wave travelling cases. As shown in Figure 6.11, the shapes of the distributions of the maximum pier drifts tended to become flatter as the travelling wave velocity was decreased. This indicated that for the cases with the least dispersion the dynamic component dominated the responses over the wide range of velocities. For the cases with the greatest dispersion (d = 1) the distributions of the maximum pier drifts were relatively unpredictable. It is suggested that the pseudo-static component caused by the geometric incoherence effect dominated the response of the bridge in these cases because the differential displacements between adjacent pier bases due to the geometric incoherence effectwas random. For the cases with a dispersion factor of 10, the component of the response which dominated the total response was really dependent on the travelling wave velocity.

6.4 Summary

This chapter dealt with the seismic responses of a long bridge subjected to spatial variable input motions in which both the geometric incoherence and wave passage effects were considered. Three bridge models with different configurations and three natural earthquake records were used in the analyses. Similar patterns of the responses were obtained even

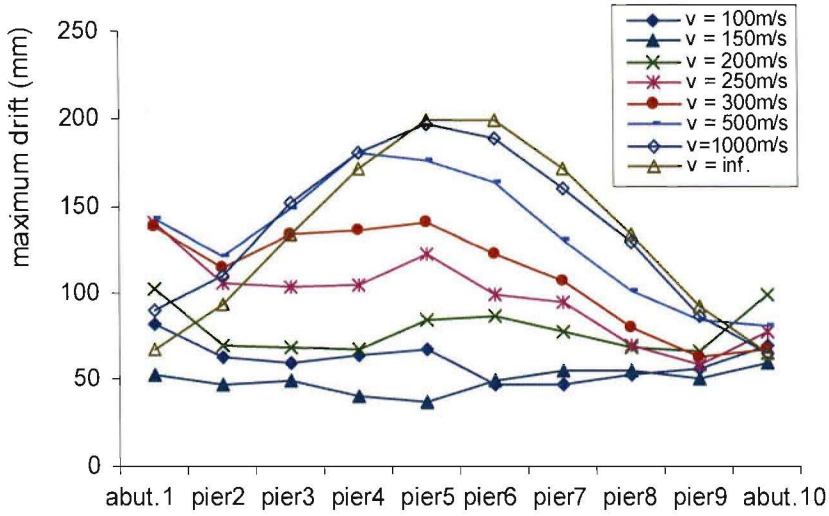

Figure 6.11 The maximum pier drifts of Model 3 to EL40NSC with d=100

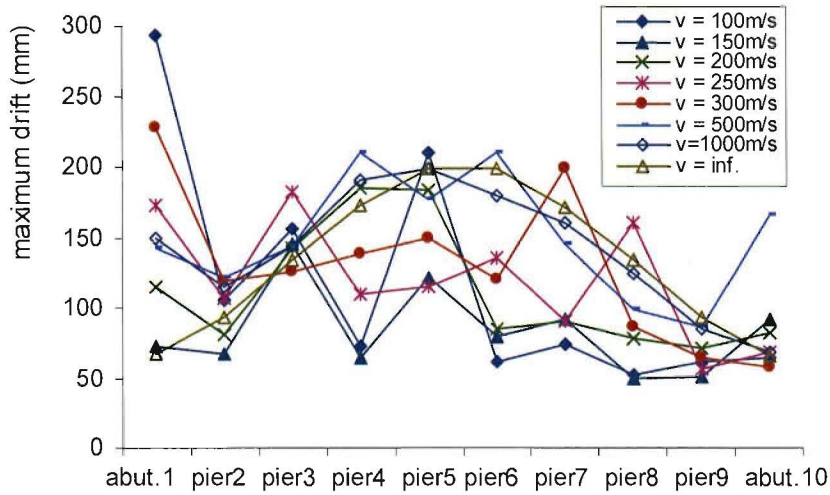

Figure 6.12 The maximum pier drifts of Model 3 to EL40NSC with d=10

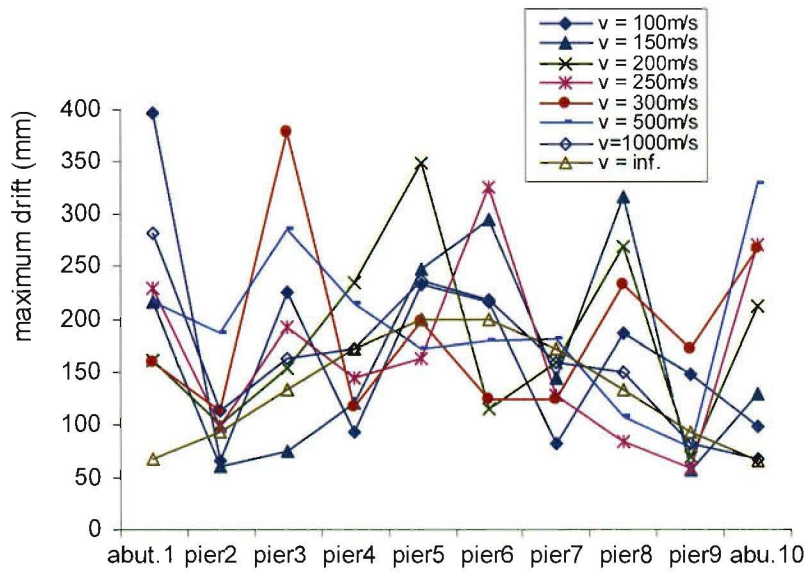

Figure 6.13 The maximum pier drifts of Model 3 to EL40NSC with d=1

though the bridge models had very different configurations. It was found that the geometric incoherence effect played an important role in the responses of these types of bridges through the pseudo-static component. For the cases with the greatest dispersion (d=1), the pseudo-static component caused by the geometric incoherence effect dominated the responses for all bridge configurations used. The influence of this component on the total response decreased as the amount of dispersion decreased. For the cases with the least dispersion (d=100), the pseudostatic component caused by the geometric incoherence effect had less influence on the total responses which were then similar to those of the travelling wave cases. Because the variations of accelerograms between different pier supports were assumed to be random, the value of the pseudo-static component due to the geometric incoherence effect was also random. The total responses were, therefore, unpredictable when the amount of dispersion was greatest.

Comparing the responses of Model 1, 3 and 5, it can be seen that the geometric incoherence effect has more influence on the bridges with irregular and/or stiffer piers. In the responses to EL40NSC, the maximum pier drift of pier 2 in the dispersion cases with d=1 reached to 24.5 times that in synchronous motion case for Model 1 (varying pier heights), however the maximum pier drift of pier 2 in the dispersion cases with d=1 were not greater than 2.3 times that in synchronous motion case for Model 3 (regular, 'taller' pier).

For Model 3 (regular symmetric, 'taller' piers), it is worth recording that in the greater dispersion cases with d=1 the maximum pier drifts of piers and the maximum shear forces in piers only was 2.3 and 2.2 times bigger than those in synchronous case. For Model 5 (regular symmetric, 'shorter' piers), the maximum pier drifts of the piers and the maximum shear forces in the piers in the greater dispersion cases with d=1 reached 6.1 and 7.6 times those in the synchronous case respectively.

Comparing the responses of Models 1, 3 and 5 in the dispersion cases, it can be see that the influences of the geometric incoherence effect on the responses of long bridges heavily depends on the stiffness of the long bridges. The stiffer the bridge, the greater the influence of the geometric incoherence effect on the responses of long bridges. The asynchronous motion case has less effect on the design demands when the long bridges are flexible enough (such as Model 3), although still giving greater demands than for the synchronous motion case. Hence if foundation compliance was included in the bridge models, the geometric incoherence effect should have less influence on the responses of long bridges.

CHAPTER 7

THE SEISMIC RESPONSE OF LONG BRIDGES WITH MOVEMENT JOINTS

7.1 Introduction

In this chapter the seismic responses of the bridges with movement joints subjected to asynchronous input motions are presented. The two response parameters investigated are the **maximum relative longitudinal displacement** of the bridge deck across the movement joint and the maximum relative longitudinal displacement between the girder end and the top of the abutment. If these displacements are large enough and seats with sufficient width or joint restrainers are not provided, these displacements may result in girder unseating and collapse, as has been observed in many earthquakes. The movement joint adopted in this chapter is shown in Figure 4.16, but the joints had no restrainers and a large enough seat width and initial opening were provided in order to ensure that the two parts of the joints are free to move without girder collapse and collision. The bridge Models 1a and 3a used in this chapter were identical to the Models 1 and 3 in Chapter 5 (see Table 5.3) except there were two movement joints in spans 3-4 and 7-8 at 7.5m from the nearest bent centreline; Figure 7.1 shows the locations of the movement joints. In Model 1a the piers have different heights and the superstructure was completely fixed at abutment 1 while the superstructure was supported on abutment 10 through sliding bearings. Model 3a has a very different configuration to Model 1a. In Model 3a all piers have a same height and the both bridge deck-ends are supported on abutments through sliding bearings. The seismic input motions acted in the bridge longitudinal direction and propagated from Abutment 10 to Abutment 1 in the bridge longitudinal direction. The East-West components of three earthquake records, the El Centro 1940 earthquake record, the Northridge 1994 earthquake record and the Kobe 1995

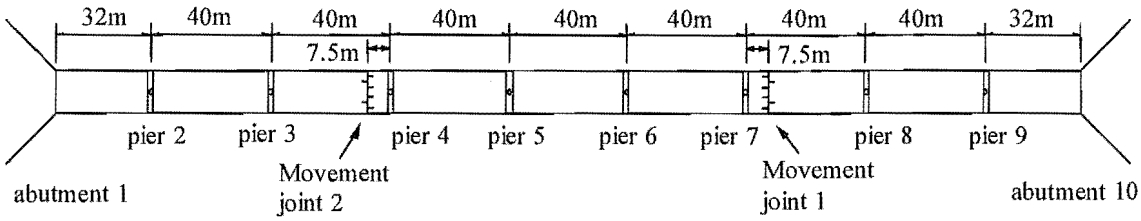

Figure 7.1 The locations of the movement joints

earthquake record were used respectively as the seismic input motion for the synchronous cases and as the specified seismic input motion at Abutment 10 for the asynchronous cases. The portions of these three earthquake acceleration records that were used in the analyses and their displacement time-histories are shown in Figures 7.2 and 7.3.

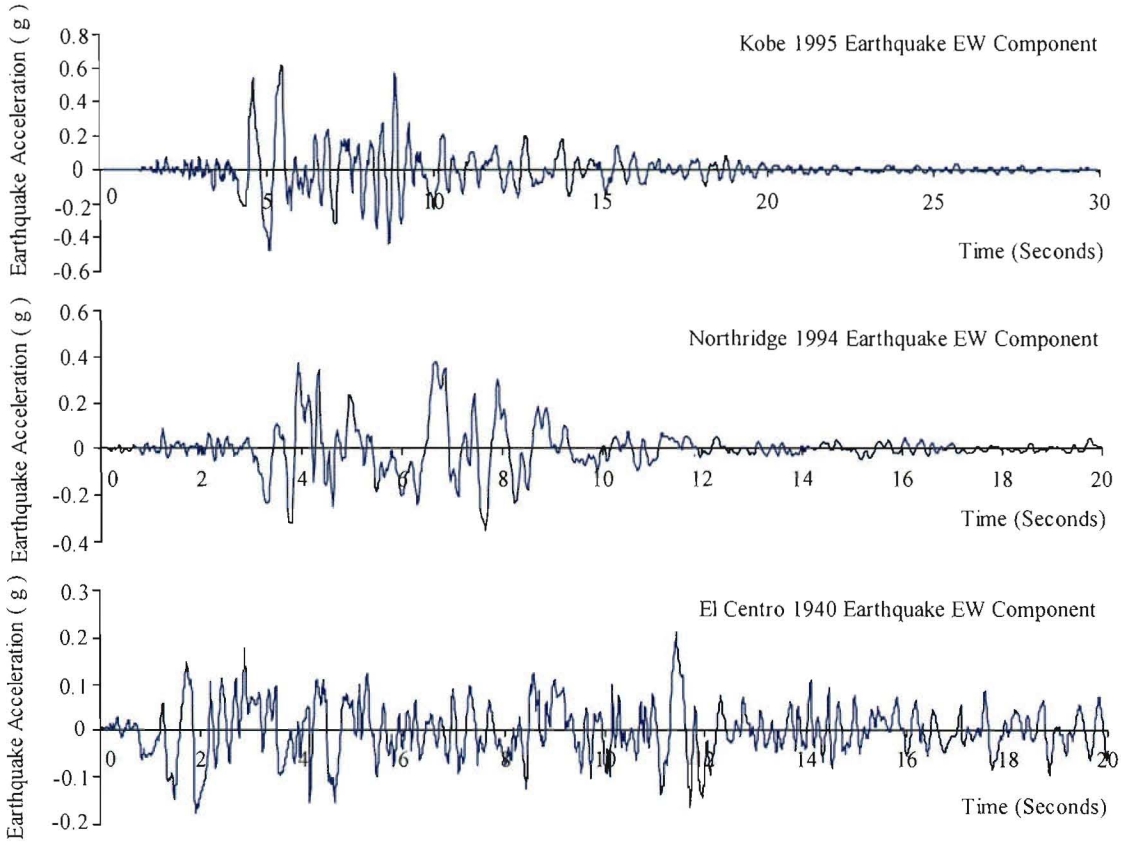

Figure 7.2 The earthquake acceleration time-histories

7.2 The Travelling Wave Cases

As in previous chapters, the travelling wave cases refer to the cases in which only the wave-passage effect of the spatial variability of the seismic input motion was considered in the responses of the bridge models.

7.2.1 The response of Model 1a

The responses of the Model 1a subjected to the East-West component of the El Centro 1940 earthquake record are presented in Figures 7.4(a) to 7.4(d), in which a positive relative displacement corresponds to an opening of the movement joint gap or the gap between the girder end and the top of the abutment 10 (see Figure 7.5) while a negative relative

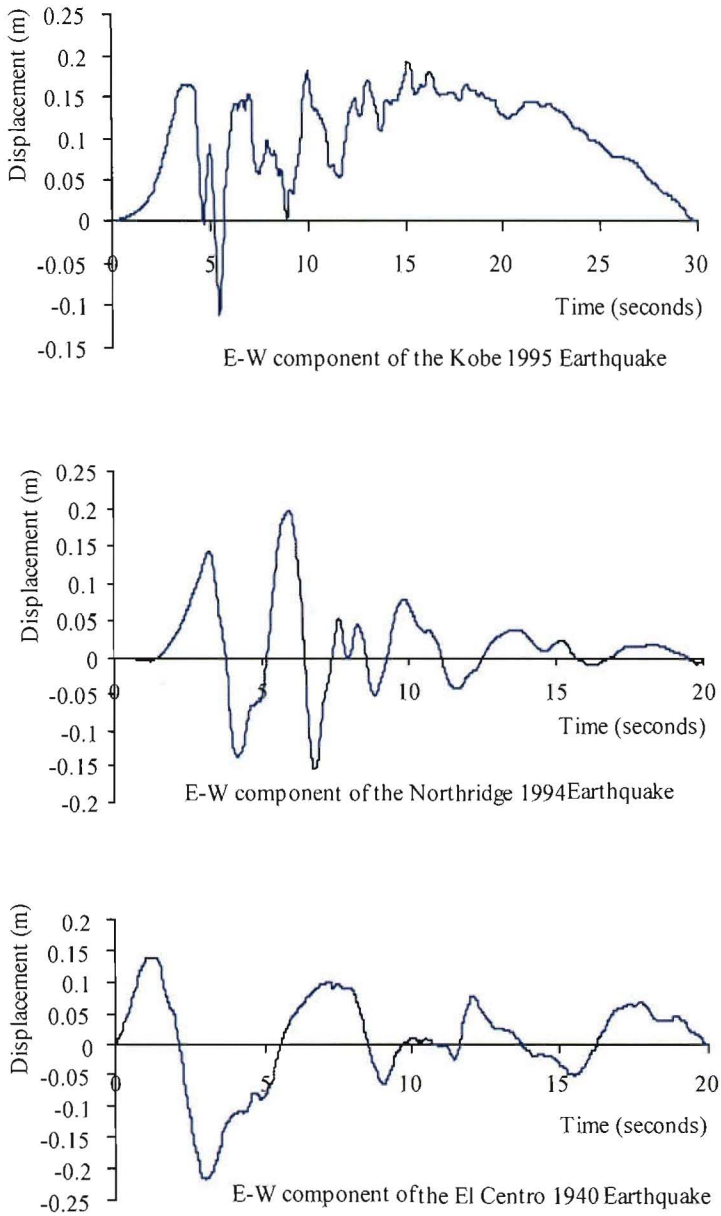

Figure 7.3 The displacement time-histories

displacement corresponds to a closing. The positive maximum relative displacement of the bridge deck across the movement joints and the positive maximum relative displacement between the girder end and the top of the Abutment 10 increased with the decrease in the travelling wave velocity although there are some local variations, as shown in Figures 7.6. These positive maximum relative displacements in the travelling wave cases reached 4 to 20.83 times those in the synchronous case (see Table 7.1). It can be seen that the wave-passage effect on the responses was significant.

In the travelling wave case, the relative displacement of the bridge deck across the movement joints and the relative displacement between the girder end and the top of the abutment 10

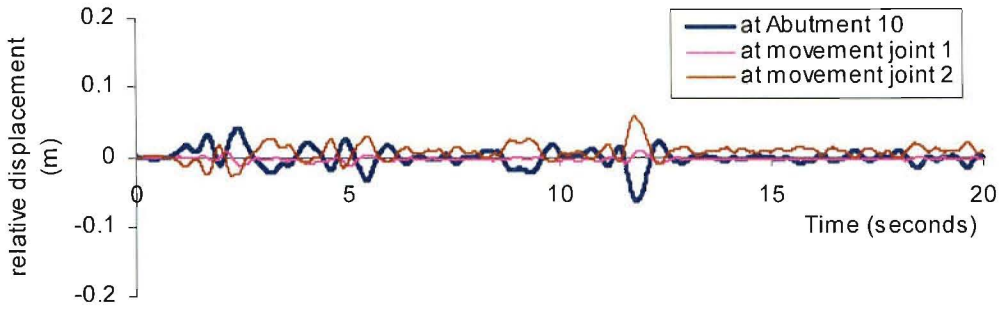

Figure 7.4(a) The response relative displacements time-histories of Model 1a to EL40EWC in the synchronous case

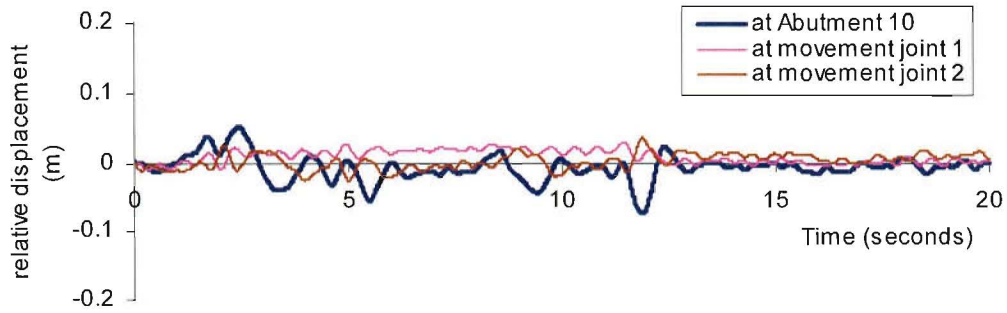

Figure 7.4(b) The response relative displacements time-histories of Model 1a to EL40EWC in the asynchronous case with travelling wave velocity of 2000m/s

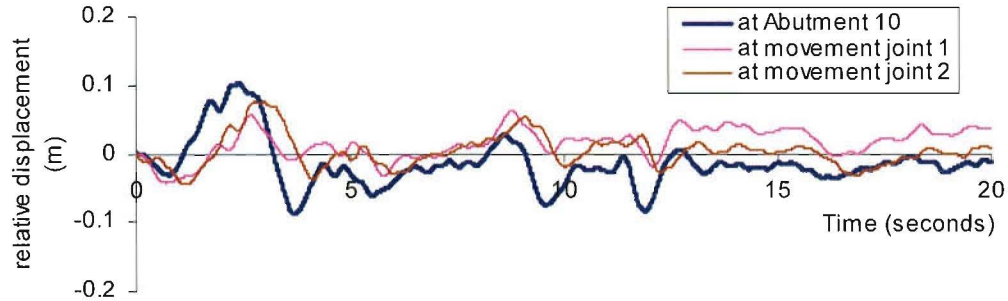

Figure 7.4(c) The response relative displacements time-histories of Model 1a to EL40EWC in the asynchronous case with travelling wave velocity of 500m/s

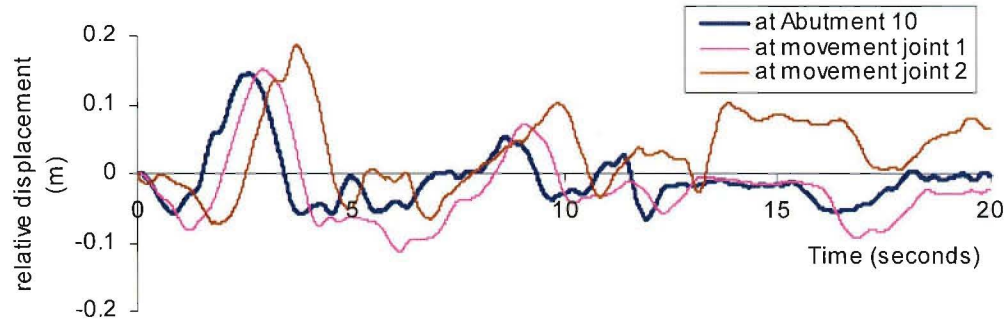

Figure 7.4(d) The response relative displacements time-histories of Model 1a to EL40EWC in the asynchronous case with travelling wave velocity of 200m/s

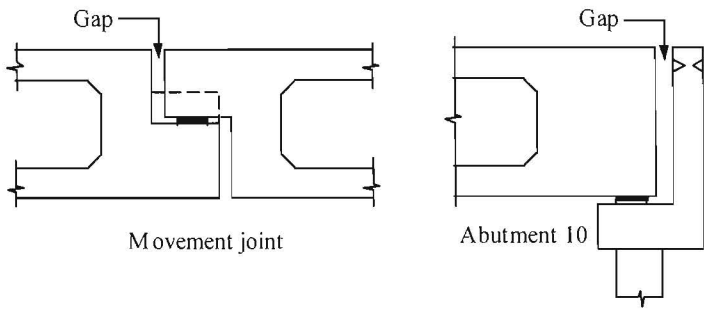

Figure 7.5 The joint gap and the gap between the girder end and the top of the abutment

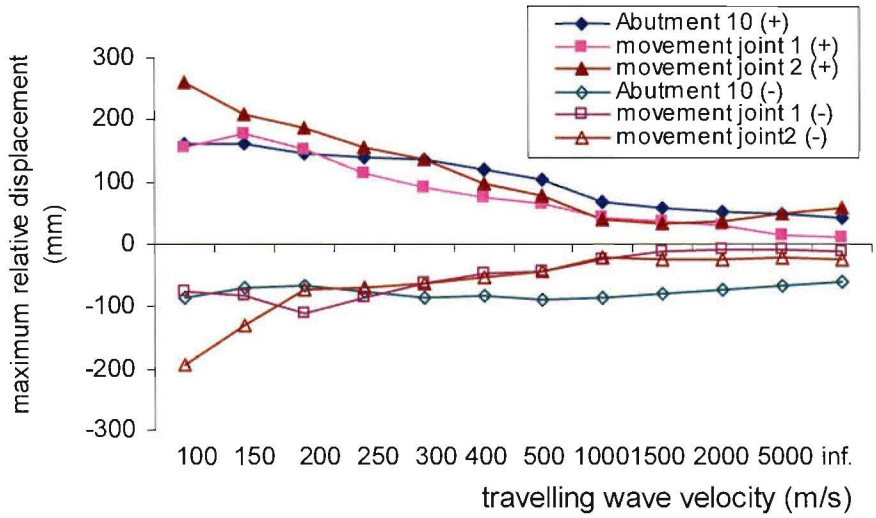

Figure 7.6 The responses of Model 1a to El Centro 1940 earthquake record

consist of two parts: one is the dynamic component due to the inertia effects arising from the difference between the vibrations of the two frames separated by the movement joint, and another is the pseudo-static component caused by the time delay between the vibrations of the separated frames. The dynamic component is affected by the stiffness of the two frames separated by the movement joint, the yield strengths of the frames, the frictional restraint of sliding, the impact on closing the joints, and the characteristics of restrainers connecting the frames [Priestley et al. 1996]. In the travelling wave cases, the dynamic component is also affected by the changes in the response time-histories of the bridge with the travelling velocity (as mentioned in Chapter 5). The vibration amplitudes of the separated frames generally decrease as the travelling wave velocity decreases because of the non-synchronism which does not allow the bridge to resonate at its fundamental frequency. The pseudo-static component is dominated by the fact that the wave-passage effect makes the

Travelling wave velocity (m/s)	Abutment 10				Movement joint 1				Movement joint 2			
	disp. (mm)	$\frac{disp.(v)}{disp.(\infty)}$	disp. (mm)	$\frac{disp.(v)}{disp.(\infty)}$	disp. (mm)	$\frac{disp.(v)}{disp.(\infty)}$	disp. (mm)	$\frac{disp.(v)}{disp.(\infty)}$	disp. (mm)	$\frac{disp.(v)}{disp.(\infty)}$	disp. (mm)	$\frac{disp.(v)}{disp.(\infty)}$
100	161	4	-85.9	1.38	153	18.21	-77.3	5.95	259	4.62	-194	7.27
150	161	4	-68.9	1.11	175	20.83	-83.4	6.42	208	3.71	-132	4.94
200	144	3.57	-65.5	1.05	149	17.74	-112	8.62	184	3.28	-73	2.73
250	137	3.4	-77.5	1.25	113	13.45	-87.2	6.71	154	2.75	-68.7	2.57
300	133	3.3	-86	1.38	88.1	10.49	-62.7	4.82	133	2.37	-63.7	2.39
400	118	2.93	-83.3	1.34	73.7	8.77	-48.8	3.75	96.1	1.71	-55.6	2.08
500	101	2.51	-88.2	1.42	62.3	7.42	-43.2	3.32	75	1.34	-45.2	1.69
1000	67.7	1.68	-86.6	1.39	42.1	5.01	-24.9	1.92	38.8	0.69	-23.9	0.9
1500	57.9	1.44	-79.8	1.28	35.3	4.2	-14.2	1.09	31.4	0.56	-25.7	0.96
2000	51.4	1.28	-74.1	1.19	27.7	3.3	-9.4	0.72	34.6	0.62	-27	1.01
5000	46.6	1.16	-66.6	1.07	12.4	1.48	-9.9	0.76	48.5	0.86	-21.2	0.79
∞	40.3	1	-62.2	1	8.4	1	-13	1	56.1	1	-26.7	1

Table 7.1 The responses of Model 1a to El Centro 1940 E-W earthquake record

Note: disp. (v) refers to the relative displacement between the two ends of the joints in the travelling wave cases.
disp. ($v = \infty$) refers to relative displacement between the two ends of the joints in the synchronous case.

separated frames vibrate out of phase with each other. In any bridge structure with dimensions greater than the characteristic length of the ground motion, different parts of the foundations can be out of phase with each other due to an asynchronous seismic input. The wave-passage effect (i.e. the phase shift of the seismic arrivals at the different parts of the structure) is sufficient to generate incoherent motion on a scale length of the order of one hundred metres [Fäh et al. 1993]. Therefore the pseudo-static component should play an important role in these relative displacements. The lower the travelling wave velocity, the longer the phase shifts between the vibrations of the two frames. Hence, the pseudo-static component changes with the travelling wave velocity.

From the response displacement time-histories of the bridge deck at the two sides of the movement joints, the girder end at Abutment 10 and the Abutment 10, it can be seen that the phase shift between the vibrations of the two frames increased with the decrease in travelling wave velocity as shown in Figures 7.7(a) to 7.7(d). The relative displacement of the bridge deck across the movement joints and the relative displacement between the girder end and the top of the Abutment 10 were the differences between these two displacements, so they were not only dependent on the phase shift, but also on the shapes of these displacement time-histories that changed with the travelling wave velocity. In these cases, the positive maximum relative displacement of the bridge deck across the movement joints and the positive maximum relative displacement between the girder end and the top of the Abutment 10 increased as the travelling wave velocity decreased (see Figure 7.6). Hence the pseudo-static component increased with the decreases of the travelling wave velocity and when the travelling wave velocity was low the pseudo-static component dominated the positive

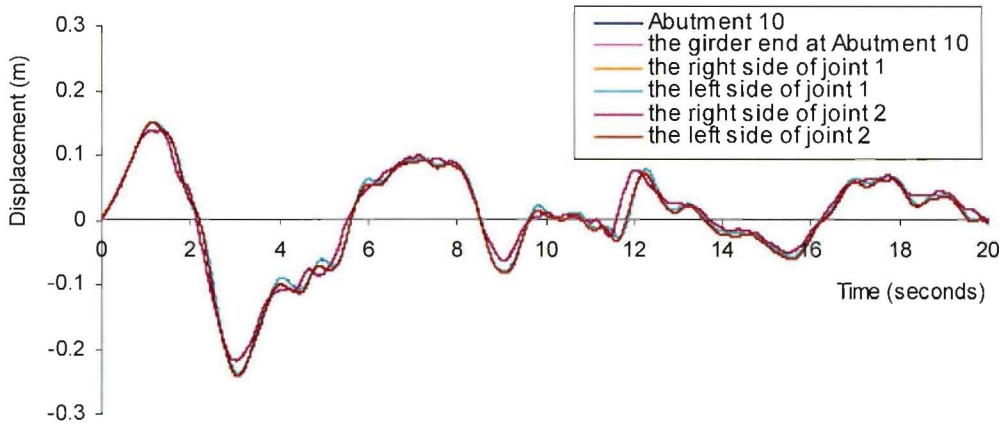

Figure 7.7(a) The response displacement time-histories of Model 1a to EL40EWC in the synchronous case

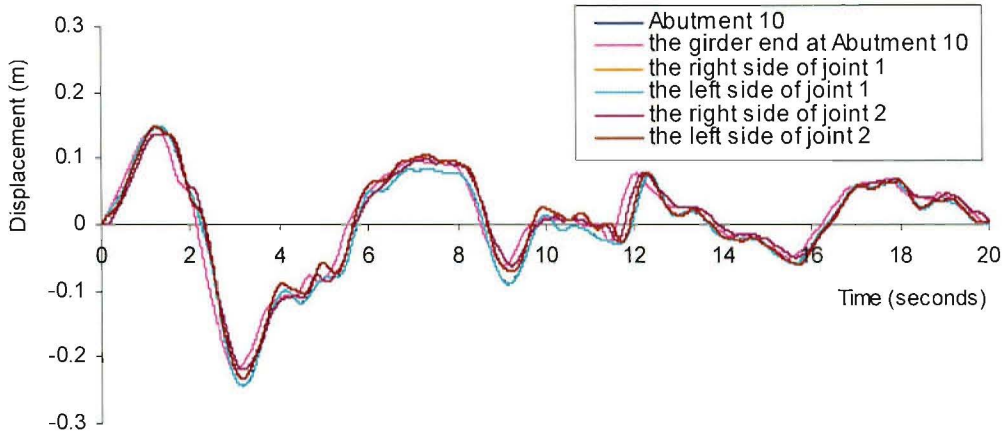

Figure 7.7 (b) The response displacement time-histories of Model 1a to EL40EWC in the asynchronous case with traveling wave velocity of 2000m/s

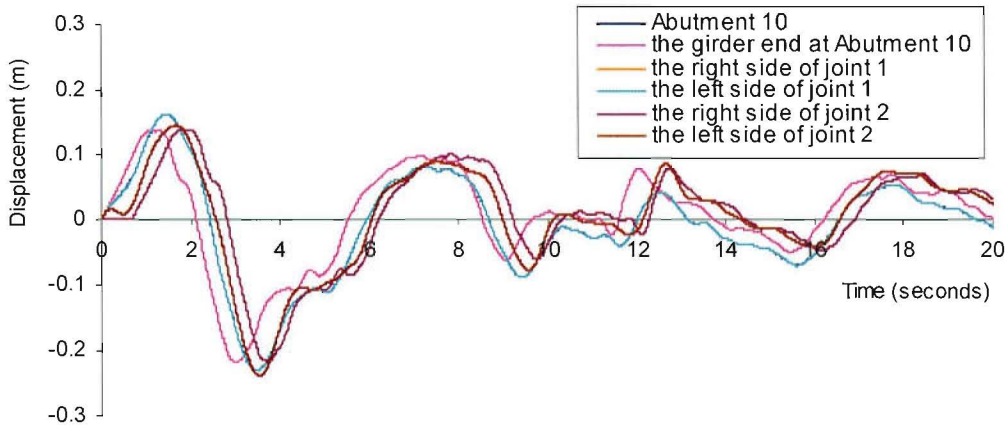

Figure 7.7 (c) The response displacement time-histories of Model 1a to EL40EWC in the asynchronous case with traveling wave velocity of 500m/s

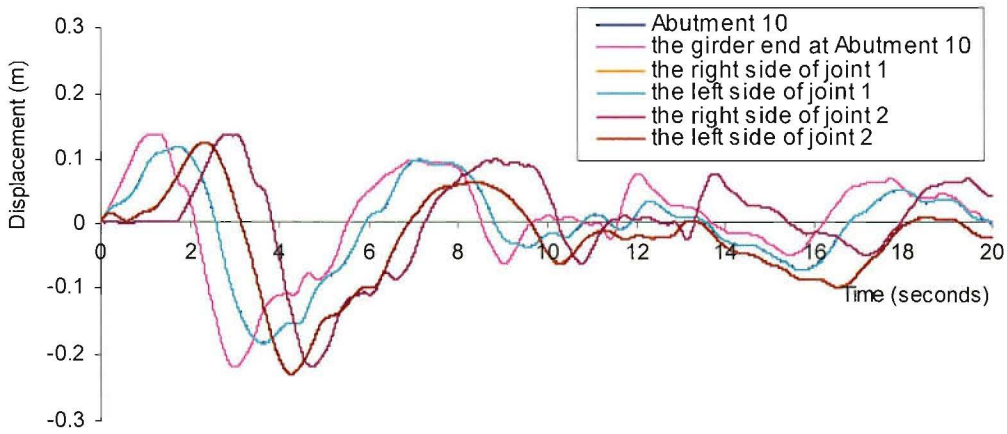

Figure 7.7 (d) The response displacement time-histories of Model 1a to EL40EWC in the asynchronous case with traveling wave velocity of 200m/s

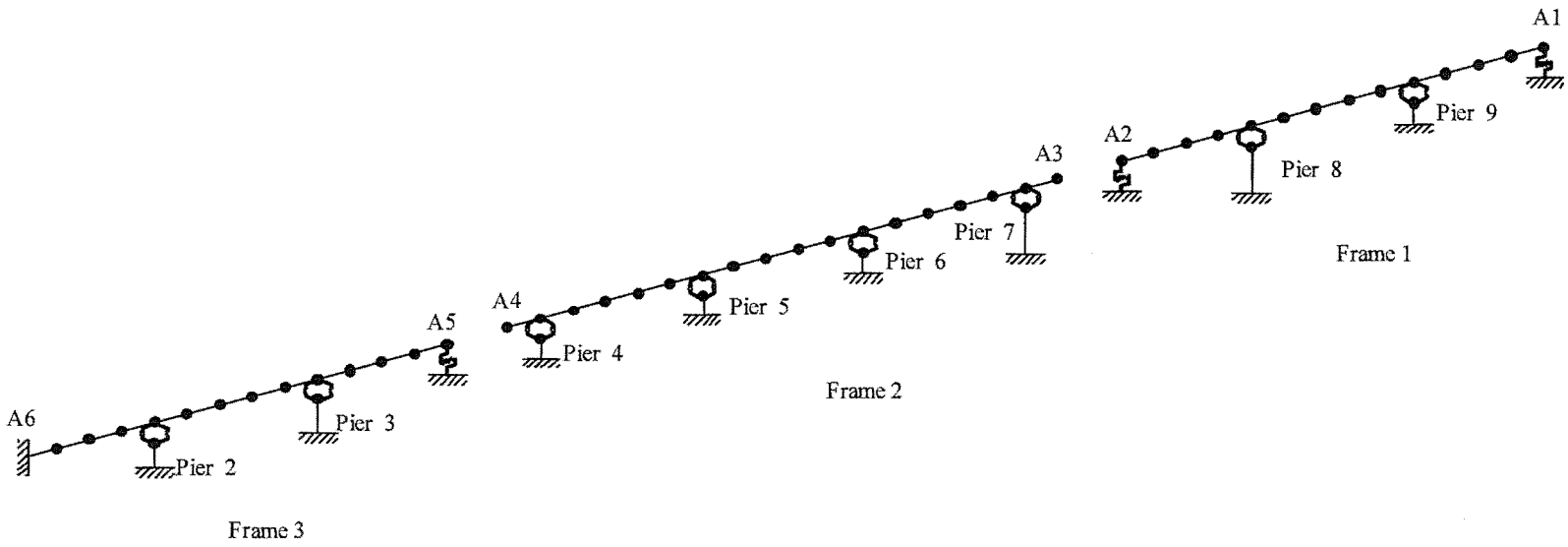

Figure 7.8 The models of the three separated frames in Model 1a

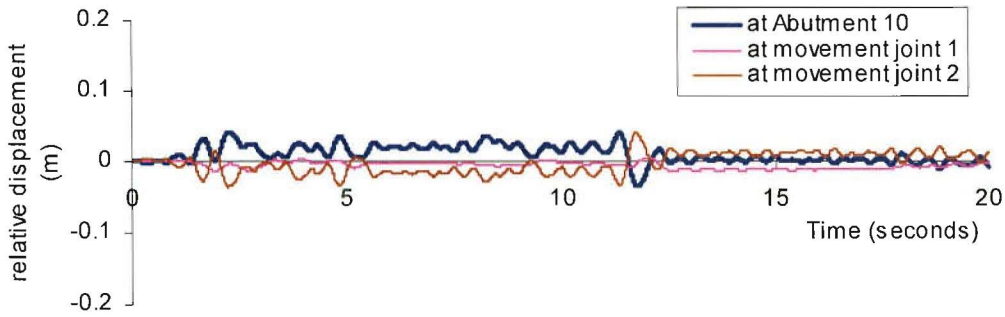

Figure 7.9 (a) The dynamic representation of the relative displacements in Model 1a for synchronous case

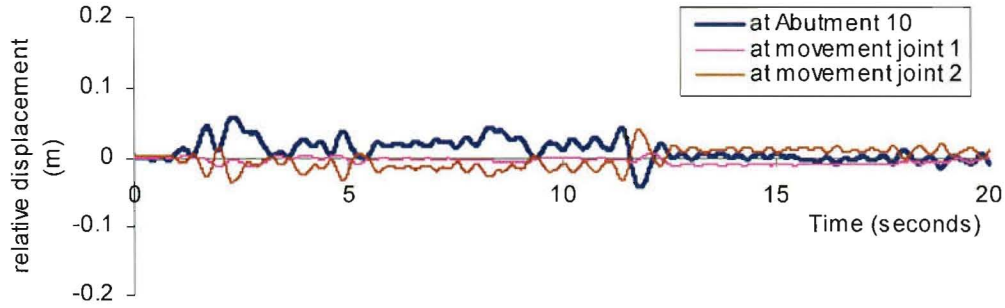

Figure 7.9 (b) The dynamic representation of the relative displacements in Model 1a for travelling wave case with v = 2000 m/s

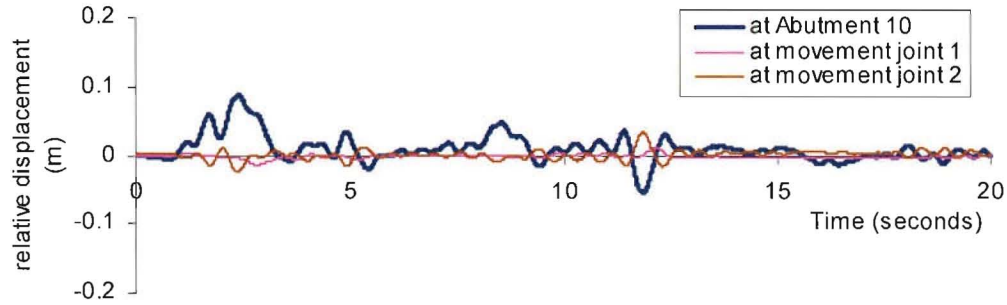

Figure 7.9 (c) The dynamic representation of the relative displacements in Model 1a for travelling wave case with v = 500 m/s

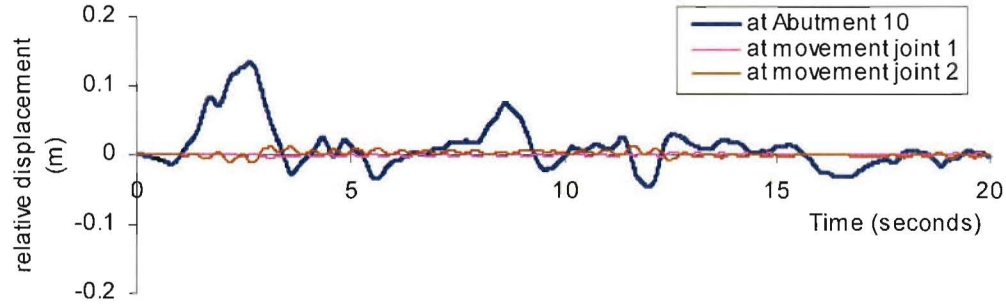

Figure 7.9 (d) The dynamic representation of the relative displacements in Model 1a for travelling wave case with v = 200 m/s

maximum relative displacements. It was also noticed that the rates of increase of these relative displacements with the travelling wave velocity were slightly different because the shapes of the displacement time-histories changed with the travelling wave velocity due to the variations of the spectrum of the whole seismic input motion to the bridge.

In order to investigate the variations of the dynamic components of these relative displacements with the travelling wave velocity, several synchronous analyses of the three frames separated by the two movement joints in Model 1a were carried out. The models of the three frames in Model 1a are shown in Figure 7.8. The input acceleration time-histories used in these synchronous cases were the averages of the input acceleration time-histories that had been applied to the bridge supports in the previous travelling wave cases corresponding to travelling wave velocities of infinite velocity (synchronous), 2000, 500 and 200 m/s. The dynamic components of the relative displacements of the bridge deck across the movement joints were represented by the difference between the displacements of the girder end A2 of the frame 1 and the girder end A3 of the frame 2, and the difference between the displacements of the girder end A4 of the frame 2 and the girder end A5 of the frame 3. The dynamic component of the relative displacement between the girder end and the top of the Abutment 10 was represented by the difference between the displacement of the girder end A1 of the frame 1 and the displacement of the Abutment 10 of the model 1a. As shown in Figures 7.9 (a) to 7.9 (d), the dynamic component representations of the relative displacements of the bridge deck across the movement joints in Model 1a decreased as the travelling wave velocity decreased because the vibration amplitudes of the separated frames decreased with the decrease in the travelling wave velocity. The dynamic component representation of the relative displacement between the girder end and the top of the Abutment 10 increased as the travelling wave velocity decreased, because the vibration amplitudes of the separated frames decreased with the decrease in the travelling wave velocity while the displacement of the Abutment 10 did not change.

The responses of the Model 1a to the East-West components of the Kobe 1995 earthquake record and the Northridge 1994 earthquake record in the travelling wave case are presented in Figures 7.10 to 7.11. The positive maximum relative displacement between the bridge girder end and the top of the Abutment 10 increased with the decrease in the travelling wave velocity, their trends being similar to that for the El Centro earthquake record. However, the response patterns for the relative displacements of the bridge deck across the movement joints are not similar to that for the El Centro earthquake record as they do not follow any noticeable

trend. However it still can be seen that some responses of the travelling wave cases were more critical than that of the synchronous case.

As shown in Figures 7.10 to 7.11, the variations of the relative displacements of the bridge deck across the movement joints with the travelling wave velocity were not large when the travelling wave velocity was greater than 1000m/s, but these variations were larger when the

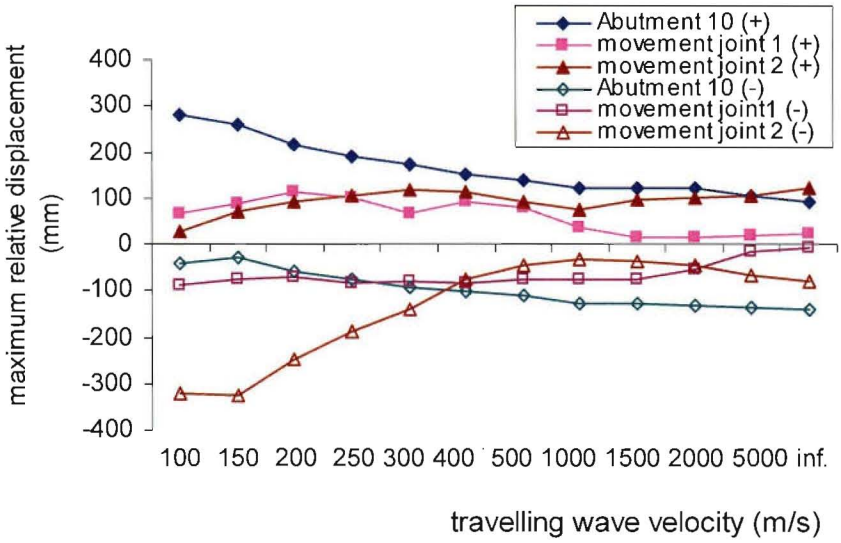

Figure 7.10 The responses of Model 1a to the Kobe 1995 earthquake record

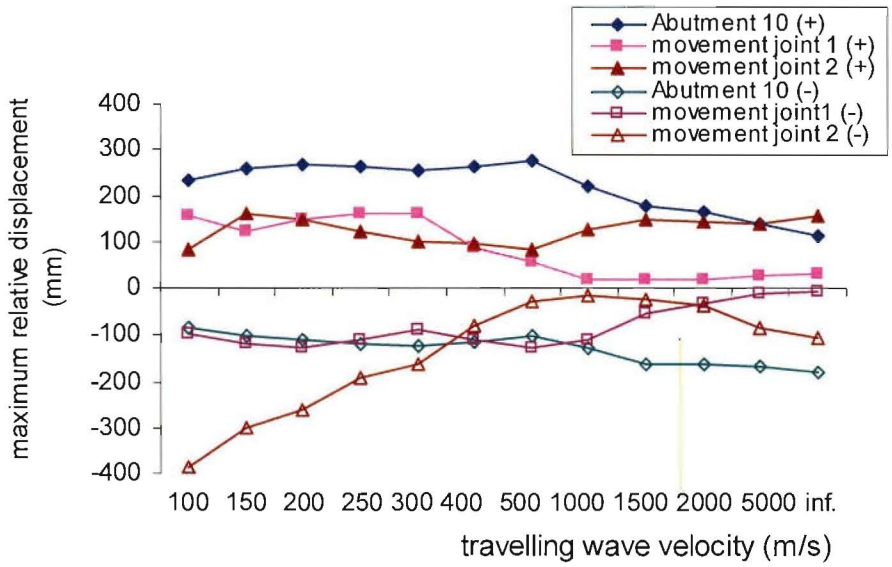

Figure 7.11 The responses of Model 1a to the Northridge 1994 earthquake record

travelling wave velocity was lower than 1000m/s. This fact also indicates that the pseudo-static component played an important role in the response relative displacements of the bridge deck across the movement joints when the travelling wave velocity was lower than 1000m/s. Although the larger the phase shifts the lower the travelling wave velocity, the pseudo-static components do not simply increase as the travelling wave velocity decreases because the values of the relative displacements also depend on the displacement time-histories of the bridge deck at the corresponding points. That is why the variations of the relative displacements of the bridge deck across the movement joints with the travelling wave velocity followed different trends for different seismic input excitations.

Figures 7.12 (a) to 7.12 (d) show the displacement time-histories of the bridge deck at the two sides of the movement joints, the girder end at Abutment 10 and Abutment 10 for the Kobe 1995 earthquake in the case with travelling wave velocities of ∞, 2000, 500, 200 m/s respectively. It can be seen that the larger the phase shifts the lower the travelling wave velocity. The differences between the two displacements depend on the phase shifts and the shape of their displacement time-histories. Furthermore, the shapes of the response displacement time-histories of the bridge deck varied with the travelling wave velocity.

7.2.2 The response of Model 3a

In order to obtain more general trends followed by the relative displacement of the bridge deck across the movement joint and the relative displacement between the girder end and the top of the abutment, the responses of Model 3a to the E-W components of the El Centro 1940 earthquake, the Kobe 1995 earthquake and the Northridge 1994 earthquake were determined. The variations of the relative displacements of the bridge deck across the movement joints and the relative displacements between the girder ends and the top of the abutments with the travelling wave velocity are shown in Figures 7.13 to 7.15. Although the response patterns of these relative displacements appear to be different from those for Model 1a, they actually show similar trends to Model 1a. This can be seen from the displacement time-histories of the abutments, the girder end and the bridge deck at the two sides of the movement joints for the El Centro 1940 earthquake. As shown in Figures 7.16 (a) to 7.16 (d), the phase shifts between the vibration of the frames separated by the joints increased as the travelling wave velocity decreased. The difference between the displacements of the bridge deck at the two sides of the joints and the difference between the displacements of the girder end and Abutment 10 increased as the phase shifts increased. Figure 7.13 shows that the positive maximum relative displacements of the bridge deck across the joints and the positive maximum relative

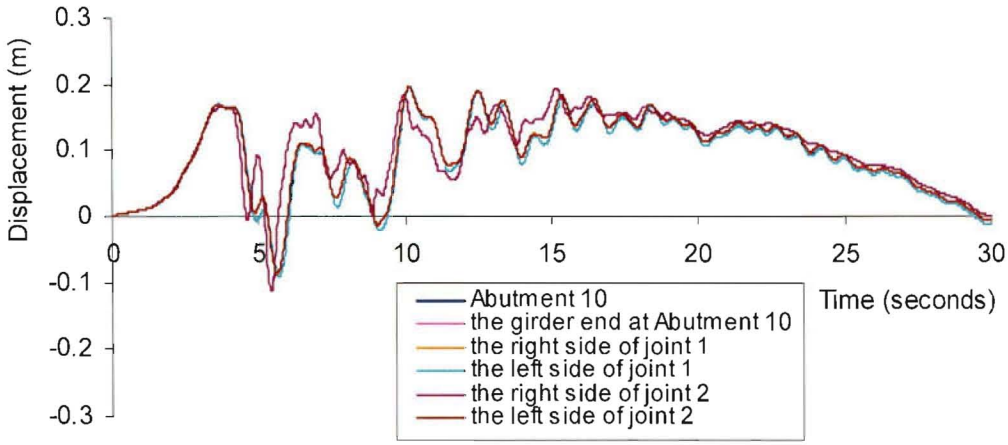

Figure 7.12 (a) The response displacement time-histories of Model 1a to KOBE95EW in the synchronous case

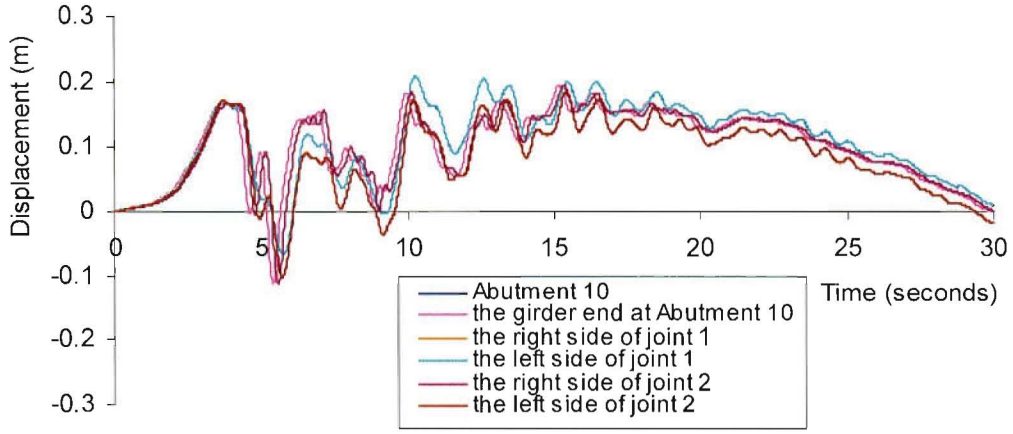

Figure 7.12 (b) The response displacement time-histories of Model 1a to KOBE95EW in the asynchronous case with travelling wave velocity of 2000m/s

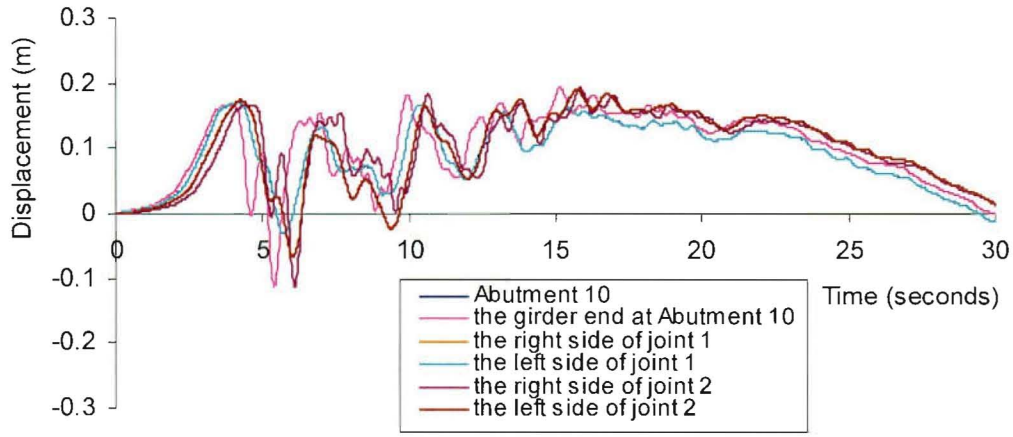

Figure 7.12 (c) The response displacement time-histories of Model 1a to KOBE95EW in the asynchronous case with travelling wave velocity of 500m/s

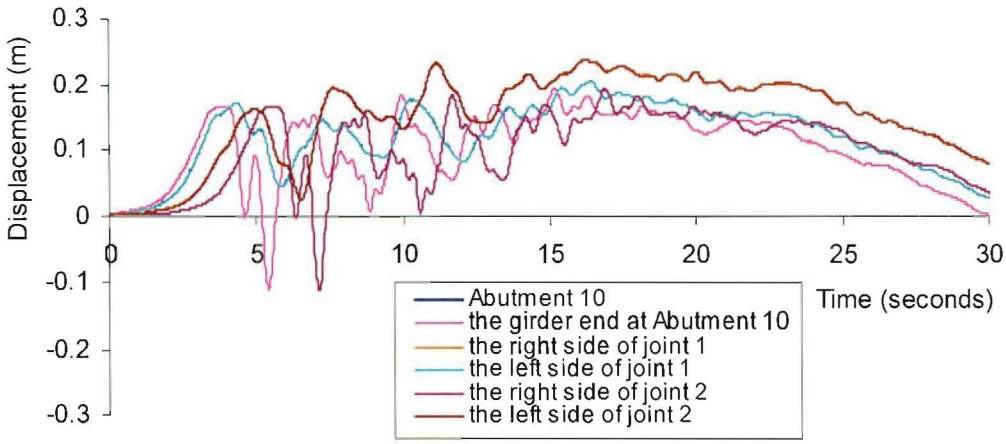

Figure 7.12 (d) The response displacement time-histories of Model 1a to KOBE95EW in the asynchronous case with travelling wave velocity of 200m/s

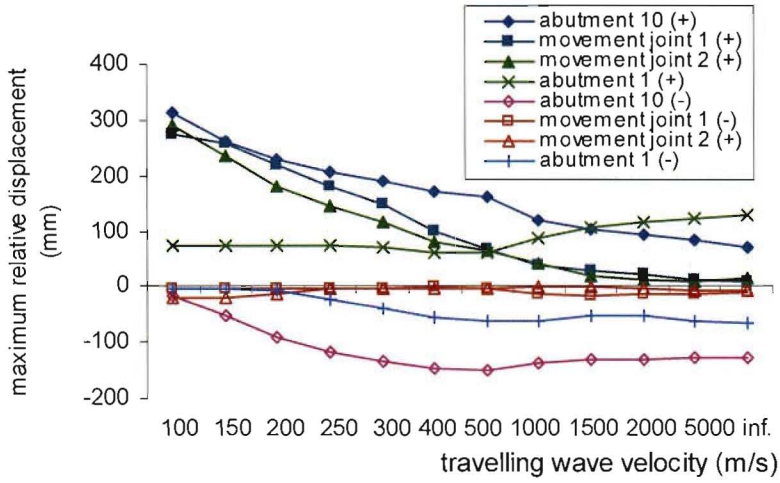

Figure 7.13 The responses of Model 3a to the El Centro 1940 earthquake record

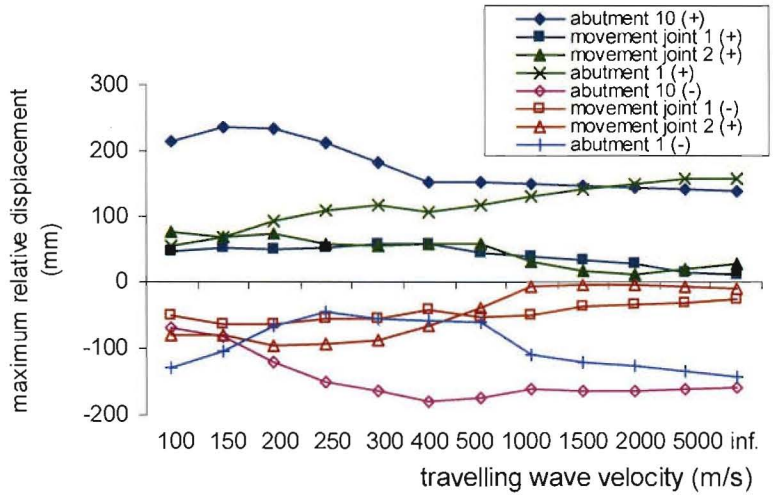

Figure 7.14 The responses of Model 3a to the Kobe 1995 earthquake record

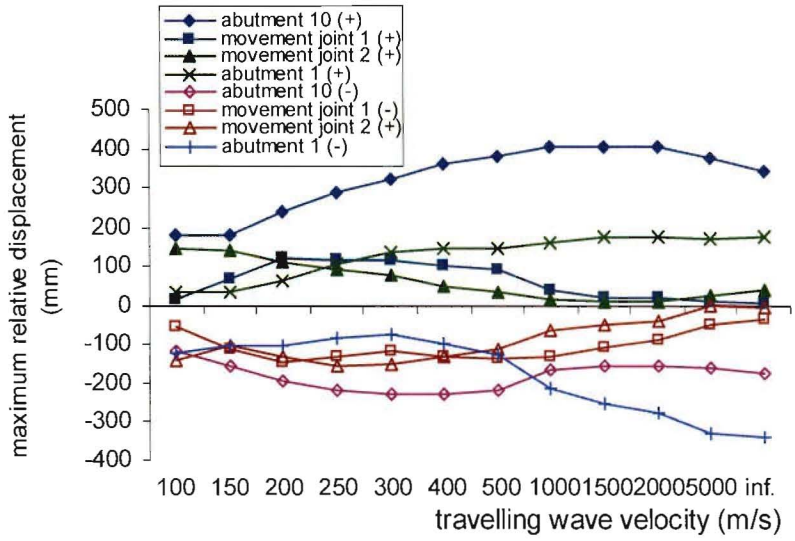

Figure 7.15 The responses of Model 3a to the Northridge 1994 earthquake record

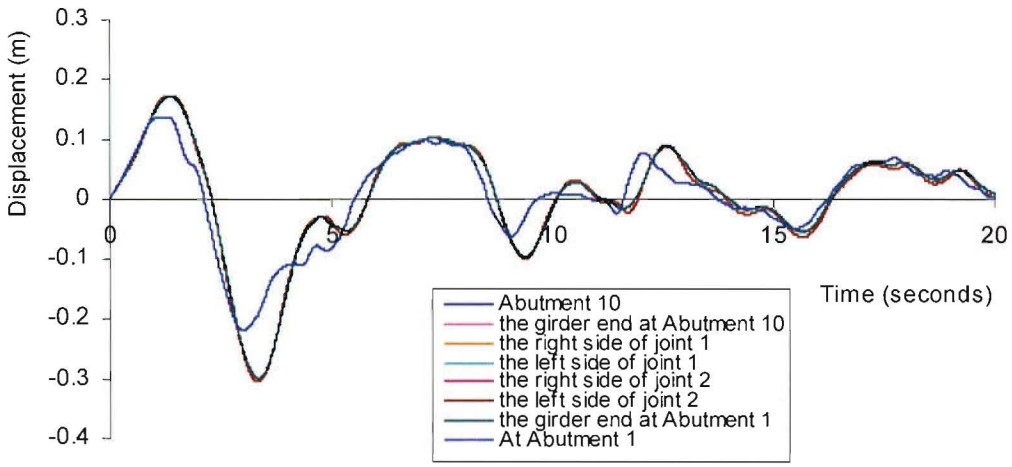

Figure 7.16 (a) The response displacement time-histories of Model 3a to EL40EWC in the synchronous case

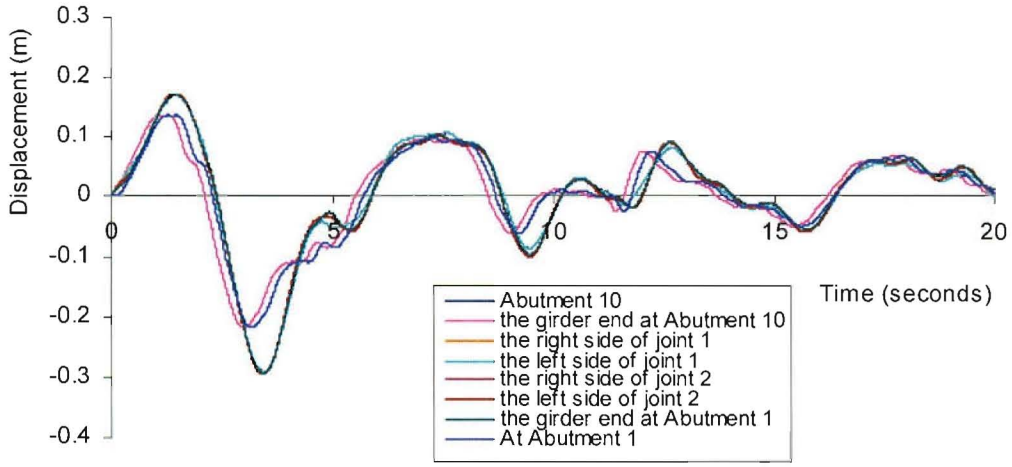

Figure 7.16 (b) The response displacement time-histories of Model 3a to EL40EWC in the asynchronous case with travelling wave velocity of 2000m/s

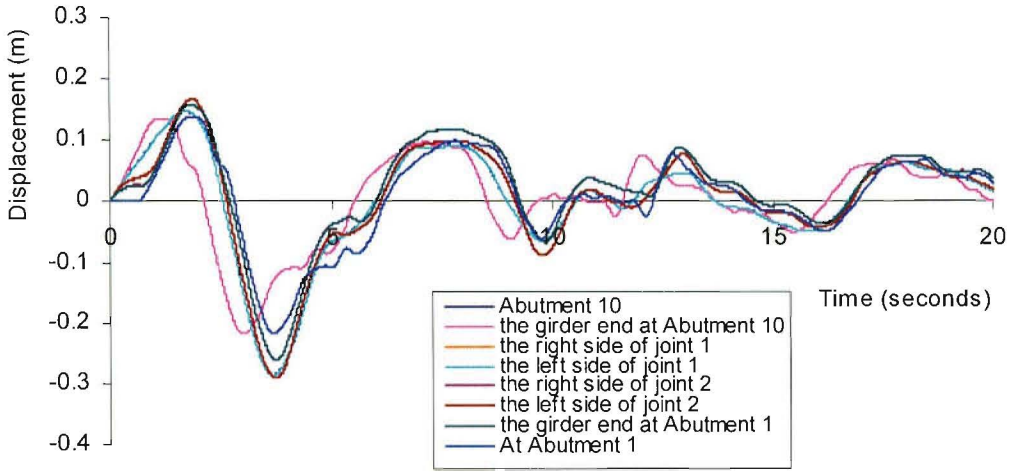

Figure 7.16 (c) The response displacement time-histories of Model 3a to EL40EWC in the asynchronous case with travelling wave velocity of 500m/s

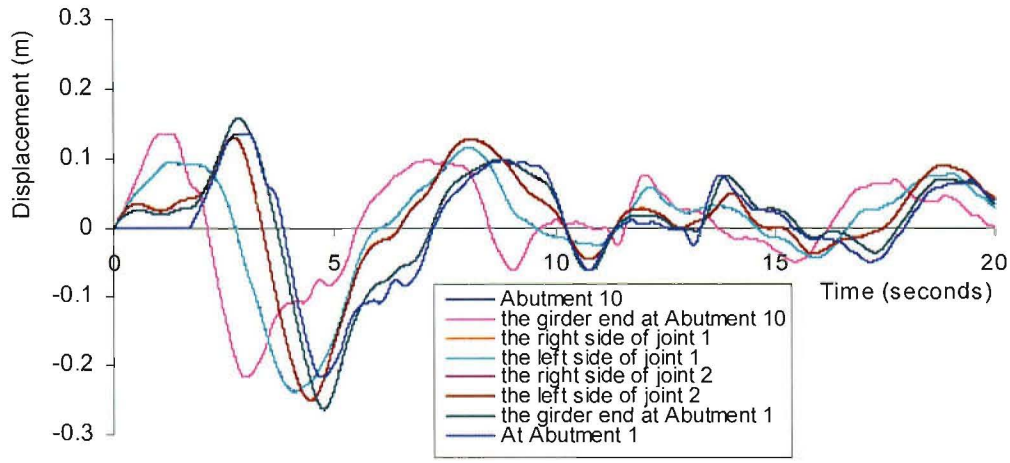

Figure 7.16 (d) The response displacement time-histories of Model 3a to EL40EWC in the asynchronous case with travelling wave velocity of 200m/s

displacement between the girder end and the top of Abutment 10 increased with the decrease in travelling wave velocity similar to that for Model 1a. However, the positive maximum relative displacement between the girder end and the top of Abutment 1 decreased as the travelling wave velocity decreased from infinity to 500 m/s, and when the travelling wave velocity was less than 500 m/s the displacement remained almost constant. This was because the difference between the displacements of the girder end and Abutment 1 decreased first as the phase shifts increased, and then increased as the phase shifts increased when the travelling wave velocity was less than 500 m/s (see Figures 7.16 (a) to 7.16 (d)). Therefore, it could be concluded that the relative displacement response of the bridge deck across the movement joints and the relative displacement between the girder end and the top of the abutment of

Model 3a also followed the same patterns as that for Model 1a. These relative displacements consist two parts: the dynamic and pseudo-static components. The pseudo-static component played an important role in these response relative displacements. Some response relative displacements in the travelling wave cases were larger than those in the synchronous case.

7.3 The Wave Dispersion Cases

In this section both the geometric incoherence effect and the wave-passage effect of the spatial variability of the ground motion were considered in the bridge seismic responses. The East-West components of the El Centro 1940 earthquake record, the Kobe 1995 earthquake record and the Northridge 1994 earthquake record were used as the seismic input motions for

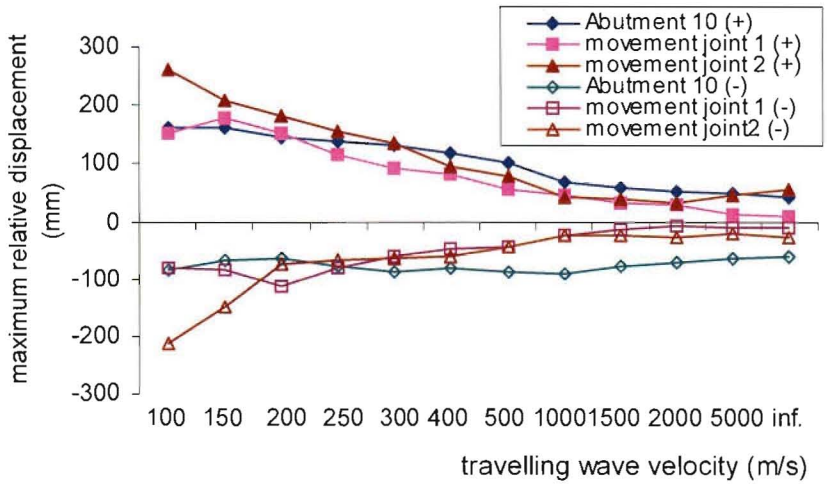

Figure 7.17 The responses of Model 1a to EL40EWC in wave dispersion cases (d = 100)

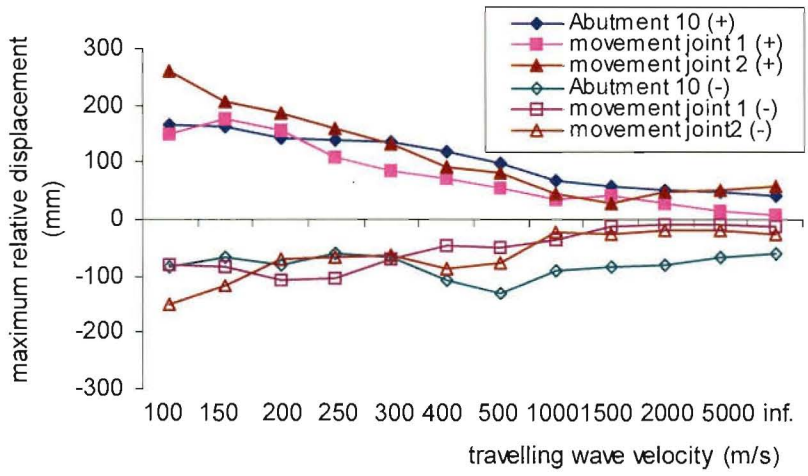

Figure 7.18 The responses of Model 1a to EL40EWC in the wave dispersion cases (d = 10)

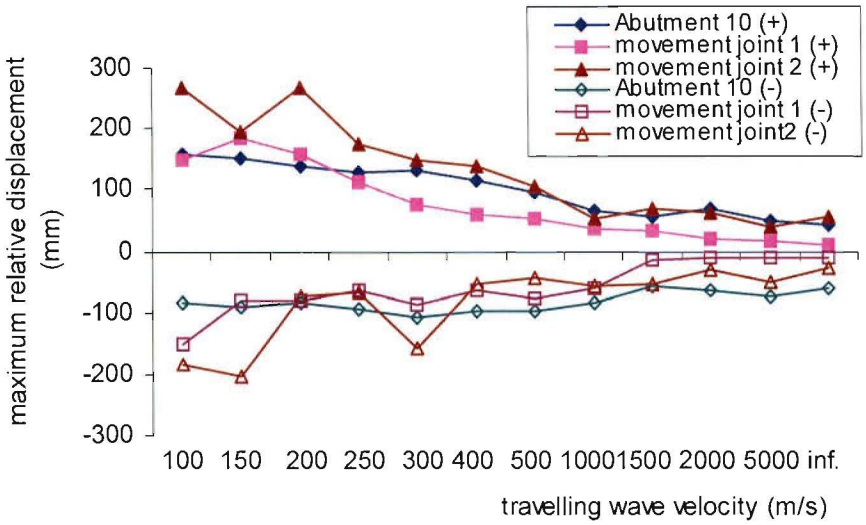

Figure 7.19 The responses of Model 1a to EL40EWC in the wave dispersion cases (d = 1)

synchronous cases and as the specified seismic input motion at Abutment 10 for asynchronous cases. The responses of the Model 1a subjected to the generated time-histories conditioned by the East-West component of the El Centro 1940 earthquake record at Abutment 10 with dispersion factors of 100, 10 and 1 are presented in Figures 7.17 to 7.19 and the comparison with the corresponding responses of the travelling wave cases for Model 1a are shown in Tables 7.2 to 7.4.

As mentioned previously, in the wave dispersion case the variation of the ground motion at different bridge supports is not only due to the difference in the arrival time of seismic waves but also is attributed to the change in shape of the seismic motions. This means that the differential displacement between pier supports in this case should be greater than that in the travelling wave cases. Figures 7.20 and 7.21 show the maximum differential displacements between pier bases in Model 1a for the travelling wave cases and the wave dispersion cases with d = 1 respectively. It can be seen that the differential displacements between pier supports for the travelling wave cases and the wave dispersion cases are completely different. On the other hand, the positive maximum relative displacements of the bridge deck across the movement joint 1 and the relative displacement between the girder end and the top of Abutment 10 in the wave dispersion cases and travelling wave cases were similar to each other (compare Figure 7.6 with Figures 7.17 to 7.19 and see Tables 7.2 to 7.4). This indicates that the pseudo-static components of the relative displacements were still controlled by the phase shifts between the vibrations of the two frames separated by the movement joints, and the differential displacements between pier supports had little effect on the relative

Travelling wave velocity (m/s)	Abutment 10				Movement joint 1				Movement joint 2			
	disp. (mm)	$\frac{disp.(d)}{disp.(v)}$	disp. (mm)	$\frac{disp.(d)}{disp.(v)}$	disp. (mm)	$\frac{disp.(d)}{disp.(v)}$	disp. (mm)	$\frac{disp.(d)}{disp.(v)}$	disp. (mm)	$\frac{disp.(d)}{disp.(v)}$	disp. (mm)	$\frac{disp.(d)}{disp.(v)}$
100	161	1	-85.9	1	152	0.99	-80	1.03	261	1.01	-213	1.1
150	160	0.99	-68.8	1	176	1.01	-84.9	1.02	206	0.99	-152	1.15
200	145	1.01	-63.1	0.96	150	1.01	-113	1.01	182	0.99	-73.2	1
250	137	1	-78.9	1.02	114	1.01	-82	0.94	155	1.01	-68.6	1
300	132	0.99	-87.3	1.02	92.2	1.05	-62.9	1	133	1	-63.5	1
400	118	1	-80.8	0.97	82.1	1.11	-48.8	1	95.1	0.99	-59.7	1.07
500	101	1	-87.7	0.99	54.7	0.88	-43.2	1	76.4	1.02	-45.1	1
1000	67.8	1	-90.4	1.04	45.1	1.07	-24.9	1	40.1	1.03	-23.8	1
1500	57.8	1	-79.2	0.99	30.8	0.87	-16.5	1.16	37.3	1.19	-24.6	0.96
2000	51.6	1	-72.4	0.98	28.3	1.02	-9.44	1	32.3	0.93	-28.8	1.07
5000	46.5	1	-65	0.98	12	0.97	-9.98	1.01	44.3	0.91	-21.8	1.03
∞	40.3	1	-62.2	1	8.4	1	-13	1	56.1	1	-26.7	1

Table 7.2 The responses of Model 1a to EL40EWC in dispersion cases with d =100

Note: disp. (d) refers to the relative displacement between the two ends of the joints in the wave dispersion cases.
disp. (v) refers to the relative displacement between the two ends of the joints in the travelling wave cases.

Travelling wave velocity (m/s)	Abutment 10				Movement joint 1				Movement joint 2			
	disp. (mm)	$\frac{disp.(d)}{disp.(v)}$	disp. (mm)	$\frac{disp.(d)}{disp.(v)}$	disp. (mm)	$\frac{disp.(d)}{disp.(v)}$	disp. (mm)	$\frac{disp.(d)}{disp.(v)}$	disp. (mm)	$\frac{disp.(d)}{disp.(v)}$	disp. (mm)	$\frac{disp.(d)}{disp.(v)}$
100	164	1.02	-85.9	1	150	0.98	-80.8	1.05	261	1.01	-150	0.77
150	162	1.01	-68.8	1	176	1.01	-83.6	1	207	1	-118	0.89
200	141	0.98	-79.9	1.22	154	1.03	-107	0.96	186	1.01	-72.3	0.99
250	138	1.01	-61.6	0.79	108	0.96	-106	1.22	158	1.03	-68.4	1
300	134	1.01	-68.3	0.79	83.5	0.95	-69.9	1.11	130	0.98	-63.5	1
400	117	0.99	-107	1.28	71.9	0.98	-48.5	0.99	92	0.96	-88.7	1.6
500	96.4	0.95	-130	1.47	52.8	0.85	-51.7	1.2	80.2	1.07	-78.7	1.74
1000	68.3	1.01	-92.2	1.06	35	0.83	-35.7	1.43	42.8	1.1	-23.4	0.98
1500	57.7	1	-82.8	1.04	39.1	1.11	-14.1	0.99	27.2	0.87	-26.3	1.02
2000	51.9	1.01	-80.6	1.09	26.9	0.97	-10.5	1.12	47.3	1.37	-20.1	0.74
5000	47.4	1.02	-68	1.02	15	1.21	-9.37	0.95	51.9	1.07	-21.4	1.01
∞	40.3	1	-62.2	1	8.4	1	-13	1	56.1	1	-26.7	1

Table 7.3 The responses of Model 1a to EL40EWC in dispersion cases with d =10

Note: disp. (d) refers to the relative displacement between the two ends of the joints in the wave dispersion cases.
disp. (v) refers to the relative displacement between the two ends of the joints in the travelling wave cases.

Travelling wave velocity (m/s)	Abutment 10				Movement joint 1				Movement joint 2			
	disp. (mm)	$\frac{disp.(d)}{disp.(v)}$	disp. (mm)	$\frac{disp.(d)}{disp.(v)}$	disp. (mm)	$\frac{disp.(d)}{disp.(v)}$	disp. (mm)	$\frac{disp.(d)}{disp.(v)}$	disp. (mm)	$\frac{disp.(d)}{disp.(v)}$	disp. (mm)	$\frac{disp.(d)}{disp.(v)}$
100	159	0.99	-85.9	1	147	0.96	-151	1.95	268	1.03	-185	0.95
150	151	0.94	-89.7	1.3	185	1.06	-81.8	0.98	195	0.94	-205	1.55
200	136	0.94	-83.9	1.28	159	1.07	-81.9	0.73	266	1.45	-75.7	1.04
250	129	0.94	-93.3	1.2	112	0.99	-65.2	0.75	175	1.14	-67.6	0.98
300	131	0.98	-109	1.27	75.9	0.86	-88.4	1.41	147	1.11	-157	2.46
400	113	0.96	-98.8	1.19	57.9	0.79	-66.1	1.35	136	1.42	-53.7	0.97
500	96	0.95	-99.4	1.13	52.7	0.85	-76.9	1.78	105	1.4	-45.8	1.01
1000	65.9	0.97	-85.9	0.99	35.1	0.83	-59.8	2.4	50.2	1.29	-58.5	2.45
1500	54.3	0.94	-59	0.74	31.6	0.9	-13.5	0.95	68.4	2.18	-55.7	2.17
2000	67.2	1.31	-64.6	0.87	18.2	0.66	-10.2	1.09	62.4	1.8	-32.4	1.2
5000	46.9	1.01	-73.2	1.1	15	1.21	-12.1	1.22	36.7	0.76	-51.1	2.41
∞	40.3	1	-62.2	1	8.4	1	-13	1	56.1	1	-26.7	1

Table 7.4 The responses of Model 1a to EL40EWC in dispersion cases with d =1

Note: disp. (d) refers to the relative displacement between the two ends of the joints in the wave dispersion cases.
disp. (v) refers to the relative displacement between the two ends of the joints in the travelling wave cases.

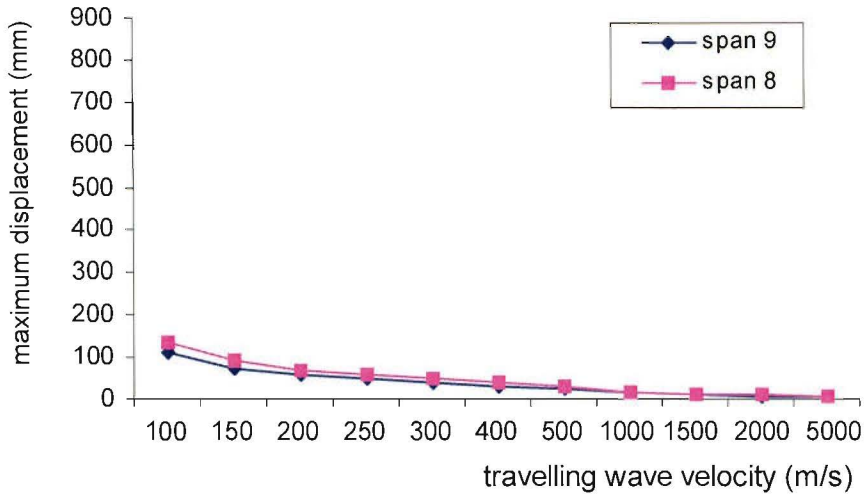

Figure 7.20 The differential displacement between pier supports in Model 1a to EL40EWC for the travelling wave cases

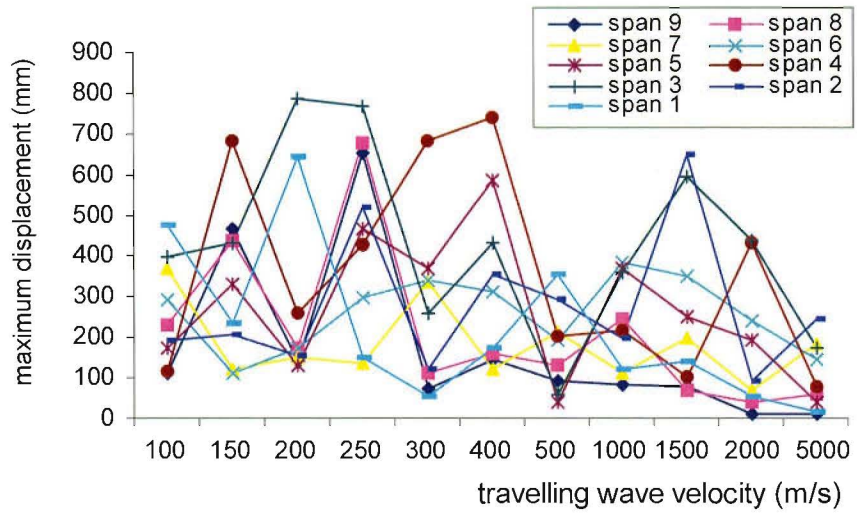

Figure 7.21 The differential displacement between pier supports in Model 1a to El40EWC for the wave dispersion cases with d = 1

displacements because the sliding bearings separated the bridge girder and the piers in the longitudinal direction. The differences of the relative displacements between the wave dispersion cases and the travelling wave cases increased as the wave dispersion factor was reduced. These were caused by the changes of their dynamic components due to the changes of the input acceleration spectra influenced by the wave dispersion.

From the displacement time-histories of the Abutment 10, the girder end and the bridge deck at the two sides of the joints in the wave dispersion cases with d = 1(in Figures 7.22 (a) to 7.22(c)), it also can be observed that the phase shifts increased with the decrease in the

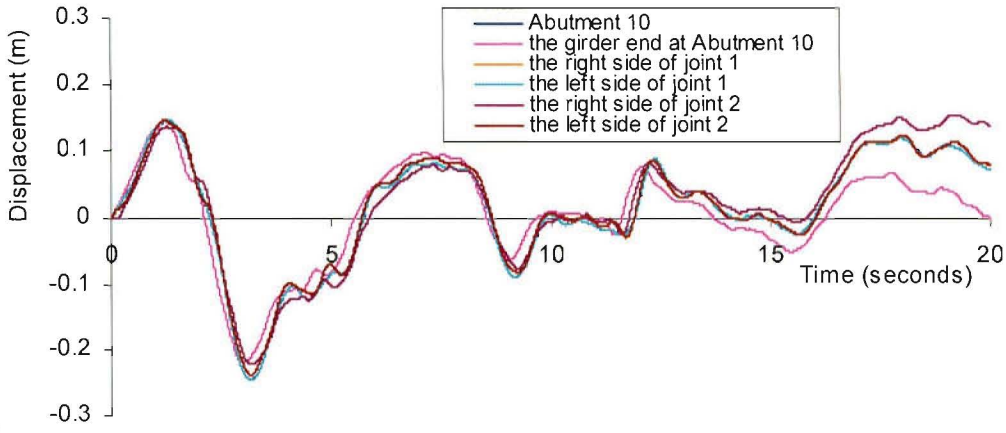

Figure 7.22(a) The response displacement time-histories of Model 1a to EL40EWC in the wave dispersion case with d = 1 and travelling wave velocity of 2000m/s

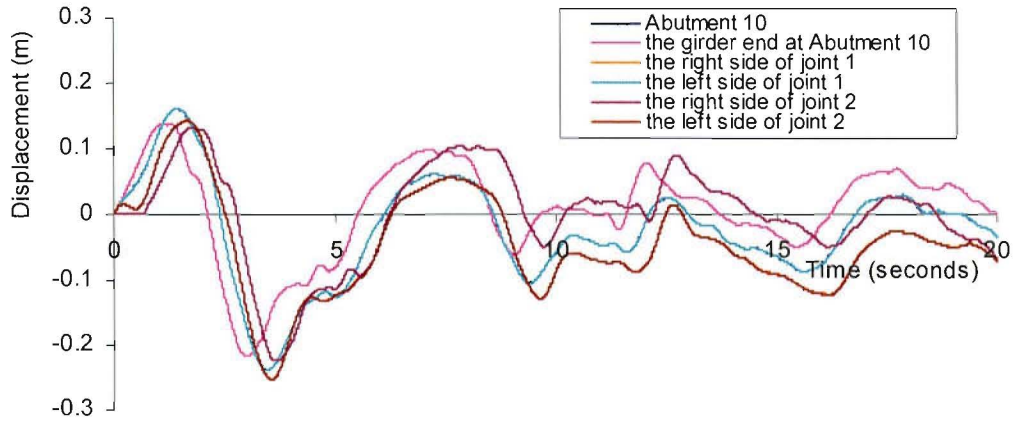

Figure 7.22(b) The response displacement time-histories of Model 1a to EL40EWC in the wave dispersion case with d = 1 and travelling wave velocity of 500m/s

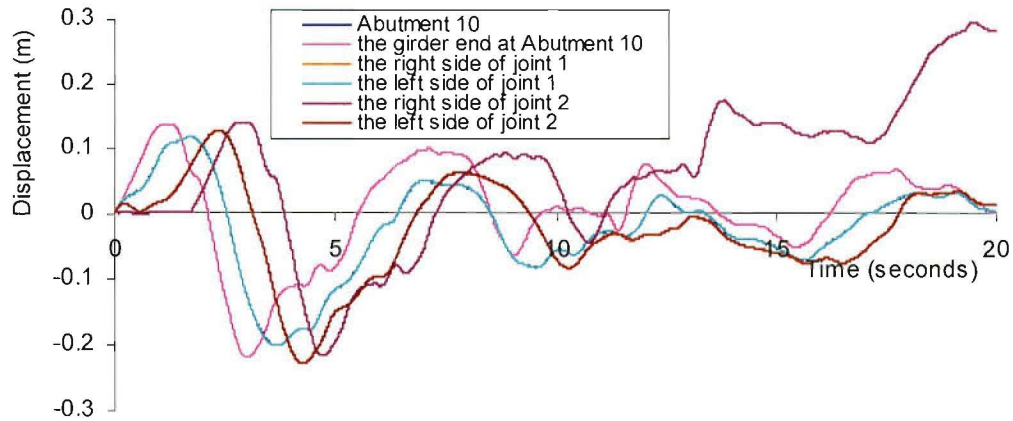

Figure 7.22(c) The response displacement time-histories of Model 1a to EL40EWC in the wave dispersion case with d = 1 and travelling wave velocity of 200m/s

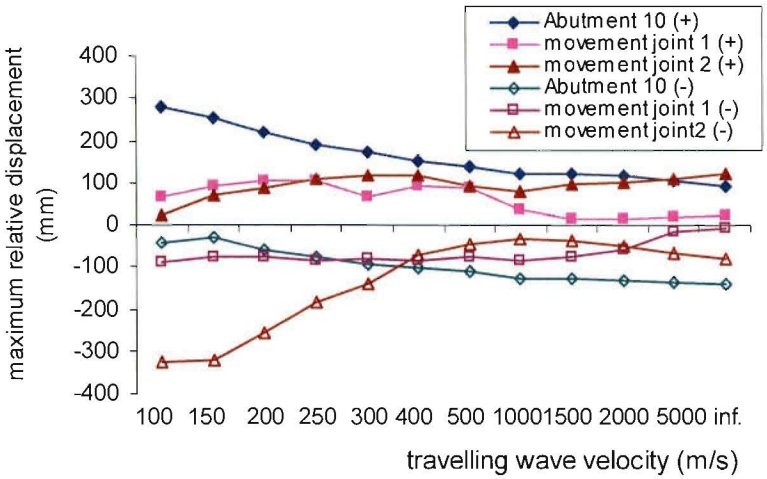

Figure 7.23 The responses of Model 1a to KOBE95EW in dispersion cases with d = 100

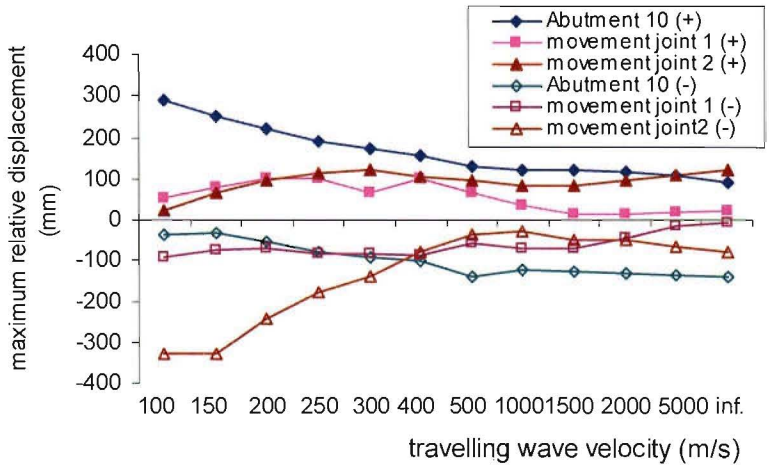

Figure 7.24 The responses of Model 1a to KOBE95EW in dispersion cases with d = 10

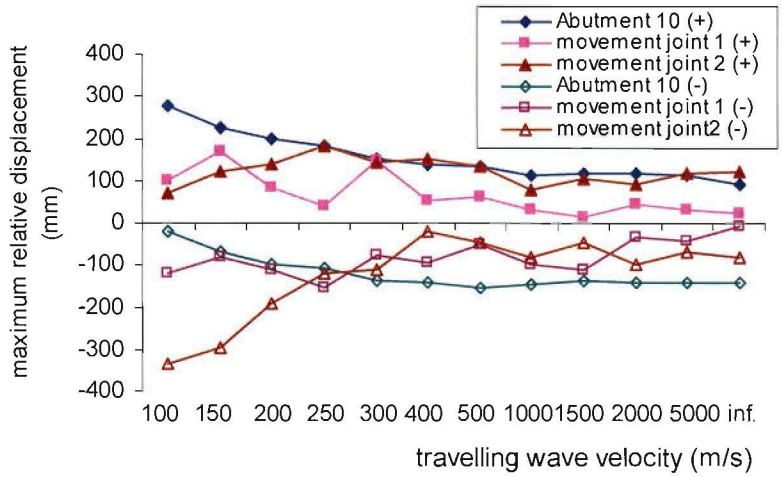

Figure 7.25 The responses of Model 1a to KOBE95EW in dispersion cases with d = 1

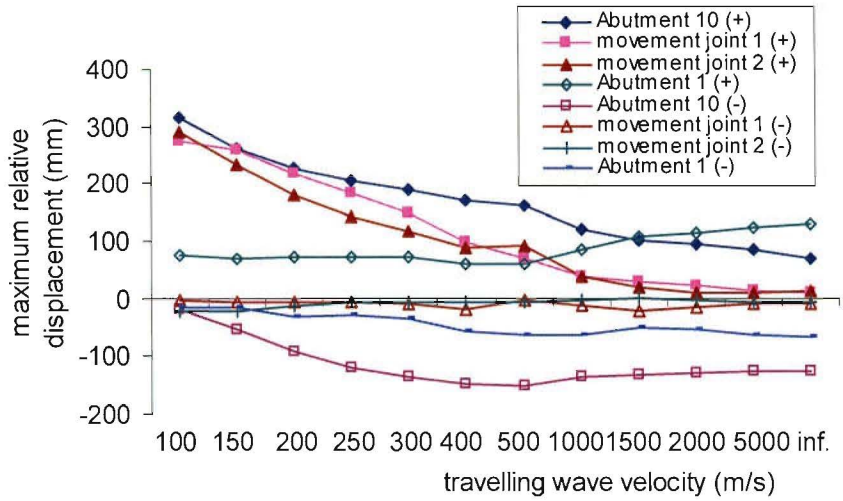

Figure 7.26 The responses of Model 3a to EL40EWC in the wave dispersion cases (d = 100)

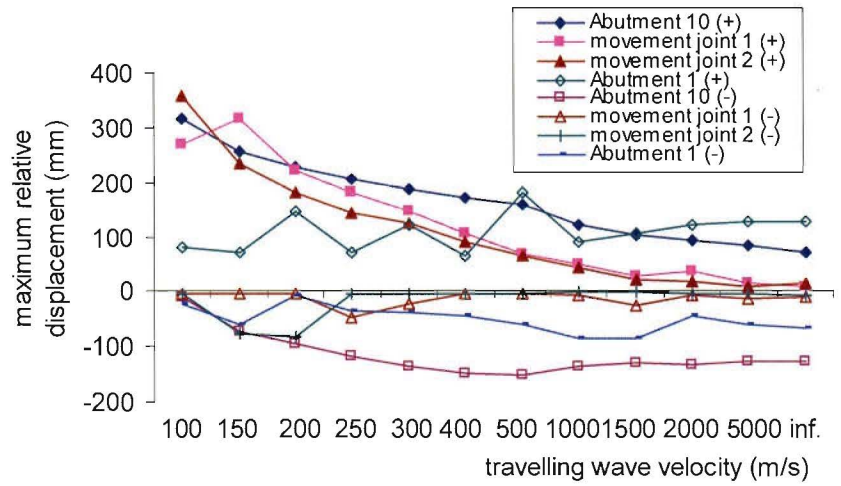

Figure 7.27 The responses of Model 3a to EL40EWC in the wave dispersion cases (d = 10)

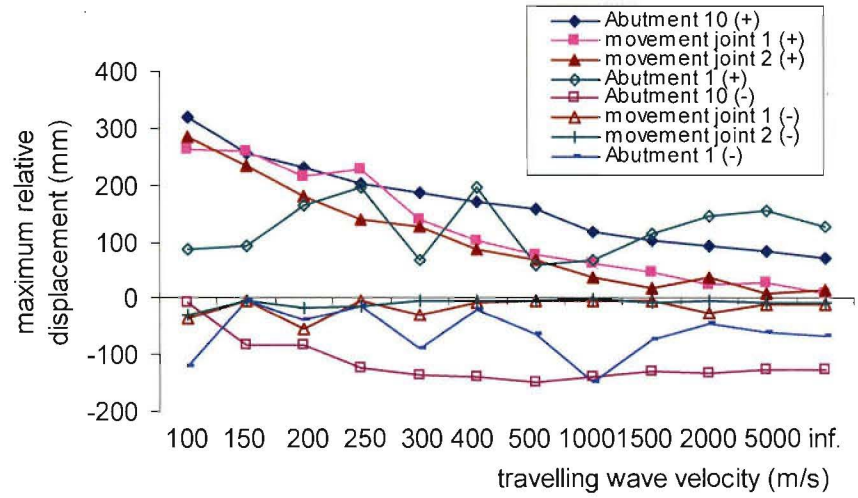

Figure 7.28 The responses of Model 3a to EL40EWC in the wave dispersion cases (d = 1)

travelling wave velocity, and the shapes of the response displacement time-histories of the bridge deck changed with the travelling wave velocity. The changes in the shapes of the response displacement time-histories of the bridge deck could also affect the response parameters.

The maximum relative displacements of the bridge deck across movement joint 2 in the wave dispersion cases showed greater differences than those in the travelling wave cases and the differences increased as the dispersion factor was reduced. This is because the displacement of the bridge deck at the left side of the movement joint 2 was almost the same as the displacement of Abutment 1. In Model 1a, the Abutment 1 was fixed and its displacement changed with the change of the asynchronous input motion that was directly affected by the geometric effect of the variability of the seismic motion. The more the input motion changed, the smaller the dispersion factor.

The seismic responses of the Model 1a to the generated time-histories conditioned by the East-West component of the Kobe 1995 earthquake record at Abutment 10 with dispersion factors of 100, 10 and 1 are presented in Figures 7.23 to 7.25. The positive maximum relative displacements of the bridge deck across the movement joints and the relative displacements between the girder end and the top of the Abutment 10 in these cases had similar trends to those in the travelling wave cases. The differences of these relative displacements between the wave dispersion cases and the travelling wave cases increased as the wave dispersion factor was reduced.

Figures 7.26 to 7.28 show the responses of Model 3a subjected to the generated time-histories conditioned by the East-West component of the El Centro 1940 earthquake record at Abutment 10 in the wave dispersion cases with dispersion factors of 100, 10 and 1 respectively. The responses showed similar trends to those of Model 1a in the corresponding cases. The positive maximum relative displacements of the bridge deck across the movement joints and the relative displacements between the girder end and the top of Abutment 10 were very similar to those in the travelling wave cases. It appears that the geometric effect does not have much effect on these relative displacements. However, the relative displacement between the girder end and the top of Abutment 1 changed with the change of the input seismic motion. These changes increase with the decrease of the dispersion factor and are unpredictable because the variations of the accelerations due to the geometric effects are assumed to be random in nature.

7.4 Summary

Analyses of the seismic responses of bridge models with movement joints subjected to different earthquake records applied in the bridge longitudinal direction were carried out. It was found that the longitudinal relative displacement of the bridge deck across the movement joints and the longitudinal relative displacement between the girder end and the top of the free abutment were sometimes greater in the asynchronous cases than those in the synchronous motion case. The longitudinal relative displacement between the joints in Model 1a in the asynchronous case (to EL40EWC) was up to 22 times that in the synchronous case. Hence the effect of the asynchronous input motions may be one of the main reasons for many bridges spans to collapse in the past earthquakes due to inadequate seating widths.

In the case of asynchronous motion, the relative displacements of the bridge deck across openings consist of two parts: the dynamic component due to the difference between the vibrations (inertia effects) of the two frames separated by the openings, and the pseudo-static component caused by the phase shifts between the vibrations of the two separated frames. The pseudo-static component dominated the total relative displacements when the travelling wave velocity was low.

Although the phase shifts increased as the travelling wave velocity decreased, the pseudo-static components of these longitudinal relative displacements did not increase in the same way. The pseudo-static components of the relative displacements not only depended on the phase shifts but were also related to the shapes of the response displacement time-histories of the bridge deck. These will change with the travelling wave velocity in the asynchronous motion cases.

The differential displacements between the pier supports had little effect on the investigated parameters even in the wave dispersion cases because the bridge deck was separated from the piers by the sliding bearings. Hence the geometric incoherence effect has little influence on the maximum longitudinal relative displacements between the joints. For Model 1a (varying pier heights) to EL40EWC, the relative displacement between the joints in the travelling wave case reached up to 20.8 times that in the synchronous case, and the relative displacement between the joints in dispersion case (d=1) reached up to 22.8 times that in the synchronous case. For Model 3a (regular, 'taller' pier) to EL40EWC, the relative displacement between the joints in travelling wave case reached up to 14 times that in the synchronous case, and the

relative displacement between the joints in the dispersion case (d=1) reached up to 14.5 times that in the synchronous case.

From the responses of Model 3a, the 'direction of travel' dependence of the responses to travelling waves also can be noticed. The trends of the longitudinal relative displacement between the girder end and the top of the free abutment were different for Abutments 1 and 10. In a design situation engineer would have to consider wave travel from both directions.

For Model 3a, the maximum longitudinal relative displacement between the girder end and the top of the free abutment at Abutment 10 in the asynchronous cases varied from 1.2 to 4 greater times than that in the synchronous case for different input earthquake records. The maximum longitudinal relative displacement between the movement joints between adjacent section of bridge in Model 3a in the asynchronous cases varied from 4 to 14 times greater that in the synchronous case for different input earthquakes.

CHAPTER 8

SUMMARY OF THIS RESEARCH

8.1 The Generation of the Asynchronous Input Seismic Motions

A nonlinear analysis of a bridge subjected to asynchronous input motion does not present more computational difficulties than those involved in a synchronous analysis, provided that appropriate asynchronous input time-histories are used. Hence, the first issue in this research was to develop a method of easily generating appropriate asynchronous input time-histories. The earthquake input ground motions were assumed as a homogeneous n-variate Gaussian random vector field $\mathbf{f}(x) = [f_1(x), f_2(x), \cdots, f_n(x)]^T$, with zero-mean and cross-covariances $R[f_k(x_i), f_l(x_j)] = E[f_k(x_i) f_l(x_j)]$ for (k, l = *1, 2, ... , n*); and $\mathbf{g}(x_i)$ (i =*1, 2, ..., N*) is a set of realizations of the vector field $\mathbf{f}(x)$ at locations x_i. Thus, the generation of the asynchronous input seismic motions became a simulation of the stochastic vector field $\mathbf{f}(x)$ under the condition that N realizations $\mathbf{g}(x_i)$ were known. Two assumptions were made by the author in order to make the conditional simulation of the seismic waves simpler and more effective.

The first assumption was that the spatial correlation function only depended on the predominant frequency of the earthquake motion. Actually, the loss of coherency of seismic waves is frequency dependent with more significant effects at higher frequencies. For frequencies lower than 1 Hz, the coherence is close to 1; it starts to decrease significantly for frequencies higher than 5 Hz [Luco and Wong 1986, Oliveira et al. 1991]. The correlation of the band of frequencies was represented by one spatial correlation function for reasons of simplicity in the proposed method. This assumption enabled the simulation of conditional ground motion to be performed in the time domain without involving computations of convolution integrals. The second assumption was that in the time domain, there was no correlation between elements in the same record.

With the aid of these two assumptions, the modified Kriging method proposed by Hoshiya could be easily used to conditionally simulate ground motions in the time domain. The numerical examples showed that the method was effective and could be easily implemented in engineering analyses. The results were reasonable because the spectra of the simulated time-histories and the specified earthquake record were very close to each other. The variation in the simulated accelerations with separation distance between the supports and wave propagation velocity followed the rules expected, which are based on the main characteristics of the spatial variability of the seismic motion indicated by the extensive analyses of the records from arrays of strong-motion seismographs.

In this study, the results have not been compared with those obtained from other approaches and have also not been directly compared with the incoherence observed in recorded ground motions. This would be a useful next step for future research, and give users added confidence. Also the 'd' factor needs correlation and validation with real field local geological and topographical conditions to allow engineers to produce asynchronous motions suited to the characteristics of a particular site.

8.2 The Wave Passage Effect on the Seismic Response of Long Bridges

The geometric incoherence effect can be neglected if only low-frequency (long-period) regions of the response spectrum are of interest, and only the wave passage effect needs to be taken into consideration. Chapter 5 dealt with the wave passage effect of the spatial variability of the seismic motions on the transverse responses of both regular bridges and irregular bridges with piers of different heights. It was found that the velocity of propagation of seismic waves had a significant effect on the transverse response of long bridges. Despite the bridge models having quite different configurations, the variations of transverse response with the travelling wave velocity followed very similar trends for all three natural earthquake records used in both the elastic and the inelastic analyses. Generally, when the travelling wave velocity was between 150m/s to 300m/s the transverse responses had a minimum value. When the travelling wave velocity was less and greater than those values, the transverse responses increased. The responses for the travelling wave cases could be more critical than that of the synchronous case as shown for example in Tables 8.1 to 8.3 and Tables 8.4 to 8.6, where the ratios of the responses of the Models 1 (varying pier heights) and 3 (regular 'taller' piers)

	Pier 2	Pier 3	Pier 4	Pier 5	Pier 6	Pier 7	Pier 8	Pier 9
100m/s	5.42	2.46	1.67	0.6	0.83	1.04	1.17	1.07
125m/s	4.5	2.32	0.9	0.72	0.72	0.73	0.62	0.99
150m/s	4.08	1.98	1.16	0.97	0.65	0.84	0.82	1.06
200m/s	2.6	0.89	0.51	0.56	0.45	0.37	0.4	0.88
250m/s	2.22	0.89	0.54	0.57	0.45	0.36	0.37	0.88
300m/s	1.83	0.57	0.9	0.7	0.55	0.48	0.5	0.87
400m/s	2.18	1.72	1.32	1.1	0.69	0.68	0.7	0.9
500m/s	2.75	2.16	1.64	1.31	0.83	0.83	0.82	1.08
1000m/s	1.68	1.72	1.71	1.45	0.92	0.83	0.97	1.23
1500m/s	1.47	1.56	1.52	1.39	0.95	0.8	0.86	1.1
2000m/s	1.38	1.47	1.43	1.32	0.98	0.84	0.81	1.02
synchronous	1	1	1	1	1	1	1	1

Table 8.1 The ratios of the response maximum pier drifts of Model 1 to EL40NSC

	Pier 2	Pier 3	Pier 4	Pier 5	Pier 6	Pier 7	Pier 8	Pier 9
100m/s	3.91	2.51	2.02	1.53	1.23	1.6	1.71	1.14
125m/s	3.54	1.91	1.38	1.53	1.16	1.23	1.28	1.11
150m/s	3.08	1.58	1.06	1.53	1.16	1.35	1.27	1.23
200m/s	2.62	1.17	1.11	0.97	0.75	0.64	1.13	1.07
250m/s	2.09	0.79	0.9	0.71	0.61	0.74	1.02	1.14
300m/s	1.68	0.52	1.14	0.74	0.69	0.69	0.91	1.17
400m/s	1.28	0.79	1.26	0.89	0.92	0.68	0.64	1.24
500m/s	1.11	0.85	1.31	0.95	0.98	0.84	0.84	1.22
1000m/s	0.85	0.53	1.3	0.97	0.9	0.67	0.85	1.11
1500m/s	0.84	0.61	1.2	1.01	0.87	0.56	0.79	1.08
2000m/s	0.92	0.75	1.16	1.03	0.92	0.58	0.84	1.03
synchronous	1	1	1	1	1	1	1	1

Table 8.2 The ratios of the response maximum section curvature ratios of the piers of Model 1 to EL40NSC

	Pier 2	Pier 3	Pier 4	Pier 5	Pier 6	Pier 7	Pier 8	Pier 9
100m/s	7.19	3.46	2.7	0.83	1.04	1.5	1.63	1.12
125m/s	4.96	2.24	1.09	0.98	0.88	1.02	1.02	1.08
150m/s	4.08	1.88	1.14	1.24	0.7	1.23	1.12	1.28
200m/s	3.08	1.12	0.73	0.7	0.44	0.52	0.98	0.98
250m/s	2.42	0.9	0.71	0.65	0.39	0.5	0.84	1.02
300m/s	2.04	0.59	1.02	0.74	0.47	0.54	0.67	1.04
400m/s	1.88	1.32	1.53	1.18	0.67	0.65	0.74	1.05
500m/s	1.96	1.56	2.01	1.53	0.9	0.87	0.91	1.18
1000m/s	1.12	1.12	2.13	1.72	0.86	0.87	1.09	1.32
1500m/s	1.08	0.88	1.73	1.59	0.91	0.79	0.95	1.12
2000m/s	1.08	0.9	1.5	1.53	0.95	0.77	0.91	1.02
synchronous	1	1	1	1	1	1	1	1

Table 8.3 The ratios of the response maximum pier shear forces of Model 1 to EL40NSC

	Pier 2	Pier 3	Pier 4	Pier 5	Pier 6	Pier 7	Pier 8	Pier 9
100m/s	0.68	0.48	0.35	0.29	0.2	0.27	0.31	0.54
125m/s	0.54	0.43	0.25	0.17	0.15	0.21	0.32	0.52
150m/s	0.41	0.3	0.21	0.18	0.25	0.3	0.33	0.53
200m/s	0.75	0.47	0.36	0.39	0.43	0.46	0.49	0.67
250m/s	1.11	0.72	0.61	0.58	0.52	0.53	0.53	0.61
300m/s	1.28	0.89	0.79	0.71	0.62	0.6	0.6	0.66
400m/s	1.31	1.04	0.94	0.83	0.75	0.71	0.71	0.79
500m/s	1.29	1.1	1	0.89	0.82	0.79	0.77	0.88
1000m/s	1.2	1.09	1.05	0.99	0.94	0.93	0.94	0.93
1500m/s	1.18	1.07	1.06	1.01	0.97	0.96	0.97	0.92
2000m/s	1.16	1.07	1.05	1.02	0.98	0.97	0.97	0.93
synchronous	1	1	1	1	1	1	1	1

Table 8.4 The ratios of the response maximum pier drifts of Model 3 to EL40NSC

	Pier 2	Pier 3	Pier 4	Pier 5	Pier 6	Pier 7	Pier 8	Pier 9
100m/s	0.9	0.72	0.54	0.42	0.33	0.52	0.64	0.81
125m/s	0.72	0.61	0.38	0.28	0.22	0.34	0.51	0.81
150m/s	0.58	0.51	0.36	0.24	0.29	0.36	0.46	0.76
200m/s	0.94	0.49	0.34	0.35	0.4	0.51	0.61	0.94
250m/s	1.36	0.77	0.62	0.5	0.44	0.54	0.58	0.76
300m/s	1.62	0.94	0.81	0.6	0.51	0.57	0.63	0.81
400m/s	1.59	1.12	0.94	0.69	0.6	0.67	0.72	0.91
500m/s	1.48	1.16	1.02	0.76	0.65	0.72	0.76	1.01
1000m/s	1.28	1.08	1.11	0.97	0.87	0.85	0.94	0.97
1500m/s	1.23	1.06	1.15	1.02	0.93	0.88	0.98	0.97
2000m/s	1.2	1.05	1.13	1.03	0.95	0.9	1.01	0.97
synchronous	1	1	1	1	1	1	1	1

Table 8.5 The ratios of the response maximum section curvature ratios of the piers of Model 3 to EL40NSC

	Pier 2	Pier 3	Pier 4	Pier 5	Pier 6	Pier 7	Pier 8	Pier 9
100m/s	1.05	1.01	0.84	0.88	0.77	0.9	0.79	1.01
125m/s	0.85	0.82	0.66	0.62	0.51	0.59	0.71	1.03
150m/s	0.72	0.74	0.62	0.51	0.58	0.55	0.62	0.94
200m/s	1.05	0.51	0.45	0.55	0.61	0.63	0.76	1.15
250m/s	1.52	0.79	0.7	0.73	0.62	0.6	0.66	0.91
300m/s	1.65	0.97	0.91	0.86	0.7	0.63	0.68	0.91
400m/s	1.65	1.17	1.02	0.96	0.8	0.7	0.74	1.01
500m/s	1.59	1.19	1.03	0.96	0.86	0.76	0.78	1.12
1000m/s	1.31	1.06	1.02	0.99	0.96	0.88	0.97	1
1500m/s	1.25	1.03	1.02	1	0.97	0.93	0.98	1.03
2000m/s	1.22	1.04	1.02	1	0.97	0.94	0.99	1.03
synchronous	1	1	1	1	1	1	1	1

Table 8.6 The ratios of the response maximum pier shear forces of Model 3 to EL40NSC

respectively when they were subjected to the El Centro 1940 earthquake NS component record for the travelling wave cases to those in the corresponding synchronous case are listed.

The response of a bridge to asynchronous input motions consists of two components: a dynamic component induced by the inertia forces and a so-called pseudo-static component, due to the difference between the adjacent support displacements. When the travelling wave velocity was greater than between 150 m/s to 300 m/s, the seismic responses were dominated by their dynamic components, which increased considerably with the increase of the travelling wave velocity. They were close to the synchronous case values when the travelling velocity was greater than 1000 m/s. When the travelling wave velocity was less than between 150 m/s to 300 m/s the seismic responses were dominated by their pseudo-static components, which increased with the decrease of the travelling wave velocity. This was due to the fact that the differential displacements between adjacent pier supports increased sharply. Comparing the responses of Model 1 with those of Model 3, it is clear that the stiffer the bridge, the greater the pseudo-static component had effect on the responses. It was observed that the travelling wave velocity at which the transverse response had a minimum value, depended mainly on the stiffness of the bridge model; the stiffer the bridge, the higher this travelling wave velocity. The spectrum of the average seismic accelerations for the whole bridge varied with the travelling wave velocity, which caused the local variations of the transverse response with the travelling velocity.

From the designer point of view, it is important that for Models 3 and 5 (regular symmetric structures) the maximum pier drifts and section curvature ratios of most piers (including those with the greatest demands in the synchronous case) is very little changed for wave velocities down to 1000m/s and then decreases significantly with decreasing wave velocity. Only the maximum shear forces in piers in the travelling wave cases could be greater than those in the synchronous case because as the pier height decrease the pseudostatic component of the response increases. In the responses to EL40NSC, the maximum shear forces in most piers (except pier 2) of Model 3 ('taller' piers) in the travelling wave case were smaller than those in the synchronous case but the maximum shear forces in all piers of Model 5 ('shorter' piers) in the lower travelling wave velocity case were greater than those in the synchronous cases by a factor of 1.2 to 2.

From the responses of Models 3 and 5 (regular symmetric structures), the 'direction of travel' dependence of the responses to travelling waves can be noticed. The responses of long bridges

to asynchronous motions is dependent on the direction of wave travel i.e. which end of the bridge the earthquake comes from.

Comparing the responses of same models (for Models 1 ~ 5) to EL40NSC with different input scale factors, it can be seen that the same conclusions are generally valid for inelastic response as for elastic response.

The velocity of the travelling wave played an important role in the transverse response of the long bridges when only the wave-passage effect was considered.

8.3 The Effects of the Combined Geometric Incoherence and Wave Passage on the Seismic Response of Long Bridges

In Chapter 6 the combined geometric incoherence and wave passage effects of the spatial variability of the seismic motions on the transverse responses of the long bridges were investigated. These cases are referred to as the wave dispersion cases. The proposed method presented in Chapter 3 was employed to generate the asynchronous input motions in which both the geometric incoherence and the wave passage effects were considered. Three natural earthquake records were used as the specified earthquake motion at Abutment 10 when the responses of the three different bridge models were produced for the wave dispersion cases. It was found that the geometric incoherence effect played an important role in these responses through the pseudo-static component. In the wave dispersion cases the pseudo-static component consists of two parts, one is caused by the wave passage effect and the other is due to the geometric incoherence effect. The influence of the second part on the total responses increased as the amount of the wave dispersion increased and for the cases with less dispersion, it had minimal influence on the total response and was similar to the travelling wave case. For the cases with large dispersion, this part dominated the responses. The total responses are therefore unpredictable when the dispersion was large, because the pseudo-static components caused by the geometric incoherence effect was random. Tables 8.7 to 8.9 and Tables 8.9 to 8.12 show the ratios of the maximum pier drifts of the Models 1 and 3 respectively subjected to the El Centro 1940 earthquake NS component record with input scale factor of 0.5 in the wave dispersion cases (with wave dispersion factor d = 100, 10, 1 respectively) to those in the corresponding synchronous case. The influence of the pseudo-static component caused by the geometric incoherence effect on the total responses also

	Pier 2	Pier 3	Pier 4	Pier 5	Pier 6	Pier 7	Pier 8	Pier 9
100m/s	4.56	2.39	1.28	0.48	0.65	1.02	0.92	0.67
125m/s	7.63	2.8	0.96	0.61	0.65	0.77	0.58	0.61
150m/s	7.55	1.51	0.96	0.82	0.61	0.71	0.73	0.66
200m/s	2.7	0.89	0.61	0.55	0.4	0.32	0.33	0.6
250m/s	3.19	0.81	0.41	0.39	0.4	0.31	0.37	0.45
300m/s	1.7	1.07	0.61	0.51	0.45	0.41	0.41	0.46
400m/s	2.11	1.43	0.99	0.89	0.68	0.6	0.6	0.61
500m/s	3.3	1.86	1.3	1.07	0.77	0.7	0.74	0.76
1000m/s	2.8	1.83	1.52	1.23	1.02	0.89	0.91	0.83
1500m/s	1.27	1.54	1.4	1.2	1.03	0.88	0.9	0.88
2000m/s	1.48	1.31	1.38	1.15	1.03	0.92	0.9	0.91
synchronous	1	1	1	1	1	1	1	1

Table 8.7 The ratios of the response maximum pier drifts of Model 1 to EL40NSC with input scale factor of 0.5 in the wave dispersion cases with $d = 100$

	Pier 2	Pier 3	Pier 4	Pier 5	Pier 6	Pier 7	Pier 8	Pier 9
100m/s	13.22	4.16	1.64	0.5	0.65	1.38	3.23	0.68
125m/s	15.72	4.85	0.82	1.03	1.64	1.05	0.83	0.55
150m/s	16.14	2.09	2	1.91	1.09	0.85	0.64	0.68
200m/s	8.52	5.48	0.62	0.77	0.59	1.2	1.37	0.59
250m/s	4.92	3.78	0.78	0.37	0.62	1.35	0.57	0.44
300m/s	6.64	1.08	0.66	1.56	0.87	0.95	0.49	0.46
400m/s	9.25	3.32	1.74	1.16	0.63	0.64	0.83	0.62
500m/s	12.48	1.93	1.58	1.09	0.82	0.89	0.67	0.75
1000m/s	4.95	1.61	1.47	1.42	0.97	0.95	0.86	0.83
1500m/s	3.2	1.98	1.29	1.35	0.96	0.91	0.9	0.86
2000m/s	3.03	2.58	1.37	1.24	1.01	0.96	0.92	0.92
synchronous	1	1	1	1	1	1	1	1

Table 8.8 The ratios of the response maximum pier drifts of Model 1 to EL40NSC with input scale factor of 0.5 in the wave dispersion cases with $d = 10$

	Pier 2	Pier 3	Pier 4	Pier 5	Pier 6	Pier 7	Pier 8	Pier 9
100m/s	16.58	3.98	0.94	4.67	0.92	3.52	0.85	0.73
125m/s	64.72	6.78	4.92	1.72	1.42	3.58	2.87	0.47
150m/s	7.72	3.89	0.99	5.12	3.18	1.92	1.18	0.63
200m/s	7.81	5.52	2.95	2.17	0.59	1.43	1.66	0.6
250m/s	36.27	4.84	2.04	3.08	0.72	0.8	1.18	0.45
300m/s	12.89	12.96	5.31	3.97	3.56	1.34	1.02	0.46
400m/s	4.05	9.82	6.48	1.05	1.08	6.13	2.53	0.58
500m/s	6.95	6.28	1.66	1.19	0.75	2.7	2.38	0.79
1000m/s	35.2	7.31	1.61	6.15	1.83	1.13	1.46	0.84
1500m/s	12.89	2.21	1.55	2.08	2.09	3.06	1.13	0.84
2000m/s	7.55	8.52	1.28	2.04	1.01	1.12	1.17	0.93
synchronous	1	1	1	1	1	1	1	1

Table 8.9 The ratios of the response maximum pier drifts of Model 1 to EL40NSC with input scale factor of 0.5 in the wave dispersion cases with $d = 1$

	Pier 2	Pier 3	Pier 4	Pier 5	Pier 6	Pier 7	Pier 8	Pier 9
100m/s	0.66	0.44	0.37	0.33	0.23	0.27	0.39	0.6
125m/s	0.63	0.51	0.27	0.17	0.2	0.33	0.36	0.57
150m/s	0.49	0.36	0.23	0.19	0.25	0.32	0.41	0.54
200m/s	0.74	0.51	0.39	0.42	0.43	0.45	0.51	0.71
250m/s	1.12	0.77	0.61	0.62	0.5	0.55	0.52	0.63
300m/s	1.22	1	0.79	0.71	0.62	0.63	0.59	0.68
400m/s	1.31	1.06	0.92	0.85	0.75	0.7	0.72	0.8
500m/s	1.3	1.12	1.05	0.89	0.82	0.76	0.75	0.91
1000m/s	1.18	1.14	1.05	0.99	0.95	0.93	0.97	0.93
1500m/s	1.15	1.13	1.1	0.99	0.95	0.96	0.95	0.94
2000m/s	1.12	1.15	1.09	1	0.97	0.96	0.96	0.93
synchronous	1	1	1	1	1	1	1	1

Table 8.10 The ratios of the response maximum pier drifts of Model 3 to EL40NSC in the wave dispersion cases with $d = 100$

	Pier 2	Pier 3	Pier 4	Pier 5	Pier 6	Pier 7	Pier 8	Pier 9
100m/s	1.12	1.16	0.42	1.05	0.31	0.43	0.39	0.67
125m/s	0.74	0.73	0.8	0.28	0.71	0.93	0.42	0.51
150m/s	0.72	1.09	0.37	0.61	0.4	0.54	0.37	0.55
200m/s	0.87	1.07	1.08	0.93	0.43	0.53	0.58	0.77
250m/s	1.14	1.36	0.64	0.58	0.68	0.52	1.2	0.6
300m/s	1.27	0.94	0.8	0.75	0.61	1.16	0.65	0.7
400m/s	1.36	1.45	0.93	0.93	0.76	0.72	0.73	0.82
500m/s	1.3	1.07	1.22	0.89	1.06	0.85	0.74	0.93
1000m/s	1.23	1.08	1.11	1	0.91	0.94	0.94	0.92
1500m/s	1.19	1.13	1.14	1.02	1.03	0.96	1.02	0.91
2000m/s	1.2	1.11	1.02	0.99	0.97	0.96	1	0.92
synchronous	1	1	1	1	1	1	1	1

Table 8.11 The ratios of the response maximum pier drifts of Model 3 to EL40NSC in the wave dispersion cases with $d = 10$

	Pier 2	Pier 3	Pier 4	Pier 5	Pier 6	Pier 7	Pier 8	Pier 9
100m/s	0.71	1.68	0.55	1.16	1.09	0.47	1.39	1.61
125m/s	0.79	0.65	0.59	1.47	0.25	1.31	0.88	0.52
150m/s	0.64	0.56	0.7	1.24	1.48	0.85	2.37	0.6
200m/s	1.07	1.14	1.36	1.75	0.58	0.93	2	0.75
250m/s	1.04	1.43	0.84	0.82	1.63	0.75	0.63	0.64
300m/s	1.2	2.83	0.68	0.99	0.63	0.73	1.74	1.86
400m/s	2.34	1.12	0.95	0.85	1.11	0.76	0.86	0.74
500m/s	1.99	2.13	1.24	0.87	0.9	1.05	0.81	0.84
1000m/s	1.22	1.21	1	1.19	1.1	0.93	1.12	0.9
1500m/s	1.28	1.09	1.07	1.1	1.2	1.17	0.99	0.95
2000m/s	1.29	1.12	1.11	1.07	1.11	1.04	0.91	0.95
synchronous	1	1	1	1	1	1	1	1

Table 8.12 The ratios of the response maximum pier drifts of Model 3 to EL40NSC in the wave dispersion cases with $d = 1$

increased with the decrease of the travelling wave velocity, and with the increase of the distance from the abutment where the seismic motion was specified.

The geometric incoherence effect affected the total transverse responses of long bridges through the pseudo-static components of the response. The stiffer the bridge, the greater was the effect of the geometric incoherence. The responses for the dispersion cases for all configurations studied were more critical than those for the travelling wave cases and the synchronous case when wave dispersion was greater (reducing 'd' factor).

8. 4 The Effect of the Spatial Variability of the Seismic Motions on the Longitudinal Response of Long Bridges

The longitudinal responses of the long bridges in both the travelling wave and the wave dispersion cases, special emphasis was placed on the effect of the spatial variability of the seismic motions on the maximum relative displacements of the bridge deck across movement joints and between the girder ends and the top of the abutments. Two bridge models and three natural earthquake records were used in the analyses. In asynchronous motion cases, it was found that the relative displacement of the bridge deck across the movement joint and the relative displacement between the girder end and the abutment consist of two parts: the dynamic component due to the difference between the vibrations of the two frames separated by the movement joints, and the pseudo-static component caused by the phase shifts between the vibrations.

Although the phase shifts increased as the travelling wave velocity was decreased, the pseudo-static components of the relative displacements did not necessarily also increase. The pseudo-static components of these relative displacements not only depended on the phase shifts, but also were related to the shapes of the response displacement time-histories of the bridge deck which will change with the travelling wave velocity. Tables 8.13 to 8.15 show the ratios of the response parameters investigated for the longitudinal response of Model 1a subjected to the different earthquake records in the travelling wave cases to those in the corresponding synchronous case. It is important to note that some responses of the travelling wave cases were more critical than those of the synchronous case.

	At Abutment 10		At Movement joint 1		At Movement joint 2	
	positive	negative	positive	negative	positive	negative
100m/s	4	1.38	18.21	5.95	4.62	7.27
150m/s	4	1.11	20.83	6.42	3.71	4.94
200m/s	3.57	1.05	17.74	8.62	3.28	2.73
250m/s	3.4	1.25	13.45	6.71	2.75	2.57
300m/s	3.3	1.38	10.49	4.82	2.37	2.39
400m/s	2.93	1.34	8.77	3.75	1.71	2.08
500m/s	2.51	1.42	7.42	3.32	1.34	1.69
1000m/s	1.68	1.39	5.01	1.92	0.69	0.9
1500m/s	1.44	1.28	4.2	1.09	0.56	0.96
2000m/s	1.28	1.19	3.3	0.72	0.62	1.01
5000m/s	1.16	1.07	1.48	0.76	0.86	0.79
synchronous	1	1	1	1	1	1

Table 8.13 The ratios of the maximum relative displacements for Model 1a to EL40EWC in the traveling wave cases

	At Abutment 10		At Movement joint 1		At Movement joint 2	
	positive	negative	positive	negative	positive	negative
100m/s	3.17	0.29	2.71	9.56	0.23	3.94
150m/s	2.9	0.21	3.68	8.24	0.56	4
200m/s	2.45	0.44	4.83	7.67	0.74	3.08
250m/s	2.14	0.54	4.24	9.06	0.87	2.31
300m/s	1.95	0.67	2.82	8.55	0.98	1.74
400m/s	1.7	0.74	3.89	9.22	0.93	0.94
500m/s	1.55	0.79	3.27	8.28	0.76	0.59
1000m/s	1.35	0.9	1.53	8.37	0.62	0.44
1500m/s	1.38	0.9	0.52	8.18	0.78	0.49
2000m/s	1.34	0.94	0.54	5.99	0.83	0.6
5000m/s	1.19	0.97	0.76	1.79	0.88	0.87
synchronous	1	1	1	1	1	1

Table 8.14 The ratios of the maximum relative displacements for Model 1a to KOBE95EW in the traveling wave cases

	At Abutment 10		At Movement joint 1		At Movement joint 2	
	positive	negative	positive	negative	positive	negative
100m/s	2.07	0.47	5.11	10.99	0.52	3.54
150m/s	2.29	0.58	3.94	13.16	1.03	2.75
200m/s	2.37	0.61	4.83	14.33	0.96	2.38
250m/s	2.32	0.65	5.26	12.43	0.78	1.76
300m/s	2.26	0.69	5.25	9.7	0.66	1.49
400m/s	2.33	0.64	2.85	12.19	0.62	0.75
500m/s	2.43	0.56	1.79	14.38	0.53	0.29
1000m/s	1.96	0.7	0.6	12.09	0.83	0.17
1500m/s	1.56	0.9	0.63	6.05	0.95	0.23
2000m/s	1.46	0.91	0.58	3.91	0.92	0.34
5000m/s	1.24	0.91	0.81	1.26	0.89	0.79
synchronous	1	1	1	1	1	1

Table 8.15 The ratios of the maximum relative displacements for Model 1a to SYLM94D in the traveling wave cases

	At Abutment 10		At Movement joint 1		At Movement joint 2	
	positive	negative	positive	negative	positive	negative
100m/s	4	1.38	18.1	6.15	4.65	7.98
150m/s	3.97	1.11	20.95	6.53	3.67	5.69
200m/s	3.6	1.01	17.86	8.69	3.24	2.74
250m/s	3.4	1.27	13.57	6.31	2.76	2.57
300m/s	3.28	1.4	10.98	4.84	2.37	2.38
400m/s	2.93	1.3	9.77	3.75	1.7	2.24
500m/s	2.51	1.41	6.51	3.32	1.36	1.69
1000m/s	1.68	1.45	5.37	1.92	0.71	0.89
1500m/s	1.43	1.27	3.67	1.27	0.66	0.92
2000m/s	1.28	1.16	3.37	0.73	0.58	1.08
5000m/s	1.15	1.05	1.43	0.77	0.79	0.82
synchronous	1	1	1	1	1	1

Table 8.16 The ratios of the maximum relative displacements for Model 1a to EL40EWC in the wave dispersion cases with $d = 100$

	At Abutment 10		At Movement joint 1		At Movement joint 2	
	positive	negative	positive	negative	positive	negative
100m/s	4.07	1.38	17.86	6.22	4.65	5.62
150m/s	4.02	1.11	20.95	6.43	3.69	4.42
200m/s	3.5	1.28	18.33	8.23	3.32	2.71
250m/s	3.42	0.99	12.86	8.15	2.82	2.56
300m/s	3.33	1.1	9.94	5.38	2.32	2.38
400m/s	2.9	1.72	8.56	3.73	1.64	3.32
500m/s	2.39	2.09	6.29	3.98	1.43	2.95
1000m/s	1.69	1.48	4.17	2.75	0.76	0.88
1500m/s	1.43	1.33	4.65	1.08	0.48	0.99
2000m/s	1.29	1.3	3.2	0.81	0.84	0.75
5000m/s	1.18	1.09	1.79	0.72	0.93	0.8
synchronous	1	1	1	1	1	1

Table 8.17 The ratios of the maximum relative displacements for Model 1a to EL40EWC in the wave dispersion cases with $d = 10$

	At Abutment 10		At Movement joint 1		At Movement joint 2	
	positive	negative	positive	negative	positive	negative
100m/s	3.95	1.38	17.5	11.62	4.78	6.93
150m/s	3.75	1.44	22.02	6.29	3.48	7.68
200m/s	3.37	1.35	18.93	6.3	4.74	2.84
250m/s	3.2	1.5	13.33	5.02	3.12	2.53
300m/s	3.25	1.75	9.04	6.8	2.62	5.88
400m/s	2.8	1.59	6.89	5.08	2.42	2.01
500m/s	2.38	1.6	6.27	5.92	1.87	1.72
1000m/s	1.64	1.38	4.18	4.6	0.89	2.19
1500m/s	1.35	0.95	3.76	1.04	1.22	2.09
2000m/s	1.67	1.04	2.17	0.78	1.11	1.21
5000m/s	1.16	1.18	1.79	0.93	0.65	1.91
synchronous	1	1	1	1	1	1

Table 8.18 The ratios of the maximum relative displacements for Model 1a to EL40EWC in the wave dispersion cases with $d = 1$

	At Abutment 10		At Movement joint 1		At Movement joint 2	
	positive	negative	positive	negative	positive	negative
100m/s	3.15	0.3	2.74	9.38	0.19	4.02
150m/s	2.88	0.21	3.88	8.16	0.58	3.97
200m/s	2.47	0.43	4.4	8.06	0.71	3.15
250m/s	2.13	0.55	4.46	8.87	0.9	2.25
300m/s	1.94	0.67	2.68	8.79	0.98	1.74
400m/s	1.7	0.75	3.79	9.2	0.95	0.89
500m/s	1.54	0.8	3.73	8.02	0.76	0.58
1000m/s	1.34	0.9	1.47	8.89	0.63	0.42
1500m/s	1.38	0.9	0.52	8.16	0.78	0.5
2000m/s	1.33	0.93	0.54	6.16	0.82	0.61
5000m/s	1.19	0.97	0.78	1.76	0.88	0.86
synchronous	1	1	1	1	1	1

Table 8.19 The ratios of the maximum relative displacements for Model 1a to KOBE95EW in the wave dispersion cases with $d = 100$

	At Abutment 10		At Movement joint 1		At Movement joint 2	
	positive	negative	positive	negative	positive	negative
100m/s	3.24	0.28	2.29	9.82	0.2	4.07
150m/s	2.83	0.23	3.41	7.94	0.53	4.09
200m/s	2.47	0.41	4.15	7.74	0.79	3.01
250m/s	2.12	0.57	4.24	9.23	0.94	2.23
300m/s	1.93	0.66	2.74	9.01	1.01	1.74
400m/s	1.73	0.73	4.24	9.58	0.87	1.02
500m/s	1.47	1	2.82	6.19	0.78	0.5
1000m/s	1.36	0.88	1.54	7.85	0.67	0.39
1500m/s	1.38	0.92	0.6	7.77	0.69	0.62
2000m/s	1.33	0.94	0.6	5.17	0.79	0.65
5000m/s	1.2	0.97	0.76	1.81	0.9	0.84
synchronous	1	1	1	1	1	1

Table 8.20 The ratios of the maximum relative displacements for Model 1a to KOBE95EW in the wave dispersion cases with $d = 10$

	At Abutment 10		At Movement joint 1		At Movement joint 2	
	positive	negative	positive	negative	positive	negative
100m/s	3.09	0.16	4.15	12.48	0.58	4.1
150m/s	2.51	0.47	7.21	8.65	0.99	3.65
200m/s	2.25	0.69	3.55	11.67	1.15	2.38
250m/s	2.03	0.76	1.61	16.49	1.52	1.5
300m/s	1.69	0.99	6.31	8.18	1.19	1.35
400m/s	1.54	1.02	2.25	10.07	1.26	0.27
500m/s	1.51	1.1	2.62	5.37	1.12	0.59
1000m/s	1.26	1.05	1.32	10.24	0.66	1.01
1500m/s	1.33	0.99	0.64	11.99	0.84	0.56
2000m/s	1.3	1	1.85	3.62	0.77	1.21
5000m/s	1.27	1.01	1.37	4.66	0.98	0.87
synchronous	1	1	1	1	1	1

Table 8.21 The ratios of the maximum relative displacements for Model 1a to KOBE95EW in the wave dispersion cases with $d = 1$

The differential displacements between the pier supports had little effect on the investigated response parameters even in the wave dispersion cases because the bridge deck was separated by the sliding bearings from the piers in the type of bridges used in this study. The ratios of the response parameters investigated for the longitudinal response of Model 1a subjected to the different earthquake records in the wave dispersion cases to those in corresponding synchronous case are presented in Tables 8.16 to 8.21. The results for the maximum relative displacement of the bridge deck across the movement joint 1 and the maximum relative displacement between the girder end and the top of the Abutment 10 are similar to those in the travelling wave cases, but the results for the maximum relative displacement of the bridge deck across the movement joint 2 are different from those in the travelling wave cases. This is because the displacement of the bridge deck at the left side of the movement joint 2 was almost the same as the displacement of Abutment 1 (fixed to the ground) whose displacement was directly affected by the geometric incoherence effect.

Analysis of the longitudinal responses of long bridges with intermediate movement joints showed that the relative displacements across the movement joints were mainly attributed to the phase shifts between the vibrations of the two frames separated by the movement joints in the asynchronous cases. The relative displacements across the movement joints were greater in the asynchronous input cases than those in the synchronous cases. It is concluded that the effect of asynchronous input motions may be one of the main reasons for many bridge spans falling from their supports in past earthquakes.

CHAPTER 9

CONCLUSIONS AND RECOMMENDATIONS FOR FUTURE RESEARCH

9.1 The Main Achievements of This Research

1. A method for generating asynchronous input motions with dispersion from an original input has been proposed, implemented and demonstrated to successfully analyze the responses of extended structures to asynchronous input motions.
2. The elastic and inelastic responses of long bridges with different configurations to asynchronous input motions conditioned by the natural earthquake records at one pier support have been investigated.
3. The trends of the variations of the elastic and inelastic responses of long bridges to asynchronous input motions with travelling wave velocity and wave geometric incoherence were indicated.
4. Analyses of the longitudinal direction responses of long bridges with movement joints were carried out. The results indicated that the effect of asynchronous input motions might be one of the main reasons for bridge spans falling during past earthquakes.

9.2 The Conclusions Drawn from This Study

It is recognized that the spatial variability of the ground motion has an important effect on the seismic responses of extensive structures, but less well known is how the responses will be affected. The aim of this study was to gain an insight into the effect of asynchronous inputs on the elastic and inelastic response of long bridges in order to improve bridge earthquake resistant design. The main conclusions drawn from this research are listed below.

1. The proposed analytical method for generating the asynchronous input motions in the time domain conditioned by the specified earthquake record at one or more supports produces motions that the variations of simulated accelerations with the separation distance between the supports and the wave propagation velocity follow the autocorrelation function adopted and the spectra of the simulated time-histories at each support and the specified earthquake record are very close to each other. This method is simple, efficient and easily used.

2. It was found that asynchronous input motions had a significant effect on the responses of long bridges and the responses to asynchronous inputs could be more serious than those from synchronous inputs in both the transverse and the longitudinal directions. Hence the assumption of identical support (synchronous) ground motion may lead to unconservative results, especially for bridges with irregular pier heights and/or bridges with stiffer piers. Conversely, however, for regular bridges with flexible piers, the response to asynchronous inputs can be less than the response to synchronous input.

3. The velocity of the travelling wave played an important role in the transverse response of the long bridges when only the wave-passage effect was considered. The response was dominated by the dynamic component when the travelling wave velocity was high (above approximately 1000 m/s) and was little different to the response to synchronous input. The response was dominated by the pseudo-static component when the travelling wave velocity was low (below approximately 300 m/s). The velocity of the travelling wave (150 ~ 300 m/s) at which the transverse response had a minimum value, mainly depended on the stiffness of the bridge model. The stiffer the bridge, the higher this velocity.

4. The response is dependent on the direction of wave travel i.e. which end of the bridge the earthquake comes from.

5. The geometric incoherence effect affected the total transverse responses of long bridges through the pseudo-static components of the response. The stiffer

the bridge, the greater was the effect of the geometric incoherence. The responses for the dispersion cases for all configurations studied were more critical than those for the travelling wave cases and the synchronous case when wave dispersion was greater (reducing 'd' factor).

6. Comparing the responses of bridges to asynchronous input motions with same earthquake record but different input scale factors, it can be seen that the same conclusions are generally valid for inelastic response as for elastic response.

7. Analysis of the longitudinal responses of long bridges with intermediate movement joints showed that the relative displacements across the movement joints were mainly attributed to the phase shifts between the vibrations of the two frames separated by the movement joints in the asynchronous cases. The relative displacements across the movement joints were greater in the asynchronous input cases than those in the synchronous cases. It is concluded that the effect of asynchronous input motions may be one of the main reasons for many bridge spans falling from their supports in past earthquakes.

9.3 Recommendations for Future Research

1. **The dispersion factor *d***

   In this research the dispersion factor *d* in the proposed method was used to represent the degree of the wave dispersion. In order to make this method useful for engineers it is necessary to relate the dispersion factor *d* to the real site conditions by comparing the generated motions with the records from seismograph arrays at different sites.

2. **The local site effect**

   In this study only the wave-passage and geometric incoherence effects of the variability of the seismic motions were considered in the analyses of the responses of the long bridges subjected to the asynchronous input motions. However, the local site effect will affect the seismic response of a long bridge significantly if the local soil conditions differ from pier to pier. It is necessary

to establish a simple technique to consider the local site effects in seismic response analysis. It would be advisable to modify the generated asynchronous input motions according to the local site conditions.

3. **The verification of the analysis technique**

   Comparing the responses of long bridges subjected to the recorded asynchronous seismic motions with those subjected to the conditionally simulated time-histories will be valuable for the verification and the improvement of the technique for the generation of the asynchronous input motions for engineering purposes.

4. **The multidimensional seismic motions**

   In this study it was assumed that the seismic motions act in a single direction only. It is desirable that the effects of multidimensional asynchronous seismic input motions on the responses of extended structures are also considered.

5. **The foundation compliance effect**

   The foundation compliance has a significant effect on the seismic responses of the structures. It will be useful that the effect of foundation flexibility on the responses of structures to asynchronous input motions is taken into account.

REFERENCES

Abdel-Ghaffar, A., and L. I. Rubin. (1982). "Suspension Bridge Response to Multiple-Support Excitation." *Journal of Engineering Mechanics, ASCE*, Vol. 108, 419-435.

Abrahamson, N. A., et al. (1987). "The SMART-1 Accelerograph Array (1980-1987): A Review." *Earthquake Spectra*, Vol. 3 (No. 2).

Bayrak, O., (1996). "Effect of Multiple Seismic Input on the Response of Long Multi-span Bridges." *Eleventh World Conference on Earthquake Engineering*. Acapulco, Mexico, June 23 ~ 28

Berrah, M., and E. Kausel. (1992). "Response Spectrum Analysis of Structures Subjected to Spatially Varying Motions." *Earthquake Engineering and Structural Dynamics*, Vol. 21, 461-470.

Bogdanoff, J. L., J. E. Goldberg, and A. J. Schiff. (1965). "The effect of Ground Transmission Time on the Response of Long Structures." *Bulletin of the Seismological Society of America*. Vol. 55 (No. 3), 627-640.

Bowles, J. E. (1982). *Foundation Analysis and Design* (Third Edition), McGraw-Hill Kogakusha Ltd,

Carr, A. J. (2001). "RUAUMOKO3D." Department of Civil Engineering, University of Canterbury, Christchurch, New Zealand.

Carter, D. P. (1984). "A Nonlinear Soil Model for Predicting Lateral Pile Response." *Report No. 359*, Department of Civil Engineering, University of Auckland, New Zealand.

Clough, R. W., and J. Penzien. (1993). *Dynamics of Structures*, McGraw-Hill, New York.

Collins, M. P., and D. Mitchell. (1991). *Prestressed Concrete Structures*, Prentice Hall, Englewood Cliffs, N. J.

Dagpunar, J. (1988). *Principles of Random Variate Generation*, Clarendon Press, Oxford.

Deodatis, G., and Shinozuka, M. (1989). "Simulation of Seismic Ground Motion Using Stochastic Waves." *Journal of Engineering Mechanics, ASCE*, Vol. 115(No.12), 2723-2737.

Dodd, Larry (1992). "*The dynamic behaviour of reinforced-concrete bridge piers subjected to New Zealand seismicity* " a thesis submitted in partial fulfilment of the requirements for the degree of Doctor of Philosophy in Civil Engineering at the University of Canterbury, Christchurch, New Zealand

EERI. (1995). "Northridge Earthquake Reconnaissance Report." *Earthquake Spectra*, Special Supplement to Vol. 11.

EERI. (1991). "Costa Rica Earthquake Reconnaissance Report." *Earthquake Spectra*, Special Supplement to vol.7.

EERI. (1990). "Loma Prieta Earthquake Reconnaissance Report." *Earthquake Spectra*, Special Supplement to Vol. 6.

Fäh, D., Iodice, C., Suhadolc, P. and Panza, G.F. (1993). "A New Method for the Realistic Estimation of Seismic Ground Motion in Megacities: the case of Rome." *Earthquake Spectra*, Vol. 9, 643-668.

Fenves, G. L., and M. Ellery. (1998). "Behavior and Failure Analysis of a Multiple-Frame Highway Bridge in 1994 Northridge Earthquake." *Report No. PEER 98/08*, University of California, Berkeley, California.

Fung, G. G., et al. (1971). "Field Investigation of Bridge Damage in the San Fernando Earthquake." *Technical Report*, Bridge Department, Division of Highways, California Department of Transportation, Sacramento, California.

Hao, H., C. S. Oliveira and J. Penzien. (1989). "Multiple-Station Ground Motion Processing and Simulation Based on SMART-1 Array Data." *Nuclear Engineering Design*, Vol. 111, 293-310.

Harichandran, R. S. (1999). "Spatial Variation of Earthquake Ground Motion" Department of Civil and Environmental Engineering, Michigan State University

Harichandran, R. S. (1991). "Estimating the Spatial Variation of Earthquake Ground Motion from Dense Array Recordings" *Structural Safety*, Vol. 10, 213-233

Harichandran, R. S., and W. Wang. (1988). "Response of Indeterminate Two-Span Beams to Spatially Varying Seismic Excitation." *Earthquake Engineering and Structural Dynamics*, Vol. 19, 173-187.

Harichandran, R. S., and E. H. Vanmarcke. (1986). "Stochastic Variation of Earthquake Ground Motion in Space and Time." *Journal of Engineering Mechanics, ASCE*, Vol. 112, 154-174.

Heredia-Zavoni, E., and E. H. Vanmarcke. (1994). "Seismic Random-Vibration Analysis of Multisupport Structural Systems." *Journal of Engineering Mechanics, ASCE*, Vol.120(No.5).

Hoshiya, M. and K. Ishii (1983). "Evaluation of Kinematic Interaction of Soil-Foundation Systems by a Stochastic Model." *Soil Dynamics and Earthquake Engineering*, No. 2, 128-134.

Hoshiya, M. (1995). "Kriging and Conditional Simulation of Gaussian Field." *Journal of Engineering Mechanics, ASCE*, Vol. 121(No. 2), 181-186.

Hoshiya, M. (1994). "Conditional Simulation of Stochastic Field." *Structural Safety and Reliability*, G. I. Schueller, M. Shinozuka, and J. T. P. Yao, ed., Balkema, Rotterdam.

Hoshiya, M., and O. Marugama. (1994). "Stochastic interpolation of Earthquake wave propagation." *Structural Safety and Reliability*, G. I. Schueller, M. Shinozuka, and J. T. P. Yao, ed., Balkema, Rotterdam.

Housner, G. (1990). "Competing Against Time, report to Governor George Deukmejian from the Governor's Board of Inquiry on the 1989 Loma Prieta Earthquake." Department of General Services, State of California, North Highlands, CA.

Iannuzzi, A., and P. Spinelli. (1987). "Artificial Wind Generation and Structural Response." *Journal of Structural Engineering, ASCE*, Vol. 113(No. 12), 2382-2398.

Jankowski, R., and K. Wilde. (2000). "A Simple Method of Conditional Random Field Simulation of Ground Motions for Long Structures." *Engineering Structures*, Vol. 22, 552-561.

Journel, A. G. (1974). "Geostatistics for Conditional Simulation of Ore Bodies" *Economic Geology*, Vol. 69, 673-687

Journel, A. G. and C. J. Huijregts (1978). *Mining Geostatistics*, Academic Press, London, England.

Kameda, H., and H. Morikawa. (1994). "Conditioned Stochastic Process for Conditional Random Fields." *Journal of Engineering Mechanics, ASCE*, Vol. 120(No. 4), 855-875.

Kameda, H., and H. Morikawa. (1992). "Interpolating Stochastic Process for Simulation of Conditional Random Fields." *Probabilistic Engineering Mechanics*, Vol.7(No.4), 243-254.

Kameda, H., and H. Morikawa. (1991). "Simulation of Conditional Random Field - a Basis for Regional Seismic Monitoring for Urban Earthquake Hazards Mitigation." *U.S.-Italy-Japan Workshop/Seminar on Intelligent System*, University of Perugia, Italy.

Kareem, A., and Y. Li. (1992). "Digital Simulation of Wind Load Effects." *ASCE Specialty Conference on Probabilistic Mechanics and Structural and Geotechnical Reliability*, New York, N. Y.

Kareem, A. (1978). "Wind Exited Motion of Building," PhD thesis, Colorado State University, Fort Collins, Colo.

Kiureghian, A. D. (1996). "A Coherency Model of Spatially Varying Ground Motions." *Earthquake Engineering and Structural Dynamics*, Vol. 25, 99-111.

Kiureghian, A. D., and A. Neuenhofer. (1992). "Response Spectrum Method for Multiple-Support Seismic Excitation." *Earthquake Engineering and Structural Dynamics*, Vol. 21, 713-740.

Krige, D. G. (1966). "Two-Dimensional Weighted Moving Average Trend Surfaces for Ore Valuation." *Journal of South African Institute of Mining and Metallurgy*, 13-38.

Loh, C. H., and Y. Yeh (1988). "Spatial Variation and Stochastic Modelling of Seismic Differential Ground Motion" *Earthquake Engineering and Structural Dynamics*, Vol. 16, 583-596

Luco, J. E., and H. L. Wong. (1986). "Response of a Rigid Foundation to a Spatially Random Ground Motion." *Earthquake Engineering and Structural Dynamics*, Vol. 14, 891-908.

Matheron, G. (1967) "Kriging or polynomial interpolation procedures" *Can. Inst. Min. Bull.* 60, 1041.

Monti, G., C. Nuti, and P. E. Pinto. (1996). "Nonlinear Response of Bridges Under Multisupport Excitation." *Journal of Structural Engineering, ASCE*, Vol. 122(No. 10).

National Oceanic & Atmospheric Administration Website. "www.ngdc.noaa.gov."

Oliveira, Carlos S., Hong Hao and J. Penzien (1991). "Ground Motion Modeling for Multiple-Input Structural Analysis." *Structural Safety*, 10, 79-93

Park, R. (editor) (1994). "*Seismic Design and Retrofitting of Reinforced Concrete Bridges*" Proceedings of the Second International Workshop held in Queenstown, New Zealand, August 9 ~ 12.

Park, R., et al. (1995). "The Hyogo-Ken Nanbu Earthquake of 17 January 1995, Report of the NZNSEE Reconnaissance Team." *Bulletin of the New Zealand National Society for Earthquake Engineering*, Vol. 28(No. 1).

Poulos, H. G. (1971). "Behaviour of Laterally Loaded Piles _ Single Piles." *Journal of the Soil Mechanics and Foundation Division*, ASCE, Vol. 97(No. SM5)

Priestley, M. J. N., F. Seible, and G. M. Calvi. (1996). *Seismic Design and Retrofit of Bridges*, John Wiley & Sons, Inc.

Priestley, M. J. N., F. Seible, and G. MacRae. (1995). "The Kobe Earthquake of January 17, 1995: Initial Impressions from a Quick Reconnaissance." *Report SSRP-95/03*, University of California, San Diego.

Priestley, M. J. N., F. Seible, and Yuk Hon Chai. (1992). "Design Guidelines for Assessment Retrofit and Repair of Bridges for Seismic Performance." *Report Number SSRP 92/01*, Department of Applied Mechanics and Engineering Science, University of California, San Diego.

Priestley, M. J. N., and R. Park. (1984). "Strength and Ductility of Bridge Substructures." *Bulletin No.71*, Road Research Unit, National Roads Board, Wellington, New Zealand.

Ramadan, O., and M. Novak. (1993). "Simulation of Spatially Incoherent Random Ground Motions." *Journal of Engineering Mechanics, ASCE*, Vol. 119(No. 5), 997-1016.

Reed, D. A., and R. H. Scanlan. (1984). "Autoregressive Representation of Longitudinal, Lateral, and Vertical Turbulence Spectra." *Journal of Wind Engineering and Aerodynamics*, Vol. 17, 199-214.

Ren, Y. J., I. Elishakoff, and M. Shinozuka. (1995). "Conditional Simulation of Multi-Variate Gaussian Fields via Generalization of Hoshiya's Technique." *Chaos, Solitons & Fractals*, Vol. 5(No. 11), 2181-2189.

Rice, S. O. (1954). "Mathematical Analysis of Random Noise." Noise and Stochastic Processes, N. Wax, ed., Dover, New York.

Samaras, E., M. Shinozuka, and A. Tsurui. (1985). "ARMA Representation of random Vector Processes." *Journal of Engineering Mechanics, ASCE*, Vol. 111(No. 3), 449-461.

Shinozuka, M., and R. Zhang. (1996). "Equivalence Between Kriging and CPDF Method for Conditional Simulation." *Journal of Engineering Mechanics, ASCE*, Vol. 122(No. 6), 530-538.

Shinozuka, M., and G. Deodatis. (1991). "Simulation of Stochastic Processes by Spectral Representation. " *Applied Mechanics Reviews,* Vol. 44 (No. 4), 191-204.

Shinozuka, M. (1987). "Stochastic Fields and Their Digital Simulation." Stochastic Methods in Structural Dynamics, G. I. Shueller, and M. Shinozuka, ed., Martinus Nijihoff, Dordrecht, The Netherlands.

Shinozuka, M. (1974). "Digital Simulation of Random Processes in Engineering Mechanics with the Aid of FFT Technique." Stochastic Problems in Mechanics, S. T. Ariaratnam, and H. H. E. Leipholz, ed., University of Waterloo Press, Waterloo.

Shinozuka, M. (1972). "Monte Carlo Solution of Structural Dynamics." *Computers and Structures*, Vol. 2, 855-874.

Shinozuka, M., and C. M. Jan. (1972). "Digital Simulation of Random Processes and its Applications." *Journal of Sound and Vibration*, Vol. 25(No. 1), 111-128.

Shuang Jin, L. D. L., and Shahram Sarkani. (1997). "Efficient Simulation of Multidimensional Random Fields." *Journal of engineering Mechanics, ACSE*, Vol. 123(No. 10), 1082-1089.

Singh, S. P., and G. L. Fenves, (1994). "Earthquake Response of ' Structure A' Using Nonlinear Dynamic Analysis" *Seismic Design and Retrofitting of Reinforced Concrete Bridges,* Proceedings of the Second International Workshop held in Queenstown, New Zealand, August 9 ~ 12.

Somaini, D. R. (1987). "Seismic Behavior of Girder Bridges for Horizontally Propagating Waves." *Earthquake Engineering and Structural Dynamics*, Vol. 15, 777-793.

Spanos, P. D., and M. P. Mignolet. (1990). "Simulation of Stationary Random Processes: Two-Stage MA to ARMA approach." *Journal of Engineering Mechanics, ASCE*, Vol.116(No. 3), 620-641.

Tseng, W. S., and J. Penzien. (1973). "Analytical Investigations of Seismic Response of Long Multiple Span Highway Bridges." *Report No. EERC 73-12*, College of Engineering, University of California, Berkeley, California.

Tzanetos, N., et al. (1998). " Inelastic Dynamic Response of RC Bridges to Non-synchronous Earthquake Input Motion" *ESEE Research Report* No 98-6, Department of Civil Engineering, Imperial College of Science and Technology, London, UK

Vanmarcke, E. H., E. Herdia-Zavoni, and G. A. Fenton. (1993). "Conditional Simulation of Spatially Correlated Earthquake Ground Motion." *Journal of engineering Mechanics, ASCE*, Vol. 119(No. 11), 2333-2352.

Vanmarcke, E. H., and G. A. Fenton. (1991). "Conditional Simulation on Local Fields of Earthquake Ground motion." *Structural Safety*, Vol. 10, 247-264.

Vanmarcke, E. H. (1977). "Structural Response to Earthquakes." Seismic Risk and Engineering Decision, C. Lomnitz, ed., McGraw-Hill, New York, N. Y.

Venkataramana, K., K. Kawano, and S. Tamae (1996). "Earthquake Response of Multi-Span Continuous Bridges." *Eleventh World Conference on Earthquake Engineering*, Acapulco, Mexico, June 23-28.

Vesic, A. S. (1961) "Beams on Elastic Subgrade and the Winkler Hypothesis." *Fifth International Conference on Soil Mechanics and Foundation Engineering*, Paris, Vol. 1.

Wald, D. J., L. J. Burdich, and P. G. Somerville. (1988). "Simulation of Acceleration Time Histories Close to Large Earthquakes." Proc., Earthquake Engineering and Soil Dynamics II-Recent Advances in Ground Motion Evaluation, J. L. V. Thun, ed., ASCE, New York, N. Y.

Werner, Stuart D., Li Chi Lee, Hung Leung Wong, and Mihailo D. Trifunac (1979). "Structural Response to Traveling Seismic Waves " *Journal of the Structural Division, Proceedings of the American Society of Civil Engineers*, Vol. 105, No. ST12

Yang, R., M. J. N. Priestley, F. Seible, and J. Ricles. (1994). "Longitudinal Seismic Response of Bridge Frames Connected by Restrainers." *Structural Systems Research Project, Report SSRP-94/09*, University of California, San Diego.

Yang, J.-N. (1973). "On the Normality and Accuracy of Simulated Random Processes." *Journal of Sound and Vibration*, Vol. 26(No. 3), 417-428.

Yang, J.-N. (1972). "Simulation of Random Envelop Processes." *Journal of Sound and Vibration*, Vol. 25(No. 1), 73-85.

Zerva, A. (1992). "Seismic Ground Motion Simulations form a Class of Spatial Variability Models." *Earthquake Engineering and Structural Dynamics*, Vol. 21, 351-361.

Zerva, A., and M. Shinozuka. (1991). "Stochastic Differential Ground Motion." *Structural Safety*, Vol. 10, 129-143.

Zerva, A. (1990). "Response of Multi-Span Beams to Spatially Incoherent Seismic Ground Motions." *Earthquake Engineering and Structural Dynamics*, Vol. 19,

Appendix

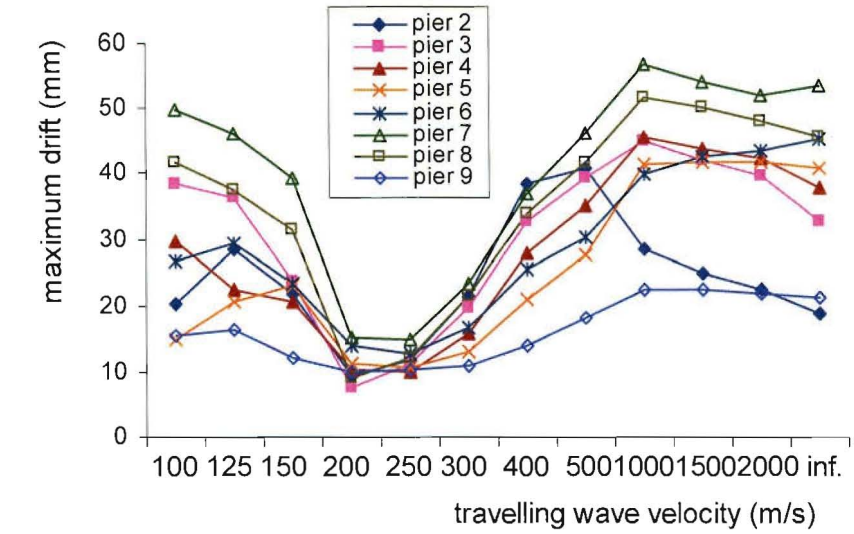

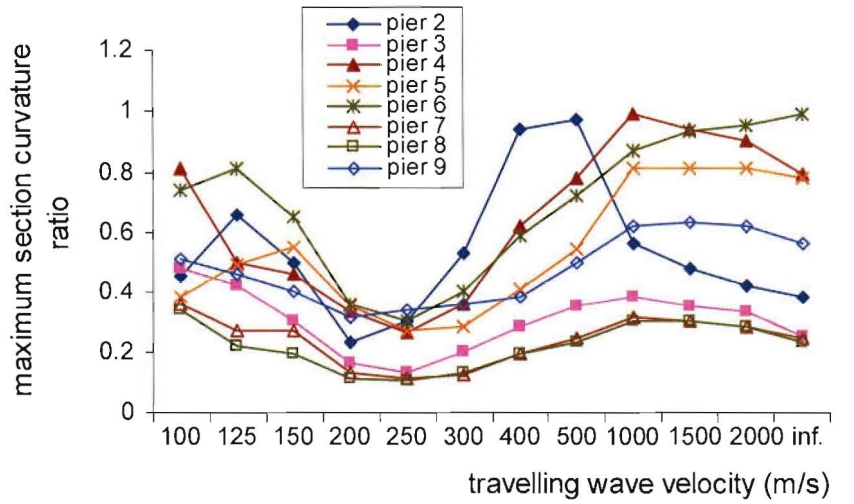

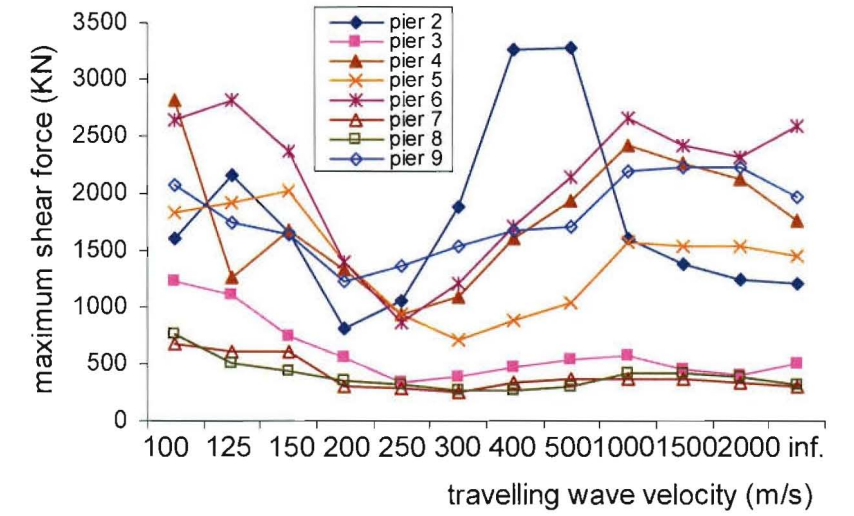

Figure A.1 The responses of Model 2 to EL40NSC with an input scale factor of 0.5

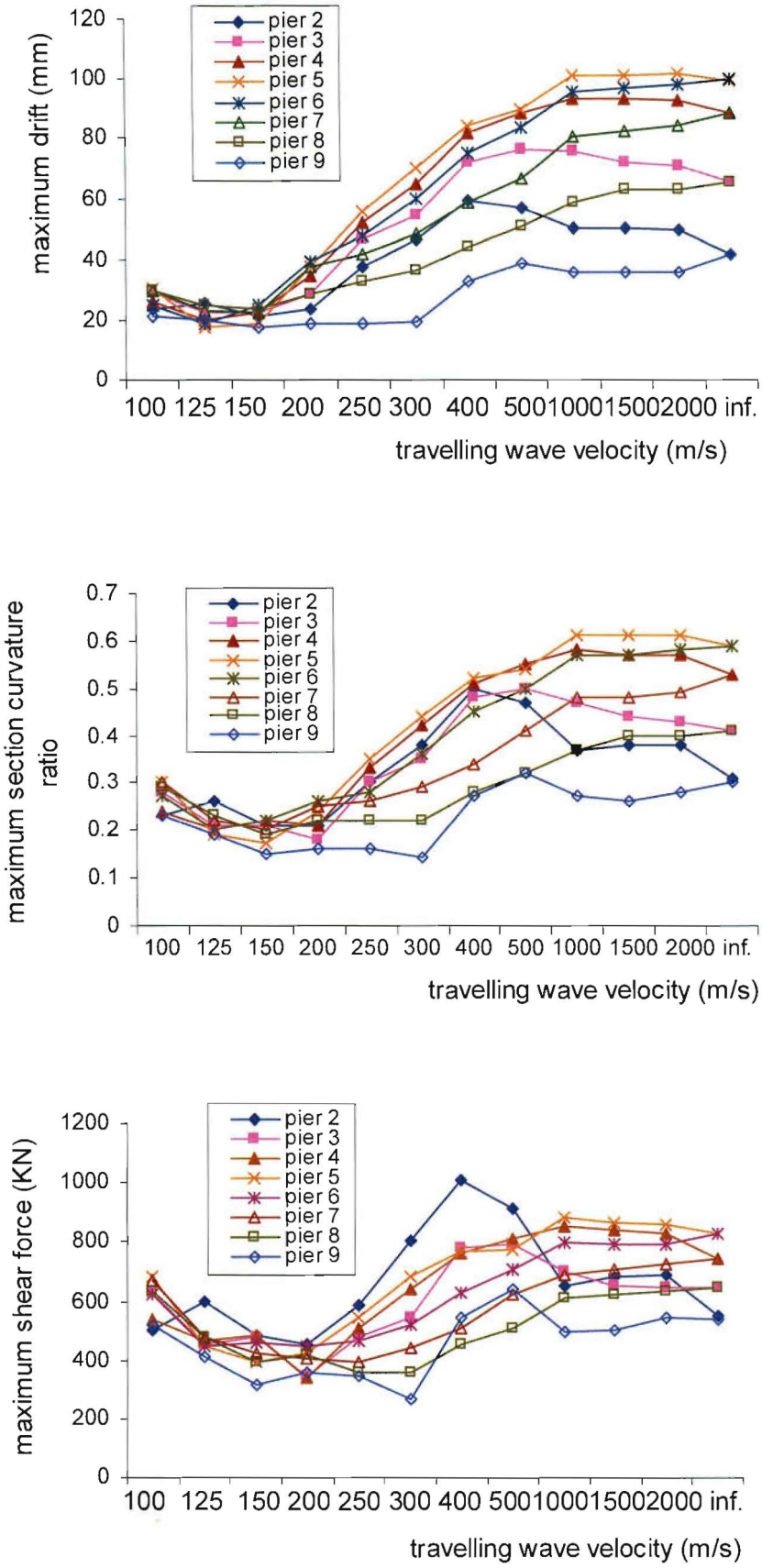

Figure A.2 The responses of Model 3 to EL40NSC with an input scale factor of 0.5

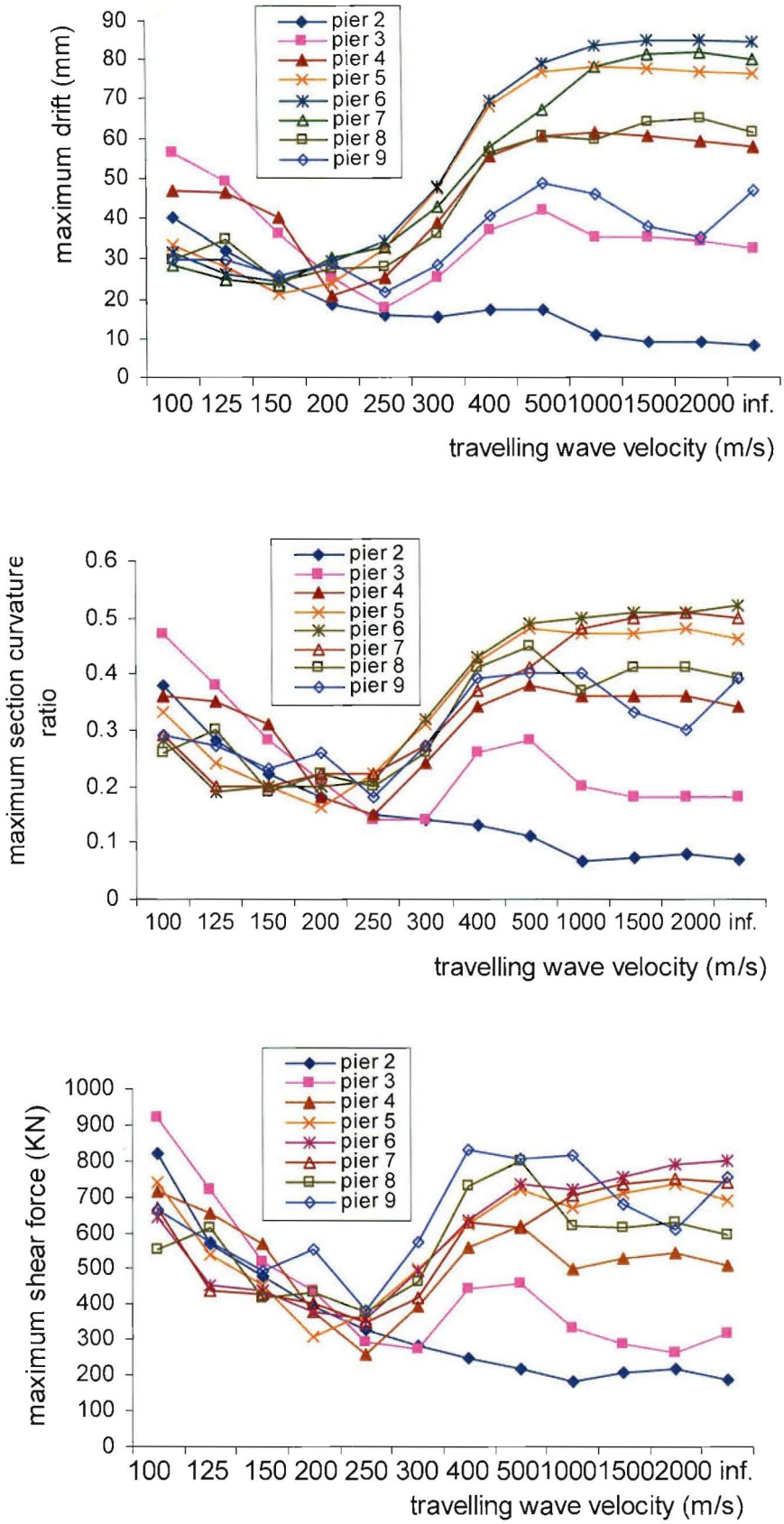

Figure A.3 The responses of Model 4 to EL40NSC with an input scale factor of 0.5

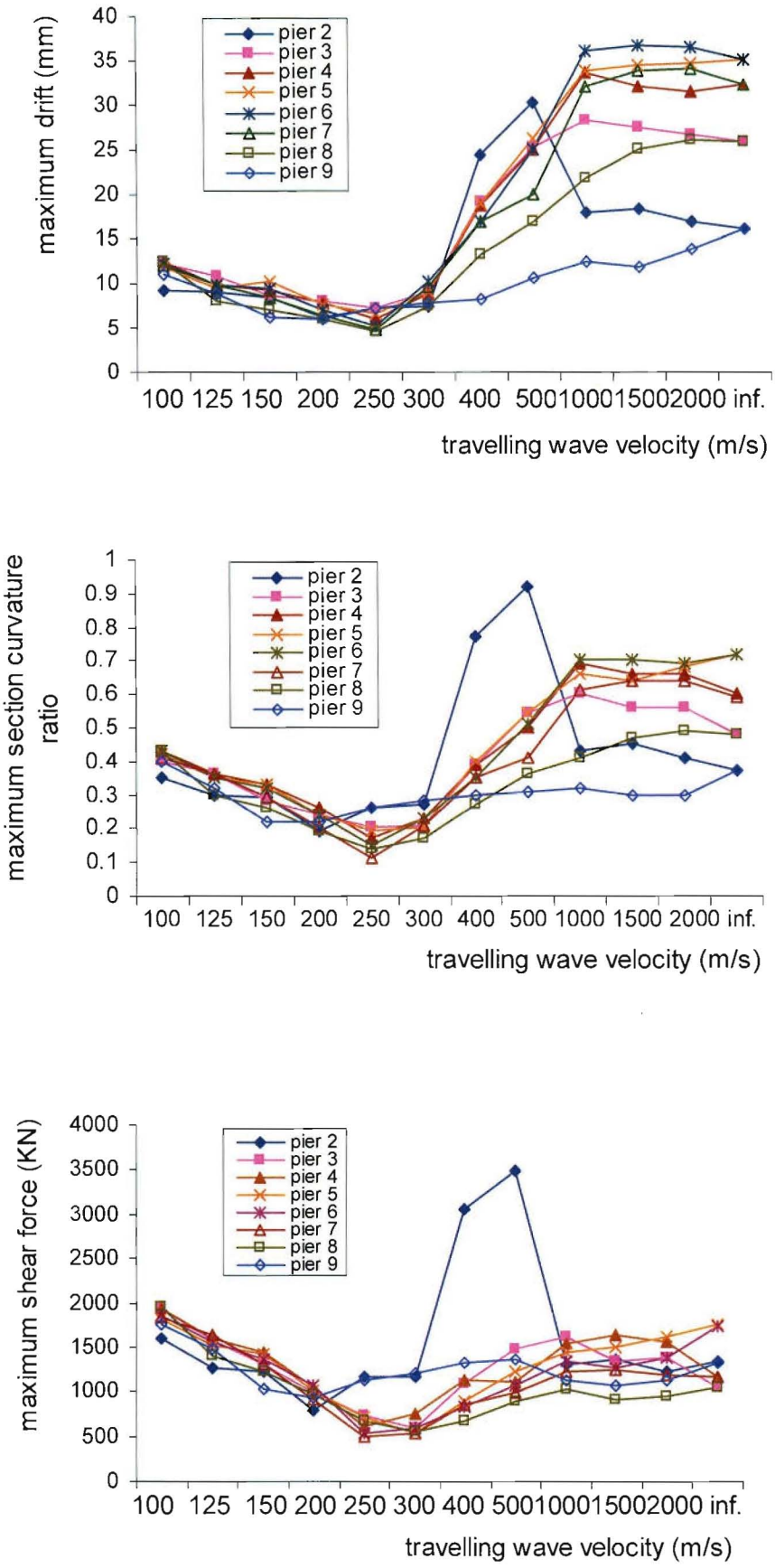

Figure A.4 The responses of Model 5 to EL40NSC with an input scale factor of 0.4

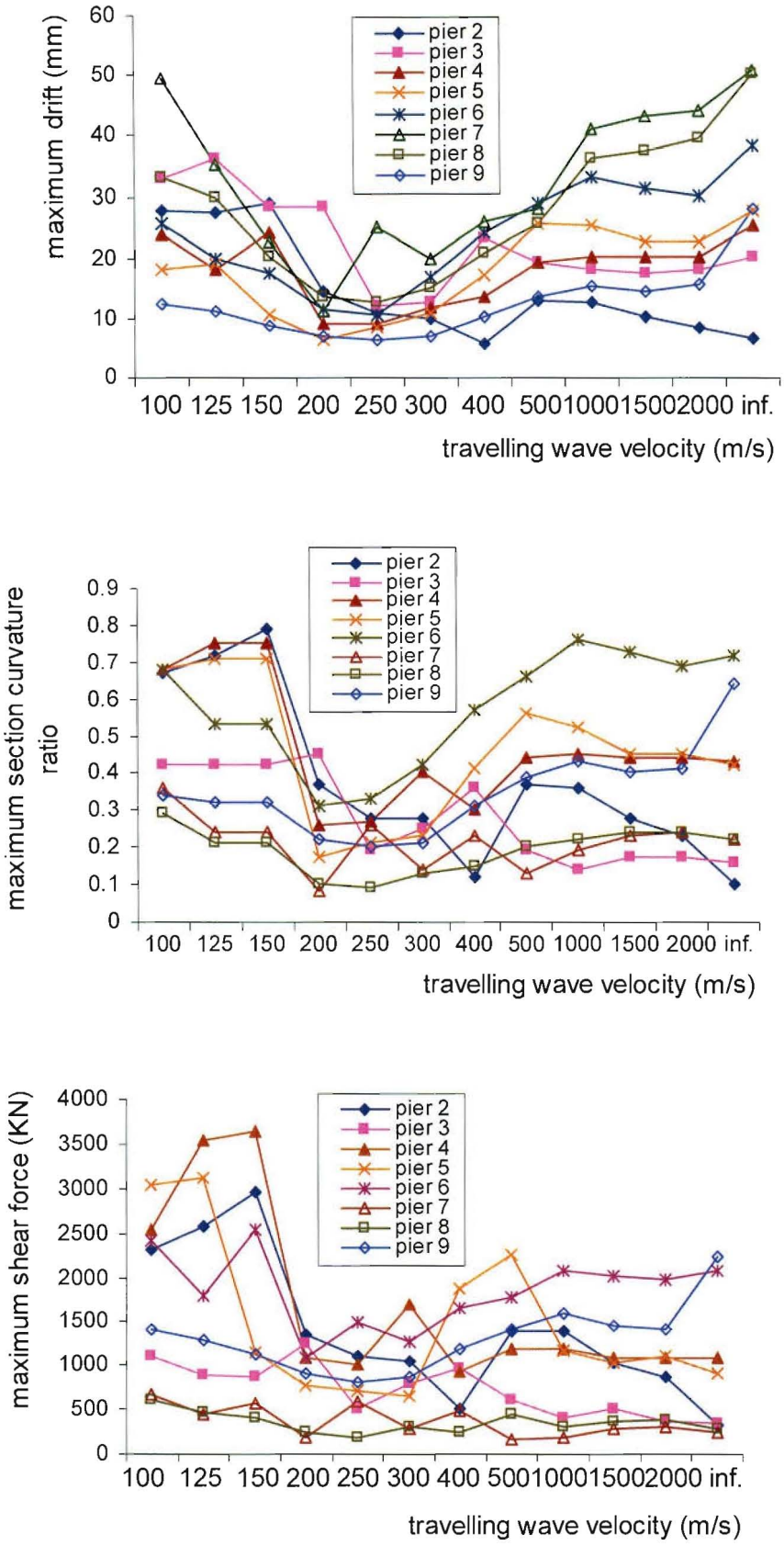

Figure A.5 The responses of Model 1 to SYLM949 with an input scale factor of 0.15 at Abutment 10 and the generated time-histories at the other supports with a dispersion factor d = 100

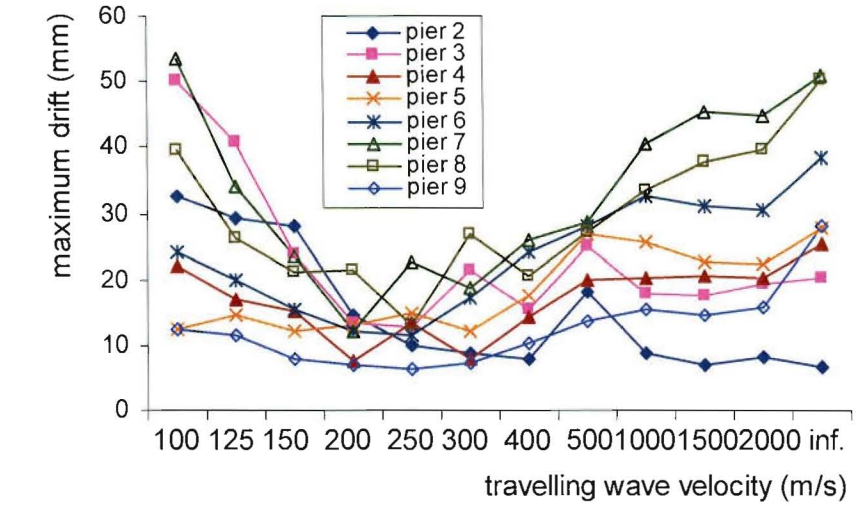

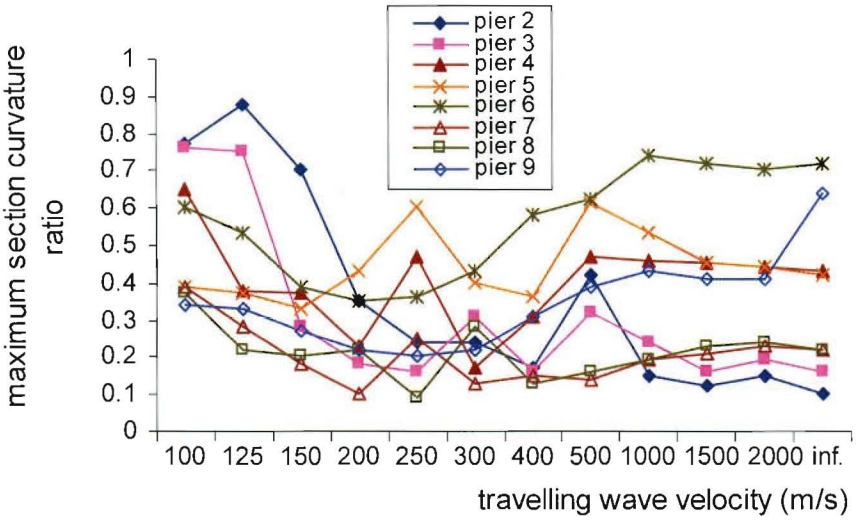

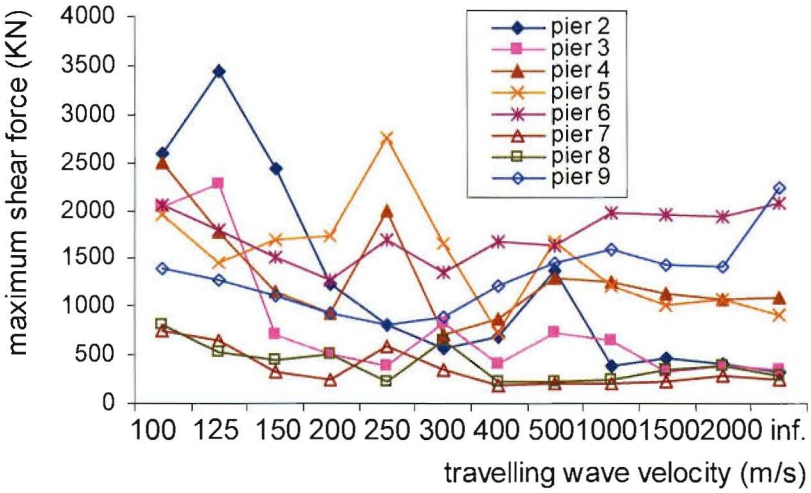

Figure A.6 The responses of Model 1 to SYLM949 with an input scale factor of 0.15 at Abutment 10 and the generated time-histories at the other supports with a dispersion factor d = 50

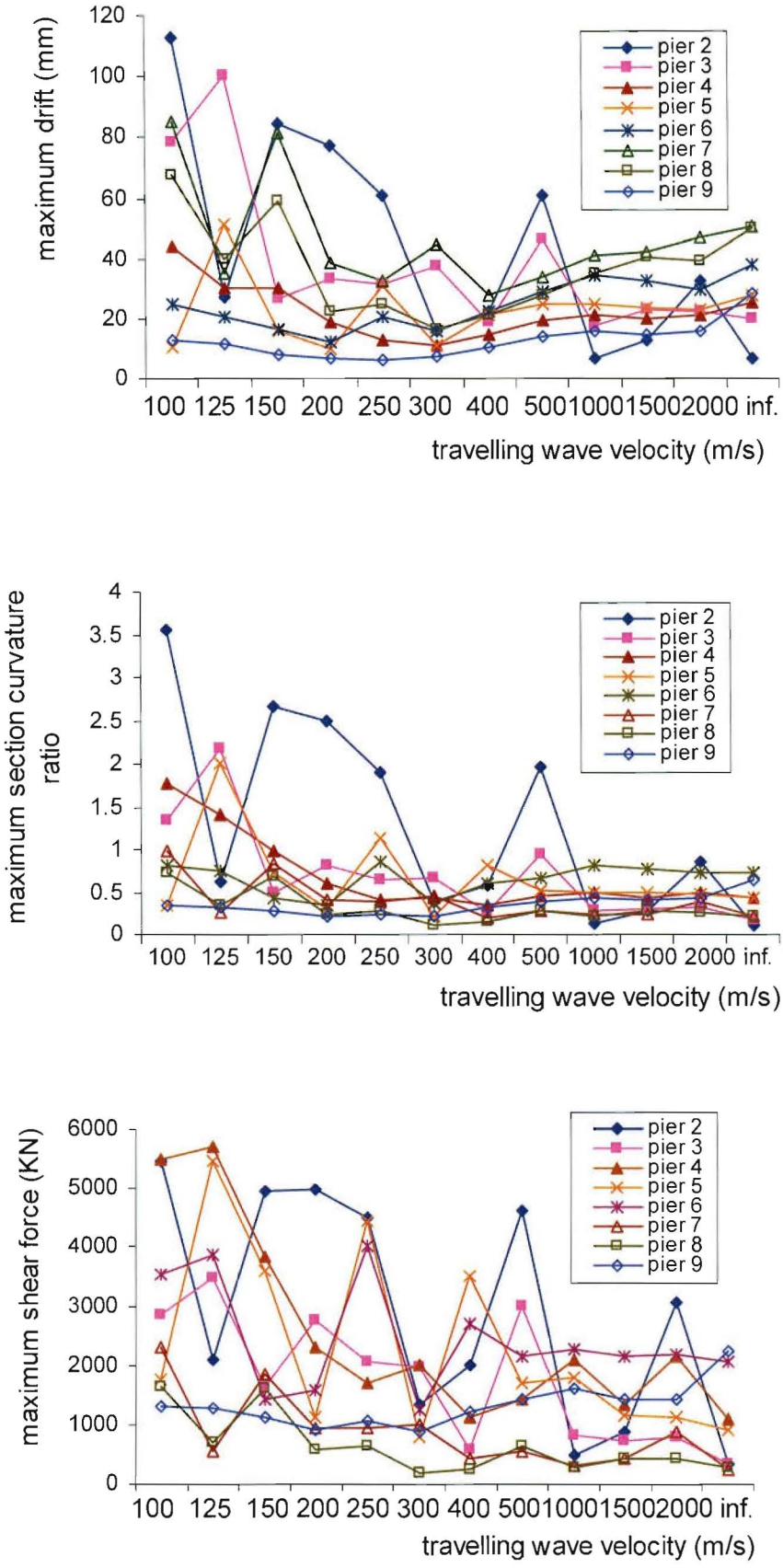

Figure A.7 The responses of Model 1 to SYLM949 with an input scale factor of 0.15 at Abutment 10 and the generated time-histories at the other supports with a dispersion factor d = 10

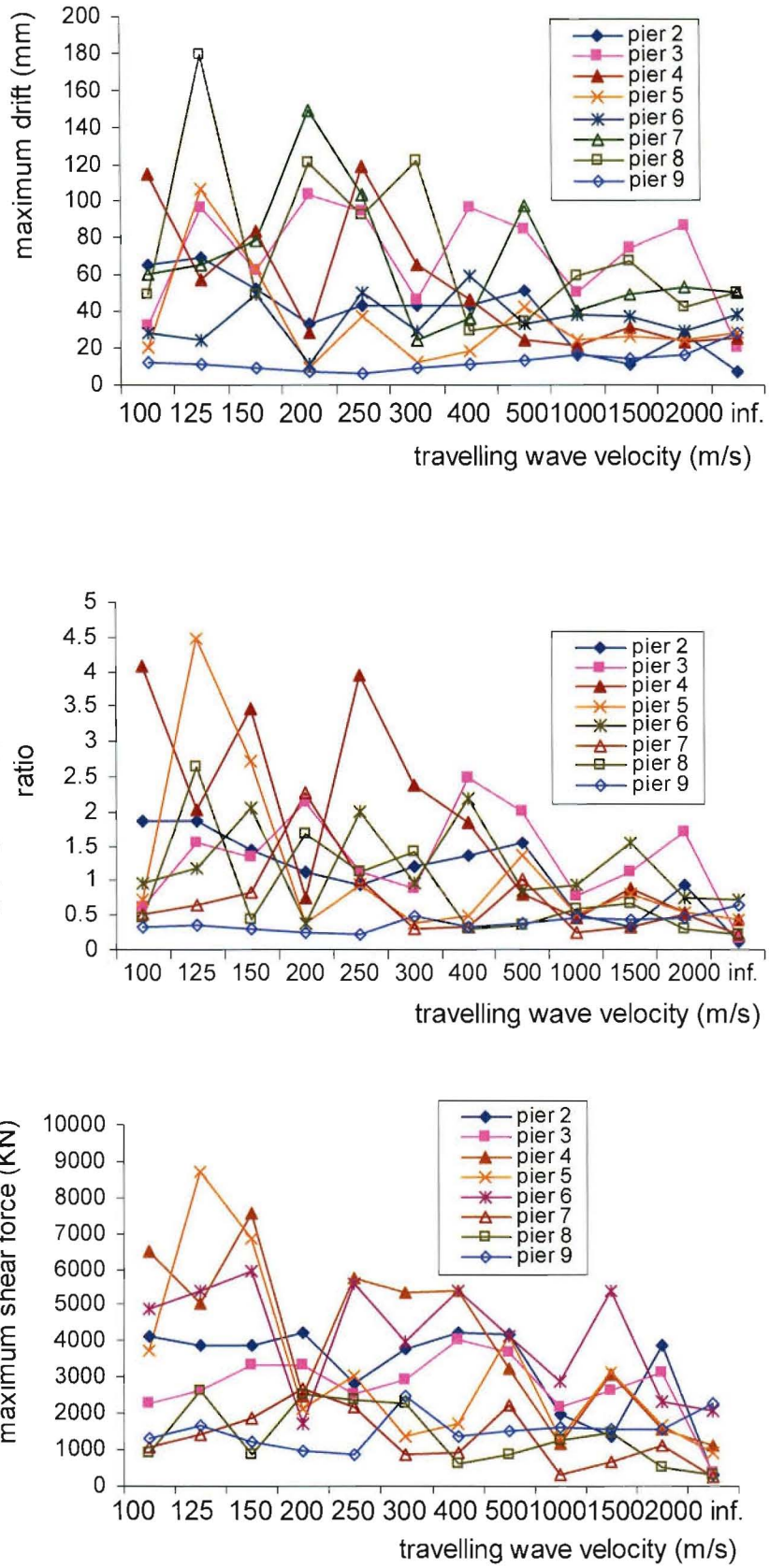

Figure A.8 The responses of Model 1 to SYLM949 with an input scale factor of 0.15 at Abutment 10 and the generated time-histories at the other supports with a dispersion factor d = 1

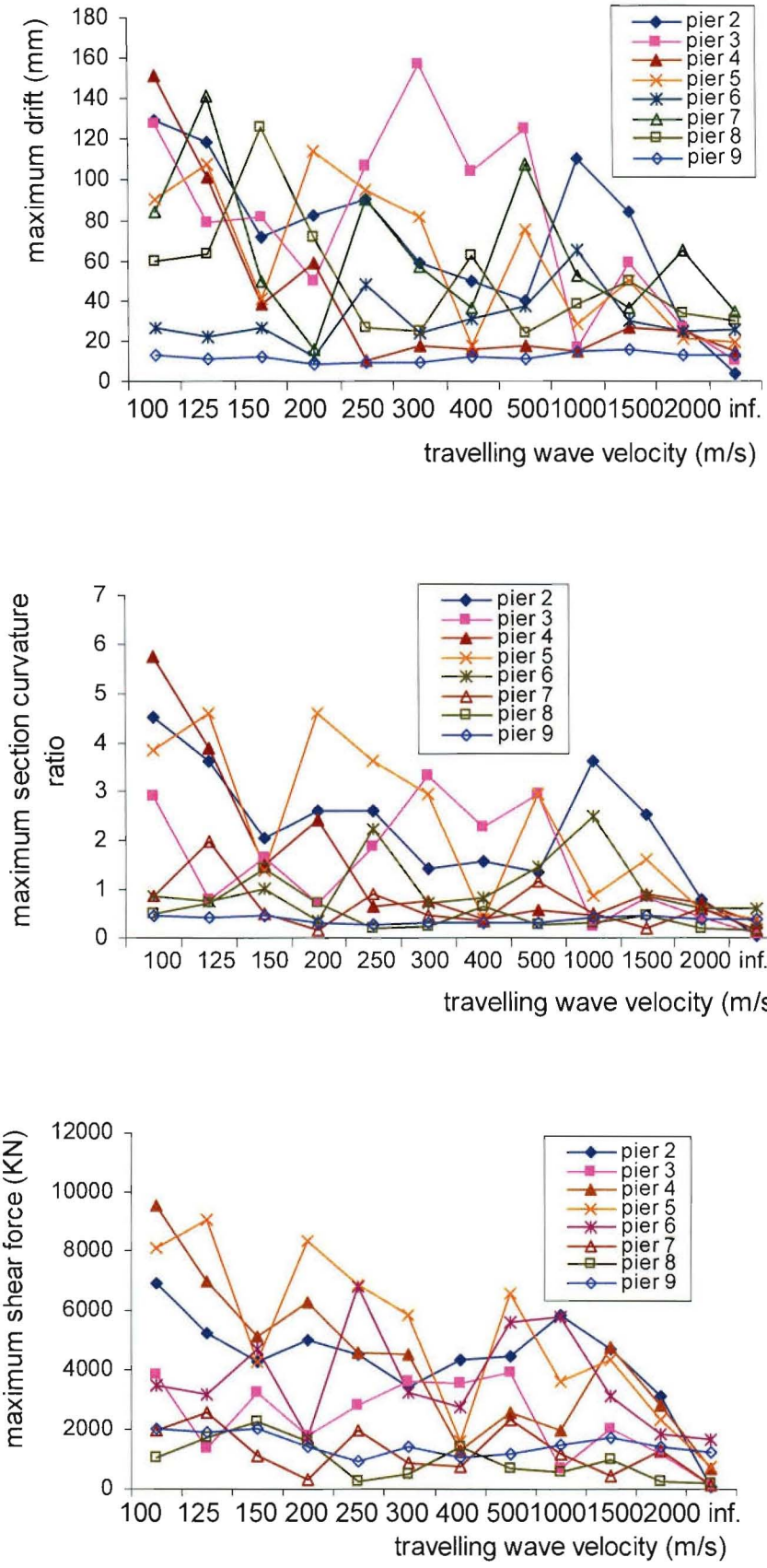

Figure A.9 The responses of Model 1 to MEXSCT1L with an input scale factor of 0.5 at Abutment 10 and the generated time-histories at the other supports with a dispersion factor d = 100

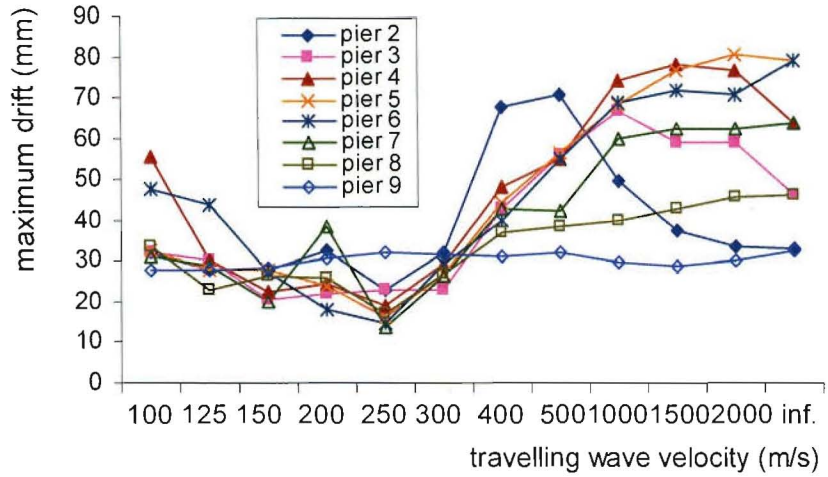

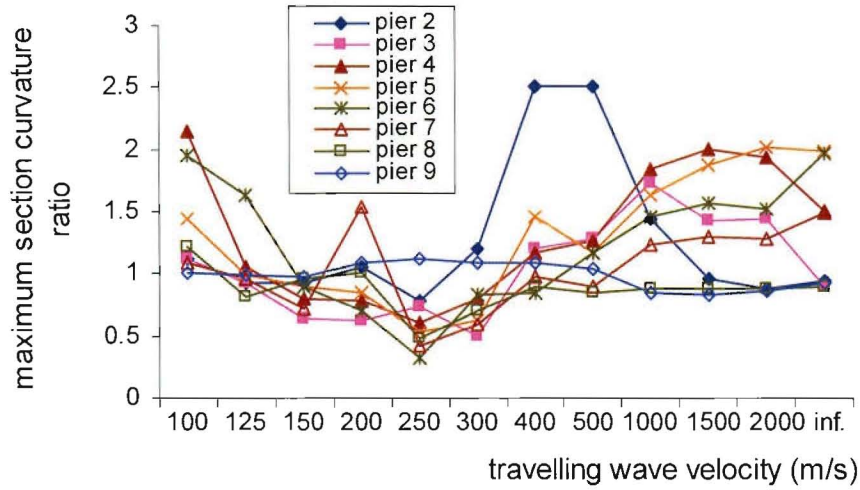

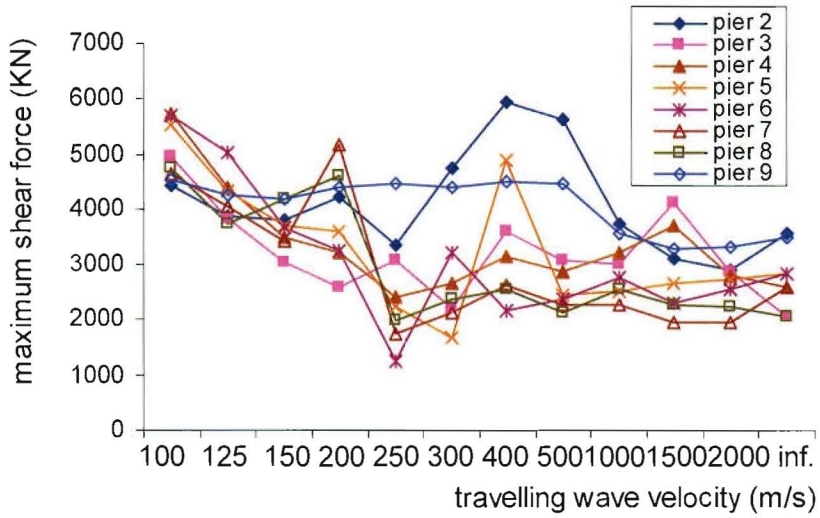

Figure A.10 The responses of Model 5 to EL40NSC with an input scale factor of 1 at Abutment 10 and the generated time-histories at the other supports with a dispersion factor d = 100

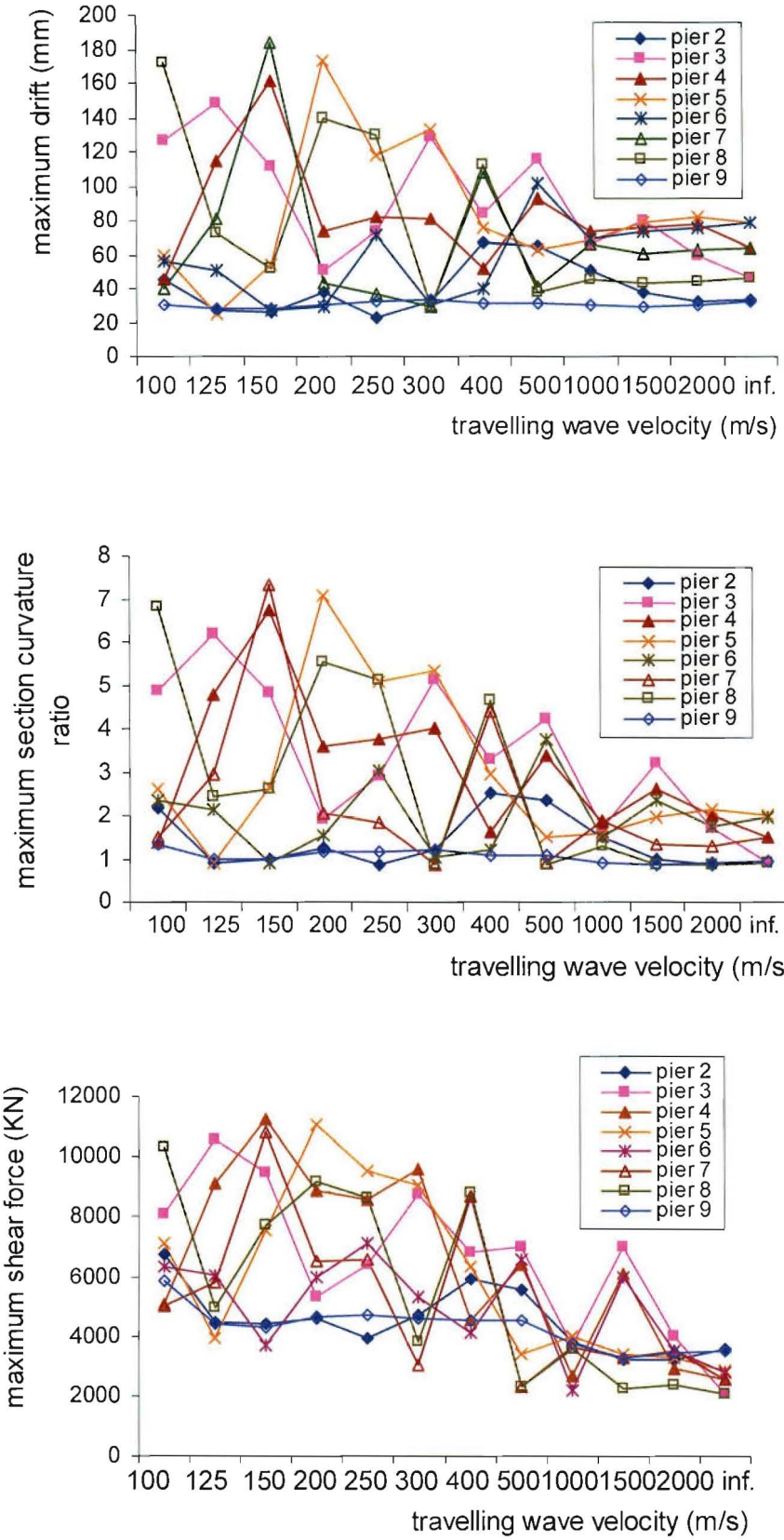

Figure A.11 The responses of Model 5 to EL40NSC with an input scale factor of 1 at Abutment 10 and the generated time-histories at the other supports with a dispersion factor d = 10

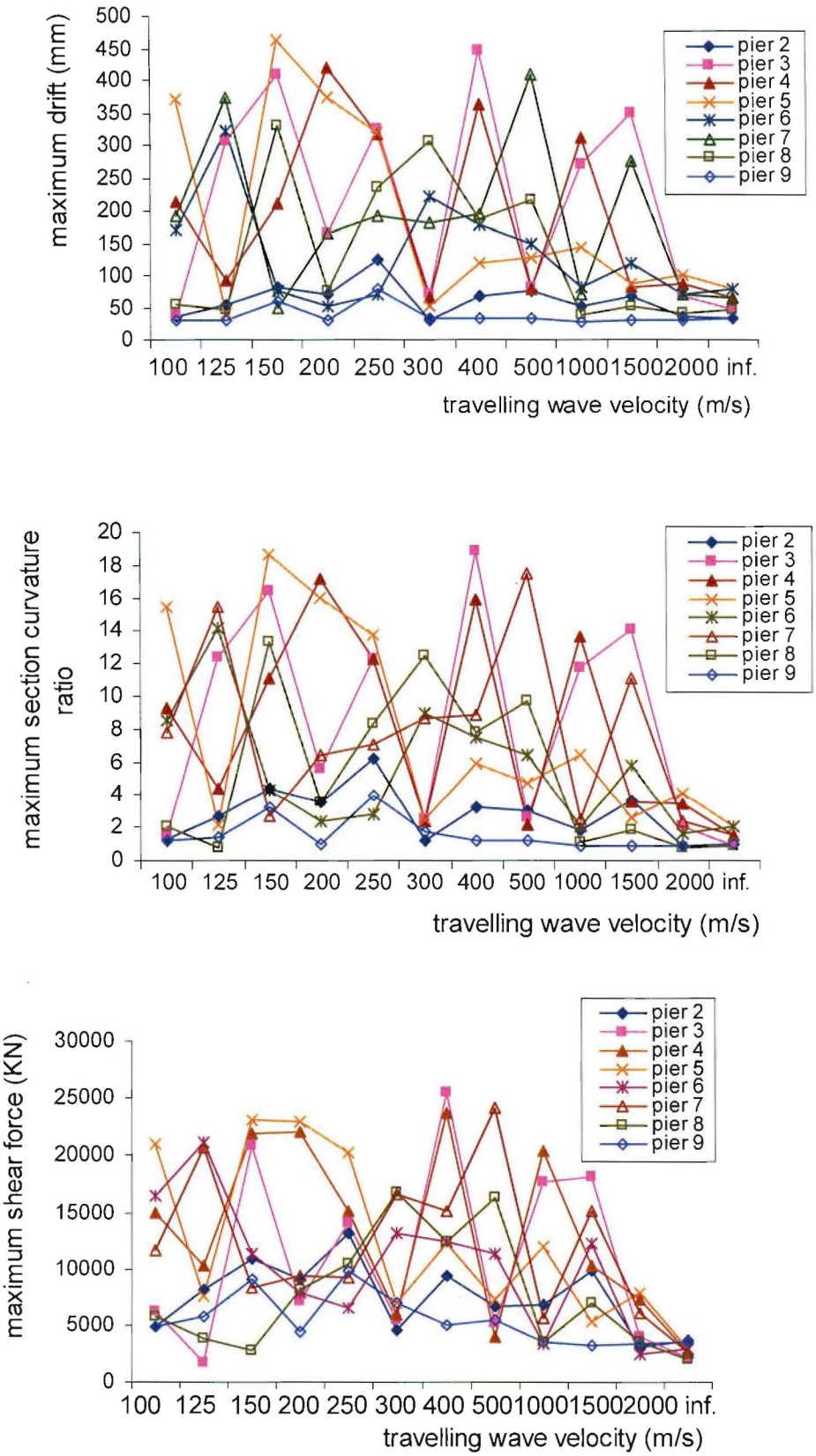

Figure A.12 The responses of Model 5 to EL40NSC with an input scale factor of 1 at Abutment 10 and the generated time-histories at the other supports with a dispersion factor d = 1